2014

# System Analysis with Improved Thermo-Mechanical Fuel Rod Models for Modeling Current and Advanced LWR Materials in Accident Scenarios

Ian Edward Porter
*University of South Carolina*

## Recommended Citation

Porter, I. E.(2014). *System Analysis with Improved Thermo-Mechanical Fuel Rod Models for Modeling Current and Advanced LWR Materials in Accident Scenarios.* (Doctoral dissertation). Retrieved from https://scholarcommons.sc.edu/etd/3362

# SYSTEM ANALYSIS WITH IMPROVED THERMO-MECHANICAL FUEL ROD MODELS FOR MODELING CURRENT AND ADVANCED LWR MATERIALS IN ACCIDENT SCENARIOS

by

Ian Edward Porter

Bachelor of Science
University of South Carolina, 2010

Master of Science
University of South Carolina, 2011

---

Submitted in Partial Fulfillment of the Requirements

For the Degree of Doctor of Philosophy in

Nuclear Engineering

College of Engineering and Computing

University of South Carolina

2014

Accepted by:

Travis W. Knight, Major Professor

Jamil A. Kahn, Committee Member

Patrick Raynaud, Committee Member

Elwyn Roberts, Committee Member

Lacy Ford, Vice Provost and Dean of Graduate Studies

ProQuest LLC.
789 East Eisenhower Parkway
P.O. Box 1346
Ann Arbor, MI 48106 - 1346

# DEDICATION

This work is dedicated to my fiancé Maggie and family, who has stayed behind me through all of my years of schooling and has kept pushing me through all of the ups and downs along the way.  I couldn’t have done this without them.

# ACKNOWLEDGEMENTS

I would like to acknowledge the U.S. Nuclear Regulatory Commission in its support of my education through the NRC Fellowship and internship opportunity. I would specifically like to acknowledge Dr. Patrick Raynaud at the NRC for bringing me onboard this project and for his support in this research. I would also like to acknowledge the support of my advisor, Dr. Travis Knight, for giving me the opportunity to pursue a PhD at the University of South Carolina. Lastly, I would like to give thanks to Dr. Elwyn Roberts for all of his advice and help in understanding fuel performance.

# ABSTRACT

A nuclear reactor systems code has the ability to model the system response in an accident scenario based on known initial conditions at the onset of the transient. However, there has been a tendency for these codes to lack the detailed thermo-mechanical fuel rod response models needed for accurate prediction of fuel rod failure. This proposed work will couple today's most widely used steady-state (FRAPCON) and transient (FRAPTRAN) fuel rod models with a systems code TRACE for best-estimate modeling of system response in accident scenarios such as a loss of coolant accident (LOCA). In doing so, code modifications will be made to model gamma heating in LWRs during steady-state and accident conditions and to improve fuel rod thermal/mechanical analysis by allowing axial nodalization of burnup-dependent phenomena such as swelling, cladding creep and oxidation. With the ability to model both burnup-dependent parameters and transient fuel rod response, a fuel dispersal study will be conducted using a hypothetical accident scenario under both PWR and BWR conditions to determine the amount of fuel dispersed under varying conditions. Due to the fuel fragmentation size and internal rod pressure both being dependent on burnup, this analysis will be conducted at beginning, middle and end of cycle to examine the effects that cycle time can play on fuel rod failure and dispersal.

Current fuel rod and system codes used by the Nuclear Regulatory Commission (NRC) are compilations of legacy codes with only commonly used light water reactor materials, Uranium Dioxide ($UO_2$), Mixed Oxide ($U/PuO_2$) and zirconium alloys.

However, the events at Fukushima Daiichi and Three Mile Island accident have shown the need for exploration into advanced materials possessing improved accident tolerance. This work looks to further modify the NRC codes to include silicon carbide (SiC), an advanced cladding material proposed by current DOE funded research on accident tolerant fuels (ATF). Several additional fuels will also be analyzed, including uranium nitride (UN), uranium carbide (UC) and uranium silicide ($U_3Si_2$). Focusing on the system response in an accident scenario, an emphasis is placed on the fracture mechanics of the ceramic cladding by design the fuel rods to eliminate pellet cladding mechanical interaction (PCMI). The time to failure and how much of the fuel in the reactor fails with an advanced fuel design will be analyzed and compared to the current $UO_2$/Zircaloy design using a full scale reactor model.

# TABLE OF CONTENTS

# LIST OF TABLES

# LIST OF FIGURES

# LIST OF SYMBOLS

| | |
|---|---|
| m | Meter |
| cm | Centimeter (1x$10^{-2}$ meters) |
| mm | Millimeter (1x$10^{-3}$ meters) |
| µm | Micrometer (1x$10^{-6}$ meters) |
| $\rho$ | Density |
| $\varepsilon$ | Emissivity |
| E | Elastic modulus |
| ftd | Fraction of theoretical density |
| T | Temperature |
| $T_C$ | Temperature (Celcius) |
| $T_K$ | Temperature (Kelvin) |
| $T_{melt}$ | Melting temperature |
| k | Thermal conductivity |
| $c_p$ | Specific heat |
| $\nu$ | Poisson’s ratio |
| $u_x$ | Deformation of type x |

# LIST OF ABBREVIATIONS

| | |
|---|---|
| ADS | Automatic Depressurization System |
| BWR | Boiling Water Reactor |
| BOC | Beginning of Cycle |
| BOL | Beginning of Life |
| BU | Burnup |
| EOC | End of Cycle |
| EOL | End of Life |
| Gen III | Generation Three |
| GEN IV | Generation Four |
| GWd/MTU | Giga-Watt Days per Metric Tonne Uranium |
| He | Helium |
| LOCA | Loss of Coolant Accident |
| LBLOCA | Large Break LOCA |
| LWR | Light Water Reactor |
| MOC | Middle of Cycle |
| MOX | Mixed Oxides |
| MWD/MTU | Mega-Watt Days per Metric Tonne Uranium |
| NRC | Nuclear Regulatory Commission |
| PARCS | Purdue Advanced Reactor Core Simulator |

| | |
|---|---|
| PCMI | Pellet Cladding Mechanical Interaction |
| PWR | Pressurized Water Reactor |
| RIA | Reactivity Initiated Accident |
| SBLOCA | Small Break LOCA |
| SBO | Station Black Out |
| SiC | Silicon Carbide |
| SiC/SiC | SiC fiber/matrix composite |
| TH | Thermal Hydraulic |
| TMI | Three Mile Island |
| TRACE | TRAC/RELAP Advanced Computational Engine |
| $U_3Si_2$ | Uranium Silicide |
| UC | Uranium Carbide |
| UN | Uranium Nitride |
| $UO_2$ | Uranium Dioxide |
| VBA | Visual Basic for Applications |
| Zirc-2 | Zircaloy-2 |
| Zirc-4 | Zircaloy-4 |
| $ZrO_2$ | Zirconium Dioxide |

# CHAPTER 1

## INTRODUCTION

### 1.1 THERMAL HYDRAULIC AND THERMO-MECHANICAL COUPLING MOTIVATION

Thermal hydraulics codes are used by the United States' Nuclear Regulatory Commission to validate the safety of current and proposed nuclear power plants in both normal day to day operations and in accident scenarios. The flagship thermal hydraulic code used by the NRC for systems modeling is the TRAC/RELAP Advanced Computational Engine, also known as TRACE. The TRACE code is designed to look at the systems response in accident scenarios but has limited fuel rod thermal/mechanical response models. It is common practice in the nuclear industry to also use the NRC's fuel rod response codes FRAPCON for steady-state analysis and FRAPTRAN for transient analysis of fuel performance. Looking at a systems response in an accident scenario, an emphasis should be placed on the oxidation mechanics and fracture mechanics of the cladding material. In order to properly model these phenomena, it is important to know the fuel rod conditions at the onset of the transient due to their significant impact on heat transfer and stress distribution in the cladding. Coupling TRACE with FRAPCON can provide this important information at various times within the cycle at which the accident can occur.

Deformation is a complex thermo-mechanical process in which there is a feedback mechanism between temperature and pressure, ultimately affecting the stress distribution in the cladding. As the fuel heats up in reactivity initiated accident (RIA) scenarios, thermal expansion will cause the fuel to expand outwards leading to pellet clad mechanical interaction (PCMI) which will induce stress on the cladding. If sufficiently high, this interfacial pressure can move the cladding's hoop stress from compression into tension, ultimately leading to cladding failure. [However, TRACE currently does not take into account the effects of changing internal pressure on the cladding due to fuel expansion or high temperature fission gas release.] In LOCA scenarios, the cladding can reach sufficiently high temperatures to balloon, which is not modeled in TRACE. For oxidation modeling, the TRACE code was designed to calculate the equivalent cladding reacted (ECR) to compare against regulatory limits, the oxidation reaction energy source term, and the hydrogen release into the coolant.[TRACE V5P3 Theory Manual] Unlike FRAPTRAN, TRACE currently does not model the degradation of the cladding strength due to oxide layer formation. The TRACE code is further limited by not having the ability to model the burnup degradation of fuel and cladding thermal and mechanical properties. Limited fuel and cladding material changes that result from burnup can be input into TRACE when calculated from another code, such as FRAPCON.

It is understood that the TRACE code is designed to be used as a conservative tool for system response. However, not having any type of feedback with more detailed fuel rod analysis limits the ability to accurately predict fuel rod failure and the amount of fuel that has failed in the reactor. By utilizing the steady-state fuel performance models of FRAPCON, transient fuel performance models of FRAPTRAN and the thermal hydraulic models of TRACE, a more robust system code can be developed to more accurately predict the timing and amount of fuel failure.

## 1.2 FUEL DISPERSAL

It has been shown through various studies at the Halden and Studsvik research reactors that under hypothetical accident scenarios in which rod rupture occurs, fuel can be dislodged from the fuel rod and released into the coolant.[P. Raynaud, 2012] The Nuclear Regulatory Commission is currently involved in LOCA related fuel dispersal analysis due to the potential adverse effects on plant safety. NRC's proposed consequences of fuel dispersal include increased activity levels in the coolant and containment, pump erosion from trapped fuel, debris load in the sump or core inlet, and the additional heat load from these particles potentially leading to coolant flashing at pump inlet leading to pump cavitation.[Generic Issue Proposal, 2011] Furthermore, this phenomena is important to understand due to current licensing not taking into account fuel dispersal in safety analyses. It is known that fuel dispersal occurred in the TMI-2 accident and is believed to have occurred at the Fukushima accident as well. Currently, the amount of fuel dispersed during a hypothetical LOCA accident has yet to be fully evaluated.

The currently understood parameters that have an effect on the quantity of dispersed fuel include burnup at the point of rupture, cladding strain at rupture and the fuel particle size threshold for dispersal.[M. Flanagan, 2012] For cladding rupture to occur, either sufficiently high temperatures or cladding stress must be reached (or a combination of both). For estimating how much fuel will be dispersed in a reactor, it is important to know both the burn-up dependent and system-dependent parameters for material properties and coolant conditions, respectively. To achieve this goal, both fuel performance and thermal hydraulic codes will be used to determine the number of failed rods and the state of the rods at failure. By comparing these values to experimentally derived failure criteria, the quantity of fuel dispersed in an accident can be determined. Due to the coolant conditions varying by plant type and type of accident, several accidents will need to be analyzed in order to achieve a better understanding of this phenomena.

### 1.3 ADVANCED FUELS MOTIVATION

Two of the most prominent nuclear accidents, the Three Mile Island Unit 2 (TMI-2) in the United States and the Fukushima Daiichi disaster in Japan, were worsened by the oxidation reaction of the cladding with the steam environment. Both reactors were light water reactor designs, TMI being a Babcock & Wilcox pressurized water reactor design and Fukushima being a group of General Electric boiling water reactor designs. In both cases the fuel consisted of $UO_2$ pellets sealed by a Zircaloy tube cooled by water flowing across the outside of the clad.

On Mach 28, 1979, the TMI-2 reactor experienced a failure in the non-nuclear secondary side causing the main feedwater pumps to quit supplying water to the steam generators.[GPU Nuclear Corp, NEI, 2001] Although the reactor was scrammed, the lack of water meant the primary system had no means of removing decay heat. As the fuel rods continued to heat up, cladding began to fail (as seen in Figure 1.1a) leading to the release of radioactive material to the coolant and through the stuck open PORV valve to the containment building and the auxiliary building. As the oxidation reaction began with the uncovered fuel rods, the hydrogen produced became a major concern with fears of a possible explosion. However, through venting and the conclusion that the bubble could not burn due to the lack of oxygen, these fears resided.[GPU Nuclear Corp, NEI, 2001] Cleanup concluded after 14 years at the cost of nearly $1 billion.[Peterson, 1989]

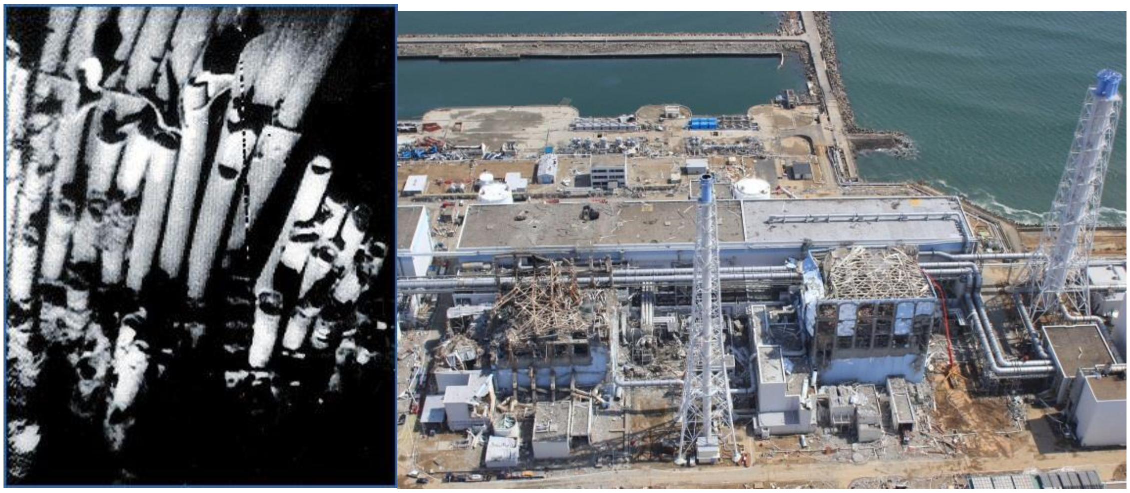

Figure 1.1: (a) Damaged Fuel from TMI-2 Reactor (b) Reactor buildings 3 (left) and 4 after hydrogen explosions at Fukushima Daiichi nuclear power plant, Japan.[The Washington Post, 1999; Pink Tentacle, 2011]

The reactors located at the Fukushima Daiichi NPP did not have as fortunate of an outcome as TMI-2. After the earthquake and ensuing tsunami, a station black out (SBO) occurred that left the reactor operators without the ability to keep the fuel adequately cooled. Over the next several days, the oxidation reaction between the steam and the Zircaloy cladding resulted in a large amount of hydrogen gas. Without having the ability to dispose of the hydrogen, the accumulation led to explosions that further crippled the reactor buildings. While the clean-up cost is not fully known, it has been previously estimated that these costs will be as high as $125 billion.[Hasegawa, 2012]

Both of these events have shown the effects that a system failure can have on the fuel and the further consequences this can lead to with regards to the safety of the reactor, the environment and the public. If adequate cooling had been maintained, the zirconium-steam oxidation reaction would have not taken place, eliminating the hydrogen production and large heat generation, compared to the decay heat of the fuel. An advanced cladding with minimal oxidation kinetics with high temperature steam would have been another way to avert these consequences. The cladding melting would have still released the gaseous fission products but would not contribute to the production of explosive gas, thereby potentially not affecting the integrity of the containment. The lack of hydrogen production would have eliminated the explosions seen at Fukushima, thereby reducing the release of radionuclides, and would have reduced the fears of a potential explosion at TMI.

Silicon carbide has been highly regarded for its excellent oxidation resistance in comparison to zirconium. Oxidation rates will affect hydrogen generation in the system as well as the additional heat source generated by the oxidation reaction. Lower oxidation rates will increase the amount of time before full cladding oxidation occurs, allowing operators more time to re-instate proper core cooling in the case of a LOCA. Silicon carbide has higher yield strength than zirconium under accident conditions, and SiC CMCs have improved resistance against crack propagation due to the fibers deflecting localized strains.

### 1.4 RESEARCH OBJECTIVE

A regulatory systems code TRACE will be used to model commercial light water reactors in varying accident scenarios, such as a LOCA. The TRACE code is a transient system analysis code and therefore cannot model the burn-up effects on fuel performance such as creep, swelling, fission gas release, oxidation, material property degradation, and so forth. To achieve this ability, the TRACE code will be coupled with the steady-state fuel performance code FRAPCON. The TRACE code will also be modified to allow for axial nodalization of these parameters, as they affect the heat transfer ability and ultimately cladding stress. Due to the limited thermo-mechanical fuel rod models in TRACE, a more robust transient analysis would be afforded by also using the regulatory transient fuel performance code FRAPTRAN. This can be accomplished by either coupling the codes or using the boundary (coolant) conditions as inputs into FRAPTRAN and calculating the best estimate fuel rod response for each rod modeled in TRACE. Additional consistencies will be made across the suite of codes, including adding the ability for FRAPCON to model gamma heating to accurately match fuel temperatures with TRACE. Transient gamma heating will also be analyzed using the neutronics code MCNP in order to better predict where the gamma energy is deposited during the progression of accident with changing coolant densities.

The second part of this research will focus on using the improved models described above to determine the amount of fuel dispersed during hypothetical LOCA scenarios. Due to varying fuel designs found in PWRs and BWRs, both plant types will be modeled. For each plant type, varying plant responses to a LOCA will also be modeled, including as designed safety system response and partial/delayed responses. The effect of cycle time at which the accident occurs will also be analyzed, as this will affect dispersal criteria values (i.e., burnup) and the initial conditions for the transient (i.e., internal rod pressure). The number of rods failed and the quantity of fuel dispersed will be analyzed for these various cases.

The third part of this research will look at the changes in fuel rod and system response with implementing new fuel and/or cladding materials, such as SiC, compared to current LWR materials. Thermal and mechanical properties, focusing largely on deformation mechanisms, as well as oxidation kinetics, will be built into the TRACE and FRAPTRAN codes. Due to the importance of fuel rod initial conditions based on burn-up and power histories at the onset of a transient, FRAPCON will also be modified to include advanced materials to determine the initial fuel conditions for TRACE. Transient analysis will be performed comparing the fuel rod response of the different materials to the results found with current LWR fuels.  The time to failure and how much of the fuel in the reactor fails with an advanced cladding will be analyzed.

# CHAPTER 2

## REVIEW OF LITERATURE

### 2.1 ADVANCED CERAMIC AND COMPOSITE MATERIALS BENEFITS

When considering a cladding material to be used in a nuclear application, there are many properties that need to be considered from a neutronic, structural, corrosive and thermal point of view. From a neutronic perspective, the absorption cross section under operating temperatures should be as small as possible. Structurally, the material must have high strength due to the pressures experienced inside a reactor during normal operating conditions (>15MPa in PWRs). For a cladding material, differences between internal and external pressures can lead to a material experiencing both compression and tension, a situation where many materials have different yield points. Swelling, fuel thermal expansion and cladding creepdown can all lead to pellet cladding mechanical interaction (PCMI) which adds increased stress on the cladding. From a corrosion standpoint, the environment of a nuclear reactor is very daunting. The high temperatures and water/steam environment can lead to oxidation which can lead to additional heat generation, hydrogen production, an additional thermal resistance layer and a reduction in material strength. From a thermal, heat-transfer viewpoint it is desired to have a high thermal conductivity and low specific heat. The high thermal conductivity will allow the energy generated in the fuel to be more easily transferred to the coolant, resulting in lower fuel temperatures.

A low specific heat combined with a high thermal conductivity will reduce the amount of energy the cladding contains during an accident scenario, such as a LOCA.

Zirconium-based claddings have been used almost exclusively in the United States since the beginning of commercial nuclear power. It has a low neutron absorption cross section, good corrosion resistance under typical LWR conditions and is relatively stable under irradiation. However, its oxidation rates and reduction in strength at high temperatures are a major cause of concern. Its affects have been seen at the most notable nuclear accidents (previously mentioned). After Fukushima, the U.S. Department of Energy (DOE) implemented the Accident Tolerant Fuel (ATF) development program with collaboration between industry, national laboratories and universities. Accident tolerant fuels can tolerate loss of active cooling in the core for considerably longer period of time while maintaining/improving the fuel performance during normal operations.[Griffith, 2013]

In comparison to metals, ceramics have many desirable characteristics for nuclear applications including reduced oxidation, high strength and hardness at elevated temperatures, high elastic modulus and low thermal expansion. Reduced oxidation at high temperatures has been one of the major reasons for SiC being a front runner in the ATF program. The increase in strength of ceramics and composites over metals, especially at high temperatures, can be attributed to the ionic and covalent bonds that hold the atoms together better than metallic bonds. [Serope Kalpakjian, 2010] For cladding and structural materials, this is a desirable property in order to retain fission products and keep the fuel in a coolable geometry. The high strength of ceramics, however, leads to an undesirable characteristic of being inherently brittle. This is a concern when dealing with crack propagation leading to failure of the cladding and the release of gaseous fission products. One way to counter this is to reinforce the ceramic cladding with fibers to redistribute the local stresses at the crack tip. This is commonly referred to as a ceramic matrix composite (CMC) and has been considered as a duplex, triplex and higher order layer composites.[Ed Lahoda, 2010;David Carpenter, 2007] The properties of SiC with regards to mechanical failure, oxidation kinetics and thermal properties are described in the following sections.

## 2.2 FAILURE MECHANISMS AND MECHANICAL PROPERTIES

For a fuel rod to be considered as having failed, the cladding is no longer capable of retaining all fission products and keeping the fuel in a coolable geometry. This can be caused by surpassing the yield strength of the cladding or by allowing the temperature of the cladding to exceed its melting point. The cladding experiences stresses as a result of the pressure difference between the inside and outside of the rod. The outside of the rod is at a pressure equal the primary system pressure, on the order of 7.1MPa for a BWR and 15.5MPa for a PWR.[Neil Todreas, 1990] However, the internal pressure of the rod initially is much less (≤ ~1 MPa for BWR, ~2-3MPa for PWR), creating a hoop stress that results in compression of the material. As the cladding spends more time in the reactor, fission gas that is released from the fuel, combined with a decrease in the amount of free volume, will increase the internal pressure of the rod, which can ultimately lead to changing the hoop stress from compression to tension. Fuel expansion and cladding creepdown can also lead to the same result of increasing the pressure on the inside of the wall to a pressure higher than what is experienced on the outside wall. Typical yield strengths of ceramics in tension as opposed to compression are on the order of ~10x less.

### 2.2.1 Mechanical Failure

The failure mechanism of ceramics is quite different than that of metals, which is also shown in the differences in their ductility. In metals, the material will elastically deform until the yield strength is reached. At that point the metal will begin to plastically deform, which is a permanent deformation that introduces new dislocations in the material's lattice. The new dislocations hinder the movement of other dislocations, causing an increase in the strength of the material commonly referred to as strain hardening. This is an intrinsic strengthening mechanism that occurs in front of the crack tip.[H.E. Khalifa, 2012] Zircaloy has been shown to reach strains of 0.1 to 0.4 before failing.[O.N. Pierron, 2003; Dawu Xiao, 2010] This value is highly dependent on the temperature and the direction in which the tensile tests are conducted given Zircaloy's hexagonal close packed (hcp) structure.

A major benefit of using silicon carbide ceramics (and fibers) in terms of material strength is the retention of a high yield strength at elevated temperature and dose.[David Carpenter, 2007;Ken Yueh, 2010;Lars Hallstadius, 2012] This is extremely important in accident scenarios where high temperatures and stresses can be experienced by the cladding. Figure 2.1 shows the ultimate tensile strength of Zircaloy and SiC fibers as a function of temperature.

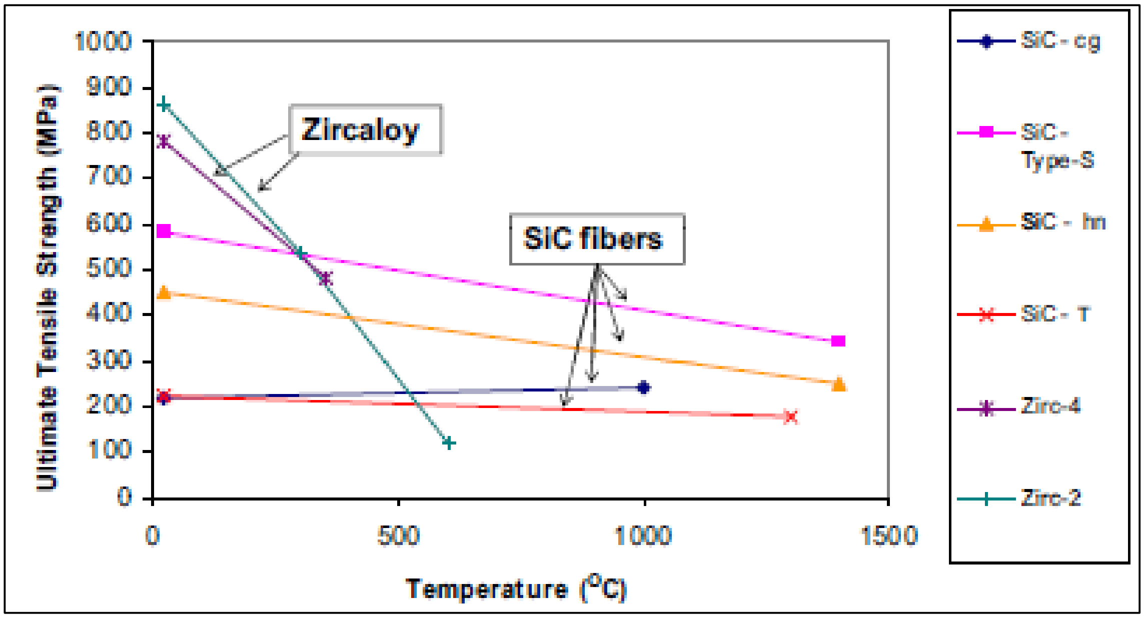

Figure 2.1: Ultimate tensile strength (UTS) versus temperature for Zircaloy and Silicon Carbide fibers.[Lars Hallstadius, 2012]

The brittle nature of ceramics leads to little plastic deformation before fracture, shown by CVD SiC in Figure 2.2. Many models to-date utilizing SiC therefore set the ultimate tensile strength equal to the yield strength of the material.[Carpenter, 2006;David Carpenter, 2007] This means that the material will only experience elastic deformation and will fail without any plastic deformation occurring. This lack of ductility in ceramics allows cracks to easily propagate through the material. One way to overcome this obstacle is to introduce silicon carbide fibers into the silicon carbide ceramic matrix. Figure 2.2 shows the increase in strain before failure by adding SiC fibers to the ceramic matrix.

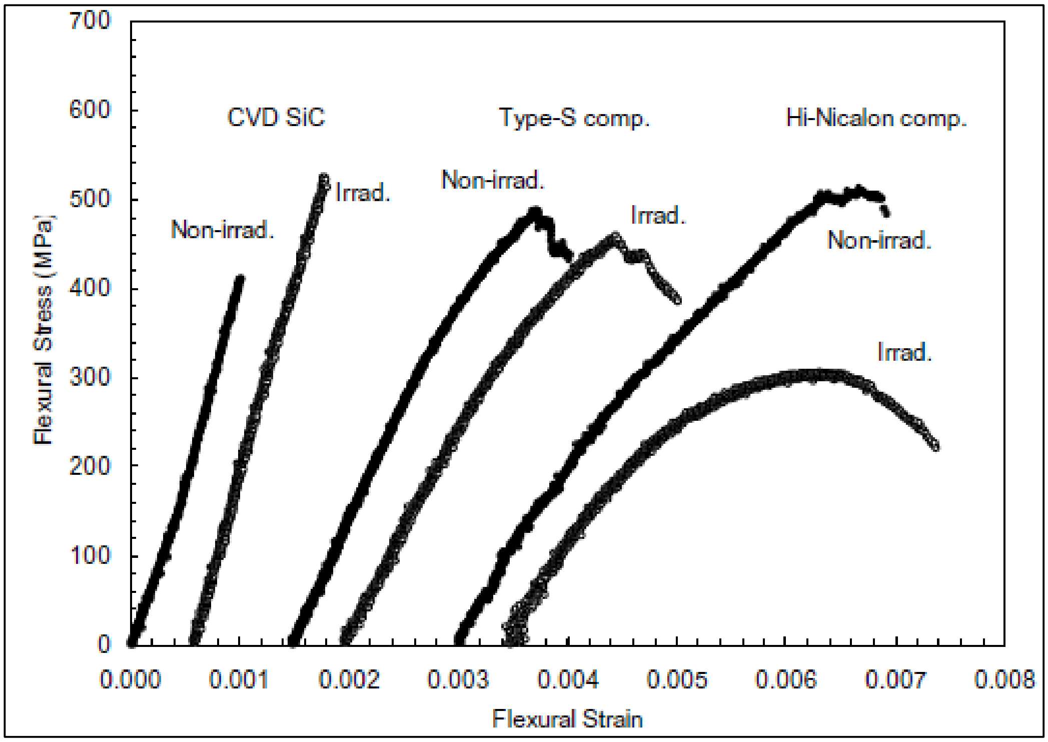

Figure 2.2: Flexural stress and strain for pure SiC ceramic (CVD SiC) and fiber reinforced SiC ceramic-Silicon Carbide fibers (Type-S and Hi-Nicalon).[George Newsome, 2007]

The woven silicon carbide fibers are encased in a silicon carbide matrix that is typically applied using chemical vapor infiltration (CVI) or liquid silicon infiltration (LSI).[H.E. Khalifa, 2012;] A silicon carbide monolithic layer is applied between the layers and on the outer and inner surfaces. The monolithic layer acts as the barrier to fission product release. The addition of the fibers prevents a crack in the monolithic from propagating through the material. The composite uses matrix cracking and fiber bridging to deflect and arrest propagating cracks in order to redistribute the stresses around regions of high strain concentration.[H.E. Khalifa, 2012; C.P. Deck, 2012] The crack will stop at the fibers and the stress will be redistributed along the fibers rather than staying concentrated and carrying through the material. An example of this is shown in Figure 2.3.

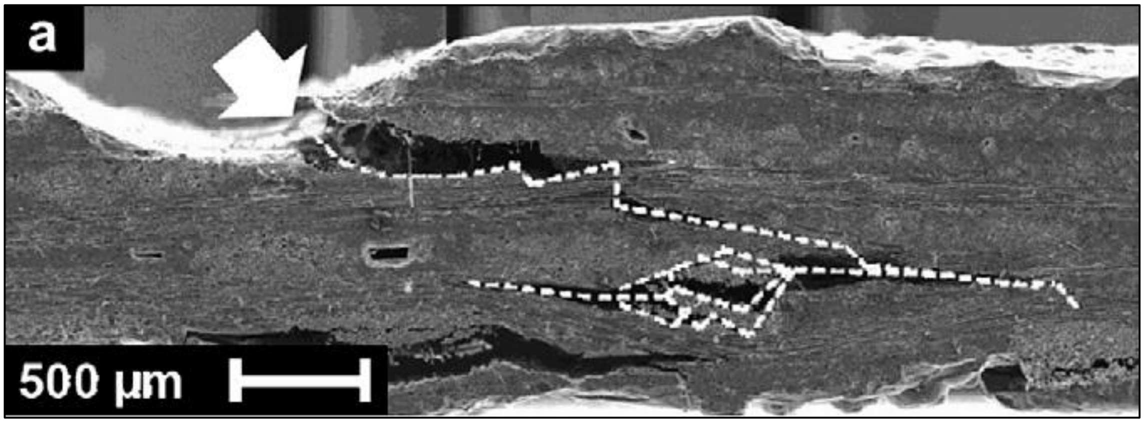

Figure 2.3: Crack deflection in SiC composite.[C.P. Deck, 2012]

Fabrication plays a major role in the strength of the SiC fiber-SiC matrix composites due to the voids that can be created during the CVI process. There is a bi-modal distribution of voids, with larger voids (>100µm) between the fiber layers and smaller voids (1-10µm) between the fibers.[C.P. Deck, 2012] Voids are created when the deposited SiC seals off inner regions of the material before it has become fully dense. Large voids enhance crack propagation, allowing a single crack to move from one void to the next with less energy. The higher composite density results in significantly higher strength which is attributed to the reduced number of initial cracks in the sample. Fewer cracks requires crack branching, intra-bundle cracking and interface de-bonding of the fibers, which requires more energy to break.[ C.P. Deck, 2012] The strength of the material as a function of composite density is shown in Figure 2.4.

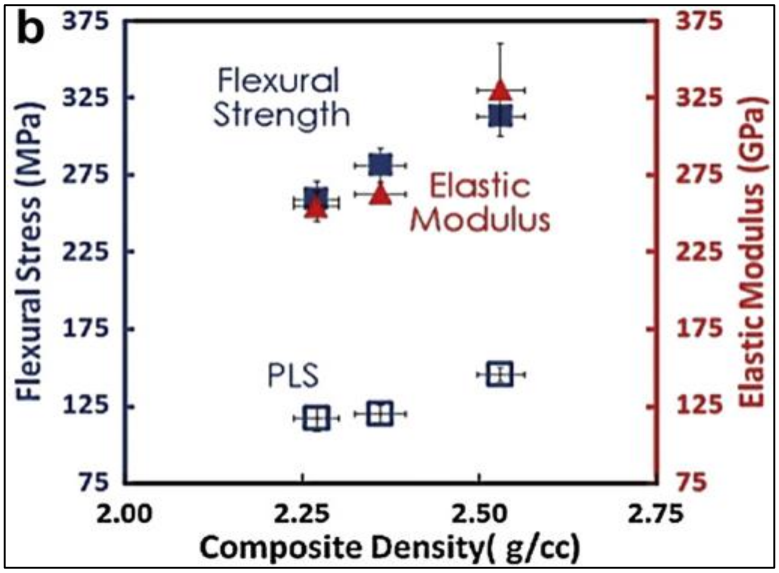

Figure 2.4: Flexural stress and elastic modulus versus composite density for SiC-fiber reinforced SiC matrix samples. [C.P. Deck, 2012]

### 2.2.2 Creep

Irradiation induced and thermal induced creep are significant phenomena for Zircaloy based claddings that reduce the fuel-cladding gap size over the operating time of the reactor. However, SiC has been highly regarded for its resistance to creep compared to that of zirconium.[C. Sauder, 2013] Ceramic Tubular Products' Silicon Carbide TRIPLEX cladding is believed to have an absence of creep.[Herbert Feinroth, 2013] This not only adds safety margin but allows for increased internal rod pressures from fission gas release at high burnup due to the inability for cladding creep out. However, this adversely creates higher fuel centerline temperatures due to larger gap size resulting from the lack of cladding creep down.

Thermal creep of CVD SiC shows a strong negative correlation between strain rate and temperature/stress. At 200 MPa and 1473K, a thermal creep rate of ~$10^{-10}$ ($s^{-1}$) was experimentally obtained, although it is noted that this is the highest creep rate obtainable due to its crystal orientation and is significantly outside its design operating temperature range.[Snead, 2007] It is evident from Figure 2.5 that extrapolated thermal creep rates will be negligible under LWR conditions.

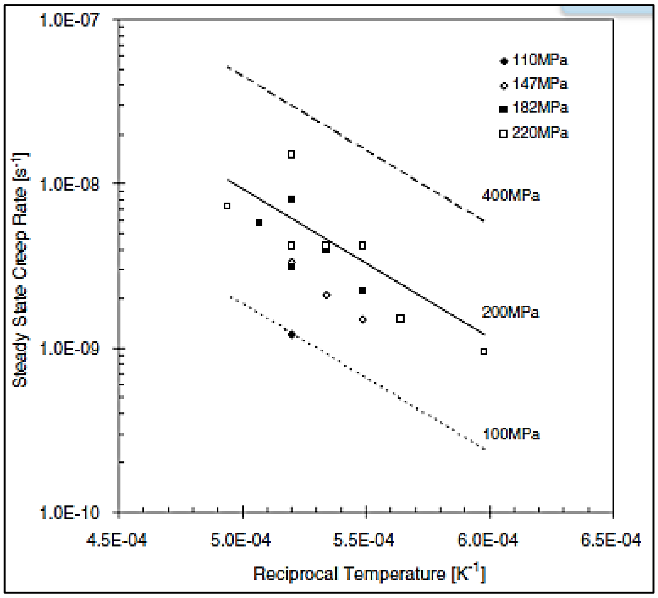

Figure 2.5: Thermal creep of CVD-SiC.[Snead, 2007]

Due to the minimal effects of thermal creep at operating temperatures, irradiation induced creep would be the driving force for creep induced cladding deformation. However, limited data exists on SiC composites on irradiation induced creep. At temperatures < 1223K, the creep strain for CVD-SiC is nonlinear due to the transient irradiation creep at beginning of life caused by the rapid development of defect clusters.[Snead, 2007] The dependency of irradiation induced creep on stress and dose, among other variables such as crystallographic orientation, allows for the creep compliance term ($I_c$,$MPa^{-1}$*$dpa^{-1}$) to be used as a linear relationship to determine irradiation creep strain. Published irradiation creep compliance values are between $5.3x10^{-7}$ and $2.0 \ x10^{-6}$ ($MPa^{-1}$*$dpa^{-1}$).[Ju Ang Jung, 2013; Snead, 2007] The larger values are from studies that have only reached 0.7 dpa, which might be skewed to the conservative side due to transient irradiation creep in the early stages of irradiation. To date, SiC cladding models have assumed that during reactor operation, SiC will not experience thermal creep due to the low operating temperature.[Carpenter, 2007; S. Ray, 2013]

### 2.2.3 Swelling

Neutron irradiation has been experimentally shown to alter the microstructure of SiC, leading to amorphization and swelling.[Yutai Katoh, 2012] Several studies have shown that this phenomena is dependent on both irradiation temperature and fluence. Under typical LWR conditions, swelling will occur isotropically with a saturated volume change of 2%.[Yutai Katoh, 2012] Higher temperatures have been shown to result in overall less swelling and increased time until swelling saturation values are reached, as shown in Figure 2.6

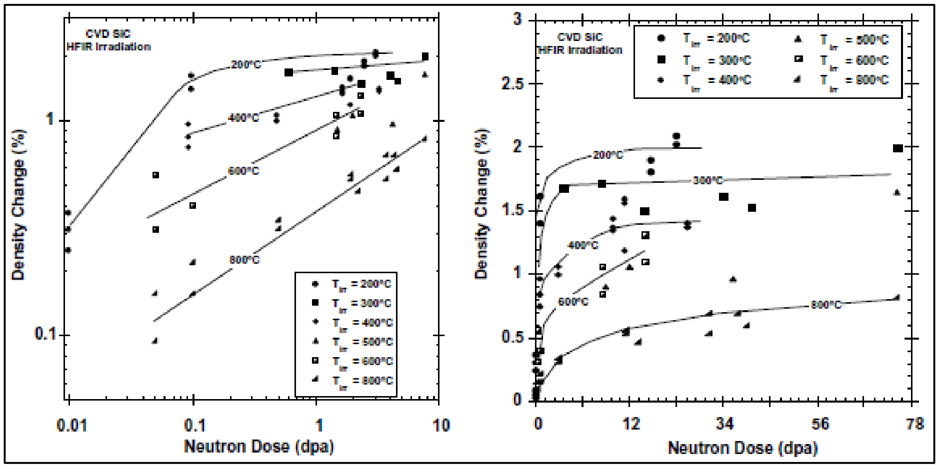

Figure 2.6: Swelling of CVD SiC.[Snead, 2007]

Comparing the swelling rates of CVD SiC, CVI-SiC matrix and Tyranno-SA3 fibers at 873K showed little difference in magnitude.[Takaaki Koyanagi, 2013] All types of SiC showed similar trends as CVD-SiC after 3 dpa of decreasing swelling rates with increasing temperatures. However, at the higher temperatures (>1000K) swelling rates were noticeably higher for the CVI-SiC matrix and SA3 fibers than for CVD-SiC. However, for LWRs these are not temperatures that would be sustained under steady-state conditions. It has also been shown that swelling values observed under neutron and ion irradiation were equivalent, indicating that total dpa is the driving force rather than the dpa rate.[Yutai Katoh, 2002]

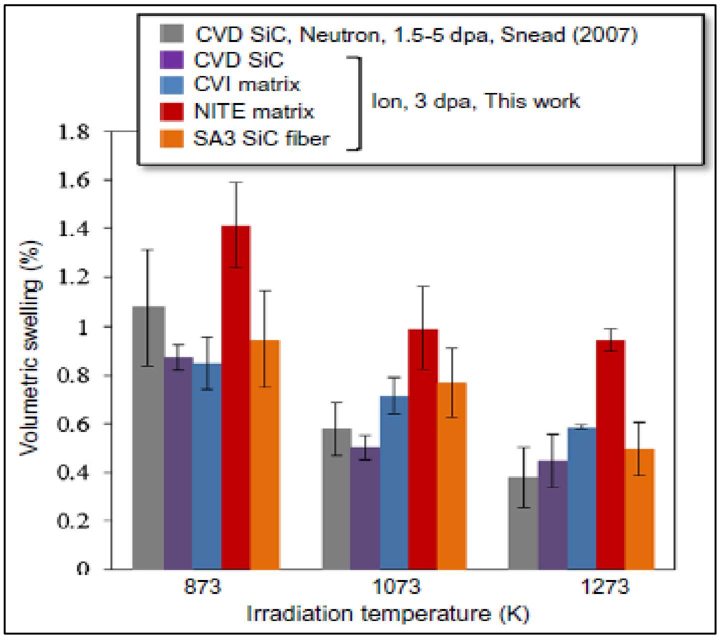

Figure 2.7: Volumetric swelling of various types of SiC.[Takaaki Koyanagi, 2013]

A swelling model was developed at MIT that assumes isotropic 2 vol% saturation swelling is shown in Equation 2.1. [Carpenter, 2006] This model assumes 95% saturation after 1 DPA.

$$\frac{\Delta L}{L} = 0.0067 * (1 - e^{-(DPA)*3}) \qquad 2.1$$

There are no models for swelling for Zircaloy based claddings in any of the NRC codes.

## 2.3 OXIDATION KINETICS

One of the major benefits of using silicon carbide is the expected slower degradation in a severe accident scenario with low corrosion and hydrogen generation.[Lars Hallstadius, 2012] Similarly to Zr, SiC reacts with oxygen to form a protective silica layer. The silica layer acts as a barrier inhibiting the diffusion of oxygen to non-reacted SiC. The formation of the silica layer is accomplished by either active or passive oxidation, shown by equations 2.2 and 2.3, respectively.[Youho Lee, 2012]

$$SiC(s) + 2H_2O(g) = SiO(s) + CO(g) + 2H_2(g) \tag{2.2}$$

$$SiC(s) + 3H_2O(g) = SiO_2(s) + CO(g) + 3H_2(g) \tag{2.3}$$

Active oxidation occurs when the oxygen partial pressure is below ~$10^{-4}$ atm, which leads to passive oxidation being the driving reaction in nuclear and most engineering applications.[Youho Lee, 2012] It is well understood that the oxide formation can be modeled by a parabolic rate constant ($k_p$), leading to a diffusion rate shown by equation 2.4 where x is the oxide layer thickness.

$$\frac{dx}{dt} = \frac{k_p}{2x} \tag{2.4}$$

Typical oxide formation leads to an increase in mass due to the diffusion of oxygen atoms into the material, as is the case with zirconium. However, $SiO_2$ has been shown to volatilize in the presence of steam at high temperatures leading to an overall decrease in mass.[Youho Lee, 2012;Joaquin Ramirez-Rico, 2012] This is due to the instability of $SiO_2$ compared to $ZrO_2$. The volatilization of the silica layer keeps the oxide scales thinner, creating a shorter diffusion path for oxidizing species. This allows the oxidation reaction to occur more rapidly, and is especially prevalent in a water vapor environment. Silica volatilization is dominated by the reaction shown in equation 2.5.

$$SiO_2 + 2H_2O(g) = Si(OH)_4(g) \tag{2.5}$$

Volatilization has been shown to be dependent on the boundary layer due to it affecting the length of the diffusion path of volatilization species. The boundary layer can be defined as the region where the effects of viscosity on the flow over a surface are seen, typically taken as the region where the flow velocity is between 0 and 99% of the free stream velocity. The larger the boundary layer, the longer the diffusion path and thus a decrease in the volatilization of the oxide layer. This layer is dependent on the flow characteristics, such as Reynold's number, velocity and mass flow rate.[Youho Lee, 2012] As Re increases, the boundary layer decreases which implies that increased flow velocities lead to an increase in volatilization.[Desktop Aeronautics, Inc., 2007] This is an important beneficial factor when considering LOCA scenarios, where reduced flow rates are experienced. Combining the oxide formation and volatilization, the diffusion rate of oxygen in monolithic SiC can be described by equation 2.6 where $k_l$ is the linear volatilization.[Youho Lee, 2012]

$$\frac{dx}{dt} = \frac{k_p}{2x} - k_l \tag{2.6}$$

A study was been conducted at Massachusetts Institute of Technology (MIT) where a monolithic α-phase SiC tube was placed in a steam environment with steam flow conditions similar to that of a LOCA accident experienced in a PWR. The results of this study concluded that oxidation is much less likely to be a key failure mechanism of cladding during accident scenarios with SiC as compared to Zirc-4 due to the significant reduction in ECR at 1200°C.[Youho Lee, 2012] Oxidation results are shown in Figure 2.8 of two types of SiC as well as Zirc-4.

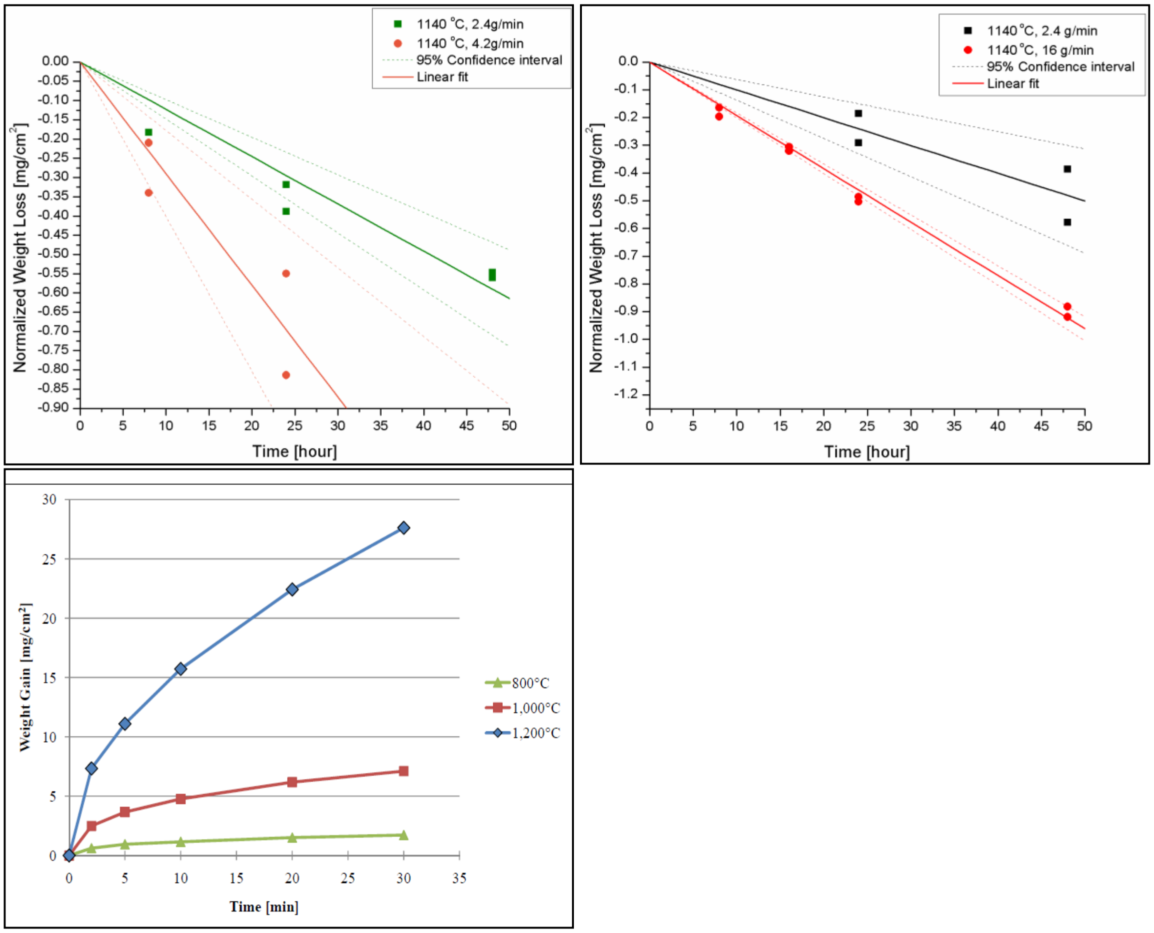

Figure 2.8: From Top Left to Right: (a) Mass loss of CTP SiC (b) Mass loss of Saint-Gobain SiC and (c) Weight gain of Zr-4, independent of flow conditions.[Youho Lee, 2012]

It is understood that pure SiC exists at only a 1:1 ratio between Silicon and Carbon, and free carbon exists when the Si:C ratio is < 1.0 and from the Pyrolytic carbon that is deposited around the SiC-fibers. Studies have shown that a protective silica layer is essential in inhibiting oxygen diffusion from attacking free carbon in the composite.[Joaquin Ramirez-Rico, 2012] A study by Rico, Fernandez & Singh analyzed the oxidation of a SiC$_f$/SiC$_m$ composite manufactured by Ube Industries in air at temperatures ranging from 800°C to 1600°C[Joaquin Ramirez-Rico, 2012]. At 800°C, weight loss was experienced and was attributed to carbon burnout due to the non-existence of a silica layer. This reaction is limited by the rate of carbon oxidation and can be fit to a parabolic rate constant. Three possible carbon oxidation reactions are shown in Equations 2.7 – 2.9 below.

$$C + \frac{1}{2}O_2 \rightarrow CO(g) \qquad 2.7$$

$$C + H_2O(g) \rightarrow CO(g) + H_2(g) \qquad 2.8$$

$$C + CO_2 \rightarrow 2CO(g) \qquad 2.9$$

Between 800°C and 1000°C, the weight loss per unit area was linear with time and was determined to be diffusion limited. From 1000°C to 1500°C, the weight loss was nearly constant for holding times of 0.1 to 5 hours. It was found that in this region carbon burnout initially dominates but is slowed by the formation of the silica layer, inhibiting oxygen diffusion by closing pores, a process also known as the “pinching effect”.[K. Matsunaga, 1999] However, at 1600°C linear weight loss with respect to time was observed and attributed to $SiO_2$ volatilization. A summary of the experimental data is shown in Figure 2.9.

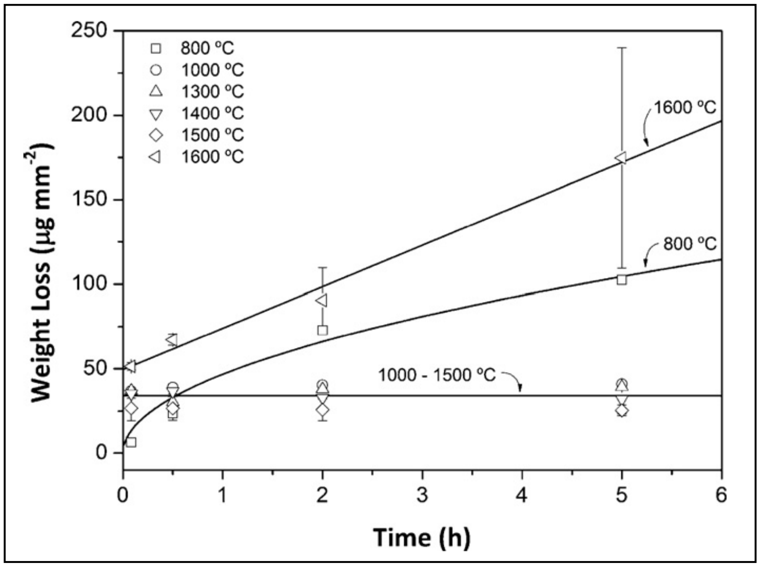

Figure 2.9: Weight loss per unit area as a function of exposure time in atmospheric air from 800°C to 1600°C starting after 0.1 hours.[Joaquin Ramirez-Rico, 2012]

The main source of free carbon is in the Pyrolytic carbon layer surrounding the SiC-fibers. The pyrolytic carbon is added to the composite to allow slip between the fibers and the matrix. Two of the main fibers being considered are Tyranno-SA and Nicalon.[Joaquin Ramirez-Rico, 2012; Naslain, 2007; N. Cocera, 2011] Nicalon fibers decompose at temperatures above 1100°C forming CO and SiO, resulting in mass loss and decrease in tensile strength.[Naslain, 2007] This is believed to be attributed to the oxygen content and by reducing the amount of oxygen present as-fabricated the fibers can remain stable from 1200-1500°C. Tyranno-SA fibers are now being more heavily considered due to their low oxygen content and enhanced oxidation and creep resistance.[Joaquin Ramirez-Rico, 2012] The burnout of free carbon on SiC fibers has been noted to occur at temperatures as low as 450°C.[Naslain, 2007] When the Pyrolytic carbon is being oxidized, there is an overall weight loss due to CO and $CO_2$ formation leading to an annular pore around each fiber, as seen in Figure 2.10.

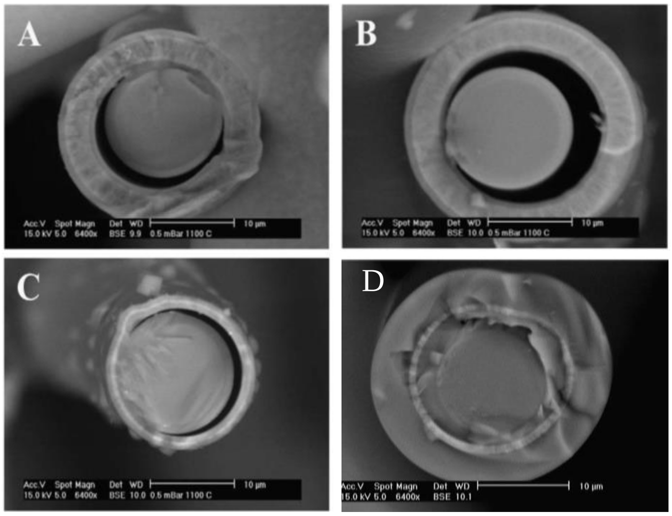

Figure 2.10: Figures A-C show the gaps created between Tyranno fibers and the SiC matrix by PyC burnout with varying thicknesses of PyC. Figure D shows a closed gap after oxidation at 1100°C for 2000 hours.[N. Cocera, 2011]

Experiments by Nasslain with a Nicalon/C/SiC composite concluded that as the oxygen diffuses along the pore, it begins to react with the SiC wall leading to silica formation and a net weight gain.[Naslain, 2007] This silica layer inhibits further diffusion of oxygen to the free carbon. At low temperatures (600°C-700°C), there is fast carbon oxidation and low silica oxidation leading to rapid weight loss due to a lack of a silica layer inhibiting oxygen diffusion. At high temperatures (>1000°C) the silica layer is quickly formed on the outer surface and seals off the pores. He concluded that it is beneficial to limit the depth of the PyC layer and to make the SiC fibers as free of oxygen as possible to reduce the carbon oxidation.

Further experiments by Cocera, Esparaza, Ocana and Sanchez showed strong agreement with the work performed by Nasslain.[N. Cocera, 2011] These experiments used three Tyranno fiber composites with varying thicknesses of Pyrolytic carbon. They concluded that the samples with the highest amount of Pyrolytic carbon had the highest mass loss rate and those with the smallest thickness have the lowest mass loss rate. Above 750°C the fibers and matrix begin to oxidize, reducing the rate of the carbon oxidation. At temperatures of 900°C, the oxidation of the PyC is still significantly high compared to that of the fiber and SiC coating. However, at temperatures of 1000°C and greater, the silica layer forms blocking further carbon burnout resulting in an overall mass gain from silica scale formation. It was concluded that the oxidation kinetics of the $SiC_f/SiC_m$ are controlled by oxygen diffusion through the silicon oxide films. This phenomenon is illustrated in Figure 2.11.

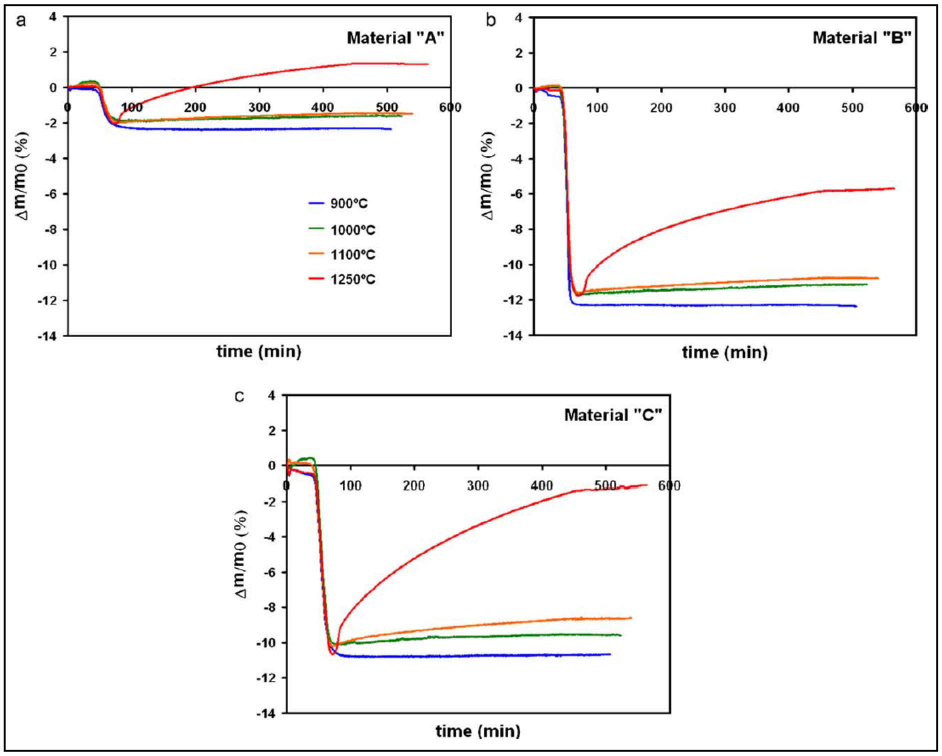

Figure 2.11: Weight loss as a function of exposure time in air from 900°C to 1250°C for three fiber composites with varying PyC coating thicknesses.[N. Cocera, 2011]

It can be concluded from these studies that it is necessary to have a silica layer formed on the outside of the cladding to prevent significant carbon oxidation. Without an initial protective silica layer, the dominating reaction of carbon burnout at temperatures lower than that of silica layer formation will lead to significant material degradation in a slowly progressing accident scenario. The depth of the silica oxide layer is dependent on the flow characteristics, with higher steam flow rates leading to increased volatilization and a shorter diffusion path for oxygen. Studies to date using fuel performance and systems analysis codes comparing SiC cladding to Zircaloy-based claddings have taken an optimistic approach by setting the oxidation reaction equal to zero.[MIT,Steve Johnson Westinghouse] This gives the best possible outcome for an advanced cladding but is not consistent with literature and therefore not a valid assessment when comparing different cladding types from a safety assessment standpoint.

## 2.4 THERMAL PROPERTIES

From a safety standpoint, it is essential that the heat generated within the fuel be easily transferred to the coolant in order for the fuel to remain below certain limits. In steady-state scenarios, this is solely dictated by the thermal conductivity of the material, but in transient scenarios the density and specific heat play an important role in the time required for heat removal from the fuel. As seen with silicon carbide's mechanical properties, its thermal properties are also influenced by the manufacturing process of the ceramic and can vary greatly from one manufacturer to another. This section will describe the thermal properties of monolithic SiC and SiC CMCs obtained from literature and compare them to typical zirconium properties. The models for Zirconium-based claddings are from matpro, which are the equations used in the NRC codes FRAPCON and TRACE irrespective of the zirconium-based alloy cladding type.[TRACE Theory Manual]

### 2.4.1 Thermal Conductivity

Thermal conductivity is highly dependent on the grain size and impurity content, both results of the manufacturing process, as well as temperature. Highly pure, single crystal SiC has shown a thermal conductivity of ~480W/m*K at 240K, while porous poly-crystal SiC has a thermal conductivity of ~40W/m*K at the same temperature.[Snead, 2007] Similar to $UO_2$, thermal conductivity of SiC degrades with increasing temperatures due to the phonon-phonon scattering effect.

Although very high at the beginning of life in the reactor, SiC thermal conductivity has been shown to quickly degrade due to radiation damage, reaching a saturation point around 1 DPA.[Maruyama, 2004] SiC composites have a lower thermal conductivity at beginning of life (BOL) than monolithic SiC but follow the same trend, showing saturated thermal conductivity values of ~3-5 W/m*K under steady-state LWR conditions.[Katoh, 2012] Current modeling of SiC thermal conductivity assumes saturation of 1DPa (equivalent to 1E25 neutrons/m$^2$) at 4 W/m*K, irrespective of temperature, and uses a power relation between BOL and 1dpa for thermal conductivity as a function of DPA and temperature.[Carpenter, 2006] A comparison of thermal conductivity between zirconium cladding and SiC (irradiated and unirradiated) is shown in Figure 2.12. The values for SiC are from the model developed by Carpenter.

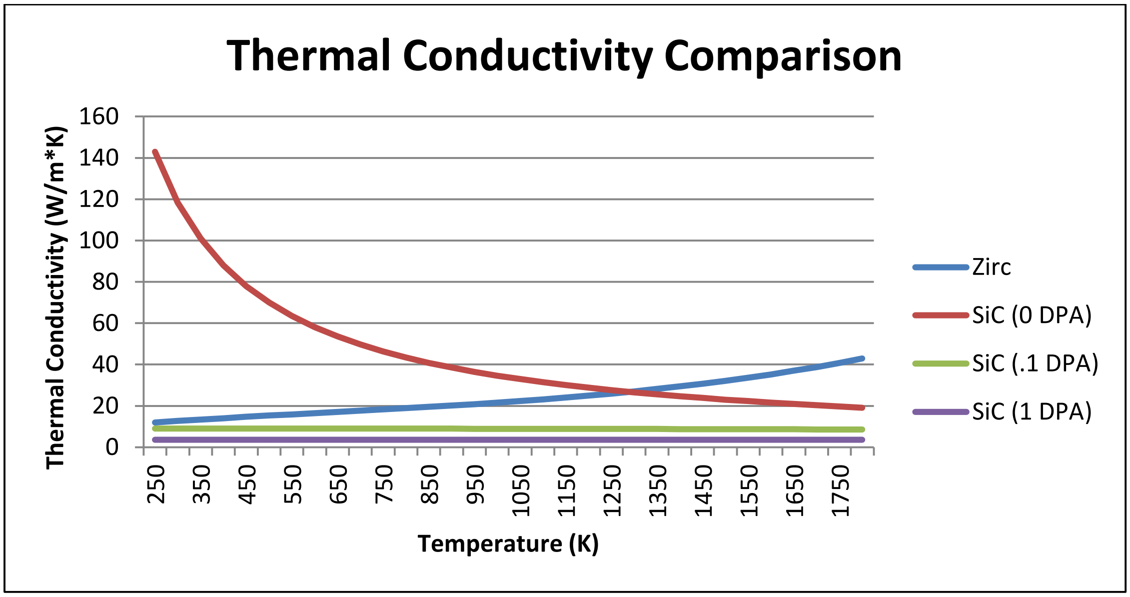

Figure 2.12: Thermal conductivity comparison of SiC and Zirconium

### 2.4.2 Density

The lattice parameter varies across the over 200 polytypes of SiC, and has shown to increase slightly with increasing temperatures for all polytypes. Of the most commonly desired structures of SiC, β-SiC has a lattice parameter of 0.4358nm, resulting in a density of 3.21g/cm$^3$. [Snead, 2007] The lattice parameter can be modeled using the following temperature dependent equation where T is in Kelvin and $a$ is in nm:

$$a(T) = 0.43577 + (1.3887E-6) * (T-273) + (7.8494E-10) * (T-273)^2$$
$$-(2.4434E-13) * (T-273)^3 \qquad 2.10$$

The lattice parameter can be related to density by knowing the structure of β-SiC as FCC (meaning 4 atoms per unit cell) and the molar mass of Si and C is 28.0855 and 12.0107amu, respectively.

$$density(T) = \frac{(4\ atoms\ per\ unit\ cell) * (28.0855 + 12.0107amu)}{a(T)^3 * (6.022E23 atoms/mol)} \qquad 2.11$$

Monolithic Silicon Carbide is approximately half as dense as Zircaloy, as shown in Figure 2.13.

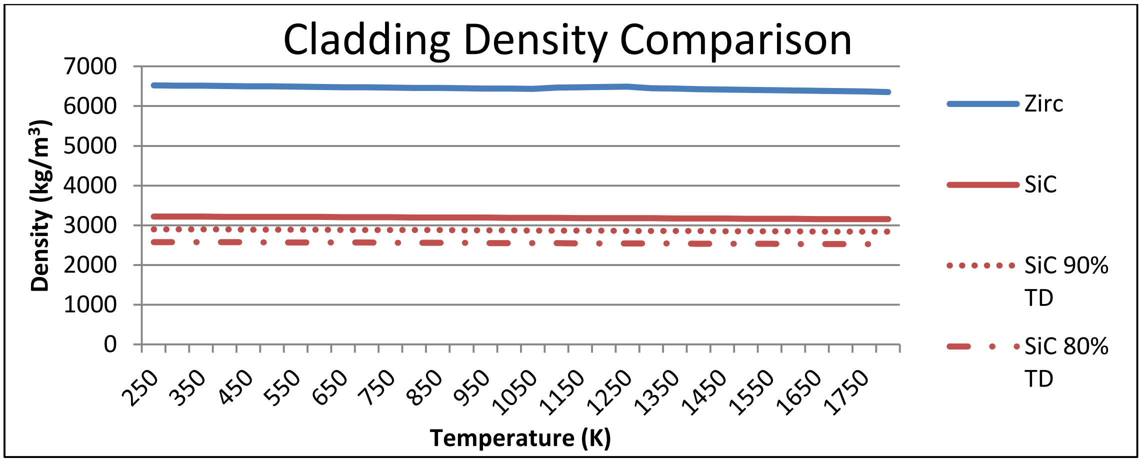

Figure 2.13: Density comparison with monolithic SiC and varying fractional TD values

Although pure SiC has a theoretical density of 3.22 g/cm$^3$, the density of the composites decreases with increasing fiber fraction. Fiber type and fabrication technique, along with fiber fraction, will greatly affect the overall density. Chemical Vapor Infiltration with a vacuum force has shown the highest achieved theoretical densities (in comparison to pure SiC) of 3.13g/cm$^3$, or ~97% TD. [Parlinduan Yonathan, 2009]

However, typical values of CVI SiC/SiC composites show much lower densities, as shown in Table 2.1.

Table 2.1: Density values for various SiC/SiC fabrication techniques.[P. Yonathan, 2009]

| **Researcher** | **Preparation method fiber used (vol%)** | **Density ($g/cm^3$)** | **Maximum flexural strength (MPa)** |
|---|---|---|---|
| Yano et al. | Slurry impregnation and tape stacking Nicalon, Hi-Nicalon | 2.38-3.07 | 260 |
| Pasquier et al. | CVI (35.1-38.2) | 2.34-2.62 | - |
| Yamada et al. | CVI and PIP Hi-Nicalon (26-35) | - | 380 |
| Ortona et al. | CVI and PIP NL 207 fiber (32-40) | 1.58-1.80 | 247 |
| Cheng et al. | CVI Hi-Nicalon (40-45) | 2.46-2.49 | - |
| Yoshida et al. | Slurry impregnation and tape stacking Hi-Nicalon (40-52) | 2.79-3.05 | 460 |
| Yarg et al. | CVI Tyranno™ SA (43) | 2.58-2.63 | 296 |
| Lee et al. | Slurry infiltration and reaction sintering Tyranno™ SA (10-15) | 2.20-3.00 | 505 |
| Katoh et al. | Slurry infiltration Tyranno™ SA (30) | 2.77-2.93 | 710 |
| Nammetti et al. | CVI and PIP Hi-Nicalon (40) | 2.19-2.23 | 761 |
| Kang et al. | Whisker growing and CVI Tyranno™ SA | 2.54-2.67 | - |
| Taguchi et al. | PIP CVD and reaction bonding Hi-Nicalon (33) | 2.65-2.70 | 280 |
| Katoh et al. | CVI Tyranno™ SA (35-40) | 2.42-2.74 | 304 |
| Yoshida et al. | Tape stacking and reaction sintering Hi-Nicalon | 2.90 | 200 |
| Lim et al. | Slurry infiltration and tape stacking Tyranno™ SA | 2.95-3.10 | 370 |
| Yoshida et al. | EPD and tape stacking Tyranno™ SA | 2.75-2.92 | 123 |

### 2.4.3 Specific Heat

For CVD deposited SiC, the specific heat is shown to have no distinguishable differences based on the atomic structure.[Snead, 2007] Using calorimetry measurements, at low temperatures the specific heat shows a linear relationship with temperature and follows a log trend afterwards, as shown in Figure 2.14.

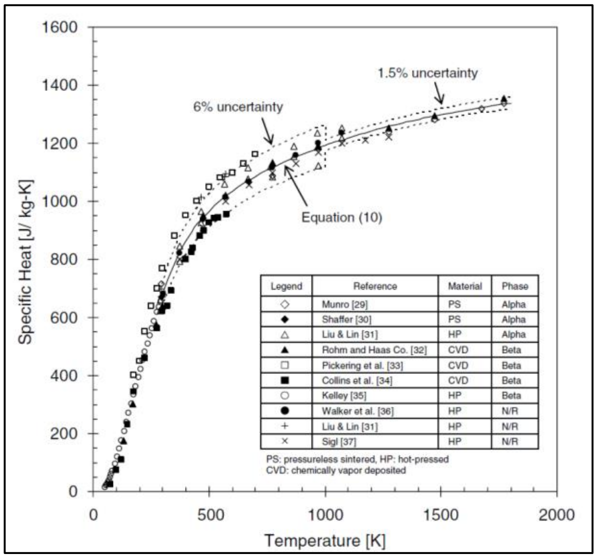

Figure 2.14: Specific heat of alpha and beta phase SiC from various experiments.[Snead, 2007]

In the temperature range of interest (>200K), specific heat can be expressed by equation 2.12, where T is in Kelvin and specific heat ($C_p$) is in J/kg*K.

$$C_p = 925.66 + 0.3772 * T - 7.9259E - 5 * T^2 - \frac{3.1946E7}{T^2} \qquad 2.12$$

As illustrated in Figure 2.15, it has been shown that CVD SiC shows negligible changes in specific heat under irradiation.[C.W. Lee, 1982]

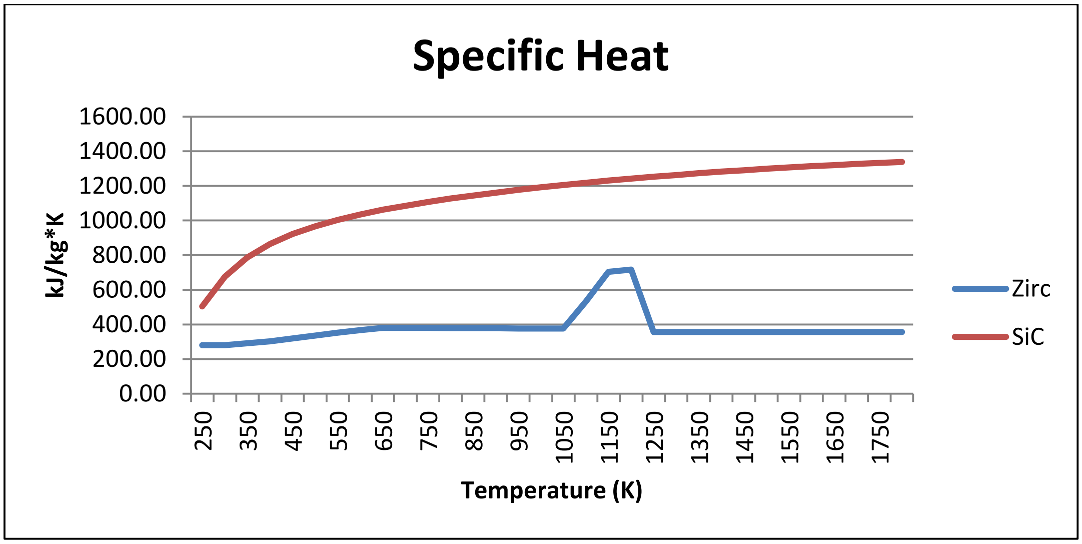

Figure 2.15: Specific heat of Zircaloy and SiC.

### 2.4.4 Thermal Expansion

Due to the small change in lattice parameter with respect to temperature (Eq. 2.10), similar results should be expected for thermal expansion of SiC. This phenomena can be attributed to the strong covalent bonds with the carbides. As with Zircaloy, the hexagonal crystal structures of SiC experience anisotropic thermal expansion in the a and c axis.[Z, Li. 1986] However, with β-SiC in the face-centered cubic structure, the thermal expansion is considered isotropic and can be modeled using equations 2.13 [Rohm and Haas Co] at temperatures below 550K, 2.14 [Z. Li,1986] at temperatures between 550K-1273K, and 2.15 at temperatures greater than 1273K.[Snead, 2007]

$$\alpha\left({10^{-6}}/{K}\right) = 2.08 + 4.51E - 3 * T - 1.68E - 6 * T^2 \qquad 2.13$$

$$\alpha\left({10^{-6}}/{K}\right) = -1.8276 + .0178 * T - 1.5544E - 5 * T^2 + 4.5246E - 9 * T^3 \qquad 2.14$$

$$\alpha\left({10^{-6}}/{K}\right) = 5.0 \qquad 2.15$$

Although limited data exists on the irradiation effects on thermal expansion, it has been shown that at a neutron fluence of 5.0x$10^{25}$ n/$m^2$ with temperatures ranging from 523-973K, there was no significant change in thermal expansion.[Price, 1977] Thermal expansion values are shown in Figure 2.16.

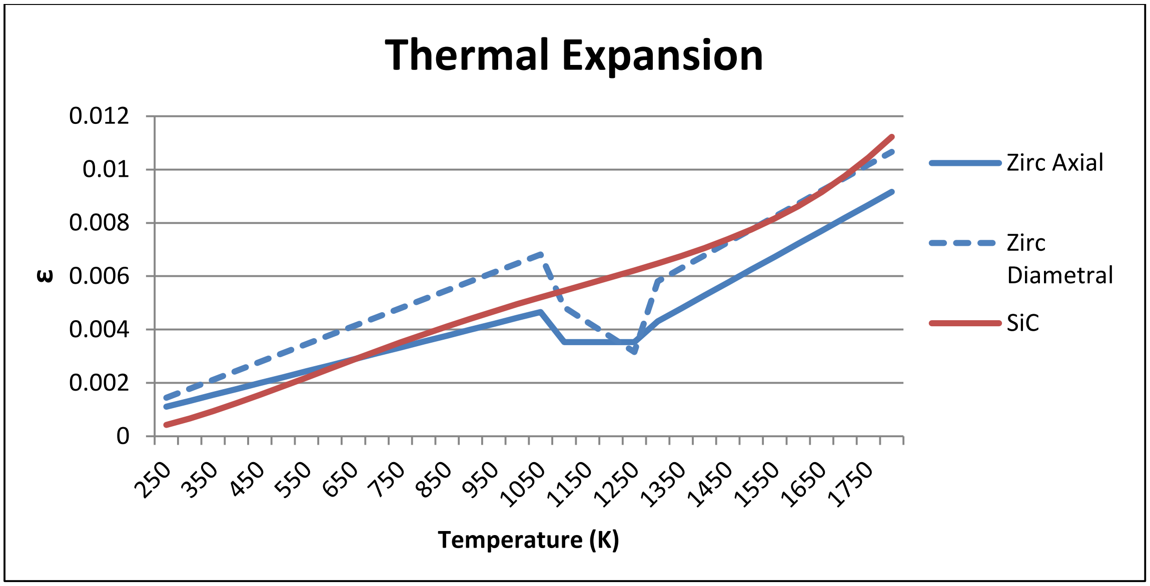

Figure 2.16: Thermal expansion in the axial and diametral directions for SiC and Zirc

## 2.5 FUEL DISPERSAL

Over the last few years, the Nuclear Regulatory Commission has taken fuel dispersal under heavy consideration as a potential safety issue for commercial power plants.[Flanagan, 2012; Raynaud, 2012] This issue came about after analyzing results from research reactors at Halden and Studsvik that showed fuel fragments in the coolant after performing hypothetical loss of coolant accidents on commercial rods. During fuel dispersal, fuel particles are expelled from ballooned and ruptured fuel rods into the coolant.[P. Raynaud, 2011] These particles can then be carried by the coolant to any parts of the primary system, including (of primary concern) coolant pumps. The potential consequences of fuel dispersal under consideration by the NRC include pump component degradation, debris load in the containment sump and/or core inlet, and increased radiation levels in the coolant. Another concern is the source term associated with these particles, largely at pump inlets where a significant source could lead to flashing of steam and ultimately pump cavitation.

The LOCA testing performed at Halden from 2003-2011 (tests IFA-650.1-.12) were performed with PWR and BWR fuels, some of which were fresh and others being at high burnup beyond the NRC’s licensed limit of 62 GWd/MTU.[E. Kolstad, 2011] The IFA-650.4 test was the first test to notice fuel dispersal into the test channel, with a cladding failure at ~790°C ($T_{clad}$) at a fuel burnup of 92 MWd/kg. Test IFA-650.9 was the second test to show fuel dispersal, with clad failure at ~810°C at a fuel burnup of 90 MWd/kg. Both of these tests were PWR fuel with high burnup and a relatively ductile cladding (low hydrogen concentration, 30-50 ppm). The other high burnup PWR tests with higher hydrogen concentrations (200-650ppm) also failed but were not reported to have experienced any significant release of fuel particles. The tests with fresh fuel rods failed but were not shown to have significant fuel particle release, thought to be due to the larger pellet fragment size compared to the high burnup fuel. It was noted that larger cladding deformations, along with significant fuel fragmentation and relocation, were experienced in the two cases of fuel dispersal. An image of the fuel fragments at the burst regions of IFA-650.4 are shown in Figure 2.17.

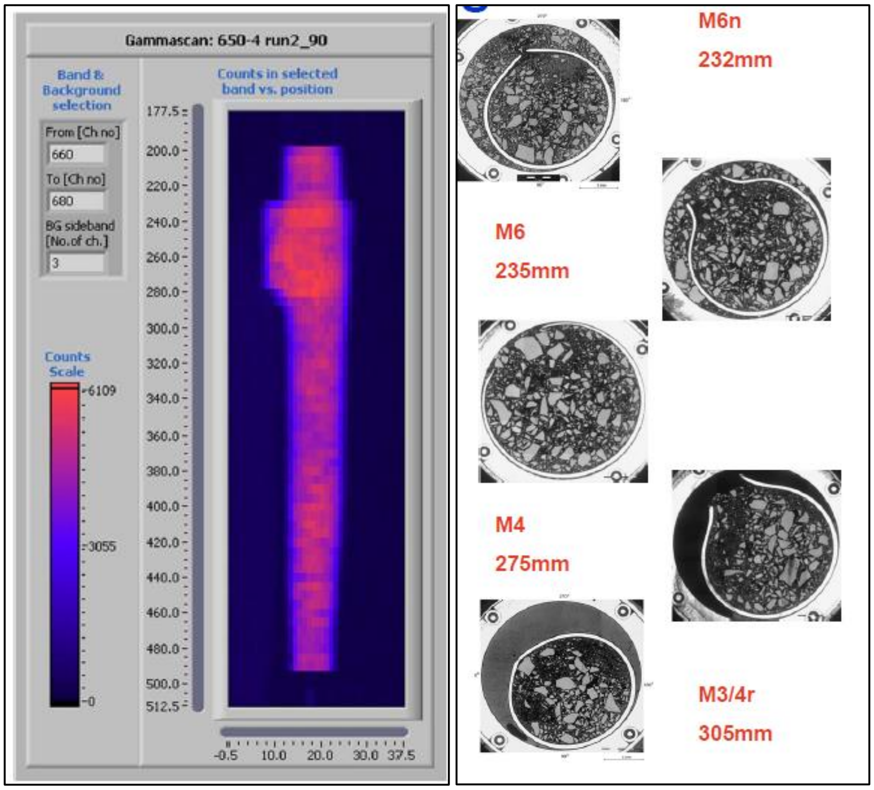

Figure 2.17: IFA-650.4 ballooned region showing dispersed fuel [E. Kolstad, 2011]

Thermal analysis of IFA-650.4 showed that after ballooning, temperatures above the ballooned region decreased while the region immediately below the balloon increased in temperature, indicating fuel movement from the upper part of the rod to the lower part of the rod.[W. Wiesenack, 2007] Pressure measurements showed that the internal rod pressure drops to system level pressure within 1 second. Pressure measurements for IFA-650.9 showed significantly different results after rupture, with equilibrium not being reached until ~110 seconds after cladding rupture. This was attributed to the high burnup fuel impeding axial gas communication thus not allowing the re-opening of the fuel-clad gap during ballooning.[E. Kolstad, 2011]

In conjunction with the NRC's LOCA research program, six LOCA tests have been performed at Studsvik Laboratory in Sweden on high burnup fuel rods.[M. Flanagan, 2012]

The rods tested were .3m rods ramped in steam at 5°C/sec with varying PCT, hold times and fuel burnup. A description of some of the parameters and results of each test are shown in Table 2.2. The total fuel mass released is the fuel released during the LOCA, bending test and shake test, in order to determine the mobility of the fuel remaining in the rod. The measured "empty" length defines the length of the rod at the rupture in which fuel release occurred.

Table 2.2: Results of LOCA tests performed at Studsvik.[M. Flanagan, 2012]

| Test ID | 189 | 191 | 192 | 193 | 196 | 198 |
|---|---|---|---|---|---|---|
| Rod Type | $UO_2$ | $UO_2$ | $UO_2$ | $UO_2$ | IFBA-$ZrB_2$ Coating | IFBA-$ZrB_2$ Coating |
| Burnup (GWd/MTU) | ~72 | ~71 | ~72 | ~71 | ~55 | ~55 |
| Hydrogen Measurement (wppm) | 176 | 271 | 288 | 187 | 149 | <149 |
| Burst Strain (%) | 48 | 50 | 56 | 51 | 25 | 25 |
| PCT (°C) +/- 20°C | 950 | 1160 | 1160 | 1160 | 960 | 1160 |
| Fill Pressure (bar) | 110 | 110 | 82 | 82 | 82 | 82 |
| Rupture Pressure (bar) | 113 | 104 | 77 | 77 | 72 | 74 |
| Rupture Temperature (°C) | 700 | 680 | 700 | 728 | 686 | 693 |
| Rupture Opening Width (mm) | 10.5 | 17.5 | 9.0 | 13.8 | 0.2 | 1.6 |
| Rupture Opening Axial Length (mm) | 23.9 | 21.6 | 22.7 | 17.8 | 1.5 | 11.0 |
| Fuel Mass Released During LOCA (g) | >41 | 52 | 68 | 105 | 0 | 0 |
| Fuel Mass Released Total (g) | >61 | 59 | 84 | 110 | 77 | 62 |
| Measured "Empty" Length (mm) | 148 | 125 | 165 | 205 | 157 | 131 |

Several important observations were made from these tests regarding fuel release, fragmentation and mobility.[M. Flanagan, 2012] Despite the differences in internal pressure, PCT and final ECR, the "empty" length and total fuel mass released are roughly the same for all six cases. It is very evident, however, that the fuel released during the LOCA is where the distinction can be made in terms of when fuel release occurred between the high burn up cases (71-72 GWd/MTU) and the lower burnup cases (55 GWd/MTU).

The high burnup fuel rods released >2/3 of its fuel during the LOCA tests, whereas all of the fuel released from the low burnup cases came from the bend and/or the shake test. An image of the each of the rod ruptures after the LOCA tests is shown in Figure 2.18.

Figure 2.18: Rod rupture opening for Studsvik LOCA tests (left to right) 189, 191, 192, 193, 196 and 198.[M. Flanagan, 2012]

For the Halden Test IFA-650.4, fuel fragments varied in size from <0.1 to <6mm with most of the fragments being <0.2mm.[E. Kolstad, 2011] The particle size distribution and fractional area coverage is shown in Figure 2.19.

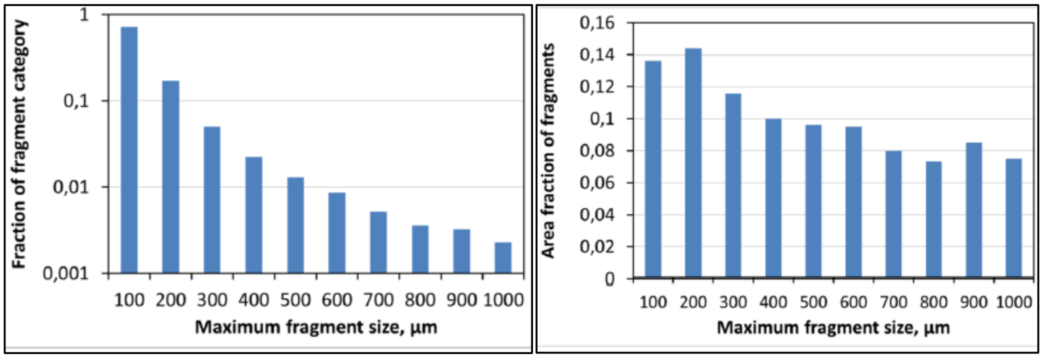

Figure 2.19: Fragment size distribution for IFA-650.4.[E. Kolstad, 2011]

Studsvik's LOCA testing showed results similar Halden's IFA-650 tests on fuel fragmentation and particle size distribution. The mobile, high burnup fuel was found to have a much smaller particle size distribution than the lower burnup fuel. Typical particle size was ≤ 2mm for the high burnup (71-72 GWd/MTU) mobile fuel fragments and > 4mm for the lower burnup fuel (55 GWd/MTU). The larger fuel fragment size coupled with the smaller rupture opening is believed to be the reason for the lack of dispersed fuel in the coolant channel for the lower burnup rods. The particle size distribution of the mobile fuel measured after the LOCA, bend and shake test is shown in Figure 2.20.

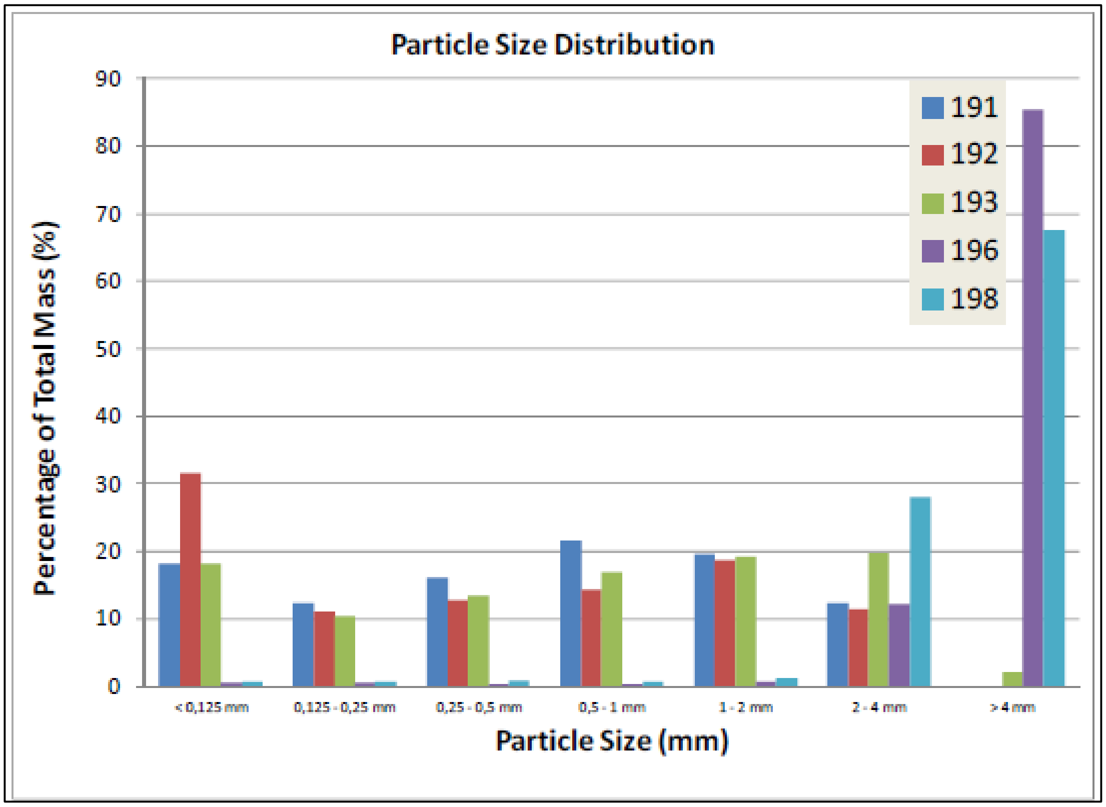

Figure 2.20: Particle size distribution for Studsvik Tests 191-193 (~71-72 GWd/MTU) and Tests 196,198 (~55 GWd/MTU).[M. Flanagan, 2012]

Halden test IFA-650.5 showed that pellet cracking is influenced by the constraint exerted on the fuel by the cladding at failure. Regions of strong pellet-clad contact showed normal operation typical cracking whereas regions where the ballooning led to failure, the sudden drop in pressure resulted in significant additional pellet cracking, as seen in the Figure 2.21.

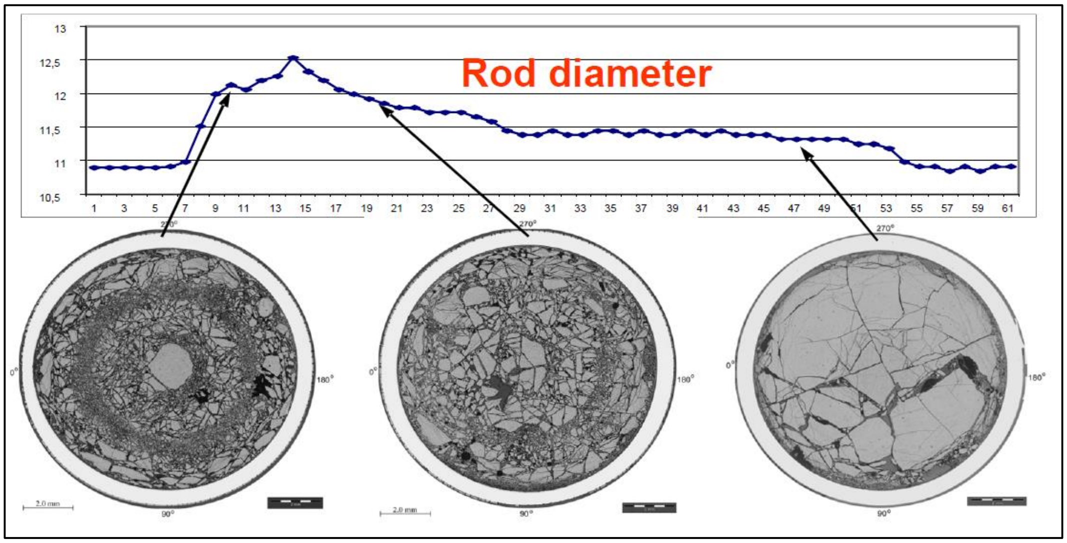

Figure 2.21: Pellet cracking under varying cladding constraints [E. Kolstad, 2011]

A last important observation made in the Studsvik tests was in determining the region around the rupture in which fuel was found to be mobile. The “empty” length of the cladding was compared to the final cladding strain at the ends of the “empty” region to determine the required minimum strain around the rupture to allow fuel mobility. The values ranged from 1-9% strain for all tests, and are consistent with results from Halden that showed strains of 13-17% are required for the fuel to be mobile.[P. Raynaud, 2012] The burst width, LOCA fuel release, and total fuel release of Studsvik Test 191 are in Figure 2.22.

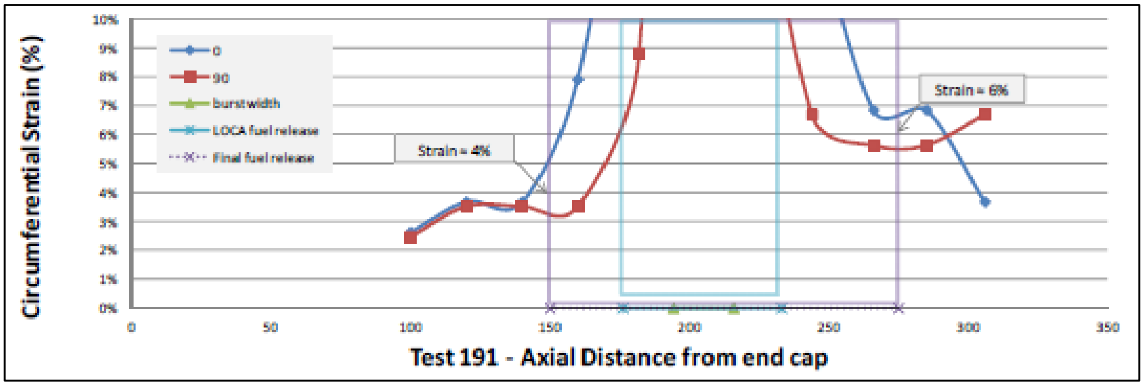

Figure 2.22: Studsvik Test 191 strains at burst and "empty" regions.[M. Flanagan, 2012]

Preliminary studies on fuel dispersal calculations of full core LOCA scenarios have begun at the NRC.[P. Raynaud, 2013] The requirements for fuel dispersal are: ballooning must occur leading to rod rupture, cladding strain must be above certain limits (3-7%), burnup must be above 50-70GWd/MTU, and a fine-enough to disperse threshold (.125-4mm) must be met. Using the NRC codes FRAPCON, TRACE and FRAPTRAN, a typical 4-loop PWR was modeled with varying safety system responses to a large break LOCA. Although very coarse assembly meshing was used in this study, it was determined that under a LOCA scenario with only one train of the emergency core cooling system (ECCS) operational, 6.7kg of fuel is expected to be expelled into the coolant. This work is to be continued and built upon as part of this dissertation research.

## 2.6 SYSTEMS RESPONSE TO ADVANCED FUELS

Systems' modeling requires having a model of a reference nuclear plant that is validated against known conditions to ensure that both the code and model being used are accurate. Due to the positive history of nuclear power in the United States, there are few models that have been validated against recorded data in accident scenarios. Some of the main United States plant models used for validation includes the Peach Bottom Unit 1 BWR, the Three Mile Island Unit 2 PWR and a Zion-like PWR. It is important to note that due to non-standardized plant designs, each plant can have different responses to the same hypothetical accident; therefore results cannot be generalized for all plant types.

An analysis of the TMI-2 accident comparing Zircaloy-2 and SiC has been conducted using EPRI's severe accident analysis MAAP v.4 software.[ Steven C. Johnson, 2012] This study looks at the core response after the reactor has been scrammed but is in an accident condition, with the comparison being the overall response due to the different cladding materials. The MAAP software only has built-in models for Zircaloy cladding which required modifying the code to implement Silicon Carbide; the modified parameters are shown in Table 2.3.

Table 2.3: Modified parameters in MAAP software for SiC modeling.[Steven C. Johnson, 2012]

| **Modified Cladding Parameters for SiC** |
|---|
| Oxidation & Heat Generation |
| Hydrogen Production |
| Average Density |
| Specific Heat |
| Thermal Conductivity |
| Melting Point |

As with any new material, regardless of the type of material, the thermal conductivity, specific heat, melting point and density needed to be updated. However, the parameter that played the largest factor in this study was the oxidation kinetics (heat generation and hydrogen generation). The silicon carbide was to experience no chemical reaction with the superheat steam, providing the maximum benefit possible for the silicon carbide in this study.[Steven C. Johnson, 2012]

As the transient progreses, the core is uncovered after 120 minutes into the accident. It reaches its peak core temperatures at 150 minutes and is reflooded at 174 minutes after the transient began. The initial heat is provided by decay heat following the scram of the reactor core. As the core becomes uncovered, the cladding temperatures increase to the point where the oxidation reaction with the steam environment begins. This produces both a heat source and a hydrogen source. The heat source generated from the exothermic reaction with Zircaloy-2 and steam causes the clad to attain a peak temperature of 2870°C, whereas the SiC reaches a peak temeprature of only 1200°C at roughly the same time.[Steven C. Johnson, 2012] The lower temperature is due to the non-existance of a modeled oxidation reaction with the SiC and steam. This lower temperature reduces the amount of molten material that is generated in the core. The SiC case produced only 3,000 pounds of molten material, due only to the melting of in-core components, whereas the Zircaloy-2 case produced 68,000 pounds of molten material which includes the melting of fuel rods.[Steven C. Johnson, 2012] The lower temperature of the silicon carbide also keeps the cladding from failing as a fission product barrier, therefore not releasing any of the internal gas from the fuel rod into the coolant.

The corresponding hydrogen generation with zircaloy oxidation produces 1000 lb. mass of $H_2$ gas, compared to no hydrogen produced with silicon carbide.[Steven C. Johnson, 2012] In the zircaloy case, the reactor coolant system pressure gradually decreases as the transient progresses until the hydrogen begins to be generated in the core. This causes the core pressure to increase to over twice as high as the case with SiC, up to 2300 psi (~15.9MPa).[Steven C. Johnson, 2012] These results are shown in Figure 2.23.

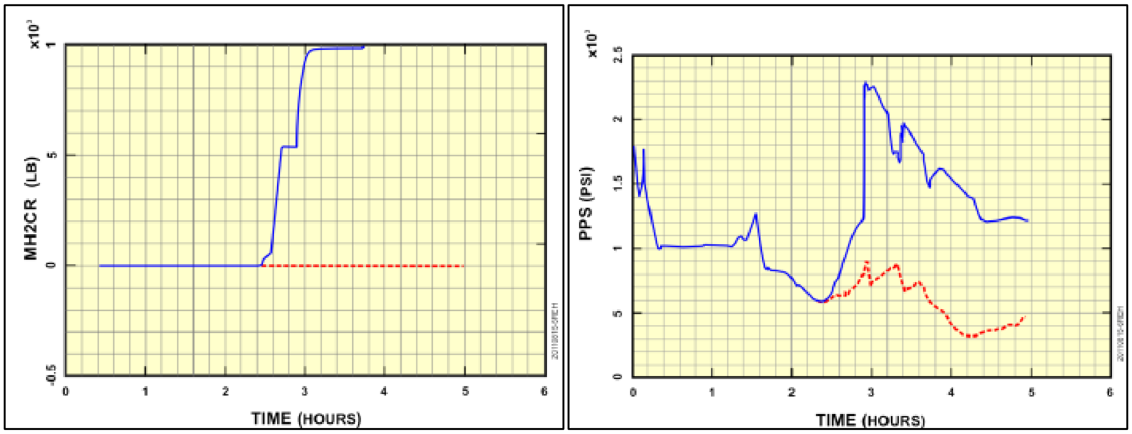

Figure 2.23: Reactor cooling system pressure (left) and corresponding mass of hydrogen produced (right) with Zircaloy cladding (blue lines) and SiC cladding (red lines).[Steven C. Johnson, 2012]

A second study was conducted with a station blackout (SBO) scenario on a Zion-like PWR.[Steven C. Johnson, 2012] In this scenario, there is no auxiliary feedwater for the steam generators, resulting in a dryout after 100 minutes and an increase in pressure that causes the safety valve to the pressurizer drain tank to open. Once the pressure in the drain tank exceeds the maximum allowable pressure, the rupture disk will fail, discharging reactor coolant to the containment leading to an uncovering of the fuel. This study concluded that the time to hot leg creep rupture, caused by natural circulation between the core and steam generators, is delayed by only ~20 minutes when using SiC (delay due to no heat being generated from the oxidation of the SiC compared to Zirc-2 cladding).

A study was performed at MIT comparing Zirc-4 and SiC under a LBLOCA scenario with a typical 4-loop Westinghouse PWR.[Ahn, 2006] The focus of this study was to determine the safety margins for both materials by analyzing the stress distribution in the cladding. The bounding conditions of cladding temperature and coolant pressure were determined using the RELAP code, and the cladding stress distribution was calculated using both primary and secondary stresses in the hoop, axial and radial directions. The primary stresses were considered to be equal for all cladding types, with SiC having the largest safety margin from its higher yield and ultimate tensile strength.

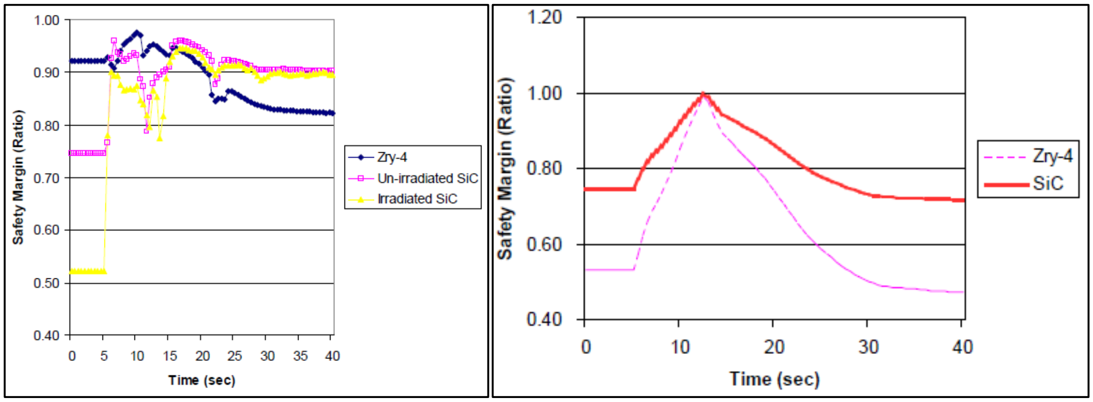

Figure 2.24: Safety margin based off primary stress only (left) and both primary and secondary/thermal (right).[Ahn, 2006]

As for secondary stresses, SiC’s low thermal conductivity the thermal stress has a significant impact at the beginning of the transient (as shown above). The thermal conductivity of SiC at the temperatures reached in a LBLOCA scenario is much lower than that for Zirc-4, and is made worse due to irradiation damage causing increased phonon-phonon scattering. The low thermal conductivity results in a higher temperature gradient across the cladding thickness, which is the driving force for the secondary (thermal only) stress distribution. As a result, the Zirc-4 cladding has a higher safety margin during the first few seconds of the transient.

A full core analysis of SiC with oxidation kinetics was performed using the MELCOR code with a TMI-2 model.[Brad J. Merrill, 2013] The material properties for Zirconium were replaced with those of SiC. The oxidation and volatilization mechanisms were both input into the code and validated against several experiments. It is important to note that the failure criteria in the MELCOR code is based solely on temperature set points. The predicted PCT for Zircaloy cladding exceeds the set point of ~2500K and causes the cladding to fail. However, the PCT for SiC was 1830K, below the melting temperature of the silica (~1873K) and the decomposition temperature of SiC (~2900K), resulting in no cladding failure. Unlike previous studies assuming no SiC oxidation, the results of this study show that the core power generated from oxidation of SiC are ~2 orders of magnitude less than that from Zircaloy oxidation. The gases produced with SiC oxidation are $H_2$ and CO, with CO being 3-4x as abundant as $H_2$; yet these gases combined are less than one-third that of the hydrogen produced by Zircaloy oxidation. The PCT and oxidation results are shown in Figure 2.25.

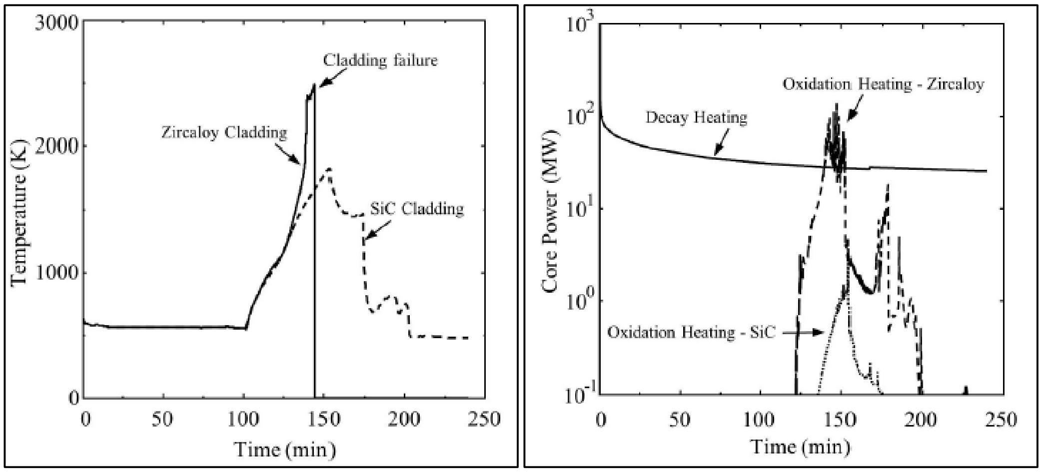

Figure 2.25: Peak cladding temperature (left) and core power (right) for SiC and Zircaloy core materials.[Brad J. Merrill, 2013]

Several parameters were not taken into account in these studies. Transitioning from a ductile metal cladding to a brittle ceramic cladding requires new correlations for modeling the deformation due to internal and external stresses, as well as temperature gradients. It is not discussed in this study as to whether any new cladding deformation models were used. The lack of oxidation kinetics [Steven C. Johnson, 2012] was shown to be the "best possible outcome" but from a safety standpoint needs to be addressed, as different accident scenarios can result in different PCTs and times at which the elevated cladding temperatures are maintained. The MIT study [Ahn, 2006] concluded that the cladding primary stress distribution is the same during the transient; however, this should not be the case when considering hydrogen generation (as seen in [Steven C. Johnson, 2012]) and different internal rod pressures at the onset of the transient due to the lack of cladding creep down. The impact of thermal stresses was shown to be significant and will be considered in this proposed work, although currently the NRC codes do not take this phenomena into account. There is a strong thermo-mechanical relationship between temperatures and cladding stress based on fuel performance, which was not addressed in the MELCOR [Brad J. Merrill, 2013] code analysis.  Also, no variances in the initial conditions were taken into account in these studies.  These assumptions will be assessed in this work with both PWR and BWR reactor scenarios.

# CHAPTER 3

## METHODOLOGY

### 3.1 CURRENT MODELING TOOLS

### 3.1.1 FRAPCON

FRAPCON-3.4 is computer code that calculates the steady-state response of light water reactor fuel rods during long-term burnup.[K.J. Geelhood, 2011] It was developed for use of the U.S. NRC by Pacific Northwest National Laboratory (PNNL) for determining steady-state fuel behavior up to the NRC licensed limit of 62 GWd/MTU. The fuel, cladding and reactor types modeled by FRAPCON are shown in Table 3.1.

Table 3.1: Materials and reactor types modeled in FRAPCON

| **Fuels** | **Cladding** | **Rx Types** |
|---|---|---|
| $UO_2$<br>MOX $(U,Pu)O_2$<br>Urania-Gd ($UO_2$-$Gd_2O_3$)<br>$UO_2$ with $ZrB_2$ coating | Zircaloy-2<br>Zircaloy-4<br>ZIRLO<br>M5 | BWR<br>PWR<br>Heavy Water Rx |

Some of significant phenomena modeled by FRAPCON includes the following:

- Fuel & Cladding Temperatures
- Fuel Swelling & Densification
- Waterside Corrosion
- Cladding strains and elastic/plastic deformations
- Fission Gas Release & Internal Gas Pressure

The FRAPCON code has the ability to model the complex thermo-mechanical interaction between the fuel pellet and the cladding. In order to accomplish this, the code has a set of iteration loops that require convergence on temperature and pressure to achieve the steady-state solution. The temperature iteration loop contains calculations for fuel and cladding deformation as well as the temperature distribution. This is cycled over each axial node in the fuel rod. The pressure iteration loop calculates the total gas in the rod, plenum temperature and the resulting gas pressure. A change in the gas pressure will alter the gap conductance as well as the cladding stress, requiring another cycling of the temperature loop. This process is repeated until convergence on the gas release loop is reached, and the next timestep is advanced. The solution scheme is considered a 1-D1/2 solution, where the radial solution is solved at each axial node using the finite difference method and the variables at any given axial node are independent of variables at all other axial nodes, resulting in no axial heat conduction.

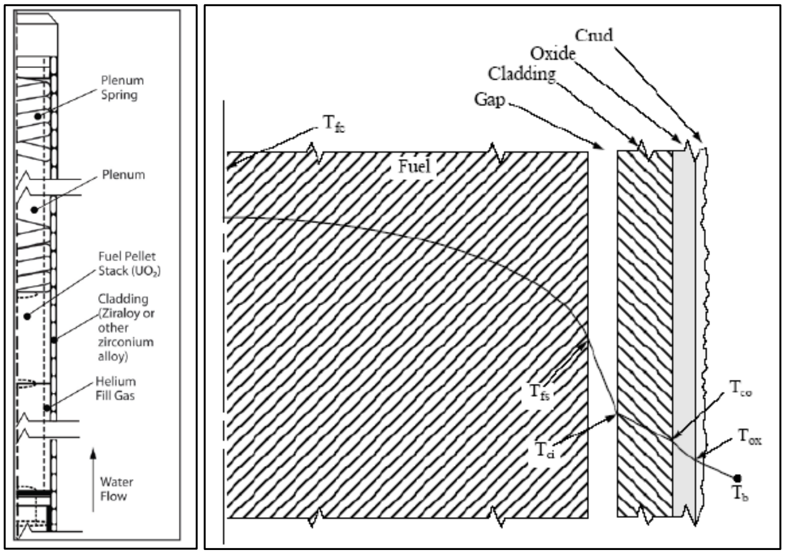

Figure 3.1: Typical design (left) and fuel temperature distribution in a LWR fuel rod.[K.J. Geelhood, 2011]

The phenomena of densification, swelling, relocation and thermal expansion, all of which are modeled by FRAPCON, play an important role in establishing the fuel temperature. These phenomena, combined with cladding creep and thermal expansion, determine the point at which PCMI occurs. This interaction will cause the cladding to deform from additional swelling and thermal expansion beyond the point at which PCMI began. However, currently the code assumes a "rigid pellet" model, preventing a feedback mechanism on the fuel from any cladding resistance. During a LOCA, the driving mechanism for additional fuel deformation will be thermal expansion and for cladding deformation will be ballooning, driven by the internal rod pressure and cladding temperature. The internal rod pressure is a function of the number of moles of gas, temperature, and free volume; the latter of which is determined by the burnup-dependent and thermal deformations previously mentioned. Due to the 1D-1/2 steady-state solution scheme in FRAPCON, it is not suitable for modeling rapid temperature transients where stored thermal energy plays an important role.

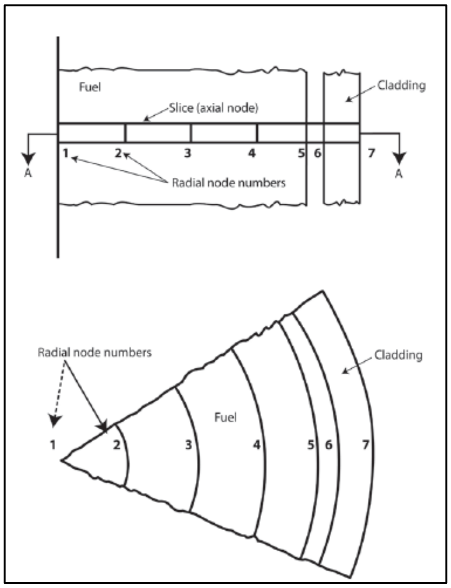

Figure 3.2: Radial nodalization at a single axial node as viewed from the side and top.[K.J. Geelhood, 2011]

### 3.1.2 FRAPTRAN

FRAPTRAN-1.4 (Fuel Rod Analysis Program TRANsient) is the U.S. NRC's transient fuel performance code for determining fuel rod performance of LWRs during reactor transients such as a LOCA, anticipated transient without scram (ATWS), and reactivity-initiated accidents (RIA).[K.J. Geelhood, 2011] Due to the transient nature, this code is typically used in conjunction with FRAPCON via a restart file that supplies the burn-up dependent data that doesn't change over the times involved in a transient scenario. The same materials and fuel types are used in both codes with common material properties derived from MATPRO. FRAPTRAN uses a transient heat conduction model requiring small timesteps to reach convergence in the temperature distribution before advancing. The phenomena of interest calculated by FRAPTRAN include:

- Radial Heat Conduction
- Heat Transfer to the Coolant
- Elastic-Plastic Fuel & Cladding Deformation
- Oxidation
- Fission Gas Release & Internal Gas Pressure

FRAPTRAN has the ability to predict fuel melt and cladding failure. Cladding failure is expected to occur via two different mechanisms depending on the cladding temperature dictated by the type of reactor transient. A RIA scenario is expected to result in a low temperature cladding failure which is caused by fuel expansion into the cladding. The RIA results in an increased fuel temperature combined with a cool cladding with high strength; the thermal expansion of the fuel will stress the cladding ultimately leading to failure. A LOCA scenario will result in high cladding temperatures at which the cladding is very ductile. When sufficiently high gas pressures are reached inside the rod to put the cladding into tension, the ductility of the clad will cause it to balloon and ultimately lead to failure. The high temperature ballooning mechanism is the driving force for the LOCA fuel dispersal studies described in the following chapters.

### 3.1.3 TRACE

TRACE-V5P3 (TRAC-RELAP Advanced Computational Engine) is a best-estimate reactor systems code that was developed by the U.S. NRC to analyze steady-state and transient behavior in LWRs.[Division of Safety Analysis, 2012] It has both thermal hydraulic (T/H) and neutronic capabilities through combining the legacy T/H codes TRAC-P, TRAC-B, RELAP5 AND ROMANA and the neutronics code PARCS. It is capable of modeling 1-D and 3-D fluid flow through the use of pipe and vessel components, respectively.

The modeling of assemblies is performed by utilizing heat structures (HTSTR) for PWRs or BWR fuel channels (CHANs). The main difference between these two types of assemblies is in the way they are cooled. The HTSTRs are allowed to have cross flow so that each axial node can have similar coolant conditions with other heat structures outside of the assembly. The CHANs are restrictive with the coolant flow and have constrained coolant inlet and outlets so that there is no cross flow ability from one assembly to the next. As for the fuel rods models, there is no difference between the two. Similar to FRAPCON/FRATRAN, the thermal properties for both the fuel and cladding are obtained from MATPRO. However, there are currently no ways to model the burnup dependent parameters and they must therefore be input from another code, i.e. FRAPCON. Also, the thermo-mechanical response is very limited compared to the fuel performance codes. For example, no additional stress on the cladding is calculated from PCMI, the change in internal rod pressure is set as the ratio of the plenum temperature to room temperature, and there is no cladding ballooning model. For these reasons, it is desired to combine the TRACE analysis with fuel performance codes such as FRAPCON and FRAPTRAN for the best-estimate fuel rod analysis. This analysis would use FRAPCON for burnup dependent parameters, TRACE for modeling the heat conduction through the rod to determine the cladding surface temperatures and FRAPTRAN for the thermal-mechanical fuel rod response with bounded cladding temperatures.

### 3.2 STEADY-STATE (BU DEPENDENT) DATA TRANSFER & MAPPING

There are several burnup dependent parameters that affect both the thermal and mechanical response of the fuel rod in a transient scenario. The thermal response is affected by thermal conductivity degradation, the gap size and constituents, and the oxidation layer thickness. The mechanical response is a result of internal rod pressure/interfacial pressure, fuel dimensional changes and corrosion. The burnup dependent parameters of fission gas release, fuel swelling/densification, relocation, waterside corrosion (oxidation and hydrogen pickup) and cladding creep all affect the thermo-mechanical response of the fuel rod. Due to TRACE’s inability to calculate these parameters, the fuel performance code FRAPCON will be used.

The time in which a transient takes place is small enough to keep the burnup dependent parameters as constants, and thus are considered initial conditions to the problem. In doing so, it allows the two codes to be coupled in a manner that allows them to be run in sequence. There are two different platforms that are currently used for building input files for each code. FRAPCON uses an Excel-based Auto Input Generator (AIG) developed by PNNL and TRACE uses the SNAP interface developed for use by the NRC. Although SNAP allows for the building of FRAPCON input files, it is still in the early stages of implementation and the AIG is the dominantly used interface by worldwide FRAPCON users. The AIG will be used as the base for developing a tool that allows steady-state data transfer. Excel-based programs are easy to manipulate through Visual Basic for Applications (VBA) scripts without the need for a compiler and Microsoft Excel is found on most machines. Building off of the AIG also allows the as-fabricated parameters used for the FRAPCON runs to be easily transferred into the TRACE input deck to ensure consistent fuel rod design such as fuel and cladding dimensions at BOL. The flow diagram for this interface is shown in Figure 3.3.

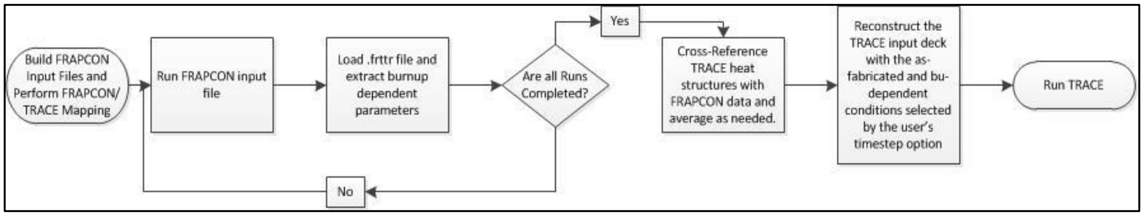

Figure 3.3: Flow diagram for coupled FRAPCON/TRACE data transfer

The first step is to build the FRAPCON input files for each rod to be modeled. Power profiles, power histories and as-fabricated parameters can vary between FRAPCON cases. With small variances (if any) in the as-fabricated parameters of the rods within a given core, the program will use Excel’s Index function to reduce the user input requirements for each rod. Once all of the input files have been generated, batch files will be created to run the FRAPCON cases across 1 or several nodes. A file (named jobstatus) will be created and deleted at the beginning and end of each FRAPCON run that will be used in conjunction with a wait timer in VBA to know when the run has completed, after which the .frttr file (described below) will be loaded into the AIG.

FRAPCON will be modified to write a new output file that contains the following information: gas gap pressure, gas molar ratios and axial nodal values for burnup, fuel swelling, fuel densification, fuel relocation, cladding permanent deformation (includes creep), gap heat transfer coefficient and oxide layer thickness. This file is designated as .frttr (FRAPCON to TRACE) and is declared in a FRAPCON input file as FILE50 and turned on by setting nfrttr=1 in the $frpcon input block. This file will be written for each timestep and contain values for all axial nodes. Another parameter under consideration to be written to the .frttr file is the radial power profile, which is also strongly influenced by the burnup and affects the fuel temperature distribution. However, this will require significant modification to the TRACE input file to implement a radial power profile at each axial node for each fuel rod. Due to the focus of this study on LOCAs where the reactor has been scrammed, a rod average radial power profile will be used in the POWER component. It is important to note that TRACE currently only allows the values for swelling/densification, cladding creep and oxide layer thickness to be input as a single value that is constant for all axial nodes. The "average" value will be input over the entire length of the rod; however, this issue will be addressed in this analysis with the goal of supplying individual values for each node.

When all of the FRAPCON runs have completed and data extracted, the next phase will be to cross reference the FRAPCON runs to the TRACE HTSTRs (or CHANS) and normalize as needed. It is common in TRACE input decks to use a coarse nodalization for modeling assemblies where several assemblies are averaged together. This program will be written to allow for this averaging or to be a direct 1:1 correspondence between a FRAPCON run and a TRACE heat structure (which may represent an individual rod or an average rod representing an entire assembly). The averaging and reconstruction will be comprised of two steps, the first of which is the read and extract the original heat structure and power data from the TRACE input file and the second is to use the user-supplied normalization chart to update the extracted heat structure data. Finally, the TRACE input deck will be re-written to contain the updated data from FRAPCON and executed, first with the steady-state run and, after completion, the transient run(s). There are several differences in the input structure of a CHAN component and a HTSTR component, and for this reason two separate variations of the auto input generator will be developed, denoted AIG-BWR and AIG-PWR.

Another important consideration for the burnup-dependent analysis is in determining the time in the cycle at which the transient occurs. With typical average assemblies reaching 15-20 GWd/MTU burnup in each cycle, the burnup dependent parameters will be vastly different at beginning (BOC), middle (MOC) and end-of-cycle (EOC). Not only will the burnup dependent parameters be different, but also the core-wide radial and axial power distributions will be different. At BOC, a fresh fuel rod will have the largest gap size resulting in very high fuel centerline temperatures. Conversely, at EOC a second or third cycle rod can have sufficiently high internal rod pressures from FGR to lead to cladding ballooning in a LOCA or sufficient swelling to allow for PCMI in a RIA accident. End of cycle will also have the highest oxidation values, potentially reducing the amount of time in the accident before the ECR limit is reached. The interface developed for steady-state data transfer will have the ability for the user to select BOC, MOC or EOC for determining at which timestep to send the burnup dependent parameters to the TRACE input deck.

### 3.3 METHODOLOGY FOR TRANSIENT ANALYSIS

Although construction of the TRACE input deck will be as described in the previous section, a transient analysis can be performed in different ways. TRACE was developed to be used as a stand-alone code for reactor transient analysis, and is therefore sufficient to be used as the final tool for determining the number of failed rods in the core. Several studies have been conducted using stand-alone system codes such as RELAP, MELCOR and MAAP for determining fuel rod failure.[Ahn, 2006; Brad J. Merrill, 2013; Johnson, 2012] From the previously described shortcomings of TRACE, a "best-estimate" analysis for fuel rod failure would be to use the TRACE code for the systems response to determine the coolant boundary conditions and use FRAPTRAN for the fuel rod transient response, both of which will be informed with FRAPCON fuel rod initial conditions.

This dual-code analysis can be performed by using a two-step process, similar to the method described above for steady-state analysis, in which TRACE will be run to completion and the data calculated by TRACE will be put into FRAPTRAN for the final analysis. This is the current methodology being used by the NRC for fuel dispersal studies.[P. Raynaud, 2013] Another way to perform this analysis is to use on-line data communication in which the two codes will share information back and forth to provide feedback on fuel rod deformation and coolant conditions. This method is the most complex but would be the most detailed in evaluating how the coolability of the rod changes the boundary conditions. The methodology and drawbacks will be described for both methods below. Both of these methods will be explored in the ensuing transient analysis.

### 3.3.1 Two-Step TRACE/FRAPTRAN Analysis

The two-step TRACE/FRAPTRAN analysis provides a better estimate of fuel rod failure than TRACE alone due to the improved fuel rod models in FRAPTRAN. Unlike FRAPTRAN, TRACE cannot model high temperature FGR, fuel expansion into the cladding resulting in interfacial pressure, ballooning and the oxidation effects on cladding strength. This methodology uses the reverse ideas of the steady-state analysis; the boundary conditions from each rod modeled in TRACE is modeled by FRAPTRAN, with the number of FRAPTRAN runs being equal to the number of FRAPCON runs from the steady-state analysis. This type of analysis will require the steady-state analysis from FRAPCON due to the need of the restart files for initializing the FRAPTRAN runs and again the importance of the burnup dependent parameters. A schematic of the full steady-state and transient analysis is shown in Figure 3.4.

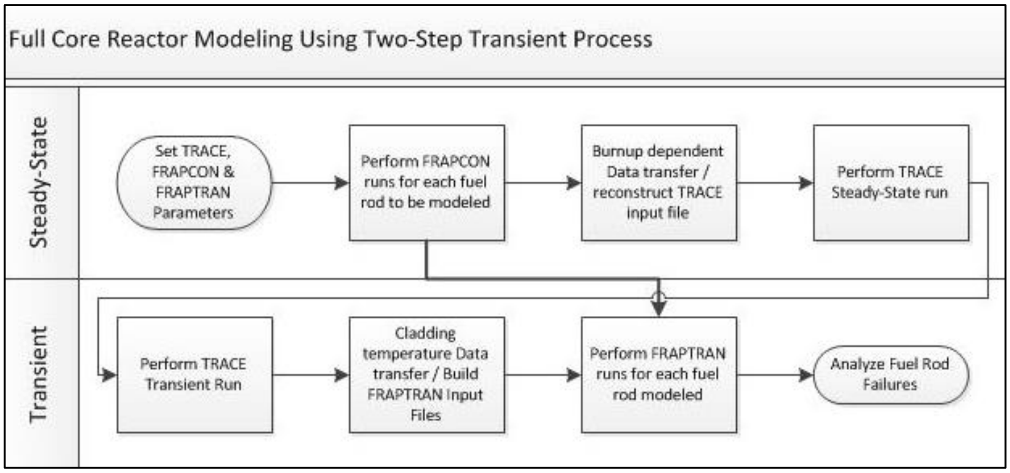

Figure 3.4: Schematic for full core transient analysis using the two-step transient process.

As with FRAPCON, FRAPTRAN is most commonly utilized via its Auto Input Generator (Here on out denoted FT-AIG to distinguish from FRAPCON's Auto Input Generator, AIG). The FT-AIG will be modified in a similar manner that allows it to cycle through building multiple input files based on the number of fuel rods to be analyzed, and subsequently run each case over a user-specified number of computer nodes. For this analysis, the cladding surface temperatures and coolant conditions are extracted from the TRACE .xtv file using the APlotter software. The APlotter software will read user-created batch files, extract and convert the .xtv data to ascii and write .csv (comma separated value) files for the data required for each fuel rod. The FT-AIG will read from the various .csv files for the conditions needed to build the FRAPTRAN input file.

The FRAPTRAN code does not have the same level of detail as TRACE in thermal-hydraulic modeling and has difficulty in modeling rapidly changing coolant conditions. For this reason, the cladding temperatures at each axial node will be used as the supplied coolant conditions along with a nearly infinite heat transfer coefficient (HTC) to force the cladding temperature equivalent to the coolant temperature. This, however, is where a major drawback comes from this type of coupling in that there is no feedback on cladding ballooning and rupture between FRAPTRAN and TRACE. Although FRPATRAN may predict cladding ballooning leading to a reduction in flow area, this will not be fed back into TRACE which can lead to an underestimation of the cladding surface temperature due to excessive cooling. This is believed to be more of a concern in BWR analysis than PWR analysis due to the advance of crossflow.

For the final analysis of fuel rod failure (and fuel dispersal) the output files of each FRAPTRAN run will be opened and read in the same manner the .frttr files are read. The first thing to be read is the final timestep. FRAPTRAN does not have the timestep backup ability that TRACE uses, so when a timestep is too large for code stability the code will simply crash. If the last timestep is not equivalent to the final timestep specified in the input file, the FT-AIG will reduce the timestep value specified before the code crashed and restart the run.  FRAPTRAN runs can last up to several hours, depending on the number of timesteps and how quickly the coolant conditions change.  If the case runs to completion, FT-AIG will extract the same parameters that would be found in the TRACE output file with additional information related to the ballooning strain, rupture node, ECR, temperatures, etc.  At this point the fuel dispersal analysis will also be calculated based on the values extracted from the output file.

### 3.3.2 Real-Time TRACE/FRAPTRAN Coupling Analysis

Real-time coupling of TRACE and FRAPTRAN will require either building the FRAPTRAN source code into TRACE or using a message passing interface (MPI).  If building into TRACE, the FRAPTRAN program would replace the heat transfer module that is currently used for both channels and heat structures.  A namelist flag will be added to the TRACE code, use_FRAPTRAN=.TRUE., that will tell the code when to use FRAPTRAN's routines rather than the original routines.  The coolant conditions will be sent to FRAPTRAN and the fuel rod state (temperatures, deformations, stress/strains, etc) will be sent to TRACE, along with the power and percent of flow blockage for each node.

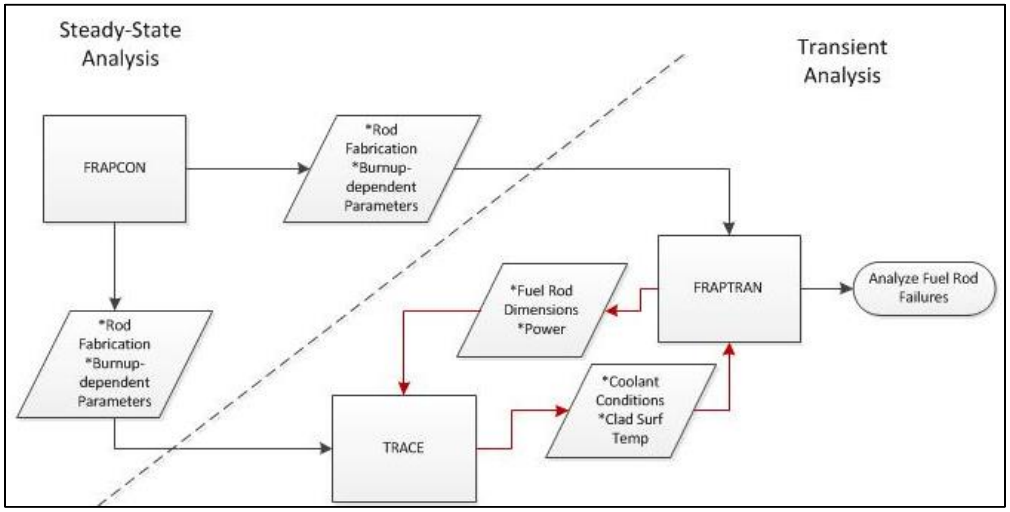

Figure 3.5: Schematic for full core transient analysis using a coupled technique.

If building FRAPTRAN into TRACE, one problem will be receiving and storing the additional fuel rod fabrication data that is required to run FRAPTRAN but is not needed in TRACE. This can be overcome by allowing the TRACE HTSTR and CHAN components to contain additional input data or by allowing FRAPTRAN to initialize this data from the FRAPCON restart files. The second problem is that FRAPTRAN is a single rod code; additional arrays will need to be developed that store the data for each parameter for each rod. FRAPTRAN will need to calculate conditions for every rod at the bottom axial location, repeat for each axial location, and then repeat again for each timestep. Due to TRACE's ability to perform a time-step backup, more than one time-step value will need to be stored in the shared memory.

To perform an external coupling of the codes, a general interface will need to be developed that allows the codes to send/receive data. This method would allow FRAPTRAN to still read and process data from a FRAPTRAN input file and FRAPCON restart file, and write data to the plot and output file. Another benefit of this method is that minimal modifications will need to be made to either code, as long as they can read and write data that will be passed from one program to another. This technique will allow the TRACE code to use its own fuel rod heat transfer calculation as long as it receives from FRAPTRAN the fuel and cladding surface displacements and the associated flow blockage from ballooning and/or rupture. This technique will also require improvements in inputting axial nodal values for permanent cladding deformation in TRACE.

## 3.4 Code Modifications for Improved Fuel Rod Analysis and Advanced Materials Modeling

### 3.4.1 Improvements for Consistencies between Codes in Thermal Modeling

In analyzing the input requirements for the TRACE code, it was determined that there are certain phenomena not fully captured along the axial length of a fuel rod that will affect the temperature distribution across the fuel. These phenomena include fuel swelling/densification and cladding creep. Currently these values are input into the code as a single value that is assumed average over the entire height of the fuel rod, with the sum of swelling and densification input as a single parameter. However, the axial power distribution is not constant over the height of the rod in either PWRs or BWRs. With $UO_2$ at normal operating temperatures, the fuel swelling is considered to be athermal and only a function of burnup, with a rate of 0.062% per GWd/MTU starting at 6 GWd/MTU. With differences in the axial power factor (APF), the swelling values for each node will vary (due to $BU_{node} = APF_{node} * Power * Time$ for each timestep; Total BU = $\int_0^{time} \mathrm{APFnode} * \mathrm{Power}\, dtime$). Swelling and densification affect the fuel surface displacement, increasing/reducing, respectively, the size of the gas-gap, ultimately affecting the fuel temperature distribution due to the large thermal resistance caused by the gap. Swelling also affects the amount of free volume in the rod that can be occupied by gases, resulting in changes in internal rod pressure and cladding stresses.

The cladding creep is input as a single value sum of thermal creep and irradiation induced creep as well as any permanent cladding deformation resulting from PCMI. With the FRAPCON code, the internal and external pressures will be the same for each axial node before hard contact due to internal rod pressure being constant on the inner surface of the cladding and no pressure drops considered in the coolant. After PCMI, the stress distribution will begin to vary once the interfacial pressure caused by fuel expansion onto the cladding exceeds the internal rod pressure for a given node leading to an outward cladding plastic deformation. The thermal induced portion of creep will vary due to differences in average cladding temperature. Similar to swelling, internal cladding creep will reduce the size of the gas-gap and the free volume available for internal rod gases.

The TRACE code defines the parameters for swelling/densification and creep as *ufswell* and *ucrpdown*, respectively. These are stored in the code as heat structure tabular values, denoted by hsTab(idx)%, that are specific to each heat structure defined via the input deck. These will be converted to allocatable arrays (hsAr(idx)%) that will be sized based on the number of axial nodes for the heat structure. For the thermal calculation solution in TRACE, the gap size will now vary for each axial node providing a more accurate temperature distribution and estimation of fuel centerline temperature. The axially noded *ucrpdown* value will also be used when coupling TRACE and FRAPTRAN by allowing FRAPTRAN to specify the amount the cladding node has ballooned, resulting in a change in the coolability of the rod. Disregarding the feedback between ballooning and resulting flow-blockage is currently the largest drawback when using the two step transient analysis method.

### 3.4.2 Direct Moderator Heating

When modeling a full reactor core, the phenomena of heating of the coolant and structures caused by gamma ray absorption and neutron scattering must be taken into account. The gamma heating is a result of the gamma rays created from fission and decay being absorbed by the coolant and structural materials (which is ultimately transferred back into the coolant). Heating of the moderator is dominated by neutron slowing due to elastic scattering, while heating of structural materials by neutrons is a result of both elastic and inelastic scattering. The amount of energy deposited in the fuel, coolant and structural materials is different for each reactor type due to the differences in the amount of zirconium, iron and other structural materials in the reactor, as well as the moderator densities. Typical values are shown in Table 3.2.

Table 3.2: Typical LWR values for direct moderator heating.[Neil Todreas, 2010]

| Quantity | PWR | BWR | PHWR (CANDU) |
|---|---|---|---|
| % of Power Deposited in Fuel Rods | 97.4 | 96.5 | 91.6 |

The TRACE code allows the user to specify a percentage of the total reactor power that is directly deposited into the moderator via the flags promheat and decaheat. What this does for the power distribution is that it allows the coolant to receive energy and heat up directly without having to be thermally carried from the fuel through the cladding and removed via an appropriate heat transfer correlation by the coolant. By reducing the amount of energy that must be thermally carried outward from the fuel pellet to the coolant, the fuel temperatures are reduced. For the coupled steady-state modeling of fuel rods using FRAPCON and TRACE, it is important that the conditions are being modeled equivalently between the two codes at the onset of the transient to ensure equivalent internal rod pressures and stored energy within the fuel.

FRAPCON's 1-D radial heat transfer solution, however, assumes that all of the energy that is deposited into the coolant is carried thermally from the fuel pellet outward. There is no ability to model direct moderator heating of the coolant. When matching the linear heat generation rate between TRACE and FRAPCON, this will result in a higher than expected fuel centerline temperature in FRAPCON with potential consequences of higher FGR or earlier than expected PCMI. If trying to match the total energy deposited within the fuel, the coolant conditions in FRAPCON will be lower thus underestimating the amount of corrosion and cladding thermal creep. To match fuel temperatures, direct moderator heating will be implemented into FRAPCON by reducing the volumetric heat generation rate in the fuel, $q'''_{fuel}$, and the surface heat flux, $q''$, by (1-*modheat*), where *modheat* is a fractional variable between 0 and 1 used to define the amount of moderator heating that goes directly to the coolant. The updated thermal equations are shown below for the fuel temperature distribution (3.1) and cladding temperature distribution (3.2). The temperature drop across the gas-gap, oxide layer, crud layer and film layer will all use the modified surface heat flux value shown in Equation 3.2

$$\iint_{Surface} k(T,\vec{x})\vec{\nabla}T(\vec{x})\,\vec{n}ds = \iiint_{Volume} S(\vec{x})dV \;\; where \;\; S(\vec{x}) = q'''(\vec{x}) * (1 - modheat) \qquad 3.1$$

$$\Delta T_c = \frac{q''(z) r_o \ln(^{r_o}/_{r_i})}{k_c} \;\; where \;\; q''(\vec{x}) = \frac{LHGR}{(\pi D_o)}(1 - modheat) \qquad 3.2$$

To match the coolant temperatures, the fraction of the user supplied LHGR that is designated for gamma ray and neutron heating of the coolant will be added back to the coolant enthalpy rise model by a fraction of 1/(1-*modheat*). To get the total energy deposited in the coolant node, the coolant enthalpy rise model multiplies the surface heat flux by the perimeter of the cladding and integrates over the axial node length. The relationship between surface heat flux and LHGR allows the bulk coolant enthalpy rise model to be updated as shown in Equation 3.3 below.

$$T_b(z) = T_{in} + \int_0^z \left[\frac{(\pi D_o) q''(z)}{(1-modheat) C_p G A_f}\right] dz \qquad 3.3$$

During normal operation, beta (β) and gamma radiation account for approximately 7% of the total thermal power output of the reactor.[John R. Lamarsh, 2001] Immediately after shutdown, the two major sources of heat generation are from fissions caused by delayed neutron emissions and from fission product decay (resulting in beta and gamma emissions). After 10s, the gamma and beta radiation account for ~70% of the total decay power.[Samuel Glasstone, 1981; Neil Todreas, 1990] Although all of the energy from beta particles is deposited in the fuel, only a fraction of the gamma energy is deposited in the fuel.[Neil Todreas, 1990] The rest of the gamma energy is deposited within structural and other core materials. A simplified representation of the ratio of decay power to initial reactor power caused by various sources is shown in Figure 3.6.

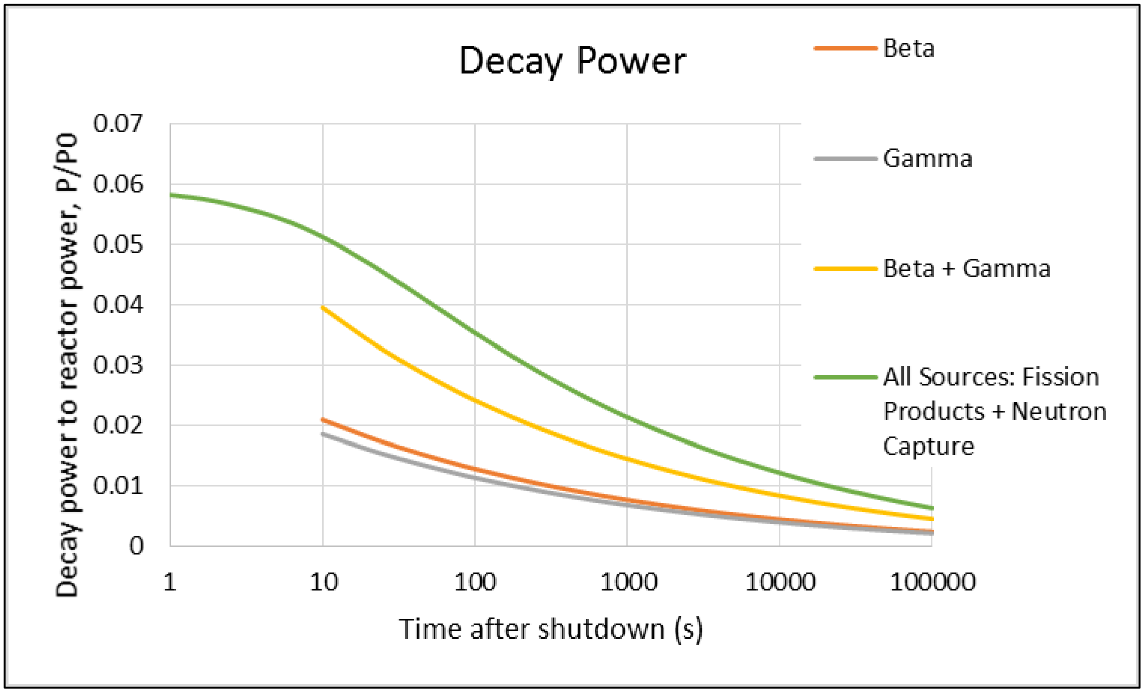

Figure 3.6: Ratio of decay power to reactor power from beta, gamma and all sources after one year of reactor operation. Graph constructed from equations 3-70a, 3-70b and 3-71 from Nuclear Systems 1.[Neil Todreas, 1990]

For transient analysis, the FRAPTRAN code does have the ability to model gamma ray heating of the coolant. However, the code does not have the ability for the user to specify the amount of gamma ray heating (to match the value used for the TRACE analysis). Gamma ray heating is proportional to the power (2%) of the modeled rod and there is no variation of gamma ray heating with the void fraction of the coolant (amount of liquid/gas). The first issue will be overcome by allowing the user to specify the amount of gamma ray heating via the input file or the FRAPCON to FRAPTRAN restart file. The second and third issue will be addressed by performing neutronics calculations using MCNP and/or SCALE. This analysis will first be used to determine how much reactor power is coming from direct gamma ray heating of the coolant via structures and fission product decay and how this relates to the current rod power. The distribution of gamma ray heating will then be analyzed to determine where the gamma ray energy from fission product decay is deposited, whether it be in structural materials, directly in the coolant or back into the fuel rod. Lastly, the change in the gamma ray energy distribution based on the liquid density in the core will be calculated and used to provide a new correlation in FRAPTRAN for determining where the gamma energy is deposited based on the amount of liquid with respect to the particular node in the core.

### 3.4.3 Pellet Clad Mechanical Interaction (PCMI) and Cladding Rupture Modeling

Pellet Clad Mechanical Interaction, or PCMI, is a phenomenon that occurs when the fuel pellet and the cladding come in physical contact with one another. Once the contact occurs, new stresses are applied to both the fuel and the cladding as a result of further fuel outward expansion or cladding creep down. If these stresses continue to grow, it can eventually lead to failure of the cladding by rupture. There are several phenomena in both the fuel and the cladding that can lead to pellet clad mechanical interaction.

Currently modeled, the fuel is susceptible to thermal expansion, swelling, densification and relocation. The cladding can experience mechanical deformation (elastic and/or plastic), creep and thermal expansion. The deformations that each experience in the reactor are outlined in equations 3.4 and 3.5 for the fuel and cladding, respectively.

$$u_f = u_{tf} + u_s + u_d + u_r \tag{3.4}$$

$$u_{ci} = u_{tc} + u_{cc} + u_e + u_p \tag{3.5}$$

Table 3.3: Deformation parameters of fuel and cladding

| Symbol | Description | FRAPCON | FRAPTRAN | TRACE |
|---|---|---|---|---|
| $u_{tf}$ | Fuel thermal expansion | Yes | Yes | Yes |
| $u_s$ | Fuel swelling | Yes | No – Input | No – Input as sum |
| $u_d$ | Fuel densification | Yes | No – Input | |
| $u_r$ | Fuel relocation | Yes | Yes* | Yes* |
| $u_{tc}$ | Cladding thermal expansion | Yes | Yes | Yes |
| $u_{cc}$ | Cladding creep | Yes | No - Input | No – Input |
| $u_e$ | Cladding elastic deformation | Yes | Yes | Yes* |
| $u_p$ | Cladding plastic deformation | Yes | Yes | Yes* |

*Simplified analysis compared to FRAPCON

There are two regimes of PCMI, one denoted as soft contact and the other as hard contact. Soft contact occurs as a result of fuel thermal expansion, swelling, relocation and cladding creep. In this regime, the contact of the fuel onto the cladding surface does not result in an interfacial pressure due to the void volume in the pellet created as a result of fuel cracking and relocation. Based on experimental $UO_2$/Zirc data, once 50% of the relocation value at soft contact is recovered through further fuel thermal expansion and swelling, a hard contact regime begins that allows an internal pressure to be applied to the cladding that is taken as the maximum value of either the gas pressure or fuel/clad interfacial pressure. At hard contact, fuel expansion onto the cladding results in an outward displacement of the cladding surface that is equivalent to the amount the outer surface of the fuel was displaced. In FRAPCON, there is no feedback mechanism based on the elastic modulus of the cladding to provide the same amount of interfacial pressure back onto the fuel. This is likely due to the much lower elastic modulus of Zircaloy based claddings compared to that of $UO_2$.

With a SiC cladding the elastic modulus is of the same magnitude as $UO_2$ and could therefore result in a resistant force that causes an elastic inward deformation and a reduction of the swelling of the fuel pellet by allowing creep of the fuel into the cracks caused by relocation. The elastic modulus of $UO_2$ was provided by the FEMAXI code and is compared to that of Zirc and SiC in Figure 3.7. The elastic inward fuel deformation ($u_{fe}$) will be caused by the interfacial pressure resulting from the cladding resistance to outward expansion. The stress and strain distribution of the fuel is shown below.

$$\sigma_{f,radial} = -P_{interfacial} \tag{3.6}$$

$$\sigma_{f,axial} = MAX(P_{gas}, P_{spring}) \tag{3.7}$$

$$\varepsilon_{f,radial} = \frac{1}{E_f}(\sigma_{f,radial} - \nu_f \sigma_{f,axial}) \tag{3.8}$$

$$\varepsilon_{f,axial} = \frac{1}{E_f}(\sigma_{f,axial} - \nu_f \sigma_{f,radial}) \tag{3.9}$$

$$u_{fe} = \varepsilon_{f,radial} r_{fo} \tag{3.10}$$

This swelling can only be reduced to the point of the fuel pellet becoming fully dense, after which the fuel will continue to expand onto the cladding in an unrestricted manner. The total fuel surface displacement is shown in Equation 3.11 with the inclusion of fuel creep ($u_{fc}$).

$$u_f = u_{tf} + u_s + u_d + u_r + u_{fe} + u_{fc} \tag{3.11}$$

Metals and ceramics deform differently under mechanical stresses. Metals have the ability to deform plastically, which in the case of cladding materials can relieve some of the applied stress while at the same time increasing the elastic modulus of the material by introducing dislocations. Ceramics are expected to experience a brittle failure once the yield stress is exceeded. For modeling silicon carbide, only an elastic deformation regime will be considered. Due to the magnitude of cladding creep being several orders less than that of Zirconium based claddings, both thermal and irradiation induced creep will be neglected. However, a swelling term will be added to account for the irradiation induced swelling caused by the formation of interstitial clusters, saturating with a linear strain of 0.67% after 1 DPA. The sources of cladding deformation for SiC is shown in Equation 3.12.

$$u_{ci} = u_{tc} + u_e + u_{c,swell} \tag{3.12}$$

For TRACE, the stress distribution on the cladding is based solely on the internal rod pressure and external coolant pressure. In TRACE V5P3, the internal rod pressure is input by the user as the rod pressure at room temperature and changes throughout the transient by the ratio of the plenum temperature to the reference temperature (298K, which is set internally within the code). There is no accounting for the effects of thermal expansion and cladding deformation (i.e. ballooning) that allow for changes of the internal rod pressure. For this reason, the FRAPTRAN code provides the best estimate of internal rod pressure through its thermo-mechanical feedback of temperature and pressure. The TRACE and FRAPTRAN elastic deformation regime of the cladding is based on the hoop and axial stress($\sigma_h, \sigma_z$), poisson ratio($\upsilon$) and elastic modulus($E$), as shown below.

$$u_e = r_{cm} * \left(\frac{\sigma_h - (\upsilon * \sigma_z)}{E}\right) \tag{3.13}$$

$$\sigma_h = \frac{P_g r_{ci} - P_f r_{co}}{r_{co} - r_{ci}} \tag{3.14}$$

$$\sigma_z = \frac{P_g r_{ci}^2 - P_f r_{co}^2}{r_{co}^2 - r_{ci}^2} \tag{3.15}$$

The poisson ratio for Zircaloy is $\upsilon = 0.3$ and will be set for SiC with $\upsilon = 0.21$.[Snead, 2007] The elastic modulus of Zirc (For T < 1090K, in Pa) and SiC (MPa), as well as that for $UO_2$ (MPa), is shown in Equations 3.16-3.18 and in Figure 3.7. Note that the elastic modulus for SiC is greatly influenced by the as-fabricated porosity, with typical as-fabricated densities previously mentioned. The lowest documented achieved porosity is 3%. The equations provided by Snead for monolithic SiC have been modified to account for thermal degradation due to both as-fabricated porosity and burnup. The porosity correction term was further modified to match the data provided by [C.P. Deck, 2013] on the elastic modulus of SiC-SiC composites at various composite densities at room temperature.

$$E_{Zirc}(T, O_2Conc, coldwork) = (1.088e11 - 5.475e7 * T + c1 * O_2Conc + c3 * coldwork)/c2 \tag{3.16(a)}$$

where $c1 = (1.16e11 + T * 1.037e8) * 5.7015$ 3.16(b)

$$c2 = 1.0\ if\ fast\ fluence\ is < 1.0e22\,\frac{neutrons}{m^2}, else: \tag{3.16(c)}$$

$$c2 = 0.88 * \left(1.0 - e^{\left(-\frac{fastflu}{1e25}\right)}\right) + e^{\left(-\frac{fastflu}{1e25}\right)} \tag{3.16(d)}$$

$$c3 = -2.6e10 \tag{3.16(e)}$$

$$E_{SiC,SiC}(T, dpa, \rho) = \left[460 - \left(0.04 * T * e^{-962/T}\right)\right] * [1 - 0.4 * (1 - e^{-0.15*dpa})] * e^{-3.57*(1-\frac{(2.833-\rho)}{2.833})} \tag{3.17}$$

$$E_{UO_2}(T, P) = 229 - 0.0201 * T - 587 * P \tag{3.18}$$

| Symbol | Description |
|---|---|
| $T$ | Temperature (K) |
| $O_2$Conc | Oxygen concentration (kg oxygen / kg Zircaloy) |
| coldwork | Cladding cold work (unitless) |
| fastflu | Fast fluence (neutrons/$m^2$) |
| $dpa$ | Displacements per atom |
| $\rho$ | As-fabricated density (g/$cm^3$) |
| $P$ | Porosity (fraction) |

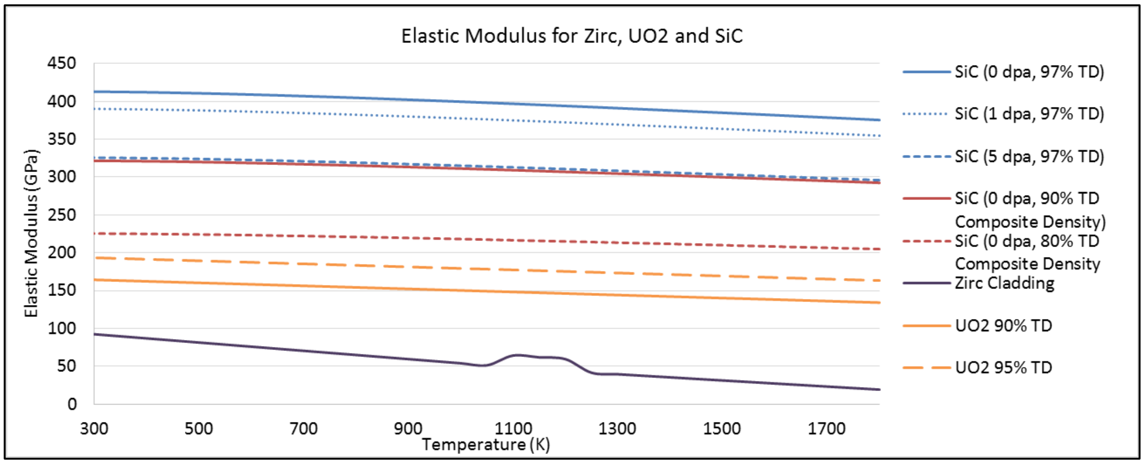

Figure 3.7: Elastic modulus of SiC, Zircaloy and $UO_2$ with varied fabrication and irradiation parameters

For cladding failure, Zircaloy is expected to have two failure modes: low temperature PCMI failure and high temperature cladding ballooning failure. However, with SiC's high elastic modulus and brittle failure mechanisms at normal operation and accident temperatures, the high temperature ballooning model will not be used. Therefore, failure of the SiC cladding will be a result of either fuel expansion onto the cladding or a sufficiently high hoop stress caused by high internal rod pressure and a low coolant pressure during an accident. The cladding will fail once the flexural strength of the material is reached, which is a function of predominately as-fabricated porosity and fluence and greatly varies from one manufacturer to another. The flexural stress for SiC/SiC composites have been reported between 250 and 315 MPa for composite densities between 2.25 and 2.55 g/cm$^3$, respectively.[C.P. Deck, 2012] It has also been shown that under irradiation, the flexural stress of SiC increases with a saturation at ~ 1dpa.[Snead, 2007] The typical ratio of irradiated to unirradiated flexural stress is 1.2-1.3 up until 10 dpa, beyond which the irradiation effects on flexural strength are is not clear. The failure mechanism for SiC will be reached when the flexural stress is exceeded, which will be a function of both the as-fabricated density and dpa, with a conservative increase in the flexural stress saturating at 1.1 times the initial flexural stress after 1 dpa.

It has been shown with SiC that the poor thermal conductivity as a result of burnup degradation can result in extreme thermal stresses in the material in an accident scenario.[Ahn, 2006] For this reason, thermal stress calculations will be built into FRAPTRAN to determine if thermal stress coupled with the primary (external) stress will lead to failure in a scenario where primary stresses alone are not enough to fail the material. The TRESCA theory will be employed using the thermal stresses Equations 3.19-3.21 for the radial, hoop and axial stresses respectively.[Harvey, 1963; Ahn, 2006]

$$\sigma_r^{th} = \frac{\alpha E \Delta T}{2(1-\nu)\ln(\frac{R_{co}}{R_{ci}})}\left[-\ln\left(\frac{R_{co}}{r}\right) - \frac{R_{ci}^2}{R_{co}^2 - R_{ci}^2}\left(1 - \frac{R_{co}^2}{r^2}\right)\ln\left(\frac{R_{co}}{R_{ci}}\right)\right] \quad 3.19$$

$$\sigma_\theta^{th} = \frac{\alpha E \Delta T}{2(1-\nu)\ln(\frac{R_{co}}{R_{ci}})}\left[1 - \ln\left(\frac{R_{co}}{r}\right) - \frac{R_{ci}^2}{R_{co}^2 - R_{ci}^2}\left(1 + \frac{R_{co}^2}{r^2}\right)\ln\left(\frac{R_{co}}{R_{ci}}\right)\right] \quad 3.20$$

$$\sigma_z^{th} = \frac{\alpha E \Delta T}{2(1-\nu)\ln(\frac{R_{co}}{R_{ci}})}\left[1 - 2\ln\left(\frac{R_{co}}{r}\right) - \frac{2R_{ci}^2}{R_{co}^2 - R_{ci}^2}\left(1 - \frac{R_{co}^2}{r^2}\right)\ln\left(\frac{R_{co}}{R_{ci}}\right)\right] \quad 3.21$$

One more significant difference between the failure of SiC and Zircaloy is that when Zircaloy ruptures after plastically deforming it results in a percentage of flow blockage based on the heating rate and rupture temperature at failure. This reduces the coolability of the fuel rod and, without sufficient crossflow, can cause an increase in cladding temperatures at axial nodes above the ruptured node. Due to the brittle nature of SiC, it has been shown that strains as low as 0.2% will cause cladding failure. In TRACE, the smallest burst strain for Zircaloy of 10% results in a flow blockage of 6.5%, regardless of the rupture temperature. With such a small burst strain in SiC, it is expected that the flow blockage will be almost negligible. For conservative analysis, a flow blockage of 1% per % of burst strain will be used if rupture occurs.

### 3.4.4 Oxidation Kinetics

The oxidation reaction of zirconium with high temperature steam is understood to be a major drawback of the cladding in accident scenarios in light water reactors. Zirconium reacts actively with oxygen to produce an oxide layer, $ZrO_2$, as shown in Equation 3.22.

$$Zr + 2H_2O = ZrO_2 + 2H_2 \tag{3.22}$$

Under normal operating conditions the oxide layer is a protective layer, but over time it can start to grow at a linear rate leading to a reduced strength of the cladding resulting in spalling.[Henri Bailly, 1999] For this reason, the NRC has imposed limits of the oxide layer not exceeding 0.17 times the total cladding thickness before oxidation.[U.S. NRC] The oxygen from the water that reacts with the zirconium also releases hydrogen, of which 10-20% diffuses into the cladding.[Henri Bailly, 1999] The hydrogen can form hydrides, which can significantly embrittle the cladding thus enhancing crack propagation. At temperatures above 1000°C, the rate of oxidation is proportional to the square root of time.[Division of Safety Analysis, 2012].

The hydrogen uptake into the cladding is a summation of the as-fabricated hydrogen concentration in the clad, the released hydrogen from as-fabricated water in the fuel, and the hydrogen uptake from the coolant. The hydrogen uptake into the cladding is not considered to affect the strength coefficient of Zircaloy in steady-state scenarios.[K.J. Geelhood, 2011]. The amount of hydrogen in the cladding is only used as an input into FRAPTRAN, which takes the ppm of hydrogen into account when determining plastic elongation of the cladding at low temperature PCMI failure.

The goal of the oxidation calculation in TRACE is much different than that of FRAPCON. The three parameters calculated by the oxidation calculation include the ECR, the amount of hydrogen released into the coolant and the energy source term that is associated with the oxidation reaction. Whereas FRAPCON starts with an initial oxide thickness of 0, the TRACE code requires the user to define the initial oxidation state (as calculated by a FRAPCON-like code) at the onset of the transient. TRACE has two choices for oxidation, the Cathcart-Pawel and Baker-Just models, which are turned on only when the cladding temperature exceeds 1000 or 1073K, respectively. A volumetric heat generation ($q'''_{mw}$) term is calculated based on the amount of zirconium oxidized, shown in Equation 3.23.

$$q'''_{mw} = \frac{m'_{Zr} * H_{reaction}}{A * \Delta t} \tag{3.23}$$

Assuming a cylindrical geometry, Equation 3.23 can be re-written as:

$$q'''_{mw} = \frac{\rho_{Zr} * \left[ \left( r_{co} - d^{n}_{Zr} \right)^2 - \left( r_{co} - d^{n+1}_{Zr} \right)^2 \right] * H_{reaction}}{\Delta t * \left( r^2_{co} - r^2_{ci} \right)} \tag{3.24}$$

This source term is added to each radial node that correlates to the cladding. This is due to the high thermal diffusivity of zirconium and the fact that cladding transient results are not greatly influenced by the source term being in one radial or all radial cladding nodes.[Division of Safety Analysis, 2012]

With modeling SiC, both steady-state and transient oxidation kinetics will need to be known and implemented into both TRACE and FRAPTRAN. Previous steady-state modeling of SiC cladding has set the oxidation reaction equal to 0.0, meaning no oxide layer will build up no matter time spent in the reactor.[D. Carpenter, 2012] However, studies described in Chapter 2.3 have shown that it is vital to have a small oxide layer on SiC to reduce the ability of the oxygen to reach the carbon and cause carbon burnout. For steady-state corrosion of SiC, passive oxidation will be considered as the driving force, producing a silica ($SiO_2(s)$) scale and carbon monoxide and hydrogen gases. Although most models with silicon carbide consider it not to oxidize under steady-state conditions, the oxide layer formation will be modeled using a parabolic rate constant, as shown below.

$$\frac{dx}{dt} = \frac{k_p}{2x} \qquad 3.25$$

$$where\ k_p = k^0_{p,O_2} e^{-E_a/RT}\left(p_{O_2}/p^m_{O_2}\right)^n \qquad 3.26$$

| |
|---|
| R, universal gas constant, 8.314 J/mol*K |
| $E_a$, activation energy, 190 kJ/mol |
| $p_{O_2}$, oxygen gas pressure |
| $p^m_{O_2}$is the pressure at which $k^0$ was derived |
| n = 1/2 |
| $k^0_{p,O_2}$, pre-expoential constant, 6.48E-5 |

For the transient analysis, the volatilization of $SiO_2$ will be modeled using a linear volatilization rate ($k_l$) that is dependent on both the coolant temperature and the mass flow rate of the steam. TRACE has the ability to calculate both coolant temperature and mass flow rate of steam for each azimuthal sector and radial ring within an axial segment when modeling the core with a vessel component. The transient oxidation equations will be based off of work by Opila and compared to that of Lee and Fox.[Opila, 2003]

$$\frac{dx}{dt} = \frac{k_p}{2x} - k_l \qquad 3.27$$

$$where\ k_l = 0.664Re^{1/2}Sc^{1/3}\frac{D\rho_v}{L} = 0.664\left(\frac{L\upsilon\rho}{\eta}\right)^{1/2}\left(\frac{\eta\rho}{D}\right)^{1/2}\left(\frac{D\rho_v}{L}\right) \qquad 3.28$$

| | |
|---|---|
| $Re$ | Reynolds Number |
| $Sc$ | Schmidt number |
| $D$ | Interdiffusion coefficient of $Si(OH)_4$ in the boundary layer gas |
| $\rho_v$ | Equilibrium concentration of volatile $Si(OH)_4$ |
| $L$ | Characteristic length |
| $\upsilon$ | Gas velocity |
| $\eta$ | Gas viscosity |
| $\rho$ | Concentration of the boundary layer gas |

This work will assume that a protective silica layer has been formed at the onset of the transient around the fibers to minimize the effect of carbon burnout.

There is the possibility of three different gases being produced from SiC oxidation. For producing hydrogen, the passive oxidation process will produce three moles of $H_2$ per mole of oxidized SiC. Passive oxidation will also produce 1 mole of CO for every mole of oxidized SiC. There are several proposed volatilization reactions, all of which produce a gas consisting of various ratios of Si/O/H. The process modeled will produce one mole of $Si(OH)_4$ per mole of volatilized $SiO_2$, as shown below.

$$SiO_2 + 2H_2O(g) = Si(OH)_4(g) \qquad 3.29$$

To calculate the energy source term ($q'''_{mw}$) shown in equation 3.24, the mass per unit length of the cladding material that is consumed by oxidation ($m'_{Zr}$) and the energy released ($H_{reaction}$) need to be known. The mass of the material consumed will be calculated based on the penetration depth of the oxide layer plus any oxide material that has volatilized. The energy released per kg of oxidized cladding material will be updated as shown in Table 3.4.

Table 3.4: Energy released per kg of oxidized cladding material

| **$H_{reaction}$** | **J/kg** |
|---|---|
| Zirc | $6.45x10^6$ |
| SiC | $6.582x10^6$ |

### 3.4.5 Thermal Properties

The thermal properties of thermal conductivity, density, specific heat and thermal expansion to be used in this analysis have been outlined in Chapter 2.4. These properties will be implemented in FRAPCON, FRAPTRAN and TRACE. There are two significant differences between using SiC and Zirc in terms of thermal conductivity and density. SiC experiences significant thermal conductivity degradation with burnup whereas Zirconium claddings are assumed to be dependent on temperature only. The density of SiC has been reported to vary between 80-97% TD whereas Zirconium claddings are assumed to be at 100% TD. This is important in transient thermal analysis as well as in cladding mechanical strength. The codes will be modified to allow the user to input the as-fabricated density of the cladding. They will also be modified to model the burnup degradation by correlating a fluence of $10^{25}$ neutrons/$m^2$ to 1dpa.

## 3.5 FUEL DISPERSAL CRITERIA

The NRC has defined a set of parameters used to determine the amount of fuel dispersed in an accident scenario, outlined below.[P. Raynaud, 2013]

- Fuel rod ballooning must occur leading to cladding failure
- Cladding strain requirement
- Fuel burnup requirement
- Fine enough to disperse requirement (particle size requirement)

In order to assess these parameters, a coupled methodology utilizing FRAPCON/TRACE/FRAPTRAN will be employed due to the inability of TRACE to model ballooning and burnup. FRAPCON will be used to model the fuel condition for an average assembly burnup and determine the condition at each axial node, developed from core reload reports. TRACE and FRAPTRAN will be used together to determine the coolant conditions and cladding balloon strain, respectively. At the end of the FRAPTRAN run, the output file will be read to extract the ballooning strain at each axial node as well as the time at which the cladding failed. A VBA-Based program will be developed in Microsoft Excel that extracts these two parameters for each fuel rod.

Cladding ballooning is calculated by the FRAPTRAN code when the cladding effective plastic strain is exceeded by the cladding instability strain, derived from MATPRO. At this point, no further strain is calculated for any nodes. The cladding strain for the node that surpassed the instability strain is calculated using the BALON2 model [Hagrman, 1981] to calculate the extent of the deformation and coolability of the rod due to flow blockage. The cladding is considered to have failed in the ballooning node when the cladding true hoop stress exceeds the stress limit of BALON2 or when the cladding permanent strain exceeds FRAPTRAN's empirically derived strain limits that are constant for all Zircaloy-based claddings. Although the BALON2 model uses temperature, cold work and fluence for determining the stress limit, it was determined that for ballooning occurring over 10 seconds or less, the failure strain limit is dominated by temperature; similarly, the FRAPTRAN strain limit is also a function of temperature only. The predicted stress at burst calculated by BALON2 is shown in Figure 3.8.

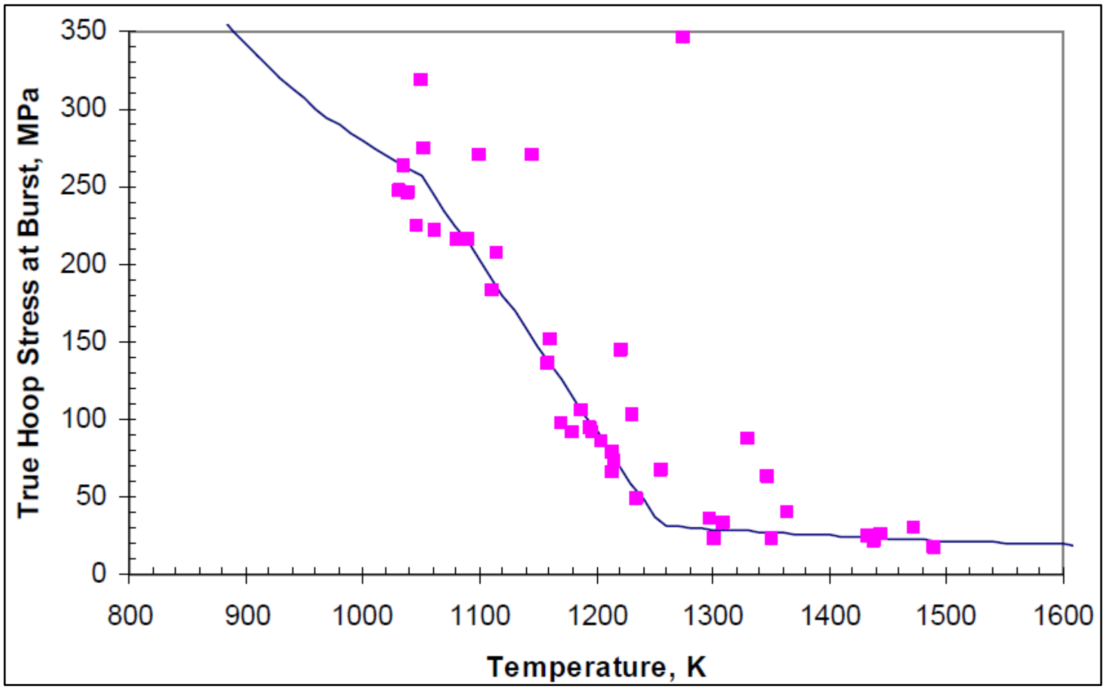

Figure 3.8: True hoop stress at burst from 940-1600K for the BALON2 model.[K.J. Geelhood, 2011]

In order to properly model ballooning strain, small timesteps will be used (<0.01s) with an accuracy of 10-25%, with smaller timesteps resulting in improved accuracy of strain predictions.[K.J. Geelhood, 2009] The issue that has not been addressed in any FRAPTRAN documentation is on the size of the node to use for modeling the fuel rod for ballooning. This can have a significant impact on the amount of dispersed fuel depending on whether a large or small node balloons and the number of axial nodes above and below the balloon that meet/exceed the cladding strain requirement. Test results from Studsvik showed that the rupture opening axial length of a ballooned rod varied beteen 1.5mm-23.9mm.[M. Flanagan, 2012] If the node size is set at 25mm, this would require ~150 axial nodes for a 3.8m tall fuel rod, which will greatly increase the computational requirements. The integral assessment cases used to validate FRAPTRAN against experimental data for LOCA scenarios used node lengths of 30.48cm (3.66m rod with 12 nodes). However, the comparisons were based on failure time and residual hoop strain, not the axial length of the ballooned region. Variations in the number of axial nodes will be performed and results compared to the Studsvik and Halden data to assess an optimal node length for the full core studies.

The cladding strain requirement is used to determine the regions around the rupture opening that are capable of producing dispersible fuel fragments. As previously mentioned, the "empty length" of the fuel rods tested at Studsvik indicated that a certain strain value must be met in the rod for the fuel to be mobile. Although not all of the fuel measured by the "empty length" was released during the LOCA (nearly all was released in the high burnup cases while almost none was released in the low burnup cases) the fuel was still found to be mobile. For a conservative estimate, it will be concluded that all fuel that is in the axial node that meets the strain requirement will be capable of being dispersed. The current estimated cladding strain value required for mobile fuel is 5% strain, noting that there are LOCA tests reporting that strains as low as 1% and as high as 13% are required.[P. Raynaud, 2012] Variations of the strain value and its effect on fuel dispersal calculations will be conducted. The nodalization within the codes used in this analysis provides an average value over each node (axial length segment). Linear interpolation will be used between nodes to determine if any fuel in an adjacent node that doesn't meet the strain value for the entire node will meet the cladding strain requirement for a fraction of the node.

The fuel burnup requirement dictates which particle size distribution will be used in the analysis, as outlined in Chapter 2.5 - Fuel Dispersal. A coarse particle size distribution is expected for fuel below a certain burnup threshold and a fine particle size distribution is expected for fuel above a certain threshold. The particle size distributions found at Studsvik for tests 196 & 198 with a burnup of ~55 GWd/MTU were found to be of a "coarse" particle size distribution with an average size >4mm. Studsvik tests 191-193 and Halden IFA-650 showed that fuel above 72 and 90 Gwd/MTU, respectively, have a much finer particle size distribution with average particle sizes < 2mm. The transition between the coarse and fine particle distributions is between 50 and 70 GWd/MTU, with an average expected transition value of ~60 GWd/MTU. Fuel with a burnup lower than the burnup required threshold for coarse to fine transition will follow a coarse particle size distribution typical of Studsvik tests 196 & 198 while fuel with a burnup above the burnup threshold will follow a fine particle size distribution typical of Studsvik tests 191-193. It is not currently clear whether there is a sharp change in particle size distribution (i.e. a true threshold for fine particle distribution) or if it is a more smooth transition between the particle sizes found at 50 GWd/MTU and those at 70 GWd/MTU. This will be explored more closely in the continued research. By extracting the axial node burnup values provided by FRAPCON and setting the burnup threshold for fine particle size fragmentation, the particle size distribution for the node can be determined. Multiplying this value by the fuel in an axial node length will determine the mass of fuel for each particle size in the node.

The strain and burnup of each axial node is all that can be currently modeled. The criteria for the fine enough to disperse threshold is a chosen value; currently the rupture opening size cannot be determined. Based on Studsvik tests 189-198, the minimum value of the rupture opening width and axial length was ~9mm for tests with rods > 71 GWd/MTU and .2mm for rods < 55 GWd/MTU.[M. Flanagan, 2012] However, it has also been noted that fuel mobility may be influenced by the wetness of the fuel, thus preventing some of the larger particles from moving out of the rod once they are wet. Current assumptions on the fine enough to disperse threshold are that fuel particles greater than 1mm are considered coarse particles and will stay in the rod while particles <1mm are considered fine enough to disperse and are expected to be released from the rod.[P. Raynaud, 2013]

Following the outlined criteria above, the amount of dispersed fuel during different hypothetical LOCA scenarios will be calculated. First, the determination of ballooning will be made and, if ruptured, the cladding strains will be extracted from FRAPTRAN. If no rupture occurs, the fuel dispersal will be set to 0. By setting a burnup threshold to determine the particle size distribution for the axial node, the mass of each particle size can be determined for the node. Setting a strain threshold will determine whether or not the axial node has mobile fuel, and if so, it will be assumed that the fuel is capable of being dispersed. Lastly, by setting a particle size requirement to disperse from the rod, the mass of fuel released from the rod will be calculated. This process will be repeated for each fuel rod modeled in the transient and the amount of fuel dispersed from each modeled rod will be multiplied by the number of rods that the modeled rod represents (whether it be a single rod, entire assembly or multiple assemblies). Summing all rods together will result in the amount of fuel dispersed in the accident.

### 3.6 Full Core Plant Models and Fuel Rod Design

In order to assess both fuel dispersal and the potential improvements of advanced cladding materials, the most numerous PWR and BWR plants will be modeled, as shown in Table 3.5. Different plant conditions (i.e. coolant pressure, safety system response) will impact the cooling of the fuel. Multiple fuel rod designs will also be analyzed to determine the impacts that fabrication and in-reactor performance can have on the fuel response. Due to the proprietary nature of the both the reactor and fuel rod designs, limited specific data can be shared in this section. The reactors modeled will be denoted as a “typical BWR/4”, “4-loop Westinghouse PWR” and “typical CE-PWR”. These models are current U.S. NRC models used for validating plant safety. Modifications to these input files have been made solely to the fuel rod components (HTSTRs and CHANs) and corresponding power (POWER) components to eliminate the coarse assembly averaging.

Table 3.5: Active US commercial nuclear fleet breakdown as of September, 2014

| Plant Type | PWR | | | | | | |
|---|---|---|---|---|---|---|---|
| | W2LP | W3LP | W4LP | CE | B&W-LLP | B&W-RLP | SYS80 |
| Number of Plants | 5 | 13 | 29 | 9 | 5 | 1 | 3 |

| Plant Type | BWR | | | | |
|---|---|---|---|---|---|
| | BWR/2 | BWR/3 | BWR/4 | BWR/5 | BWR/6 |
| Number of Plants | 2 | 6 | 19 | 4 | 4 |

### 3.6.1 BWR Model

The BWR model is a BWR-4 with a Mark-1 containment. It has a thermal rating of 3,293 $MW_{th}$. The model has a mixed core of 764 assemblies, 432 of which are fuel type 1 and are in their second and third cycles and the remaining 332 being fuel type 2 and are fresh fuel. Fuel types 1 and 2 are typical 10x10 BWR fuel channels, with fuel type 2 having a lower fill gas pressure and smaller outer clad diameter. The original TRACE input deck consisted of 24 different CHAN components representing all 764 assemblies. To properly model the burnup of each assembly for the fuel dispersal studies and for “best-estimate” fuel failure, no assembly averaging was performed and the TRACE input deck was re-written with 764 CHAN components. The assembly core map is shown in Figure 3.9.

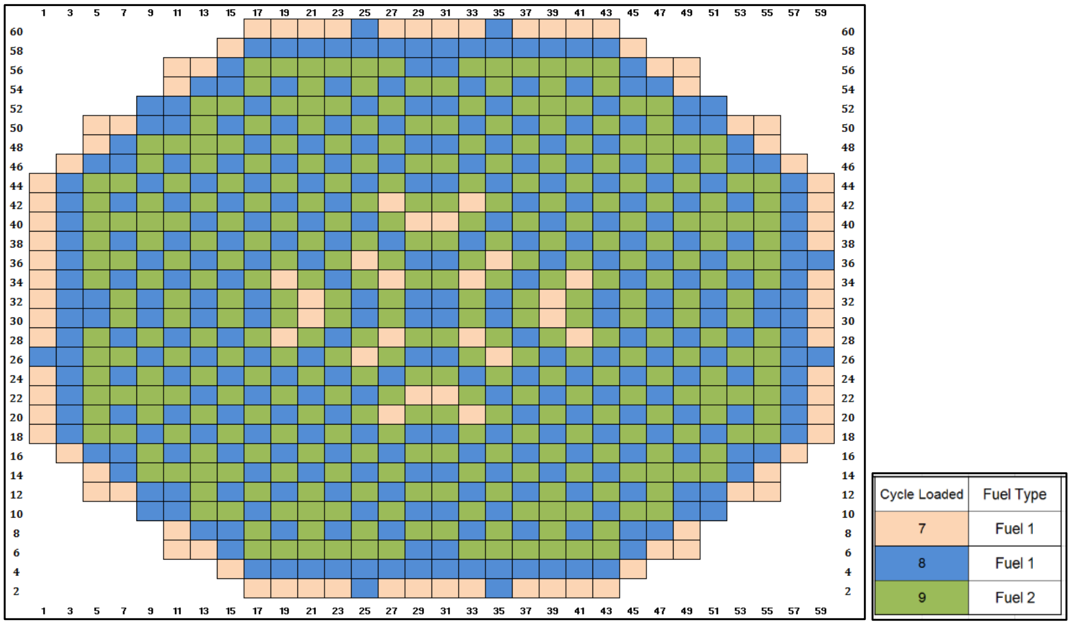

| Cycle Loaded | Fuel Type |
|---|---|
| 7 | Fuel 1 |
| 8 | Fuel 1 |
| 9 | Fuel 2 |

Figure 3.9: Core assembly map with 764 10x10 fuel assemblies

The core was modeled using a BWR-VESSEL component. The vessel is divided into 5 radial rings and 15 axial regions. The channel components' inlets are connected to the vessel at axial cell 3 and their outlets to axial cell 7. Above the channels sit four steam separator/dryers, one for each radial ring of the core that contains channels. The inner four rings containing fuel of the BWR-vessel component are shown in Figure 3.10, with ring 5 designated as the downcomer.

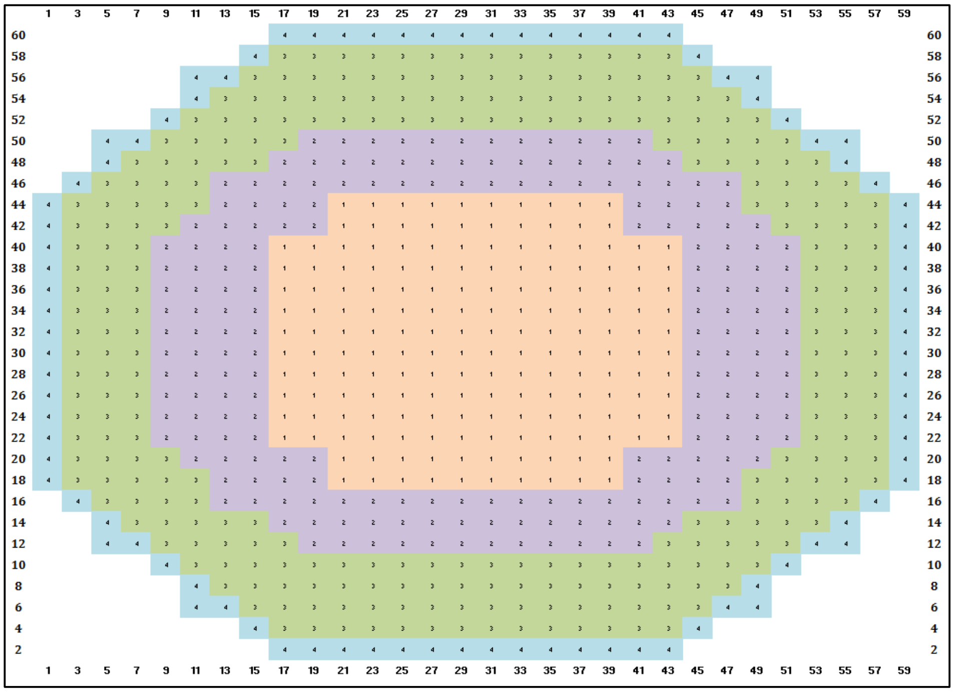

Figure 3.10: BWR-vessel rings used in TRACE model.

There are two modeled recirculation pumps for the core, along with associated piping and jetpumps. For heat removal, there is a fill that acts as the feedwater line and there are breaks that act as the turbine inlet and condenser for turbine bypass. The containment has a drywell, wetwell and containment spray system. Safety systems are triggered on and off by pressure and temperature setpoints. These systems include 2 high pressure and 2 low pressure coolant injection systems and a core spray system. The SNAP rendering of the original TRACE input deck is shown in Figure 3.11.

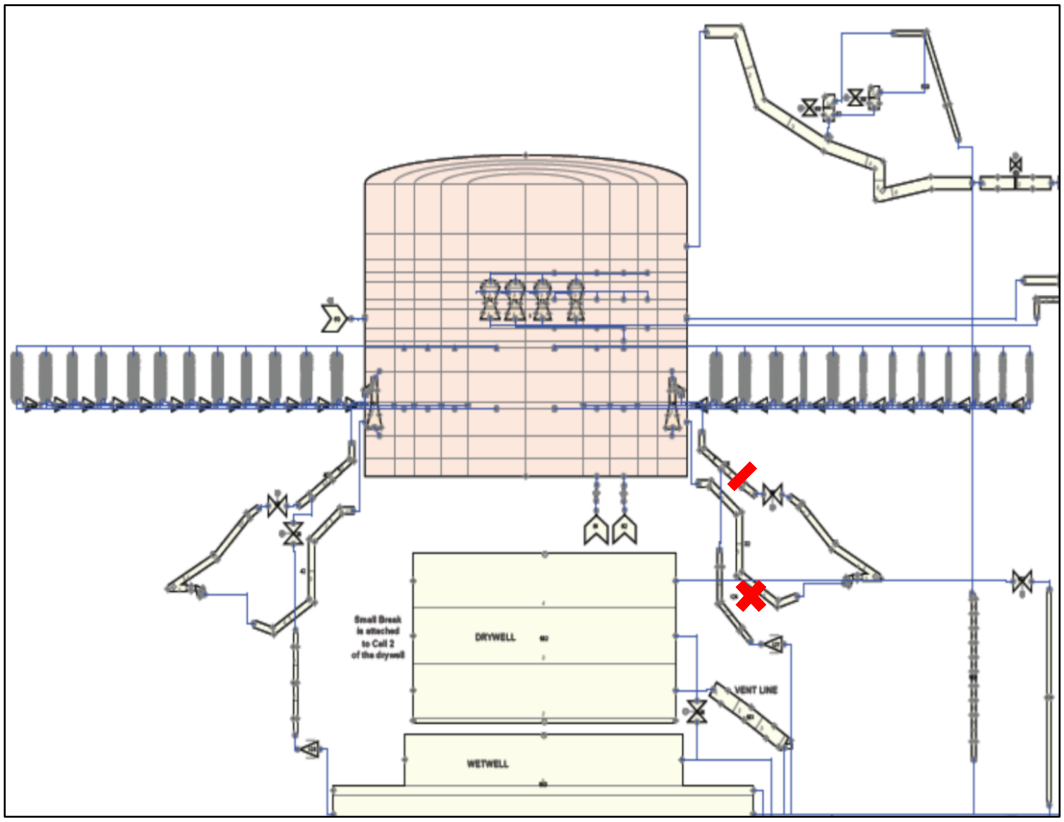

Figure 3.11: Original TRACE schematic of BWR-4. The / denotes the location of the SBLOCA and the X denotes the ruptured region for the LBLOCA.

The transients modeled are a small break LOCA (SBLOCA) and a large break LOCA (LBLOCA). The SBLOCA occurs via a 6.5x10$^{-3}$ m$^2$ break in the recirculation line modeled by PIPE 36 and is shown Figure 3.11 with the **/** symbol. The LBLOCA is a double ended guillotine break of the recirculation line (PIPE 32) with a rupture opening of 0.363 m$^2$ and is shown above with an **X**.

### 3.6.2 PWR Models

The main PWR model (due to its largest number in the US commercial fleet) is a 4-loop Westinghouse design with a thermal rating of 3,626 MW$_{th}$. The core consists of 193 assemblies with typical 17x17 PWR fuel with ZIRLO cladding. The input deck originally consisted of 11 different heat structures per azimuthal section, resulting in a total of 88 heat structures. However, one-eighth symmetry was assumed and each heat structure was identical from one azimuthal section to the other. This was modified to allow the full core to be represented on a 1:1 assembly basis by a total of 248 HTSTRs, higher than the 193 assemblies only due to the azimuthal sectors dividing some assemblies in half and the central assembly into eight sections. The core map is shown in Figure 3.12.

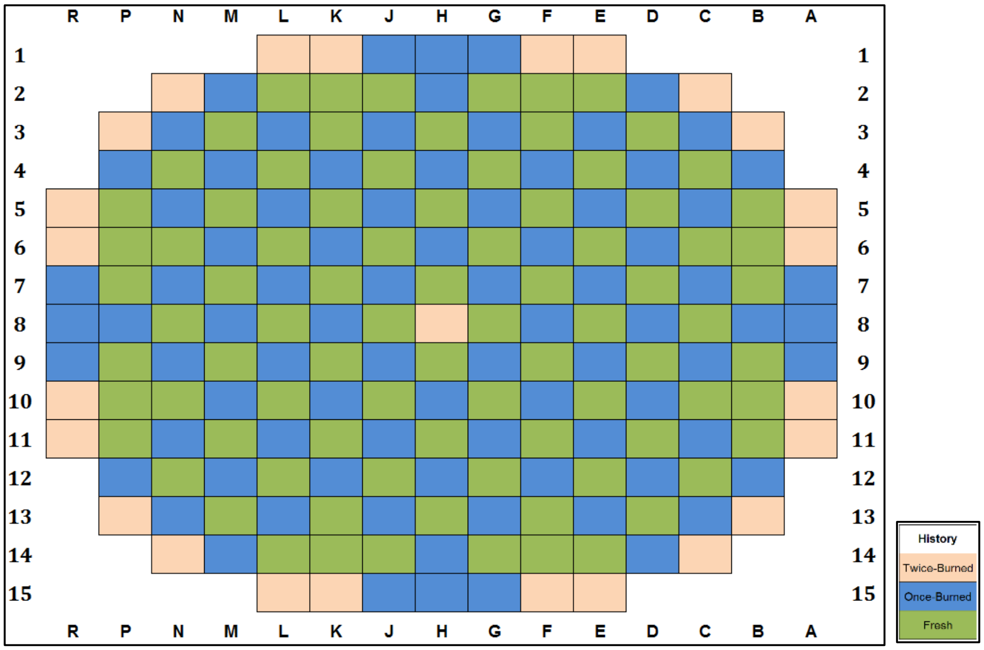

Figure 3.12: Core map of 4-loop PWR with 193 17x17 fuel assemblies

The core is modeled by a VESSEL component, which is divided into 4 rings, 8 azimuthal sections and 14 axial nodes. The assemblies are modeled by HTSTR components and are connected to the VESSEL from axial nodes 7-20. Rings 1 and 2 contain heat structures and ring 4 is for the downcomer. The vessel nodalization is shown in Figure 3.13.

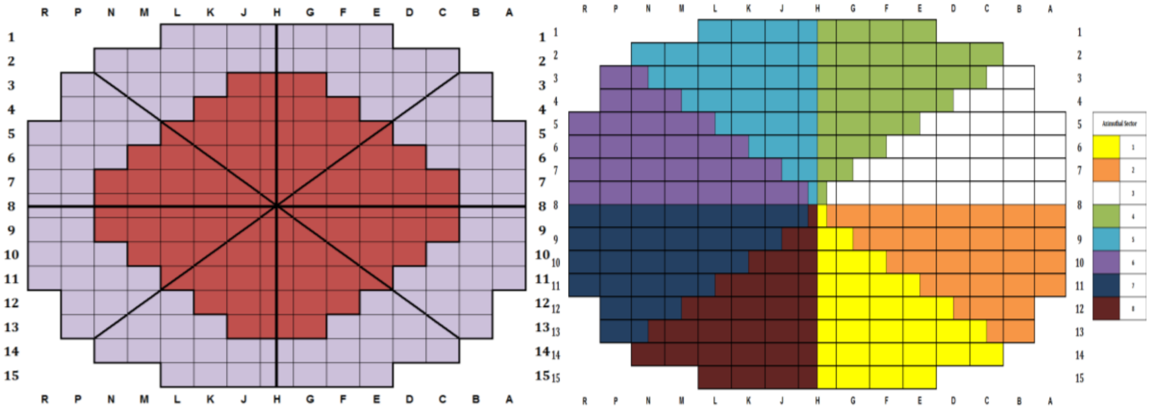

Figure 3.13: VESSEL nodalization for rings 1 and 2. The top picture illustrates the radial rings (1 and 2 from center outwards); the bottom picture illustrates the azimuthal sectors.

The secondary side of the four steam generators are supplied by FILLs and the water is taken away through BREAKs. The primary side of the steam generators are supplied through coolant loops connected to the VESSEL with recirculation PUMPs on the cold leg side of the SG. The cold leg side of each loop also contains a safety injection system and accumulator connected between the PUMP and VESSEL. A pressurizer (PRIZER) is connected to the hot leg of one of the four loops. The plant schematic is shown in Figure 3.14.

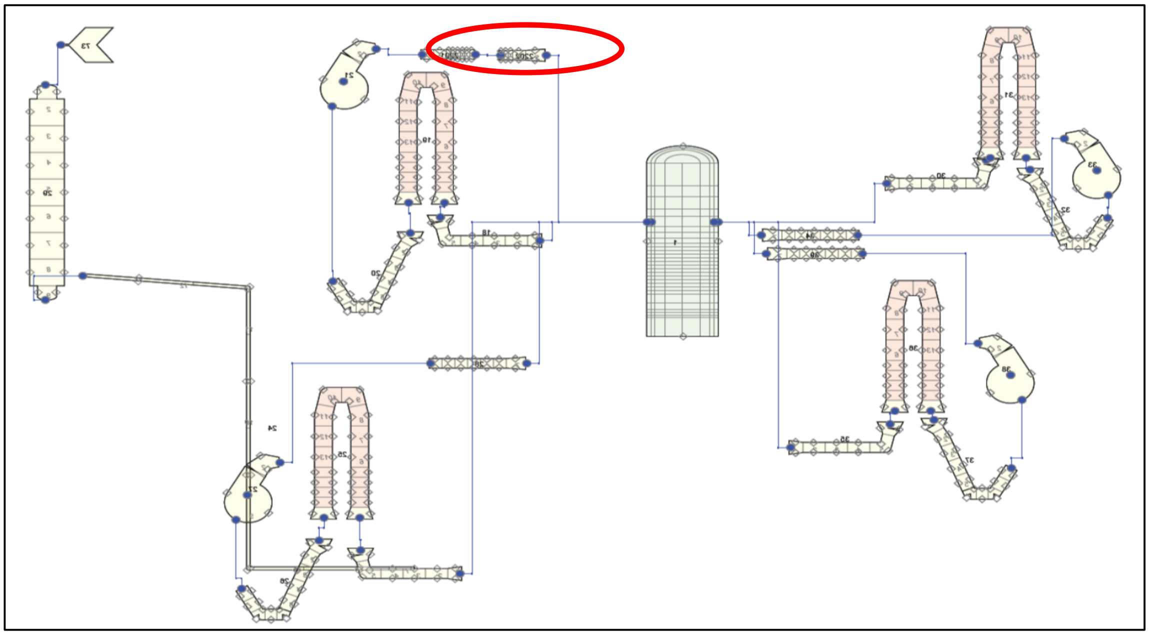

Figure 3.14: Westinghouse 4-Loop PWR schematic. The broken cold leg is shown in the red circle.

The transient that will be modeled with this PWR is a LBLOCA. The above figure shows PIPE 2201 and PIPE 2202 that break with a cross sectional area of 0.383 $m^2$. The emergency core cooling system (ECCS) responds as designed. Other analyses were performed using alternative ECCS responses (a delayed ECCS actuation representative of a loss of on-site power and a case where 1 of the 2 trains of ECCS fails) but is not presented in this work. This work was discussed during a NRC Public Meeting on fuel fragmentation, relocation and dispersal held March 13-14, 2014 at NRC headquarters. [Ian Porter, 2014] Input from industry regarding the LOCA calculations concluded in a consensus that the "realistic, best-estimate" calculations should also include the operating as designed ECCS plant response. A summary of this work can be found in Reference *Methodology for Core-Wide Estimates of Fuel Dispersal During a LOCA* (US NRC, 2014).

The second PWR model that will be analyzed is a Combustion Engineering (CE-PWR) PWR. As seen in Table 3.5, it is the most popular non-Westinghouse PWR. The

CE-PWR is a 2-loop plant with a thermal rating of 3,056 $MW_{th}$. The core consists of 217 assemblies of a 16x16 Westinghouse fuel design with Zircaloy-4 cladding. Similar to the W4LP, the CE-PWR vessel was modeled using 2 radial rings representing the fueled region but with 6 azimuthal sectors. The core assembly layout and nodalization are shown in Figure 3.15.

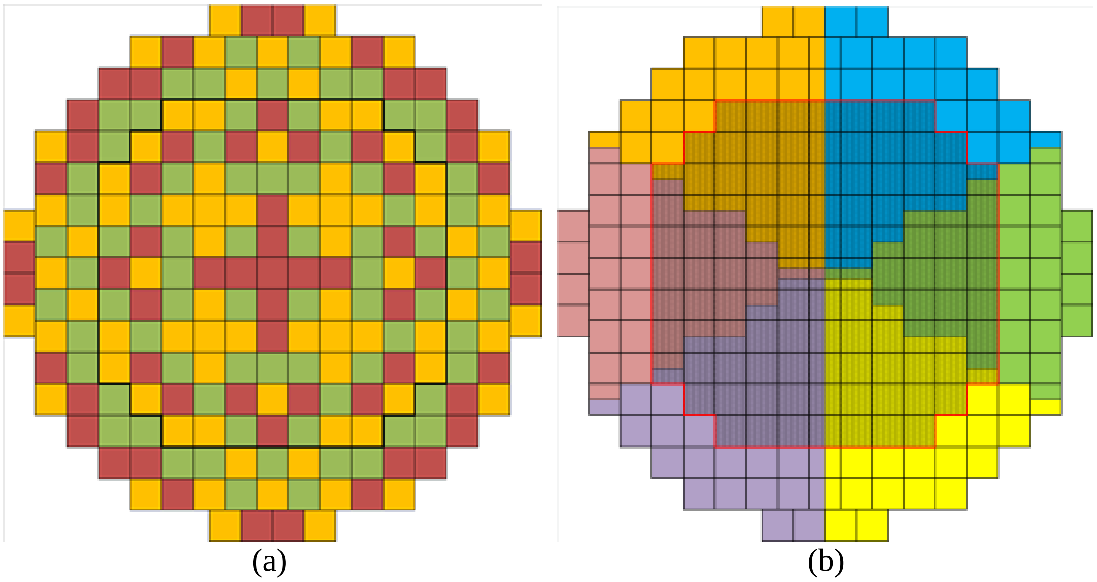

Figure 3.15: CE-PWR: (a) Assemly layout for 1st (green), 2nd (yellow) and 3rd (red) cycle assemblies; (b) TRACE nodalization with 2 radial rings and 8 azimuthal sectors.

The transients analyzed with the CE-PWR are both a SBLOCA and LBLOCA. The SBLOCA occurred at a cold leg nozzle with a limiting break size of 41.8$cm^2$. The LBLOCA was again a double-ended guillotine cold-leg break at the vessel with a break size of 0.456$m^2$. The ECCS system is modeled to operate as designed.

# CHAPTER 4

## CODE MODIFICATIONS AND IMPROVEMENTS

After analyzing the capabilities and drawbacks of the FRAPCON, FRAPTRAN and TRACE codes, it was determined that several code modifications were needed in order to perform a “best-estimate” calculation. The single-rod design of the FRAPCON and FRAPTRAN codes can’t capture the thermal hydraulic conditions existing when modeling a reactor core and lacks the ability to analyze the interplay of surrounding rods on the coolant conditions of the rod being modeled. With the TRACE code being geared towards thermal hydraulics and full core modeling rather than fuel performance, it lacks the detailed burnup-dependent phenomena that impacts fuel temperatures, stored energy and licensing limits during a LOCA. The modifications made to allow these codes to predict comparable results under the same conditions are described below and were published in the following references: *Potential Impacts of Modeling Full Reactor Cores Using Combined Fuel Performance and Thermal Hydraulics Codes* (Nuclear Technology) and *Fuel Performance Assessment when Modeling Gamma Heating Under Steady-state and Transient Scenarios* (Proceedings of ICAPP 2014). [Ian E. Porter, 2014; Ian E. Porter, 2014]

## 4.1 FRAPCON

### 4.1.1 Gamma-ray Heating

Under typical LWR conditions, direct moderator heating accounts for ~2.5 – 3.5% of the total energy generated, which is a result of both gamma-rays and neutrons. In the thermal hydraulics code TRACE, this is accounted for by reducing the energy generated in the fuel and allowing the energy to instead be directly deposited into the coolant. However, FRAPCON does not have the ability to model gamma-ray heating and therefore overestimates the energy produced in the fuel compared to TRACE. An overestimation of energy deposited in the fuel can result in higher centerline temperatures and increased FGR at EOL due to the strong dependence on fuel temperature at high burnup. From a LOCA analysis perspective, there is a potential to overestimate the amount of stored energy in the fuel, which is the driving force for PCT and fuel rod failure.

To account for gamma-ray heating, FRAPCON was modified to allow the user to supply a moderator heating fraction (*modheat*) which adjusts the user supplied LHGR, thus reducing the energy deposited directly in the fuel. This also reduces the surface heat flux, which is used to calculate the temperature drop in the cladding, oxide layer and film boundary layer. To conserve energy from a balance of plant (BOP) standpoint, the energy that was removed from the fuel is added back to the coolant through the code's single channel coolant enthalpy rise model, shown in Equation 4.1.

$$T_b(z) = T_{in} + \int_0^z \left[\frac{(\pi D_o)q''(z)}{(1-modheat)C_pGA_f}\right]dz \qquad 4.1$$

The code requirements for using the variable *modheat* are shown in Table 4.1. Default values based on plant type are 0.026, 0.035 and 0.084 for a PWR, BWR and CANDU, respectively.[Nuclear Systems 1, Edition 1, Todreas]

Table 4.1: Input requirements for using *modheat* in FRAPCON

| Variable Name | Description | Units | Limitations / Default Value |
|---|---|---|---|
| modheat (Real) | Moderator heating fraction. Specifies the fraction of total energy to be deposited directly into the coolant. To use default values based on plant type, set modheat = -1. To be used in namelist $frpcon. | Dimensionless | Default value = 0.0. |

To verify the modification was calculating the correct results, a code to code comparison was made between FRAPCON and TRACE for identical cases. The TRACE model (Figure 4.1) consisted of a pipe, fill, break and heat structure component that was representative of the fuel rod modeled by FRAPCON. The pipe is representative of the coolant channel, while the fill and break set the inlet and outlet coolant conditions, respectively. The heat structure is representative of the fuel rod and consists of the same number of axial and radial nodes to model the fuel. A schematic of the model is shown in Figure 4.1.

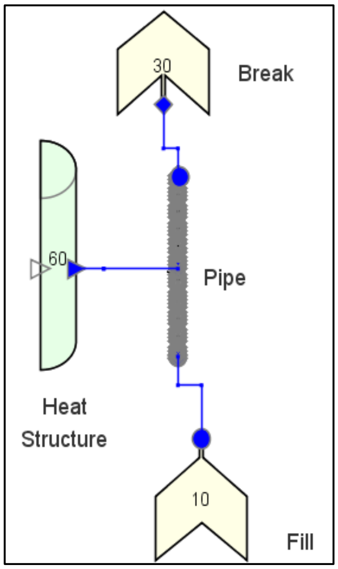

Figure 4.1: TRACE schematic of a single fuel rod

The geometry and coolant conditions used in the analysis are shown in Table 4.2. The fuel was a typical 17x17 Westinghouse assembly consisting of 95% TD $UO_2$ with Zirc-4 cladding.

Table 4.2: Coolant conditions and fuel rod power

| Condition | Value |
|---|---|
| Inlet Pressure | 15.5 MPa |
| Coolant Mass Flow | 0.299 kg/s |
| Inlet Temperature | 564.43 Kelvin |
| Linear Heat Generation Rate | 7.5 kW/ft |
| Moderator Heating Fraction | 0.0277 |

The parameter analyzed between both cases was the fuel centerline temperature. Due to differences in burnup dependent parameters that the codes use to thermally model the fuel having an impact on fuel centerline temperatures, both cases assumed fresh fuel (modeled in FRAPCON after 1 day) with the same axial and radial power profiles. The results were nearly identical, within 1 degree Kelvin difference (absolute maximum) between the codes both with and without gamma-ray heating. Both codes predicted a maximum centerline temperature decrease of 36 Kelvin when modeling the rod with 2.77% gamma-ray heating versus no gamma-ray heating, as seen in Figure 4.2.

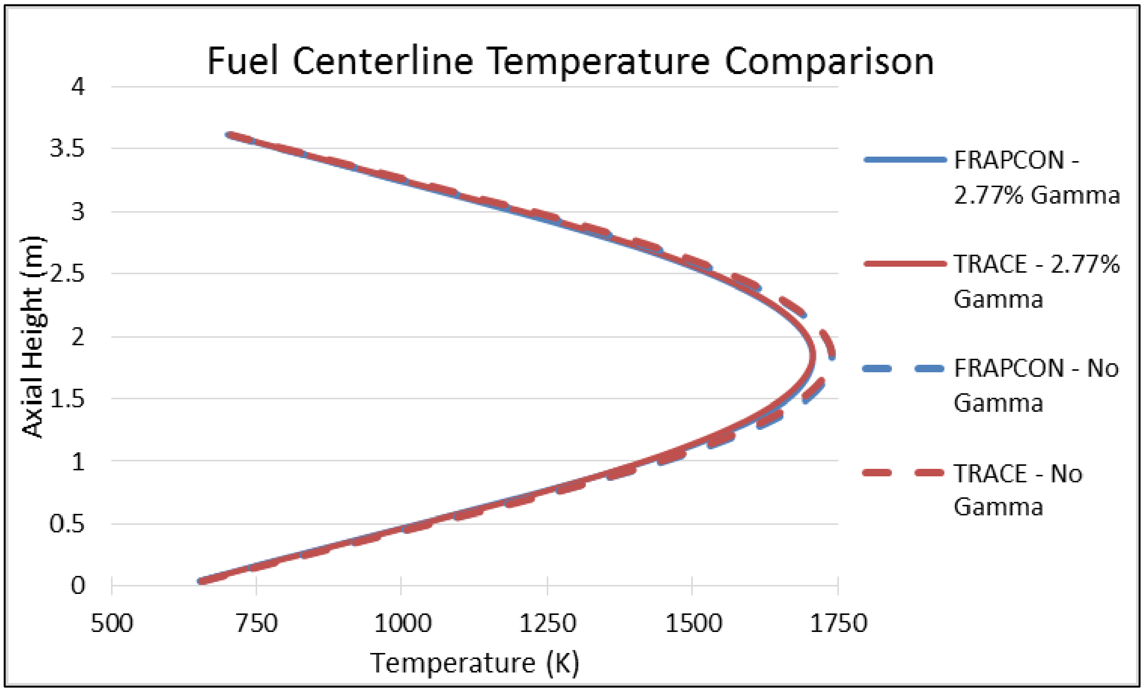

Figure 4.2: Fuel centerline temperature comparison between FRAPCON and TRACE for fresh fuel

The potential steady-state impacts on modeling gamma-ray heating are described below. Due to the slightly lower fuel temperature, all temperature dependent phenomena are expected to be lower (albeit some may be negligible). The largest impact seen at EOL by reducing the energy deposited in the fuel pellet was a lower internal rod pressure due to a decrease in FGR. At sufficiently high burnup (> ~ 45 GWd/MTU), the fission gas release becomes heavily dependent on fuel temperatures, with higher fuel temperatures resulting in an increase in fission gas release.[K.J. Geelhood, 2011] Figure 4.3 shows the effects of 2.77% gamma-ray heating for a typical 17x17 Westinghouse fuel rod that is discharged after two cycles with a final burnup of 60.9 GWd/MTU. The EOL maximum fuel temperature was decreased by 68 Kelvin. This resulted in a 3% absolute FGR decrease (9.23% compared to 12.42%, ~25% relative reduction) and a reduction in internal rod pressure of 2.34 MPa. Although these rod pressures are higher than most typical fuel rods, it is within allowable operating conditions. The inclusion of modeling gamma-ray heating can be the difference between the cladding being in compression or tension by EOL.

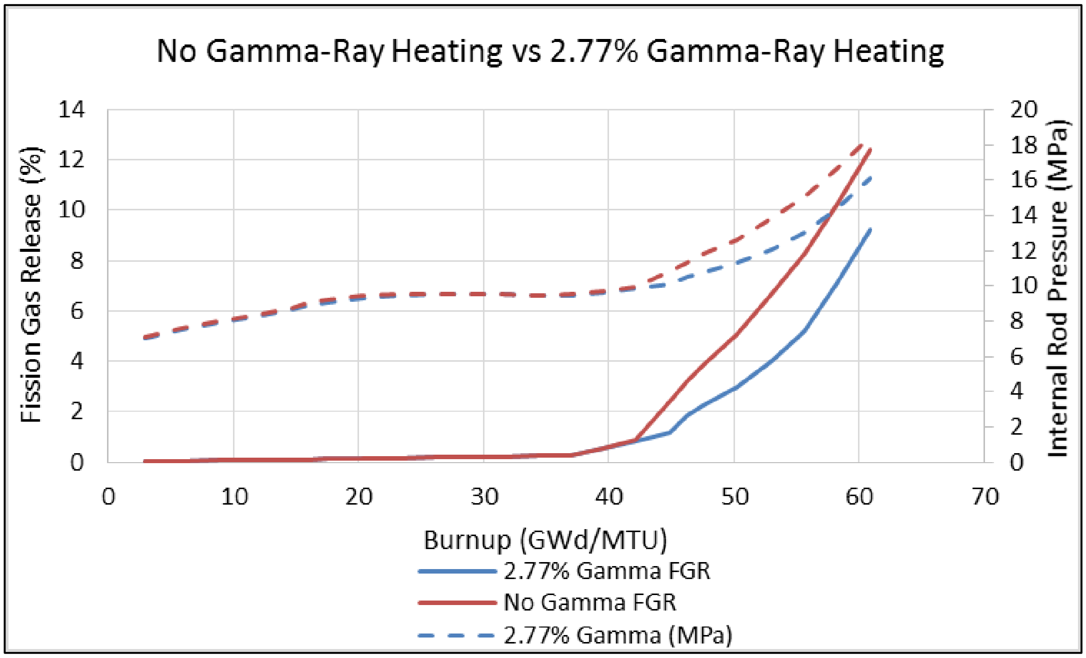

Figure 4.3: Comparison of the effects of moderator heating on FGR and internal rod pressure

Not taking into account gamma-ray heating in a LOCA analysis has the potential to introduce extra conservatism. Based on the results discussed above, there is the potential for increased stored energy in the fuel and higher internal rod pressures, which are driving forces for PCT and cladding ballooning, respectively.

### 4.1.2 Output File for TRACE Data

An additional output file was created that writes the burnup dependent fuel rod parameters calculated by FRAPCON that are needed for a TRACE calculation. This file is read by the Auto Input Generator that was developed in this work to run the FRAPCON & TRACE calculations successively. This output file number is 50 (denoted by a .frttr extension for <u>FR</u>APCON <u>t</u>o <u>TR</u>ACE) and is called by setting the namelist $frpcon flag *nfrttr* = 1. The FRAPCON code requirements are shown in Table 4.3.

Table 4.3: FRAPCON to TRACE file flag description

| Variable Name | Description | Units | Limitations / Default Value |
|---|---|---|---|
| nfrttr (Integer) | Indicator for printing data needed for TRACE using the Auto Input Generator. Set nfrttr = 1 to turn on. | Dimensionless | Default Value = 0 |

The data is written at every timestep calculated by FRAPCON so that the Auto Input Generator can extract data from BOC, MOC & EOC (and/or any other timesteps desired) conditions. The burnup dependent parameters, along with some as-fabricated parameters needed for TRACE that are calculated internally within FRAPCON, that are written to this file are shown in Table 4.4.

Table 4.4: Burnup dependent parameters written to .frttr file for TRACE input deck

| Line # | Description | Dimension |
|---|---|---|
| 1 | Fuel thermal expansion | # of axial nodes |
| 2 | Fuel swelling | # of axial nodes |
| 3 | Fuel densification | # of axial nodes |
| 4 | Fuel relocation | # of axial nodes |
| 5 | Fuel burnup | # of axial nodes |
| 6 | Cladding O.D. creep | # of axial nodes |
| 7 | Gas pressure, # Moles, As-Fabricated free void volume, As-Fabricated # of moles, Plenum volume fraction occupied by spring, fuel volume | 11 |
| 8 | Gap HTC | # of axial nodes |
| 9 | Oxide layer thickness | # of axial nodes |
| 10 | Axial power shape factor | # of axial nodes |
| 11 | Fuel stored energy (Not used as input to TRACE) | # of axial nodes |
| 12 | Radial power distribution | # of radial nodes x # of axial nodes |
| 13 | Radial distances corresponding to power distribution | # of radial nodes x # of axial nodes |

### 4.1.3 Thermal Hydraulic Data from TRACE

FRAPCON's simplistic coolant model doesn't allow for a thermal hydraulic contribution from any other fuel rods surrounding the rod being modeled. Unlike BWRs where the thermal hydraulic conditions are isolated for a given assembly due to the use of channels, PWRs have significant cross flow and the coolant conditions locally can be affected by the adjacent rods. FRAPCON does not have the ability for the user to supply coolant conditions (i.e. temperature and pressure) at each axial node, rather it allows the user to supply only the inlet conditions and uses a single channel enthalpy rise correlation to calculate the temperature rise of the coolant caused by the surface heat flux across the cladding. When analyzing a low power rod, the coolant outlet temperature predicted by FRAPCON can be significantly lower than that predicted using TRACE due to the influence of adjacent rods and the total core thermal power being constant over the cycle. Similarly, when modeling a high power rod in FRAPCON it has the potential to over predict coolant conditions compared to TRACE. For cross code consistency, the coolant conditions calculated by TRACE for each node in the core shall be the coolant conditions also used by FRAPCON. The code modifications performed to implement this ability and the impacts on important transient initial conditions are described below.

The ability for the user to specify the coolant conditions at each axial node was incorporated into FRAPCON via the namelist $frpcon flags *ifixedcoolt*, *zcoolt*, *Tcoolant* and *Pcoolant*, described in Table 4.5. The coolant conditions can be supplied for any number of axial nodes and the code will perform linear interpolation between the supplied coolant data points to determine the coolant conditions that correspond to the fuel rod axial nodes. The coolant conditions can be supplied from 1 time step up to the number of time steps that are being analyzed by FRAPCON via the power history.

Table 4.5: Input requirements for using *modheat* in FRAPCON

| Variable Name | Description | Units | Limitations / Default Value |
|---|---|---|---|
| ifixedcoolt<br>(I) | Indicator for using axial coolant temperature distribution. 0 = Coolant temperature will be calculated based on coolant enthalpy rise model. 1 = Coolant temperature will be specified by the user at each time step. | Dimensionless | Default Value = 0 |
| zcoolt(N)<br>(R) | The elevations in each coolt, Tcoolant array defining a coolant temperature profile. Note the first value should be 0.0 and the last value must = totl. Max # of elevations = na + 1 | Feet/meters | Default value = 0.0. |
| Tcoolant(N*im)<br>(R) | Bulk coolant temperatures prescribed at each node zcoolt (N) for each time step (im). If the # of coolant temperature / time pairs is < im, then the last supplied value will be used for the remaining time steps for that node. Enter all coolant values (1 to im) for each node before proceeding to the next node. | F/K | Default value = 0.0 |
| Pcoolant(N*im) | Bulk coolant pressures prescribed at each node zcoolt (N) for each time step (im). If the # of coolant pressure / time pairs is < im, then the last supplied value will be used for the remaining time steps for that node. Enter all coolant values (1 to im) for each node before proceeding to the next node. | psi/Pa | Default value = 0.0 |

The output file was analyzed to verify that the proper coolant temperatures were being used for each axial node. The FRAPCON code is valid in the temperature and pressure ranges that are being supplied to it, thus eliminating the need for additional validation of results.

To analyze the impacts of various rods in the reactor using the new coolant conditions, TRACE was run at the beginning, middle and end of the cycle for the W4LP plant. The conditions were extracted from the steady-state analysis and linearly interpolated for the time steps in between the TRACE calculations analyzed in the FRAPCON analysis. For the current cycle being modeled, the conditions were taken as those calculated by TRACE for the current position of the rod in the vessel. For previous cycles, it was assumed that the rods resided in the central ring of the core, which was typical of 1st cycle rods and ~50% of the 2nd cycle rods. The radial variation in temperature and pressure at the same axial elevation in the core was less than 8K and 0.01 MPa, respectively. The bulk coolant temperature and pressure changes across the fuel rod calculated by TRACE and FRAPCON are shown in Table 4.6 for the rod with the highest and lowest LHGR in the core.

Table 4.6: Coolant condition changes from bottom to top of fuel rod calculated using FRAPCON's default model and coolant conditions calculated by TRACE

| **Case** | **Temperature Rise (K)** | | **Pressure Drop (MPa)** | |
|---|---|---|---|---|
| | **FRAPCON** | **TRACE** | **FRAPCON** | **TRACE** |
| Highest Power (24.38 kW/m) | 47.18 | 36.01 | 0.0 | 0.188 |
| Lowest Power (5.09 kW/m) | 10.26 | 28.39 | 0.0 | 0.180 |

The difference in the bulk coolant temperature and subsequently cladding temperature, as the bulk coolant temperature is a bounding condition in FRAPCON's steady-state temperature distribution calculation, has a strong impact on the cladding oxidation and hydrogen uptake. Table 4.6 above shows that FRAPCON has the ability to both over predict and under predict the bulk coolant temperature compared to TRACE, depending on the power of the rod and its location in the core. For high power rods, FRAPCON's higher temperature prediction leads to an increase in average oxide layer thickness and cladding hydrogen content. By the EOC, the high power rods have an increase in average oxide layer thickness by as much as 31%. In contrast, the low power rods under predict the oxide layer thickness by as much as 14.7%.

Table 4.7: Corrosion analysis for a 1st cycle rod with a LHGR of 24.38 kW/m and a 3rd cycle rod with a LHGR of 5.09 kW/m

| Cladding Oxidation and Hydrogen Analysis | | **1st cycle rod** | | | **3rd cycle rod** | | |
|---|---|---|---|---|---|---|---|
| | | **FRAPCON** | **TRACE** | **Diff (%)** | **FRAPCON** | **TRACE** | **Diff (%)** |
| Hydrogen Content (ppm) | Avg. | 150.9 | 106.9 | 29.2% | 216.2 | 247.1 | -14.3% |
| | Max | 215.6 | 171.3 | 20.5% | 362.31 | 437.83 | -20.8% |
| Oxide Thickness (micron) | Avg. | 15.2 | 10.5 | 30.9% | 22.2 | 25.4 | -14.4% |
| | Max | 22.2 | 17.4 | 21.6% | 37.6 | 45.5 | -21.0% |

*TRACE Denotes that the coolant conditions were taken from TRACE calculations.
*FRAPCON denotes that the coolant conditions were calculated using FRAPCON's coolant enthalpy rise model

The low power rods, which are typically the third cycle rods location in the periphery of the core, tend to predict bulk coolant temperatures much lower than temperatures predicted by TRACE. Understanding that TRACE is not a sub-channel analysis code and might not accurately predict the coolant temperatures at all fuel locations within the assembly, it is shown that the influence of adjacent fuel assemblies can cause the bulk coolant temperature to be higher than what is expected when analyzing a low power assembly by itself. However, it should be noted that both codes use the same assumption that the rods are located in an interior sub-channel, leading to the most bounding (hottest) condition. In reality, for a 17x17 design 64 of the 264 rods are located with sub-channel conditions in the edge and/or corner designation. Nevertheless, not taking into account the location in the core can lead to non-conservatisms in terms of steady-state fuel rod licensing limits, including but not limited to ECR and hydrogen uptake.

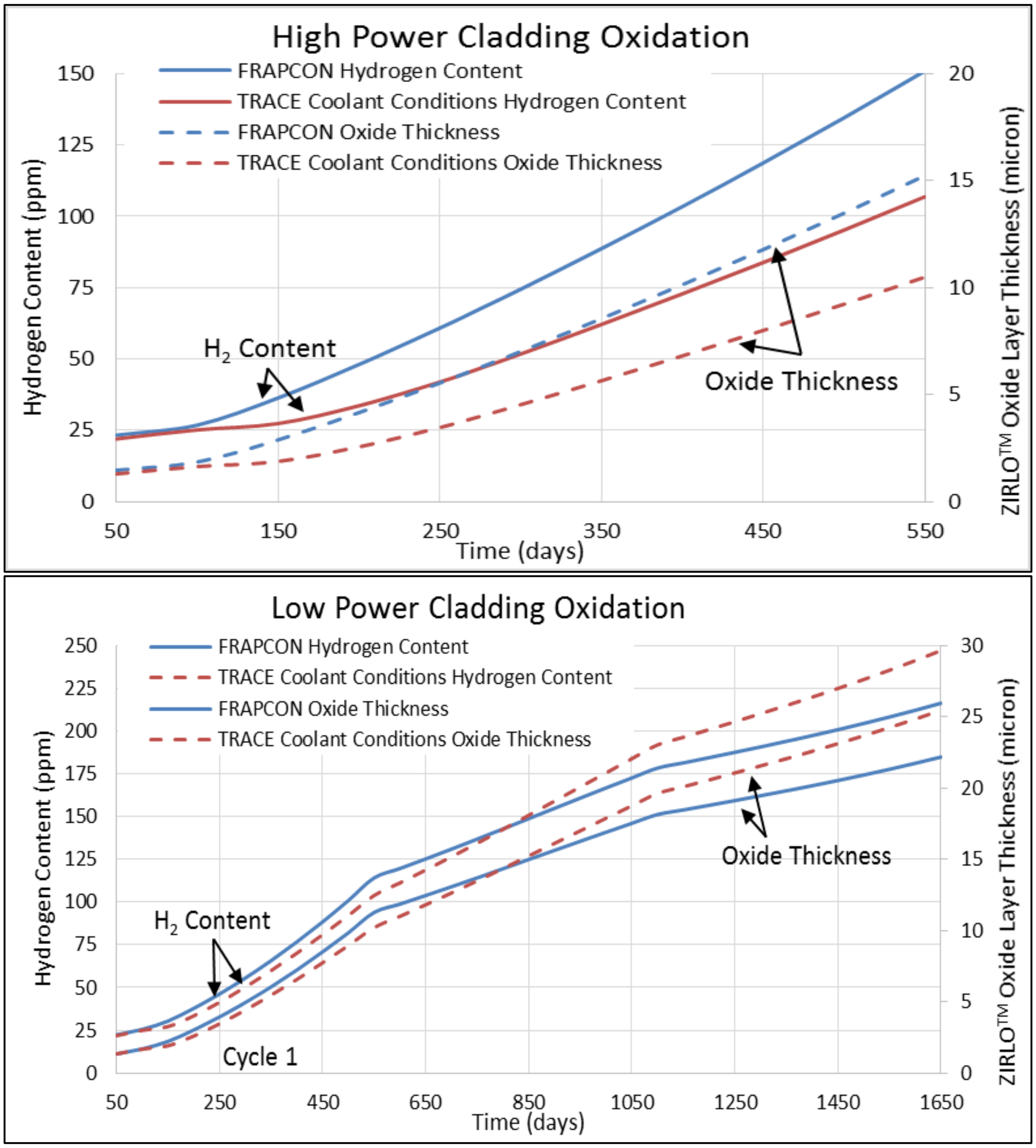

Figure 4.4: Corrosion for first and third cycle rods with ZIRLO$^{TM}$ cladding

When taking into account gamma-ray heating in addition to using the coolant conditions provided by TRACE (whereas the earlier analysis assumed that all of the energy was still deposited in the fuel), a compounding affect was seen in the high power rods in terms of an increase in internal rod pressure and FGR. FRAPCON's default (and recommended) fission gas release model is a modified Forsberg-Massih Model. This FGR model has a burnup enhancement factor after 40 GWd/MTU, which can be seen in both of the cases presented in the Figure 4.5. The influence of fuel temperature, which is accounted for in calculating the diffusion coefficient, is the driving force for the difference in fission gas release between the two cases. As a result of the lower fission gas release, the internal rod pressure at 60 GWd/MTU is ~17% lower. The absolute difference in fission gas release is 4%, decreasing to 8.4% compared to 12.4%. The decrease in internal rod pressure, which is used as the external force applied to gas bubbles, also reduces the saturation concentration of gases for the case modeled using both gamma-ray heating and TRACE TH conditions. However, this impact is overshadowed by the decrease in fuel temperatures. The fission gas release and resulting internal rod pressure as shown in Figure 4.5 with the original case denoted FRAPCON and the modified case denoted TRACE Coolant Conditions.

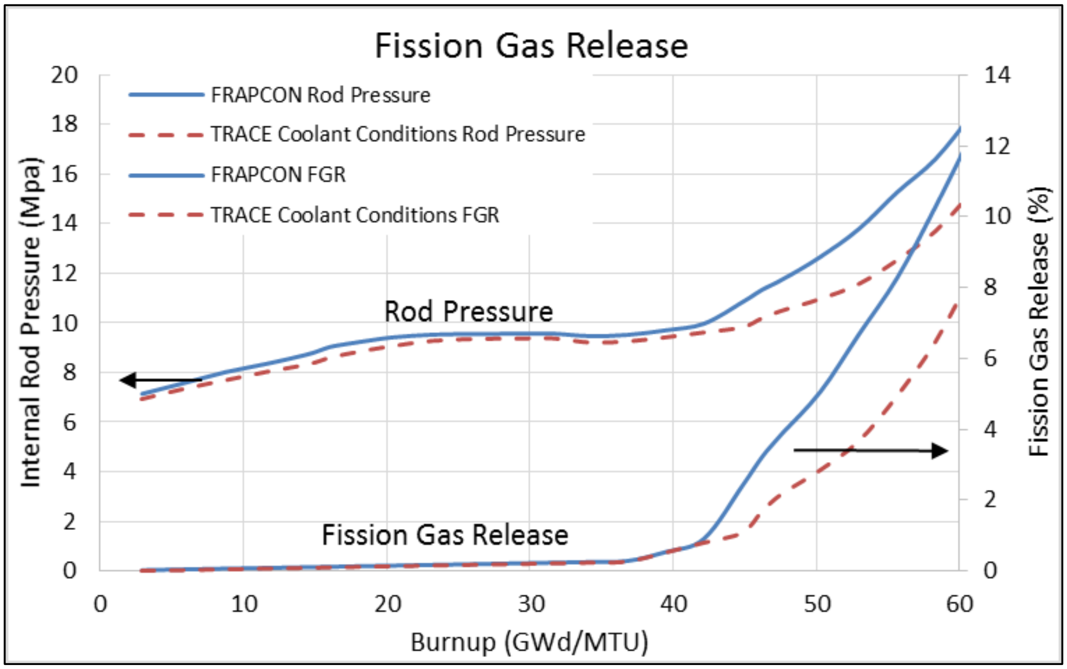

Figure 4.5: Fission gas release for highest powered second cycle rod

Pellet-cladding mechanical interaction (PCMI) as a result of outward fuel expansion and cladding creepdown, was also noted to be impacted by these modifications. FRAPCON uses a rigid pellet assumption with an unrestrained outward fuel swelling model that is dependent on burnup only. Therefore, the differences in the time until PCMI occurs in the cases analyzed are based solely on fuel thermal expansion and, to a small extent, fuel relocation, as well as cladding creepdown.

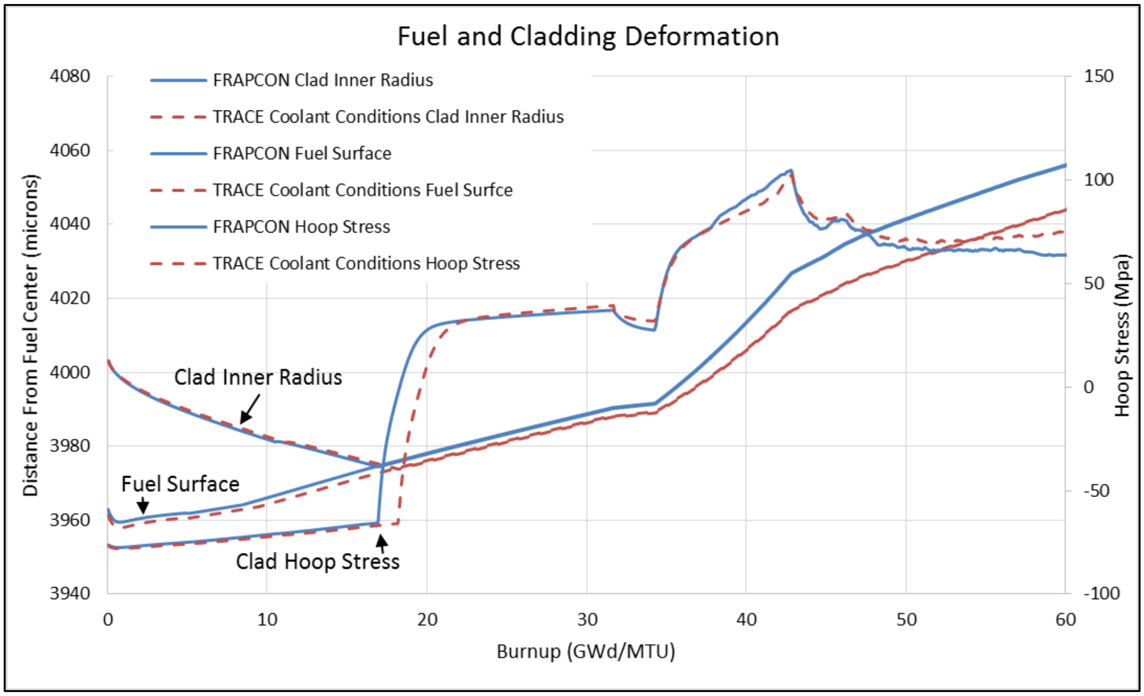

Figure 4.6: PCMI analysis for highest-powered second cycle rod

The location at which PCMI occurred varied between the cases analyzed in Figure 4.6. The initial case had its first instance of "hard contact", the point at which outward expansion of the fuel drives the cladding outward, at a node average elevation of 2.13m. The modified case first experienced hard contact at a node average elevation of 2.39m, which was three axial nodes higher. These differences are largely due to the different temperature and pressure differential on the cladding (affecting the ZIRLO$^{TM}$ creep rate) as well as the reduction in fuel thermal expansion due to the lower temperature, requiring the cladding to creep inward more before hard contact is made.

From a LOCA standpoint, it is desirable to have as little stored energy in the fuel as possible to reduce the amount of energy that must be removed via the decreasing coolant inventory. Hotter fuel results in an increase in stored energy (assuming all else is held constant), and vice versa. Due to the delay until PCMI, there is also a delay until the minimum fuel stored energy (and temperature) is reached. The significance in this is that the time at which the LOCA analysis is performed will affect the PCT due to changes in fuel stored energy. However, as illustrated in Figure 4.7, the delay in PCMI does not allow for the rods analyzed using the TRACE coolant conditions to have an increase in stored energy compared to the original FRAPCON analysis due to the lower fuel temperatures resulting from the removal of the gamma-ray energy being deposited in the fuel.

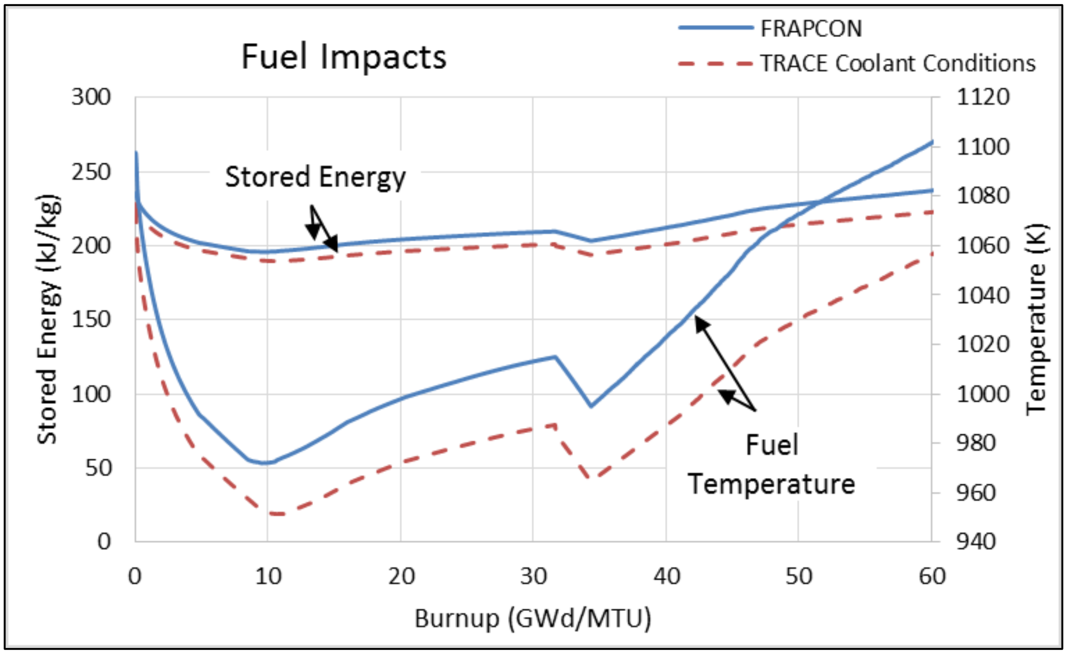

Figure 4.7: Fuel stored energy impacts for 1st cycle fuel rod

This analysis has shown that using the coolant conditions supplied by a T/H code rather than the conditions predicted by FRAPCON can have a large impact on fuel performance. It was shown that rod pressure, oxide layer thickness, cladding creep, and fuel stored energy, all of which are important parameters in LOCA analysis, are all influenced by the operational coolant conditions. The cycle time at which the rod is analyzed can also play a major role with both techniques leading to the more bounding case at different times.

### 4.1.4 Advanced Materials

Several advanced fuel and cladding materials, all of which have been considered as potential accident tolerant materials, were implemented into FRAPCON. The fuel materials implemented were Uranium Carbide (UC), Uranium Nitride (UN) and Uranium Silicide ($U_3Si_2$). The cladding material implemented was SiC. These materials have been studied at the University of South Carolina by various graduate students under steady-state conditions. A brief summary of the equations implemented into the code to model these materials during reactor operation will be described below. A more detailed explanation of the reason these equations were chosen can be found in references [Hallman, 2013; Carroll, 2014; Li, 2013; K.E. Metzger, 2014]. The material flags for the fuels (*imox*) and claddings (*icm*) are shown in Table 4.8.

Table 4.8: Fuel and cladding material flags for FRAPCON

| **Material** | **ID** |
|---|---|
| UC | imox = 3 |
| $U_3Si_2$ | imox = 4 |
| UN | imox = 5 |
| SiC | icm = 11 |

The thermal properties implemented into FRAPCON for the materials include thermal conductivity, thermal expansion and emissivity. Due to FRAPCON only solving for the steady-state conduction solution, specific heat and enthalpy are not needed for anything beyond graphically showing the stored energy in the fuel. The thermal equations implemented into FRAPCON were also implemented into TRACE and are described in Chapter 4.3.2.

The burnup-phenomena of the fuel modeled by FRAPCON that is not taken into account in TRACE includes fuel swelling, densification, relocation* and fission gas release. (*Note: Although TRACE does have a simplistic relocation model for $UO_2$, Chapter 4.3.1 describes the modification made to TRACE to allow the code to use the relocation values provided by FRAPCON instead.) It is important to note that, due to differences in uranium density for the four different fuel materials, the time duration required to reach a certain burnup limit at the same power will be extended for the advanced fuels compared to $UO_2$ assuming that the total Uranium volume remains higher. The fuel swelling for $UO_2$ is dramatically lower compared to all other fuel types. By 62 GWd/MTU, the volumetric swelling for UC, UN and $U_3Si_2$ is 2.68, 1.44 and 2.61 times higher than that for $UO_2$, respectively. The increase in fuel swelling will significantly decrease the size of the gas-gap (and consequently the gas volume) while also decreasing the time until PCMI occurs. The fuel swelling implemented into FRAPCON is shown in Figure 4.8.

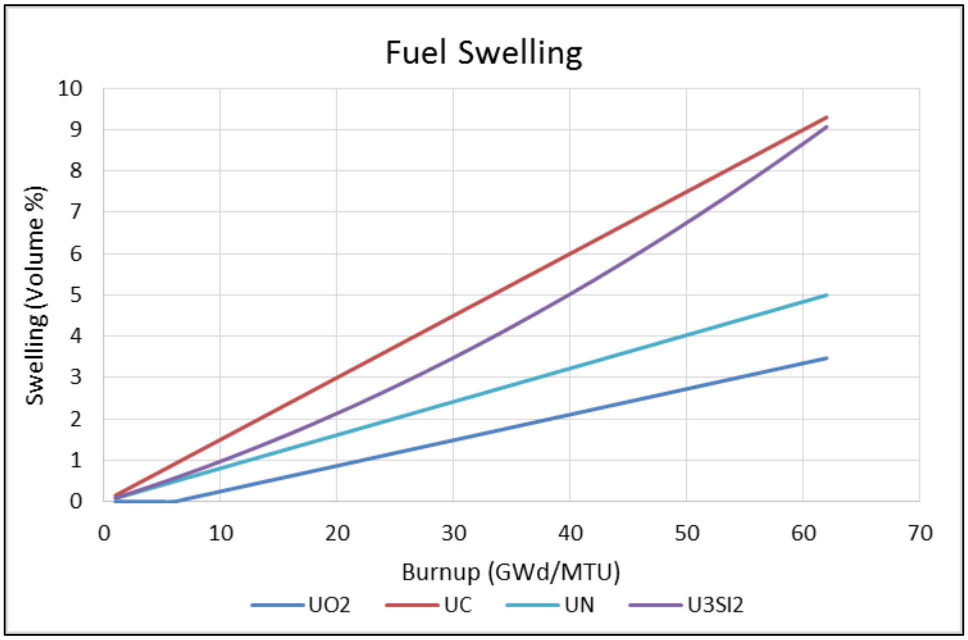

Figure 4.8: Fuel swelling for various fuel types implemented in FRAPCON

Due to the lack of available data, the fuel densification calculation has been kept consistent for UN and $U_3Si_2$ with that for $UO_2$. Unlike the model for $UO_2$, the densification model for UC is based only on a burnup value rather than the fuel temperatures and conditions at which it was fabricated.[Hallman, 2013] Uranium Carbide has a limit with densification to either stop by 6 GWd/MTU or stop when the porosity in the fuel is less than 3.33%, whereas $UO_2$ will stop densifying by 10 GWd/MTU but typically asymptotically reaches its input limit by 5 GWd/MTU.[K.J. Geelhood, 2011] However, the differences in fuel radial displacement caused as a result of densification is less significant than the differences caused by fuel swelling.

Fuel relocation, the outward movement of fuel pellets due to cracking as a result of high thermal stresses, is also much different between $UO_2$ and the advanced fuel types. The thermal conductivity of the advanced fuels is significantly higher than that for $UO_2$, resulting in a flatter temperature gradient across the pellet and a decrease in thermal stresses. For $UO_2$, the fuel relocation is determined based on the burnup and rod power. The relocation is between 0.4 and 0.5 of the gap thickness, meaning the fuel moves outward to consume 40 – 50% of the gap thickness. The recovery of relocation has been empirically set by the code for $UO_2$ to be 50% of the relocation value. To do this the code assumes that ½ of the relocation value is added to the fuel pellet as additional outward swelling while the remaining ½ of the value is added to reduce the gap thickness for thermal calculations. This allows the fuel-cladding gap to close faster for thermal calculations than for the mechanical analysis. For hard contact between the fuel and cladding (PCMI) to occur, the fuel must continue to expand outward due to swelling and thermal expansion, while the cladding continues to move inward due to cladding creepdown, until the ½ of the relocation value added to reduce the gap thickness is recovered.

The relocation for UN and $U_3Si_2$ is set to 0.0 irrespective of the linear power in the rod. For UC, the relocation is equivalent to 0.3 times the gap thickness if relocation is expected to occur. Relocation is expected to occur when the thermal stresses exceed the yield stress of the material. The thermal stress calculation ($\sigma_{t,max}$) is based off the thermal conductivity ($\kappa$) and expansion ($\alpha$), poisson's ratio ($\nu$), linear heat generation rate ($q'$) and young's modulus ($E$) and is shown in Equation 4.2 below.

$$\sigma_{t,max} = \frac{\alpha E q'}{8\pi(1-\nu)*\kappa} \qquad 4.2$$

It was determined that the LHGR under typical PWR operating conditions was not high enough to cause the thermal stress to exceed the fracture stress for UC. Therefore, for all three advanced fuel materials, no fuel relocation will exist. An absence of relocation will increase the gas-gap volume and delay the time until PCMI occurs. Furthermore, it will eliminate the ability for any gap recovery to occur – leaving only a hard contact regime between the fuel and cladding.

Due to the lack of additional information, the fission gas release models for UC, UN and $U_3Si_2$ have been kept identical to $UO_2$'s model.

Cladding creep, irradiation-induced growth and steady-state corrosion are also modeled by FRAPCON but not by TRACE. Unlike Zircaloy based claddings, where due to the pressure differential the cladding creeps inward reducing the size of the gas-gap before PCMI, SiC is modeled to not creep. This will maintain a larger gap size, thus increasing the thermal resistance while also providing a larger gas volume. It is assumed that SiC will experience brittle failure, so any form of plastic deformation is turned off. Axial growth for SiC cladding is also turned off. Although data on the corrosion kinetics for SiC is scattered and varies based on the manufacturer, the common consensus is that steady-state oxidation will be minimal compared to Zircaloy, so both the formation of an oxide layer and hydrogen uptake into the cladding are turned off. All other thermal properties were also implemented into TRACE and are described in Chapter 4, Section 3.2.

### 4.1.5 Additional/Miscellaneous Modifications

Several additional modifications were made to FRAPCON outside of the results previously mentioned. As part of the FRAPCON/FRAPTRAN development team at the NRC, it was determined that many code improvements could be made to help facilitate both this work and future work at the NRC and within its code user group. The largest task performed in this additional work was converting the code from FORTRAN 77 mixed with common files to a minimum of FORTRAN 90 standard. As FRAPCON is designed to model oxide fuels with zirconium cladding, the material properties were hard-wired into the code. In doing the conversion to FORTRAN 90, the built-in material properties were removed and placed into a module representing each material type (i.e. Uranium Dioxide). This allowed for the implementation of UC, UN, $U_3Si_2$ and SiC that was performed in tangential work. To improve code flexibility and allow better code-to-code comparisons, the fixed array sizes were removed and replaced with dynamic arrays. This includes the number of axial and radial (both thermal and fission gas release) nodes, as well as the number of timesteps. This also allowed for a sensitivity study described in Chapter 5.

For direct support of work being performed at the NRC, the FRAPCON-Dating module was fixed and implemented into FRAPCON-3.5 for support of NMSS. This module was developed for spent fuel creep modeling with FRAPCON-3.3. To expand on FRAPCON's ability to model spent fuel, the code was modified to allow the user to turn off oxidation after a given amount of time, indicative of moving the fuel to dry cask storage. For support of NRO, the ability to modify the gap conductance was added to analyze the sensitivity of the gap conductance models compared to other vendor codes.

When creating graphs to analyze the fuel outer surface displacement versus the cladding inner surface displacement, it was noticed that the fuel outer surface was being displaced beyond the cladding inner surface. From a mechanical deformation viewpoint, the fuel surface can never exceed the cladding inner surface due to the method in which the cladding stresses are calculated. Due to FRAPCON's rigid pellet model, the cladding strain is equivalent to the fuel outward strain, and from there the cladding stress values are calculated. From a thermal viewpoint, the fuel outer surface can never be closer than the temperature jump distance (the sum of the fuel and cladding surface roughness values) away from the inner surface of the cladding. It was determined that the fuel relocation value that was printed to the output file was being calculated based on the deformation of the outer surface of the cladding rather than the inner surface. As the cladding outer surface displaces farther than the inner surface, this caused the fuel relocation value to be larger than reality and the fuel to displace beyond the cladding inner surface. This error was also carried over into the plot file, so the correction to fix this issue was made in both locations. A similar error was found in the restart file written for FRAPTRAN, where the permanent cladding displacement used to reduce the gap thickness in FRAPTRAN was being based on the outer surface displacement rather than the inner surface displacement. This was found to be one of the reasons FRAPTRAN would crash during initialization for high powered cases, resulting in increased cladding stress caused by the fuel expanding further into the cladding than during the steady-state conditions. The corrections made in the output and plot files will be implemented into the next version of FRAPCON. An illustration of the original and updated fuel dimensions is shown in Figure 4.9

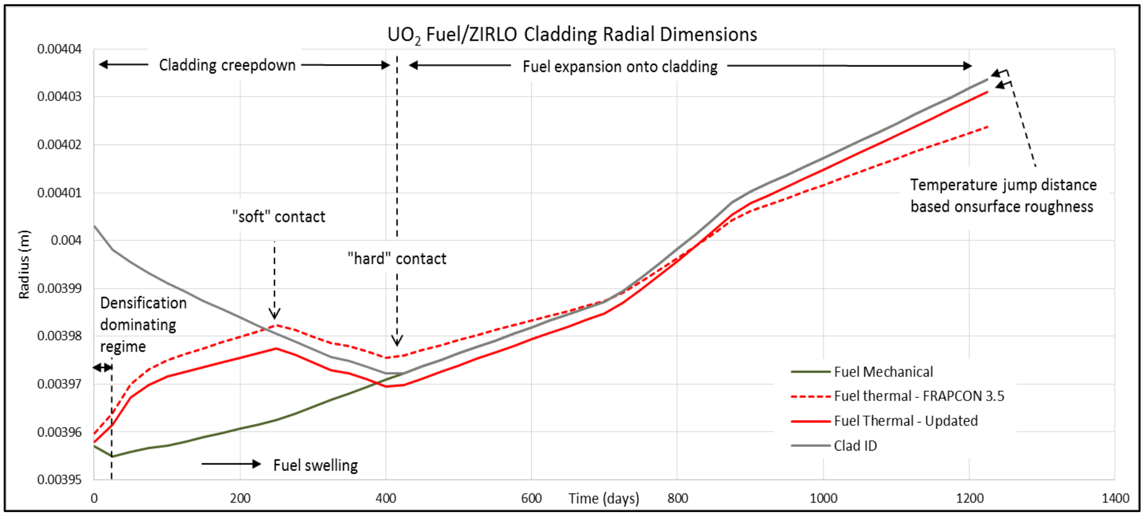

Figure 4.9: Fuel and cladding radial dimensions under PWR conditions at constant power of 20.34 kW/m

## 4.2 FRAPTRAN

FRAPTRAN was modified to better model gamma-ray heating under LOCA conditions. The code currently assumes that an additional 2% of the user-supplied LHGR will be added to the coolant, irrespective of the coolant conditions, to model this phenomena. To analyze the validity of this assumption, several scenarios were analyzed using MCNP and SCALE to determine the intensity of gamma-rays as a function of fuel rod burnup and where the energy is deposited as a function of coolant conditions and time after reactor scram. A new empirical correlation was developed for a 17x17 Westinghouse fuel design, understanding that different fuel designs (especially BWRs) will have different results caused by differences in Zirconium content and fuel rod spacing. This analysis is described below.

### 4.2.1 Gamma-ray Heating

Although under typical LWR operating conditions gamma-ray heating is relatively low, this is not the case when the power begins to come from fission products alone. As described in Chapter 3, the fraction of energy coming from gamma-rays accounts for ~31% of the total power being generated by the fuel rods 10s after shutdown. Where this energy is deposited is dependent on the coolant density due to the interaction of gamma-rays and water, the gamma-ray energy and the gamma-ray intensity. A LOCA scenario encompasses both a transient modeled after the reactor has been scrammed and rapidly changing coolant conditions. In order to better assess the impacts of gamma-ray heating during a LOCA, the gamma-ray intensity and where the gamma-rays are deposited needed to be understood. These parameters were analyzed using SCALE AND MCNP, respectively.

### 4.2.1.A SCALE – Gamma-ray Intensities

SCALE is a comprehensive modeling and simulation suite developed by Oak Ridge National Laboratory (ORNL) and supported by the Nuclear Regulatory Commission and Department of Energy (DOE). SCALE has been validated to be used for criticality, reactor physics, shielding, source term, and sensitivity and uncertainty analysis.[ORNL, 2011] For this analysis, SCALE 6.1 was used with Origen-ARP with the built-in cross section libraries developed for a Westinghouse 17x17 fuel assembly. Additional parameters used are shown in Table 4.9.

Table 4.9: Fuel design parameters used in SCALE.

| **Parameter** | **Value** |
|---|---|
| Fuel Type | w17x17 |
| Enrichment | 4.45 wt%-U235 |
| Mass of fuel | .424 MTU |
| LHGR | 24 kW/m |

An irradiation case was performed before the decay to determine the gamma-ray intensity distribution using the 47 group SCALE6 group structure. For the three burnup cases, only the cumulative time was varied to achieve the desired final burnup values. The results of the intensities obtained for the 47 energy bins are shown in Figure 4.10.

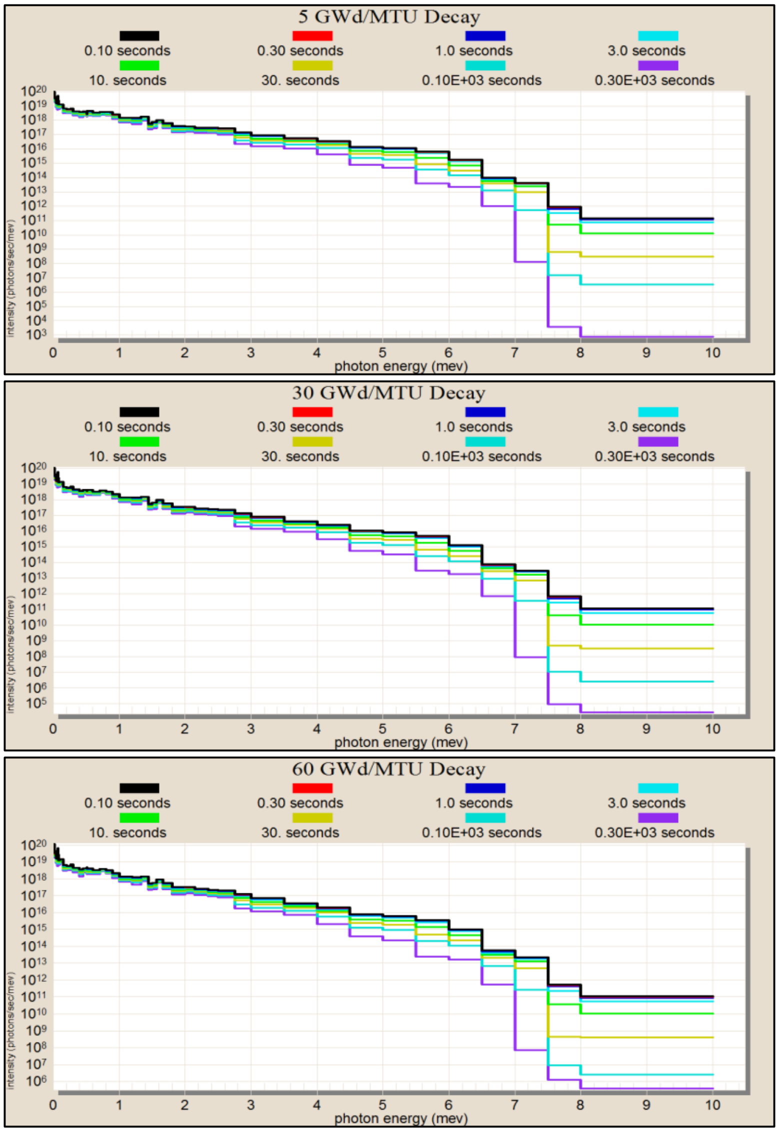

Figure 4.10: Photon intensity versus photon energy for 5, 30 and 60 GWd/MTU burnups, respectively.

There are two trends that can be seen from the above graphs. The first is that for longer time after shutdown, the photon intensities decrease, especially noticed with the higher energy photons. Although a small fraction at the beginning, as the transient progresses the higher energy photons will have even less of an impact on the energy distribution compared to the lower energy photons due to the decrease in intensity by several orders of magnitude. The second trend is that the higher burnup fuel has higher photon intensities, especially at longer times after shutdown. This is consistent with literature in that the amount of decay heat is proportional to both power (which was constant for all three cases) and the time at which the power was maintained.[Neil Todreas, 1990] The impact of these trends on the energy distribution will be examined in MCNP.

### 4.2.1.B MCNP – Energy Distribution

MCNP is a general purpose Monte Carlo transport code that can be used for neutrons, photons and electrons, either independently or combined.[Los Alamos National Lab, 2008] It was developed by Los Alamos National Laboratory (LANL) under a contract with the DOE. These analyses were performed using MCNP6. The fuel design was again a typical 17x17 PWR assembly, with the arrangement shown in Figure 4.11.

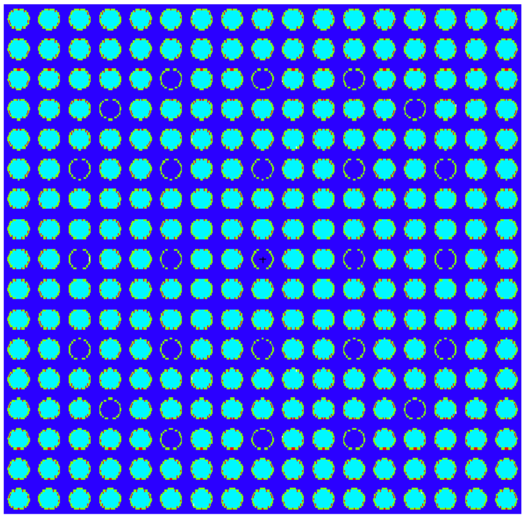

Figure 4.11: Arrangement of 17x17 PWR assembly with 264 fuel (light blue) rods and 25 water rods (dark blue).

A single fuel assembly was modeled with a periodic boundary. The fuel was $UO_2$ with a density of 10.412 g/cm$^3$, the gas-gap was Helium (He) with a density of 2.624E-3 g/cm$^3$, and the cladding was zirconium (Zr) with a density of 6.56 g/cm$^3$. For a reflector, water, zirconium (Zr) and iron (Fe, density of 7.8 g/cm$^3$) were placed above the core, and water and Zr were placed below the core. The density of water was varied between 1.0E-5 g/cm$^3$ to 1.0 g/cm$^3$. A total of 36 density values were used.

The analysis was performed using a F6 tally. This tally provides the track length estimate of energy deposition and can be used for both photons and neutrons. To get a baseline analysis of the energy distribution during steady-state, a F6:N,P (Neutrons and Photons) tally was performed using a typical PWR coolant density value of 0.665 g/cm$^3$. The results are shown below in Table 4.10 and are well aligned with the literature.

Table 4.10: Energy distribution calculated using a F6:N,P tally under typical PWR conditions

| **Location** | **Fuel** | **Cladding** | **Coolant/Structural Materials** |
|---|---|---|---|
| % of power deposited in material | 97.58 | 0.66 | 1.76 |

For the transient decay analysis, eight F6:P tallies were performed for each coolant density value, each tally representing the gamma-ray intensity at a time step of 0.1, 0.3, 1, 3, 10, 30, 100 and 300 seconds. Each time step uses the same energy bins (E) but has a different energy multiplier (EM) for intensity, extracted from the SCALE results previously mentioned. There were 36 MCNP runs (1 representing each density value) per burnup, resulting in 108 total MCNP runs, all of which contained 8 F6 tallies.

#### 4.2.1.C Burnup and Time Effects

The trend on energy distribution with burnup was determined to be that the higher burnup fuel had a larger fraction of energy deposited in the fuel. However, it was found to be no less than a 1% difference between the 60 GWd/MTU and 5 GWd/MTU cases. The energy deposited in both the cladding and coolant/structural materials decreases with the higher burnup fuel as well. When looking at the energy distribution with respect to time, the same trend is followed as that with burnup. The longer the time after the start of decay, the more energy is deposited in the fuel and less in both the cladding and coolant. The lower burnup case had a smaller increase in the amount of energy deposited in the fuel from 0.1 to 300 seconds than the higher burnup cases. The energy deposited in the fuel from a 0.665 g/cm$^3$ coolant density can be seen in Table 4.11.

Table 4.11: Effects of burnup and time after start of decay calculation on the fraction of gamma-ray energy deposited in the fuel.

| Time (s) | 5 GWd/MTU | 30 GWd/MTU | 60 GWd/MTU |
|---|---|---|---|
| 0.1 | 85.06% | 85.34% | 85.60% |
| 1 | 85.10% | 85.39% | 85.66% |
| 10 | 85.15% | 85.48% | 85.78% |
| 30 | 85.17% | 85.52% | 85.83% |
| 100 | 85.27% | 85.61% | 85.93% |
| 300 | 85.41% | 85.75% | 86.07% |

### 4.2.1.D Coolant Density Effects

The coolant density was noted to have the largest effect on the energy deposition. As expected, a decrease in the moderator density resulted in a decrease in the energy deposited in the coolant and an increase in the energy deposited in the fuel and cladding. The fuel received the majority of the energy that was lost by the coolant. In the high burnup case at nearly completely voided conditions, the fuel received ~91% of the total energy, while the cladding received ~8% and the structural material was at 1%. Compared to a normal shutdown where the coolant density is near theoretical density (1.0 g/cm$^3$), the fuel receives ~7% more of the total gamma-ray energy, while the cladding and structural materials see less than ~0.5% more of the total gamma-ray energy. This is shown in Fig. 4.12 with the 60GWd/MTU case after 0.1s.

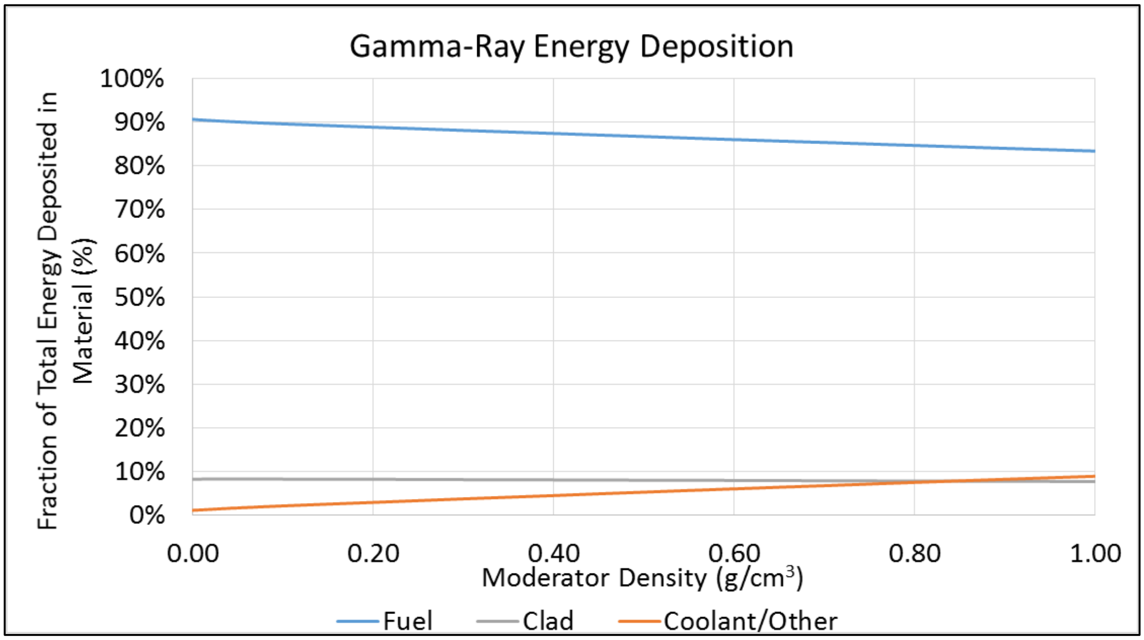

Figure 4.12: Energy distribution in the fuel, cladding and coolant/structural materials at 0.1s after start of decay with various moderator densities for 60 GWd/MTU burnup fuel.

The fraction of energy deposited at various densities for the case shown above is shown in Table 4.12.

Table 4.12: Effects of moderator density on gamma-ray energy deposition

| **Moderator Density (g/cm$^3$)** | **Fuel** | **Clad** | **Coolant** | **Structural Materials** |
|---|---|---|---|---|
| 1 | 83.92% | 7.52% | 7.75% | 0.80% |
| 0.665 | 86.07% | 7.70% | 5.37% | 0.86% |
| 1.00E-05 | 90.99% | 7.94% | 0.00% | 1.07% |

Each calculation passed all 10 statistical checks on the mean, relative error, variance, figure of merit and pdf. The relative error for the MCNP calculations was < 0.005, well below the desired value of < 0.10.

### 4.2.1.E FRAPTRAN Modifications

The time in which a transient progresses is assumed to be small enough that the burnup-dependent phenomena remains constant. The fuel radial power profile, which can be read from the FRAPCON restart file, is determined during the input processing but not updated during the transient. Due to the gamma-ray energy deposition being strongly dependent on coolant density, which can vary drastically during a LOCA, this assumption can no longer be made thus requiring the code to update the radial power distribution every time step. To make this change, a new module called GammaHeating was implemented that updates the radial power distribution based on the coolant density. Prior to calculating the new radial power profile, several subroutines were added to first calculate the new fraction of energy deposited in the cladding and coolant based on the current coolant density. Once these values are updated, the remaining fraction of energy is re-distributed across the radial dimensions of the fuel. This process is repeated at all axial nodes based on the coolant density at the node being modeled. The subroutines added to FRAPTRAN are shown in Table 4.13.

Table 4.13: Code subroutines added to model gamma-ray heating

| **Name** | **Description** | **Inputs** | **Output** |
|---|---|---|---|
| GammaHeating | Module that contains all of the subroutines needed for gamma-ray heating calculation | N/A | N/A |
| Gamma_Clad | Subroutine calculates the gamma-ray heating of the cladding | CoolantDensity | gamma_c (Cladding gamma heating fraction) |
| Gamma_Coolant | Subroutine calculates the gamma-ray heating of the coolant | CoolantDensity | gamma_cool (Coolant gamma heating fraction) |
| Update_Power_Distribution | Subroutine updates the radial power distribution based on the contributions to cladding and coolant gamma-ray heating fractions | CladdingPower | radsrc (Fuel power distribution at each axial/radial node) |

The original default value for the cladding heating fraction was 0.0, and the coolant heating fraction being an additional 2% of the fuel energy. Under typical PWR conditions, the coolant density is ~0.665 g/cm$^3$ resulting in gamma-ray energy distributions of 7.7% in the cladding and 6.23% in the coolant (assuming energy deposited in the structures is transferred back into the coolant). Based on data by Glasstone and Todreas, the fraction of energy coming from gamma rays during decay is ~31% of the total fission energy. [Samuel Glasstone, 1981; Neil Todreas, 1990] This fraction was applied to the ANS standard decay heat model (Scatena and Upham, 1973) that is used in FRAPTRAN. Consequently, the new default fraction of total energy deposited in the cladding and coolant of a 17x17 assembly under typical PWR conditions will be 2.39% and 1.93%, respectively. Due to the small overall effect that time and burnup plays on the energy distribution, the 'worst-case' scenario will be used that results in the most energy being retained in the fuel. This will be the 60 GWd/MTU case at 300s, which results in less than one third of a percent of additional energy (when factoring in the fraction of total energy that is made up by gamma rays) in the fuel compared to the 5GWd/MTU case at .1s. Due to the non-linear relationship between moderator density and fraction of gamma-ray energy deposited at low moderator densities, 2nd order polynomials shown in Eqs. (4.3) and (4.4) were implemented to calculate the percentage of total energy deposited in the cladding and coolant, respectively.

$$E_{clad}(\rho) = -0.0898 * \rho^2 - 0.0591 * \rho + 2.4682 \qquad 4.3$$

$$E_{coolant}(\rho) = -0.3228 * \rho^2 + 2.613 * \rho + 0.3453 \qquad 4.4$$

In the above equations, $E$ is given in terms of % of total energy and $\rho$ is moderator density in units of g/cm$^3$. Eq. (4.3) has a coefficient of determination value of R$^2$=0.9776 and Eq. (4.4) has a value of R$^2$=0.9997. Note that at a moderator density of 0.0, the coolant still receives a certain fraction of the energy. This is due to the grouping of the coolant and structural materials together.

### 4.2.1.F Transient Fuel Performance Analysis

At the onset of the transient, the internal rod pressure is lower as previously mentioned with the modifications performed in FRAPCON. This, combined with the coolant and cladding removing a small fraction of the energy originally held in the fuel, increased the time to rupture for a given rod analyzed in a LOCA from 110 seconds to 118 seconds. The energy deposited in the cladding and coolant during the duration of the transient can be seen in Figure 4.13.

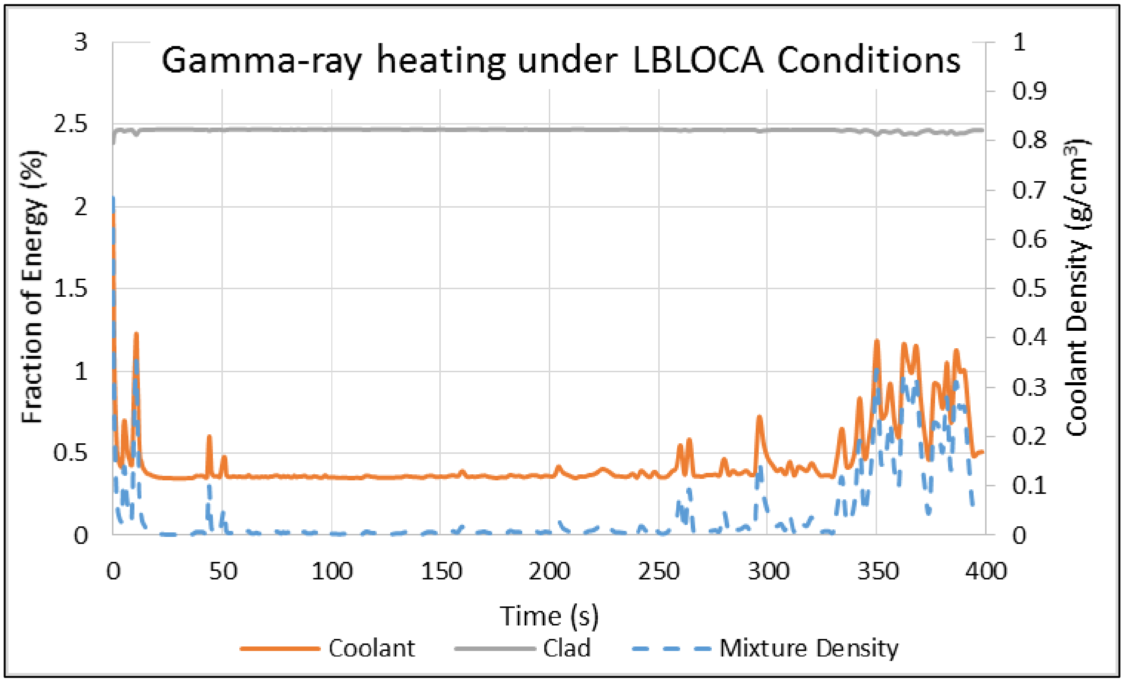

Figure 4.13: Fraction of energy deposited in the cladding and coolant during a LBLOCA.

Although only a relatively small fraction of the total energy, the influence of modeling gamma-ray heating can be seen in both the steady-state and transient analyses. It was concluded that the effects of fuel burnup and time after shutdown were overshadowed by the effect of coolant density on gamma-ray energy deposition. However, the affects seen under steady-state analysis seem to have a larger overall impact on fuel performance than on fuel rod failure conditions during a LOCA. Nonetheless, the new correlation provides a more detailed analysis of where the energy is deposited and further reduces conservatism by no longer assuming all of the energy is deposited in the fuel but rather also across both the cladding and coolant.

### 4.2.2 Additional Modifications

In a tangential fashion to the additional work performed for FRAPCON, many of the same code improvements were made to FRAPTRAN. Again, the largest task performed was converting the code from FORTRAN 77 mixed with common files to a minimum of FORTRAN 90 standard. The largest reason for this was to eliminate the differences noticed in compiled versions using a Compaq Visual Fortran compiler versus Intel Visual Fortran. In working with Ken Geelhood (PNNL), the errors found in FRAPTRAN1-4 were corrected for the official released version of FRAPTRAN-1.5. The compiled versions produced nearly identical results, although slight differences were still found during fuel rod ballooning calculations. It was agreed upon that future released executables will be compiled using Intel Visual Fortran (the same compiler used in this research).

An inconsistency was noticed between FRAPCON and FRAPTRAN when using the restart file to model identical cases. Ideally, using the restart file would produce identical results with the same power and coolant conditions. However, two key parameters were noticed to be different: internal rod pressure and cladding permanent deformation. The internal rod pressure was consistently higher with FRAPTRAN than with FRAPCON. The gram moles of gas and gas composition were identical, leaving the temperature and/or gas volume to be the root cause. Further analysis showed that the gas volumes were not identical, with FRAPTRAN's volume being lower than FRAPCON's (hence the reason for higher rod pressure). Although the FRAPTRAN code description states that FRAPTRAN takes into account the volume associated with radial cracks, it was determined that this is not the case and is one reason for the higher rod pressure. An example of the internal gas volumes is shown in Table 4.14, along with the gas volume associated with the changes made to the restart file described in the following paragraphs. Although the overall total gas volume is closer to the FRAPCON calculation, the individual gas volumes have deviated further away.

Table 4.14: Gas fractions at EOL as calculated by FRAPCON and FRAPTRAN

| Gas fraction at EOL | | | |
|---|---|---|---|
| Location | FRAPCON | FRAPTRAN | FRAPTRAN-Modified |
| Plenum | 0.759 | 0.7712 | 0.7769 |
| Gap | 0.033 | 0.0551 | 0.0727 |
| Roughness | 0.039 | 0.0249 | 0.0216 |
| Dishes | 0.153 | 0.148 | 0.129 |
| Porosity | 0.004 | 0.0 | 0.0 |
| Crack | 0.011 | 0.0 | 0.0 |
| Total gas volume ($cm^3$) | 10.24 | 9.234 | 10.65 |

The second inconsistency noticed was differences in printed values for cladding permanent strain. The values obtained from FRAPCON are typically slightly negative at the top and bottom of the rods while slightly positive near the middle regions of the rod. For example, a high powered 2 cycle rod at EOL has permanent cladding hoop strain between -0.4% and 0.5%, as shown in Figure 4.14.

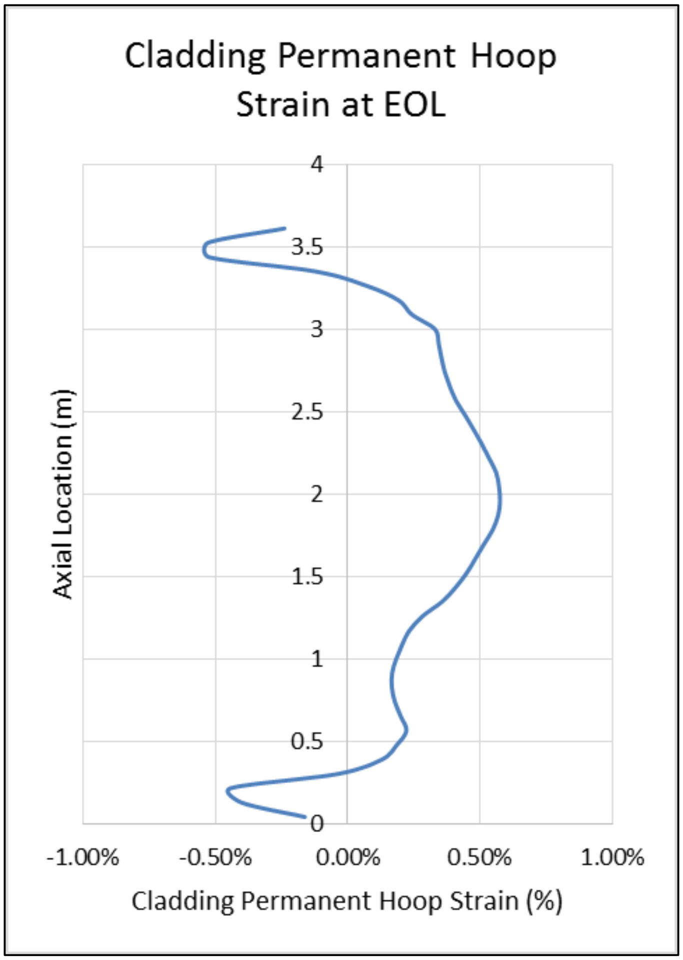

Figure 4.14: Permanent cladding hoop strain at EOL

However, it was noticed that FRAPTRAN was starting with a cladding hoop strain of 0.0 at all axial locations. The two largest concerns with this for this study were due to the changes in gap size due to cladding inward/outward permanent deformation and the fuel dispersal criteria based on the cladding hoop strain. It was determined that the way the code overcame the first issue was due to an additional radial cladding permanent deformation value being read from the restart file. This value was being added to the fuel swelling to reduce the fuel-cladding gap size. Further exploration into this revealed that it was using the wrong permanent deformation value, as mentioned previously with the FRAPCON modifications. This error was noticed to be one of the main reasons why

FRAPTRAN would crash instantly with high powered rods. The increased permanent deformation that the outside of the cladding experiences compared to the inside of the cladding caused the fuel outward expansion (since this value was added to the fuel swelling) to be so large that the cladding stress is too high for the calculation to continue.

To address the second concern related to the fuel dispersal criteria not being properly evaluated required a modification to FRAPTRAN to use the cladding permanent strains calculated by FRAPCON. The restart file read by FRAPTRAN has had the cladding permanent strains but they are simply not used by FRAPTRAN after the values have been read. Instead, they are reset to 0.0 and the cladding permanent radial displacement is used to offset the gas-gap size. If the cladding strains were used, it would not require the code to additionally know the permanent radial deformation due to the correlation that strain is equivalent to the displacement of the material compared to its original position. FRAPTRAN was modified to use the value obtained by FRAPCON (*CldPlasStrnFrapcon*) as its starting permanent strain value by adjusting the way subroutine (*restfs*) uses the value for further calculations (by setting *CldPlasStrn* = *CldPlasStrnFrapcon*). In doing this modification, the updated fuel swelling calculation was eliminated, as the gas-gap size is now reduced due to permanent cladding deformation rather than additional fuel swelling. The impacts of this modification are described in the sensitivity study of Chapter 5.

In implementing the gamma-ray heating modifications, it became clear that the bulk coolant density is not always being calculated or used by the code. This was the case in the fuel dispersal analysis where the coolant conditions were actually cladding temperatures with a sufficiently high heat transfer coefficient to impose them onto the cladding. In running FRAPTRAN this way, the coolant density is never calculated so the gamma-ray heating distribution calculation is incapable of running. However, FRAPTRAN has a requirement that the user supply a water properties file (sth2xt) which contains these values, but is not used under these circumstances. This file was converted into a new water properties module and compiled into the code, so that the subroutines always have access to the coolant density under any given pressures and temperatures. This modification will also be put into the next release of FRAPTRAN so that the user no longer has to supply a water properties file with every run.

## 4.3 TRACE

TRACE was modified to (1) account for the burnup dependent parameters that have an impact on fuel temperatures and consequently stored energy, and (2) to model advanced materials. The modifications made to the code will be presented in the following section, with an analysis of the impacts that the modifications made on the full core study being described in Chapter 5 for the W4LP.

### 4.3.1 Burnup Dependent Parameters

TRACE was modified to be able to model axial variations in fuel and cladding parameters. Rather than using single average or maximum value for rod conditions, axial arrays were implemented for burnup dependent parameters that correspond to the same axial locations used for the heat conduction analysis. A list of the arrays implemented and the input option for turning on these arrays is shown in Table 4.15.

Table 4.15: Additional input options implemented into TRACE

| Namelist Option | Description | Units | Limitations / Default Value |
|---|---|---|---|
| USE_FRPCON_N (Logical) | Input flag to specific whether or not to use axially-dependent arrays from a FRAPCON calculation. When set to .TRUE., axially dependent arrays are required for fuel swelling/densification (ufswell), cladding creep (ucrpdown) and oxide layer thickness (oxlayer). A new input option is also required for relocation (urelo), to be input after the swelling (ufswell) flag. Additional arrays required for each hot rod modeled. | Dimensionless | Default value = .FALSE. |
| USE_Oxide4Temp | Input flag to tell the code whether to axially vary the radial distance of the outermost material of the fuel rod based on the oxide layer thickness (oxlayer) flag. This allows the oxide thickness to act as a thermal barrier in additional to a diffusional barrier. | Dimensionless | Default value = .FALSE. |

In implementing these arrays, several additional modifications were made to better correlate with FRAPCON. The first modification was to implement an additional array for fuel relocation (mentioned in Table 11). FRAPCON-3.5a has a modified relocation correlation over FRAPCON-3.4 (The fuel relocation model in TRACE V5P3 is based off of FRAPCON-3.4's model). Also, the fuel relocation calculated by TRACE is dependent on the current LHGR (the condition being analyzed) which is not necessarily the conditions that existed at BOL for the rod. This is especially important for analyzing a third cycle rod that operated at a high power in its initial cycle, the time at which fuel relocation is expected to occur. By supplying the relocation value calculated by FRAPCON used for the thermal analysis, the relocation correlation from TRACE is overridden. It is also important to note that a constant value for relocation (assuming no recovery) is consistent with FRAPTRAN's assumption that the rapid nature of transients doesn't allow for the recovery of fuel relocation.[K.J. Geelhood, 2011]

The criteria for the values allowed for fuel swelling ($u_{fswell}$), cladding creep ($u_{crpdown}$) and fuel/cladding surface roughness ($rfclad$) needed to be changed to model the conditions at the extremities of the fuel rod. The code will reset the fuel and cladding deformations to 0.0 in locations with high cladding deformation and low swelling. The current criteria (Old Model) and updated criteria (New Model) are shown in Equations 4.5 and 4.6 below, respectively, noting that in the old model inward cladding deformation is input as a negative value and positive outward cladding creep is reset to 0.0.

Old Model: $u_{crpdown} + u_{fswell} + rfclad \geq 0$ 4.5

New Model: $-u_{crpdown} + u_{fswell} + rfclad \leq initial\ gap\ thickness$ 4.6

By resetting the overall deformation to 0.0, the TRACE code has the ability to under-predict fuel temperatures at the extremities of the rod by making the gas-gap smaller than it is in the densification dominated regime. This is illustrated in Figure 4.15 showing the fuel centerline temperatures are various axial distances along the height of the rod. The large differences seen in the temperatures along the majority of the height of the rod are due differences in the burnup values used to calculate the thermal conductivity of the fuel combined with the lack of varying thermal resistance with the oxide layer (described in detail in the following paragraphs). TRACE assumes that all radial nodes have the same burnup whereas FRAPCON performed a more detailed analysis keeping track of the burnup at every radial node. To make the updated criteria in Equation 4.6 have an even greater impact, the values for fuel swelling, relocation, cladding creepdown and oxide layer thickness have been converted to axial arrays rather than singular “rod average” values.

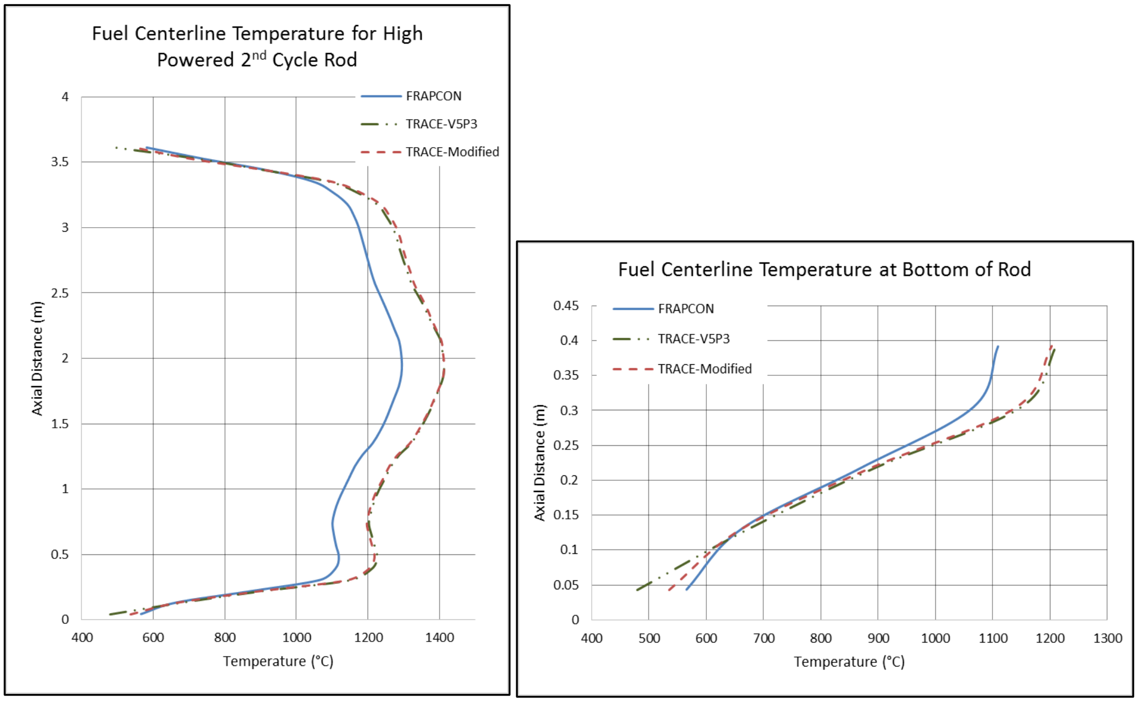

Figure 4.15: Fuel centerline temperature for highest powered second cycle rod using FRAPCON and TRACE

TRACE has two separate uses for oxide layer thickness, one being related to high temperature oxidation and the second being related to a thermal barrier. Increasing the array for oxide layer thickness (*oxlayer*) only established an axial variation in the diffusion impedance in high temperature oxidation calculations. An oxide layer as a thermal barrier requires the input of an additional material ($ZrO_2$) on the outside of the cladding. As with all materials, there is no axial variation of this dimensional value. To overcome this, the code was modified to re-establish a varying axial thickness for the $ZrO_2$ material based on the value supplied by the oxide layer flag. The code was further modified to allow the oxidation calculation to occur within the underlying Zr layer when the outermost material is set to $ZrO_2$ (whereas by default the code will not allow oxidation to occur when the outside material is not Zr). The axial variation in oxide thickness and thermal resistance as calculated by FRAPCON for the highest power second cycle rod is shown in Figure 4.16.

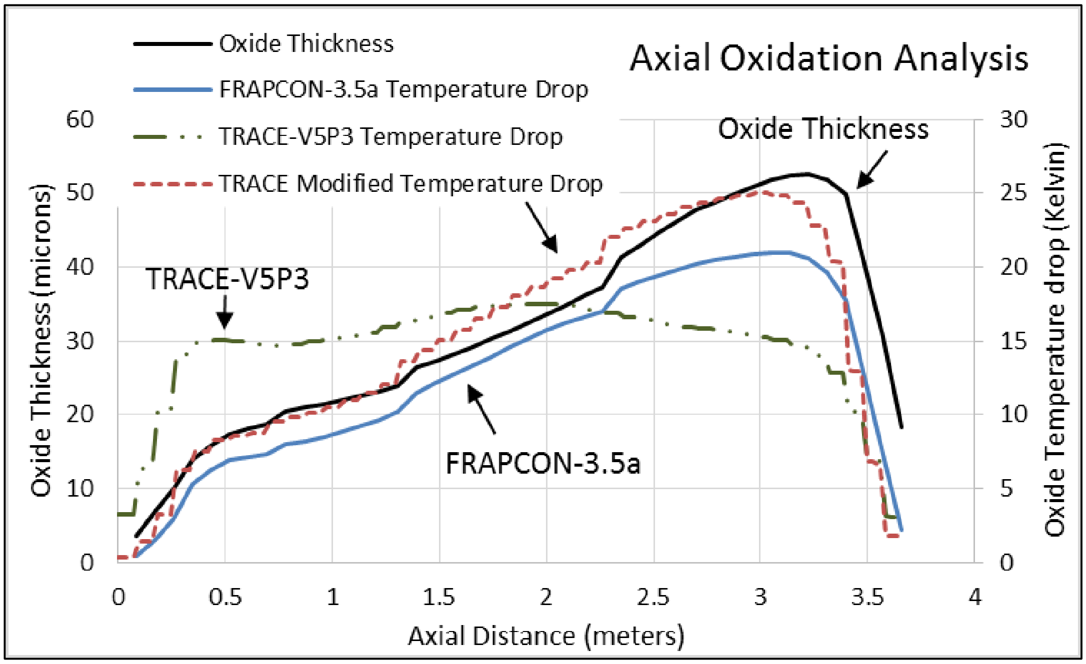

Figure 4.16: Oxidation analysis at EOC using FRAPCON-3.5a, TRACE-V5P3 and modified TRACE (using axial variation in oxide layer thickness)

### 4.3.2 Advanced Materials

TRACE was modified to allow the modeling of advanced fuel and cladding materials, with the new material options shown in Table 4.16. The fuel materials added were UN, UC and $U_3Si_2$; the cladding material added was SiC. For all of the materials, the thermal properties of interest were melting temperature, emissivity, density, specific heat and thermal conductivity. For fuel deformation, the thermal strain is the only mechanism allowing for dimensional changes of the fuel. Fuel swelling and densification are input parameters assumed to be constant during the transient. Although TRACE has a built-in model for fuel relocation, this model was not used due to it being an older model valid only for $UO_2$ fuel. Instead, the relocation values from FRAPCON were used as input parameters, again assumed as constants through the transient.

Table 4.16: Materials added to TRACE

| **Material** | **ID** |
|---|---|
| SiC | 13 |
| $U_3Si_2$ | 14 |
| UC | 15 |
| UN | 16 |

The equations implemented into TRACE for each of the materials are shown in Equations 4.7 – 4.30 for thermal strain ($\varepsilon_{thermal}$), density ($\rho$), specific heat ($c_p$), emissivity ($\varepsilon$), melting temperature ($T_{melt}$) and thermal conductivity ($k$). The temperature dependent equations are either a function of Kelvin ($T_K$) or Celsius ($T_C$).

**Thermal Strain (m/m):**

SiC: If $T_K < 550$ $\varepsilon_{thermal} = \left[2.08 + (4.51e-3 * T_K) - (1.68e-6 * {T_K}^2)\right] * (1.0e-6)$ 4.7(a)

If $550 \leq T_K \leq 1273$ $\varepsilon_{thermal} = \left[-1.8276 + (1.78e-2 * T_K) - \left(1.5544e-5 * {T_K}^2\right) + (4.5246e-9 * {T_K}^3)\right] * (1.0e-6)$ 4.7(b)

If $T_K > 1273$ $\varepsilon_{thermal} = [5.0] * (1.0e-6)$ 4.7(c)

$U_3Si_2$: $\varepsilon_{thermal} = [15.7 - (0.002 * T_K) * (1.0e-6)] * (T_K - 293)$ 4.8

UC: $\varepsilon_{thermal} = [1.007e-5 + (1.17e-9 * T_C)] * (T_C - 20)$ 4.9

UN: $\varepsilon_{thermal} = [7.096e-6 - (1.409e-9 * T_k)] * (T_k)$ 4.10

**Density ($kg/m^3$):**

The density correlation for the materials looks at the change in thermal strain only. All of the fuel materials are assumed to behave isotropically, so the density function for each material is nearly identical with the correlation being based on the material's thermal strain value and theoretical density. For SiC cladding density, a new input value was needed to allow the user to specify the fraction of theoretical density at which the cladding was fabricated. The array for fraction of theoretical density ($ftd$) was expanded to allow the user to supply a second value to represent the fractional theoretical density for the cladding when the namelist flag *CladDen* is set to true.

SiC: $\rho = (3.22e3) * \frac{ftd}{1.0+3*\varepsilon_{thermal}}$ 4.11

U3Si2: $\rho = (12.2e3) * \frac{ftd}{1.0+3*\varepsilon_{thermal}}$ 4.12

UC: $\rho = (13.63e3) * \frac{ftd}{1.0+3*\varepsilon_{thermal}}$ 4.13

UN: $\rho = (14.32e3) * \frac{ftd}{1.0+3*\varepsilon_{thermal}}$ 4.14

**Specific Heat (J/kg*K):**

SiC: $c_p = 925.66 + (0.3772 * T_K) - (7.9259e-5 * {T_K}^2) - \left(\frac{3.1946e7}{{T_K}^2}\right)$ 4.15

U3Si2: $c_p = 199.0 + (0.14 * T_C)$ 4.16

UC: $c_p = 217.8 + (0.03852 * T_K)$ 4.17

UN: $c_p = \frac{1}{0.252} * (54.1 + (2.28e-3 * T_K) + (4.37e-6 * {T_K}^2) - \left(\frac{6.81e5}{{T_K}^2}\right))$ 4.18

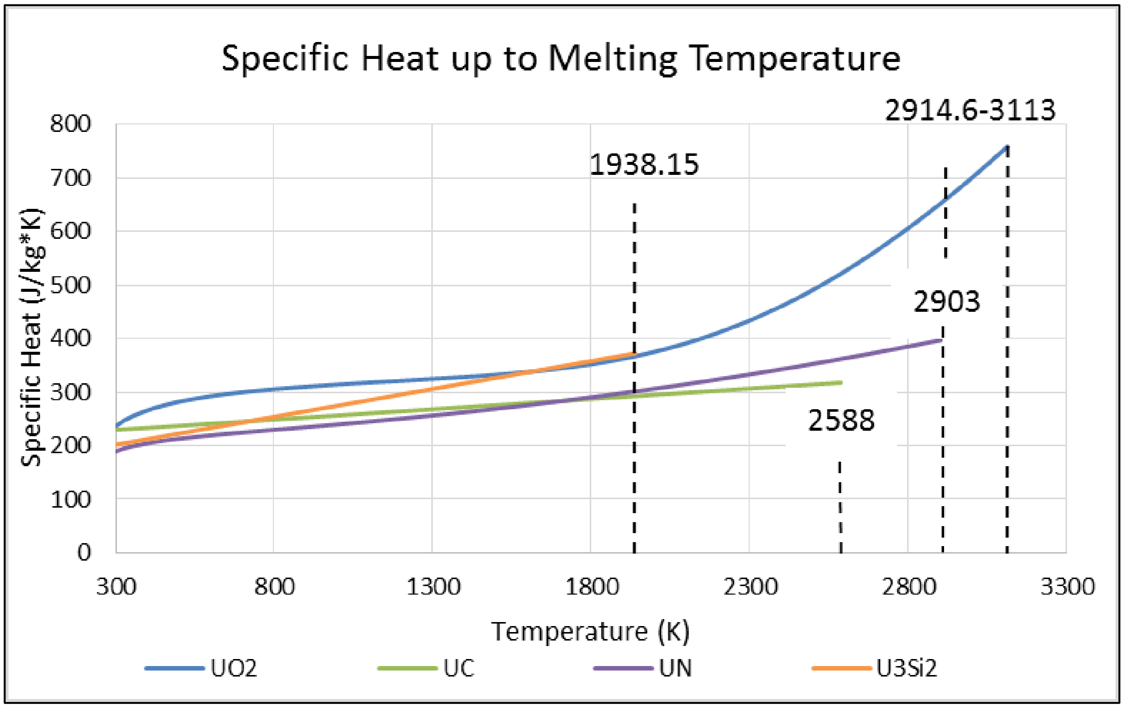

Figure 4.17: Fuel specific heat up to melting temperature

### Emissivity:

SiC: $\varepsilon = 0.8$ 4.19

$U_3Si_2$: $\varepsilon = 0.8707$ 4.20

UC: $\varepsilon = 0.45$ 4.21

UN: $\varepsilon = 0.65$ 4.22

### Melting Temperature (K):

SiC: $T_{melt} = 2900$ 4.23

$U_3Si_2$: $T_{melt} = 1938.15$ 4.24

UC: $T_{melt} = 2588.0$ 4.25

UN: $T_{melt} = 2903.15$ 4.26

### Thermal Conductivity (W/m*K):

SiC: $k = 3.6$ 4.27

$U_3Si_2$: $k = 2.16 + 0.0183 * T_K$ 4.28

UC: If $T_C \leq 500, k = \frac{ftd}{2-ftd} * (20)$ 4.29(a)

If $T_C > 500, k = \frac{ftd}{2-ftd} * (20 + (0.001 * (T_C - 500))$ 4.29(b)

UN: $k = \frac{ftd}{2-ftd} * (1.37 * \left({T_K}^{0.41}\right))$ 4.30

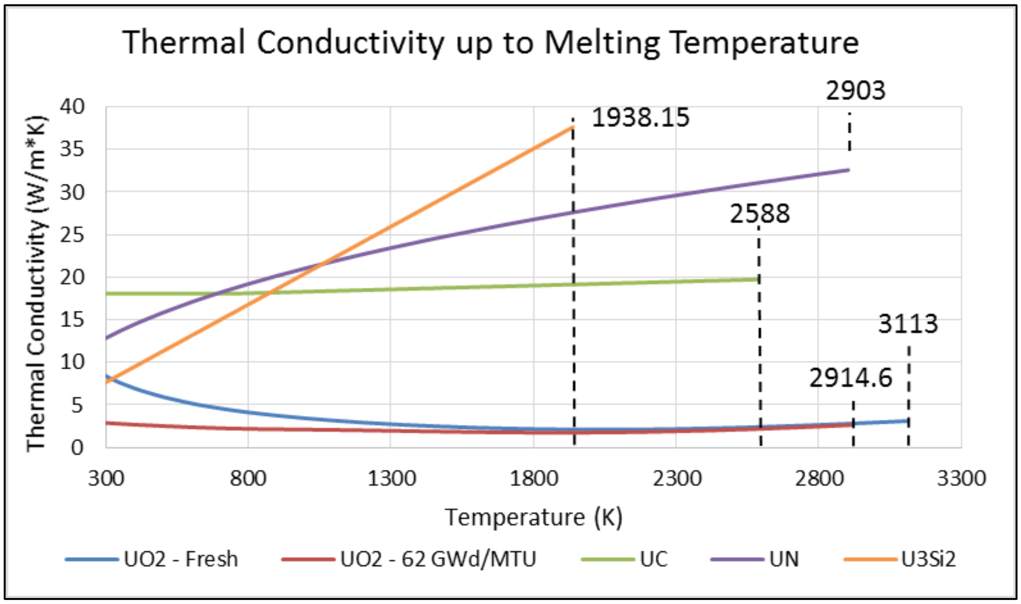

Figure 4.18: Fuel thermal conductivities up to melting temperature

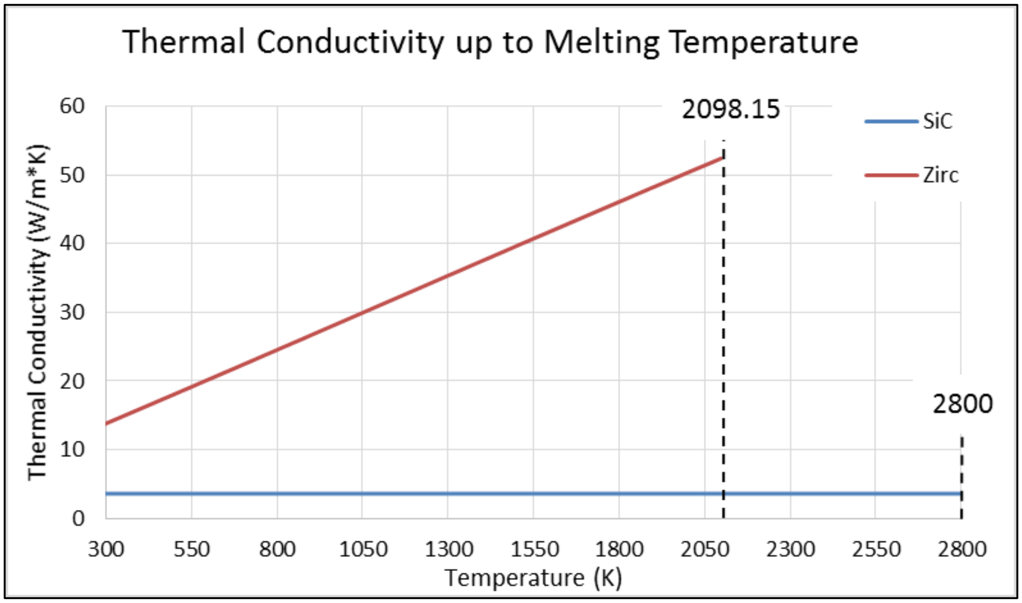

Figure 4.19: Cladding thermal conductivities up to melting temperature

**Gap Conductance**

The contact heat transfer coefficient (only calculated when fuel/cladding contact occurs) is calculated based on the relative ratio of interfacial pressure to cladding Meyer hardness. In TRACE, the Meyer hardness value is assumed constant at 680 MPa. This is nearly consistent with FRAPCON's correlation, albeit lower at higher cladding temperatures due to FRAPCON's correlation being dependent on cladding temperature. With SiC being a ceramic, the as-fabricated cladding density plays a role in determining the Meyer hardness value. The Meyer hardness equation used is shown in Equation 4.31. A comparison of the Meyer hardness values in shown in Figure 4.20.

SiC: $MeyerHardness = 27.7E9 * e^{-5.4*(ftd)}$ 4.31

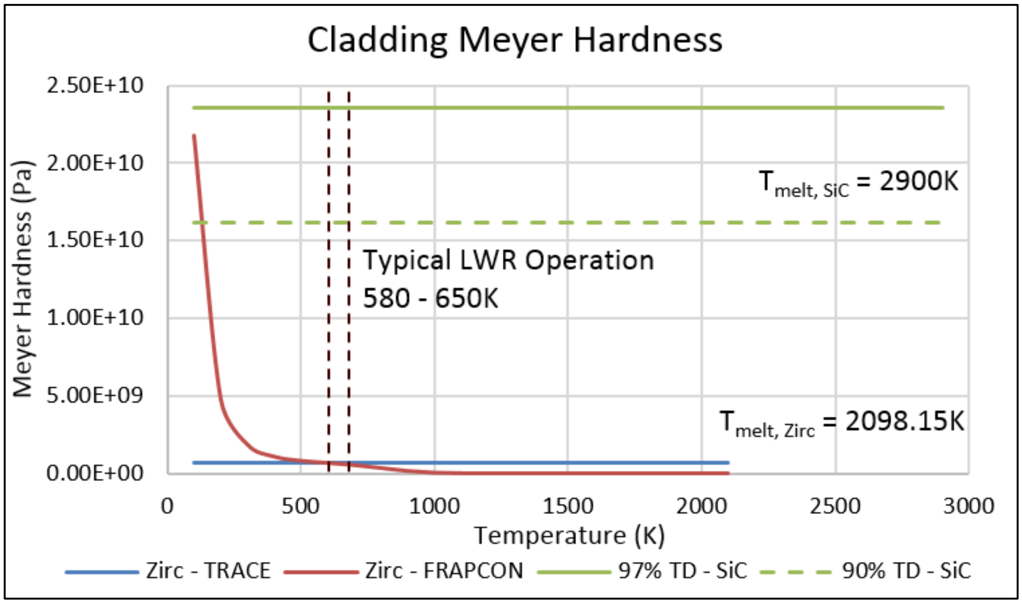

Figure 4.20: Cladding Meyer hardness values

The cladding modifications in addition to the equations previously mentioned were specific to the cladding deformation and failure analysis. The cladding deformation mechanisms used in the transient analysis include thermal expansion (the thermal strain is shown above), elastic deformation and cladding permanent deformation. Cladding creep is ignored in TRACE due to the assumption that the duration of the transient analysis is too short for creep to be of any significance (the same assumption that is made by FRAPTRAN). For the elastic deformation, the cladding material properties needed are Poisson's ratio and Young's Modulus (Equations 4.32 and 4.33, respectively). The hoop

($\sigma_h$) and axial ($\sigma_z$) stresses are based on the cladding dimensions and pressure differential across the cladding. The elastic deformation is shown in Equation 4.34.

**Elastic Deformation (SiC Only):**

Poisson's Ratio: $\upsilon = 0.21$ 4.32

Young's Modulus (GPa): $E = \left[460 - 0.04 * T_K * e^{-962/T_K}\right] * \left[1 - 0.4 * \left(1 - e^{-0.15*dpa}\right)\right]$ 4.33

Elastic deformation: $u_e = r_{cm} * \frac{\sigma_h - (\upsilon * \sigma_z)}{E}$ 4.34

The cladding failure model is based on Zircaloy failure, in which significant plastic strains can be achieved at sufficiently high temperatures. This can lead to cladding ballooning, causing flow blockage and a change in the coolability of the fuel rod. However, with SiC it is expected to have a brittle fracture mechanism and therefore the plastic deformation is turned off. As for cladding oxidation, the oxidation models will be turned off. The justification for this approach is that the studies performed for the three US plants with Zircaloy cladding have shown the PCTs are below the range in which any significant oxidation of SiC will occur. With the advanced fuels, due to the decrease in stored energy it is expected that the PCTs will be lower than with typical $UO_2$. This will be further explored in Chapter 5.

# CHAPTER 5

## RESULTS

The steady-state and transient analysis of the three reactor types modeled in this study are described in this chapter. The Final Safety Analysis Report (FSAR), combined with reload licensing reports when available, were used to reconstruct the core power and core power history. Variations in available data for each plant design required different techniques for establishing the burnup profile of the rods modeled from previous cycles. The rods were modeled using data available in the FSAR and Mechanical Design Reports. The results were published in references *Predictions of Fuel Dispersal during a LOCA* (Proceedings of TopFuel 2014) and *Best Estimate Core-wide Fuel Rod Failure and Dispersal Analysis for Typical US LWR Designs under LOCA Scenarios* (Journal of Nuclear Material). [P. Raynaud, 2014; Ian Porter, 2014]. The full core impacts of the modifications mentioned in Chapter 4 will be presented for the W4LP plant. The W4LP will be further analyzed using several advanced fuel designs, comparing the reactor conditions and fuel rod failures to the current $UO_2$/Zircaloy fuel design. These results were submitted to Progress in Nuclear Energy with the title *Advanced Fuel Design and Analysis for W4LP under Steady-State and Transient Conditions*.

## 5.1 WESTINGHOUSE 4-LOOP PWR

### 5.1.1 Steady-State Analysis

The available data in the FSAR for the W4LP was the assembly-average radial peaking factors at BOC, MOC & EOC. Linear interpolation was performed for establishing the power at times in between. Per FRAPCON recommendations, the timesteps were kept below 50 days.[K.J. Geelhood, 2011] A shuffling scheme was developed to re-create the power histories for the 2nd and 3rd cycle rods for the previous cycle(s), assuming that the core was at equilibrium conditions during those cycles. With core symmetry, there were a total of 47 different assembly-average powers (18-1st cycle, 22-2nd cycle and 7-3rd cycle) in the available FSAR data that resulted in a total of 55 power histories (18-1st cycle, 26-2nd cycle and 11-3rd cycle) to represent the core. The 55 power histories were developed to maximize the core average discharge burnup to 54.5 GWd/MTU while maintaining the assembly average discharge below ~62 GWd/MTU. The assembly-average powers are shown in Figure 5.1.

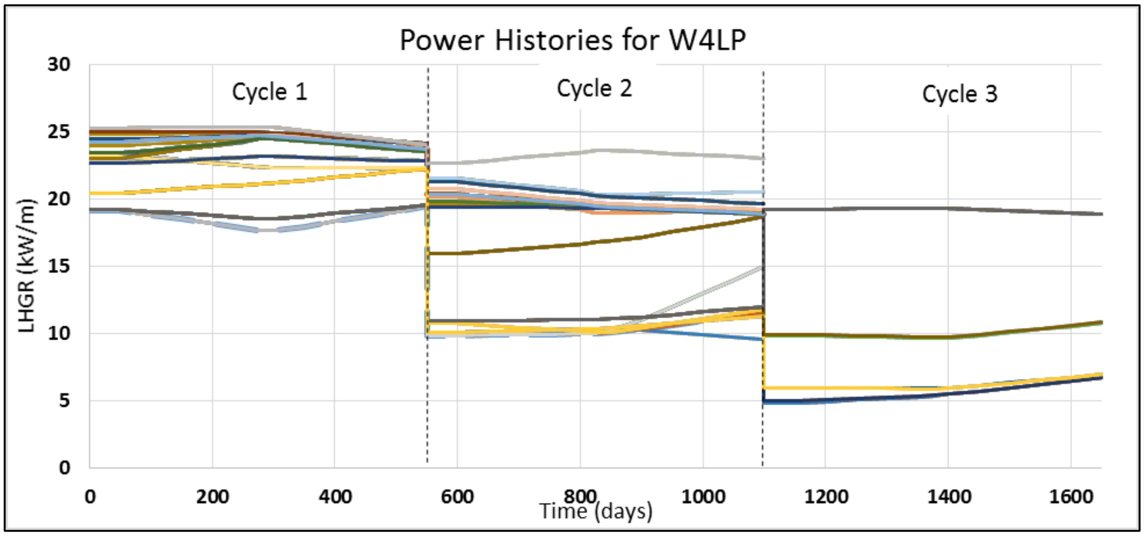

Figure 5.1: Assembly average power history for W4LP

The FRAPCON analysis resulted in a total of 248 runs representing 193 assemblies, the additional runs being due to the required division of some assemblies for the TRACE modeling within the VESSEL component. Although core symmetry existed from a power stand-point, no two runs were identical due coolant variations as a result of using the coolant conditions calculated by TRACE. The core power map at BOC and EOC is shown in Figure 5.2, noting the inward power shift towards EOC with a flatter radial power profile.


(a) (b)

Figure 5.2: Core radial power profile at (a) BOC and (b) EOC

### 5.1.2 Initial Condition Analysis

The results of the steady-state analysis that were of most importance as initial conditions to the transient study included cladding corrosion, internal rod pressure, and fuel stored energy. Each of these parameters were shown to be influenced by the coolant conditions used to model the core. Using FRAPCON's default model, the high power rods, typically 1st and 2nd cycle rods located closer to the center of the core, tended to predict coolant temperatures higher than those predicted by TRACE. Alternatively, the low power rods, which are typically the third cycle rods location in the periphery of the core, tend to predict bulk coolant temperatures much lower than temperatures predicted by TRACE. Understanding that TRACE is not a sub-channel analysis code and might not accurately predict the coolant temperatures at all fuel locations within the assembly, it was shown that the influence of adjacent fuel assemblies can cause the bulk coolant temperature to be higher than what is expected when analyzing a low power assembly by itself. With the modifications made to the FRAPCON described in the previous chapter, the steady-state analysis was compared to using the built-in models. The EOC differences in gap gas pressure and cladding oxidation due to the different modeling parameters are shown in Table 5.1.

Table 5.1: Largest W4LP EOC core-wide differences in gap gas pressure and oxide layer thickness using FRAPCON's default model and TRACE coolant conditions

| W4LP | Average Oxide Layer Thickness (µm) | | | Gap Gas Pressure (MPa) | | |
|---|---|---|---|---|---|---|
| Cycle | FRAPCON | TRACE Coolant Conditions | % Diff | FRAPCON | TRACE Coolant Conditions | % Diff |
| 3 | 25.96 | 27.47 | -5.80% | 8.966 | 9.219 | -2.83%* |
| 2 | 42.59 | 31.58 | 25.85% | 18.477 | 15.271 | 17.35%** |
| 3 | 22.2 | 25.4 | -14.40%* | 8.757 | 8.963 | -2.34% |
| 1 | 15.22 | 10.16 | 33.22%** | 9.402 | 9.199 | 2.16% |

* Fuel rod with largest difference calculated by FRAPCON's default models
** Fuel rod with largest difference calculated using TRACE coolant conditions

The core average cladding oxide thickness at EOC decreased from 25.3µm to 21.0µm using the coolant conditions supplied by TRACE. The corresponding resulting core average ECR decreased from 4.42% to 3.67%. The maximum rod average ECR decreased from 7.45% to 7.04%.

For the core average at EOC, there was a net decrease in internal rod pressure of 1.72% with the improved analysis from 10.03MPa to 9.82 MPa. The high power second cycle rods with a burnup of > 40 GWd/MTU were shown to have the largest decrease in internal rod pressure, by as much as 17.4%. The reason for this is due to the Modified Forsberg-Massih model used for fission gas release. The model utilizes a burnup influence after 40 GWd/MTU, where the influence of fuel temperature (accounted for in the diffusion coefficient) is the driving force for the difference in FGR. The low-power third cycle rods saw an increase in internal rod pressure of up to 2.83% due to the increased coolant (and subsequently, gas-gap) temperatures, a result of the influence of neighboring assemblies in the core.

The stored energy retained within the fuel (along with decay heat) can be a major driving force for PCT. Although the core power is constant throughout the cycle, the fuel stored energy varies due to changes in power distribution, fuel thermal degradation due to burnup and changes in gap conductance. A schematic of the fuel stored energy in the core at BOC and EOC is shown in Figure 5.3.


(a) (b)

Figure 5.3: Fuel stored energy at (a) BOC and (b) EOC

As seen in Figure 5.3, the fuel stored energy shifts from being dominated by the fresh fuel rods at BOC (due to the large gap size) to a flat distribution at EOC. For comparison purposes, the stored energy calculated using the original and updated FRAPCON analysis, as well as the TRACE calculation, is shown in Table 5.3. The stored energy calculated by TRACE is the only calculation that has an impact in the transient analysis, as the coolant temperatures calculated by TRACE (as a direct result of the stored energy and decay heat) are used as the boundary conditions for the FRAPTRAN analysis. Table 5.2 shows that by using the updated FRAPCON analysis, the stored energy in the core decreased by 8.9%, 6.86% and 7.21% at BOC, MOC and EOC conditions, respectively. However, the TRACE calculation shows that it provides a more conservative result than either way of performing the steady-state FRAPCON analysis due to the increase in fuel stored energy at the onset on the transient. This is caused by both TRACE's inability to match fuel temperatures to FRAPCON (even with the axial modifications mentioned in Chapter 4) due to differences in radial fuel dimensional changes and burnup, as well as differences in the specific heat correlations between the codes.

Table 5.2: Stored energy as calculated by (1) FRAPCON's default models, (2) the updated FRAPCON analysis using TRACE coolant conditions, (3) TRACE with the updated FRAPCON's ICs, (4) TRACE using FRAPCON's enthalpy correlation

| Total Stored Energy in fuel (J) | | | |
|---|---|---|---|
| | BOC | MOC | EOC |
| FRAPCON Original | 1.797E+10 | 1.685E+10 | 1.780E+10 |
| FRAPCON Updated | 1.637E+10 | 1.569E+10 | 1.652E+10 |
| TRACE-V5P3 | 1.887E+10 | 1.870E+10 | 1.977E+10 |
| TRACE-Modified* | 1.710E+10 | 1.650E+10 | 1.727E+10 |

* TRACE calculation using FRAPCON enthalpy correlation

The overall perspective on the initial state of the reactor core is that the rods that are most likely to rupture (high powered 1st and 2nd cycle) are in an improved state using the updated analysis than using the default FRAPCON analysis. The improved state indicates that the conditions are less favorable for rod rupture, largely due to the lower internal rod pressure. With a lower internal rod pressure, the cladding temperature must be hotter to reach the instability strain required for fuel rod ballooning and rupture. As for fuel rod LOCA licensing criteria, the lower oxidation thickness and cladding hydrogen uptake also allow the rod to remain at high temperature for longer (or to achieve higher temperature) before exceeding the licensing ductility requirements. However, if the coolant conditions are severe enough to allow all of the rods to reach the Zirconium alpha to beta transition temperature (~800°C), worse results could be expected with the high burnup 3rd cycle rods. Due to fuel particle size being highly dependent on burnup, the high burnup rods are of the most concern for FFRD.

### 5.1.3 Transient Analysis

The transient analyzed with the W4LP was a double-ended guillotine cold leg break LBLOCA at BOC, MOC and EOC. As shown in Figure 5.4, the PCT was 1110K at BOC, 1090K at MOC and 1095K at EOC.

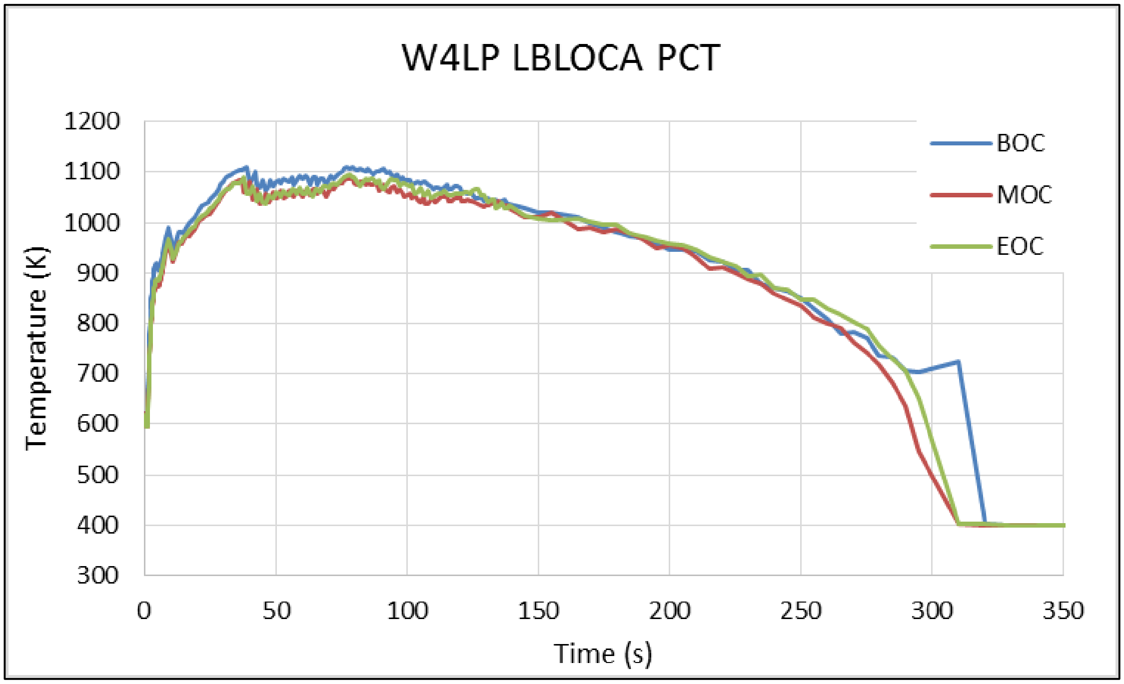

Figure 5.4: Peak cladding temperature for W4LP under LBLOCA accident conditions

Immediately after reactor scram, the peak cladding temperatures drop by ~20K within 0.2 seconds and are down to ~596K at 0.8 seconds due to the sharp drop in rod power. However, by 1 second there is a rapid shift in temperatures and the cladding rapidly heats up. For the BOC case, the instantaneous cladding heating rate is as high as 334.7K/s, allowing the cladding to change from 596.9K to over 900K in 2.5s. The cladding heat rates are shown in Figure 5.5, where negative heating rates are indicative of cladding being cooled and positive heating rates show cladding heating up.

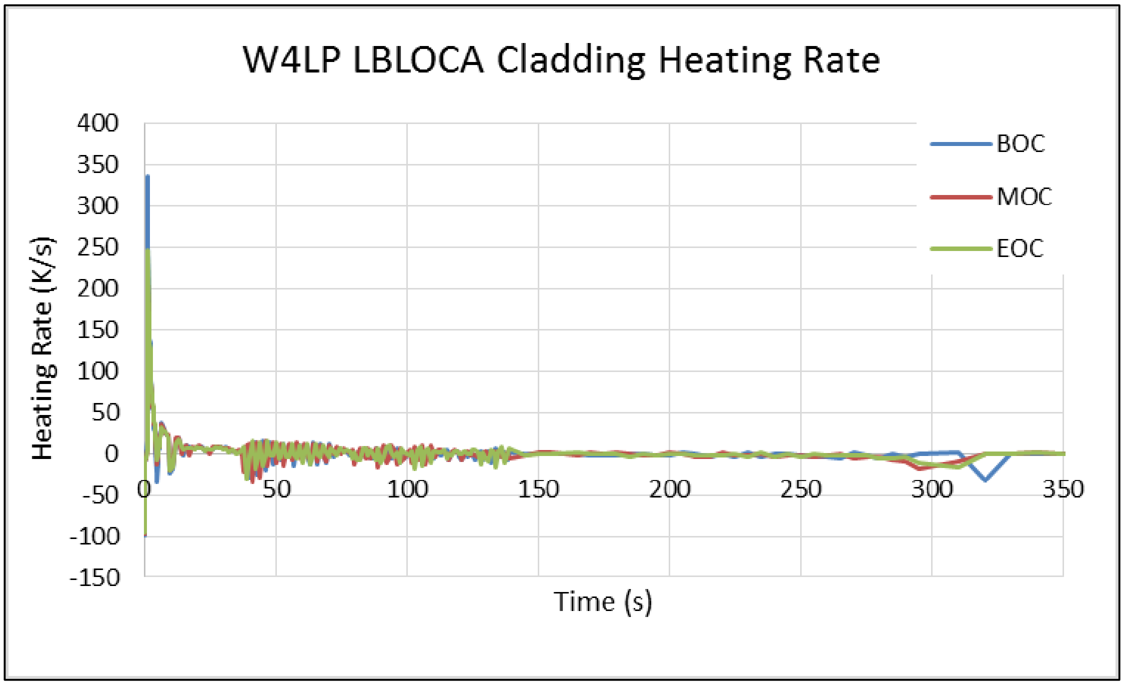

Figure 5.5: Cladding heating rates for W4LP LBLOCA

The highest PCT occurring for the BOC analysis is due to a combination of (1) having nearly the most stored energy (it is very close with EOC conditions) and (2) having the highest powered rods at BOC. Due to the rapid depressurization and coolant temperature drop, a positive reactivity is introduced and a slight power spike occurs, as illustrated in Figure 5.6. Due to the rods having the highest power at BOC, the power spike helps overcome the slight decline in stored energy compared to EOC. Also shown in Figure 5.6 is the strong influence of stored energy during the LBLOCA. At 10s, the total power transferred to the coolant comes from the stored energy that is removed is 2.78 times greater than the sum of the power generated from decay and fission. At this time, no energy has been generated from the metal-water reaction, leaving the difference due to the stored energy being removed from the fuel rods alone.

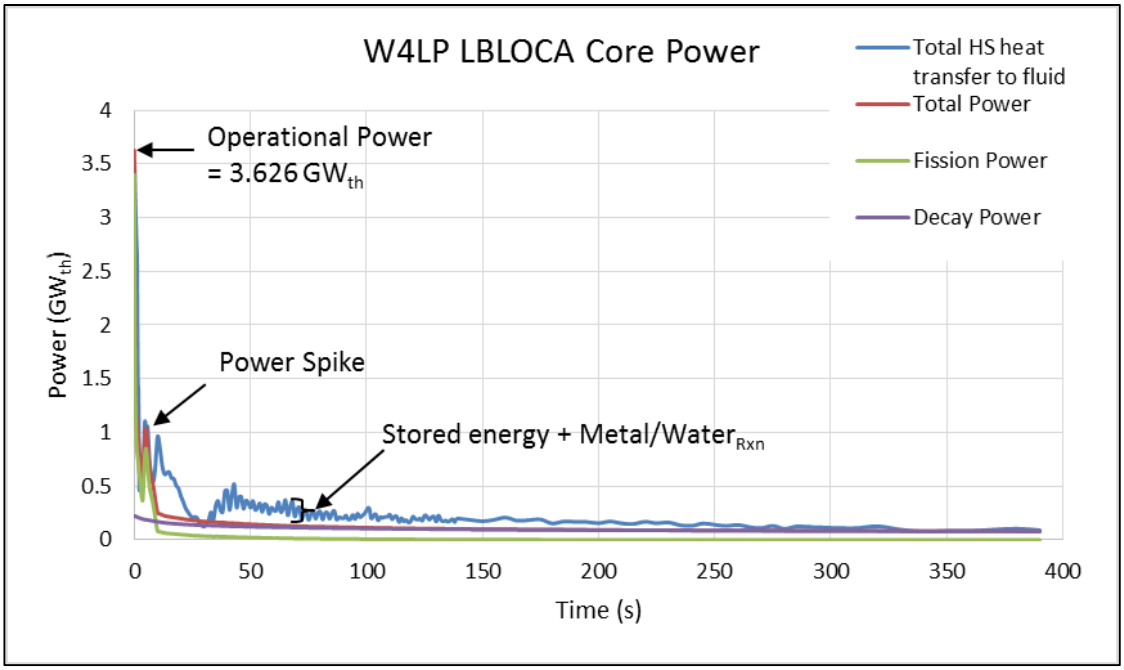

Figure 5.6: W4LP core power and fuel rod (HS) heat transfer to fluid during LBLOCA

Starting at 29s, the cladding begins to react with the high temperature steam. The oxidation reaction was modeled using the less conservative Cathcart/Pawel model (compared to Baker/Just model) which begins when the cladding reaches 1073K. The additional energy source term associated with the exothermic reaction further drives the cladding temperatures, as well as produces hydrogen. However, the fraction of cladding at which the temperature is above 1073K is limited, even for the hottest assembly. The energy source term and hydrogen produced are shown in Figure 5.7 for the hottest rod. Due to the short duration of time the cladding spent oxidizing, the energy generated from this reaction is rather small

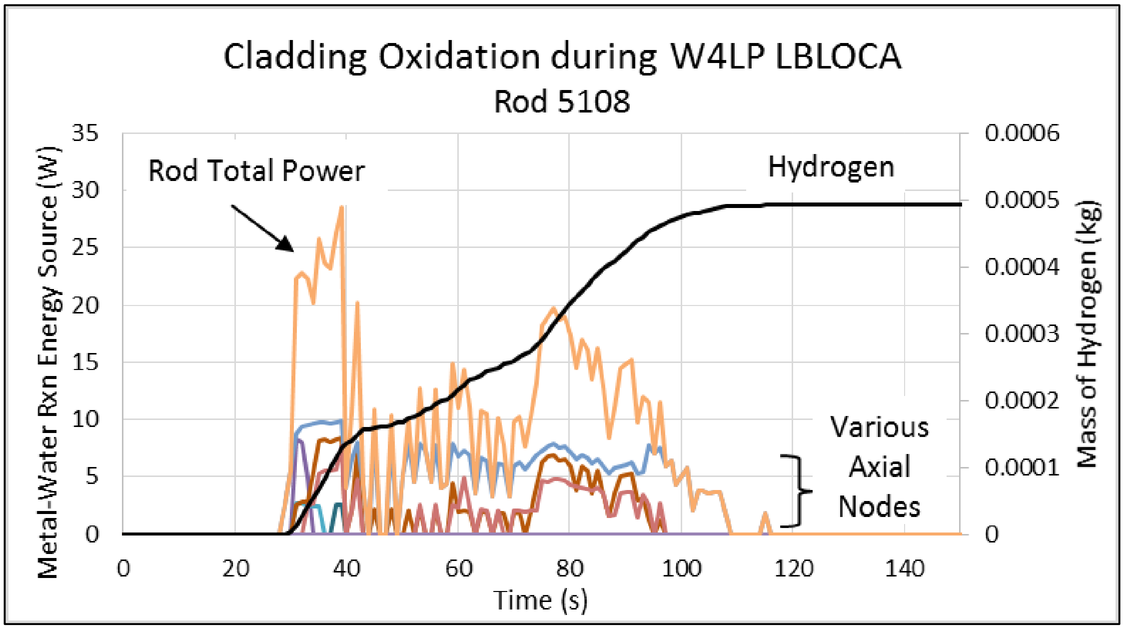

Figure 5.7: Cladding oxidation and hydrogen generation for PCT rod during LBLOCA

The time at which significant oxidation occurs (~30s) is equivalent to when the core liquid volume fraction approaches 0. At this point, there is minimal heat removal capability, resulting in both the fuel and cladding boundary conditions consisting of doubled sided insulating boundaries. The fuel and cladding continue to heat up due to the power from decay heat and cladding oxidation with no way to remove the heat. The heat removal for the hot rod is shown in Figure 5.8.

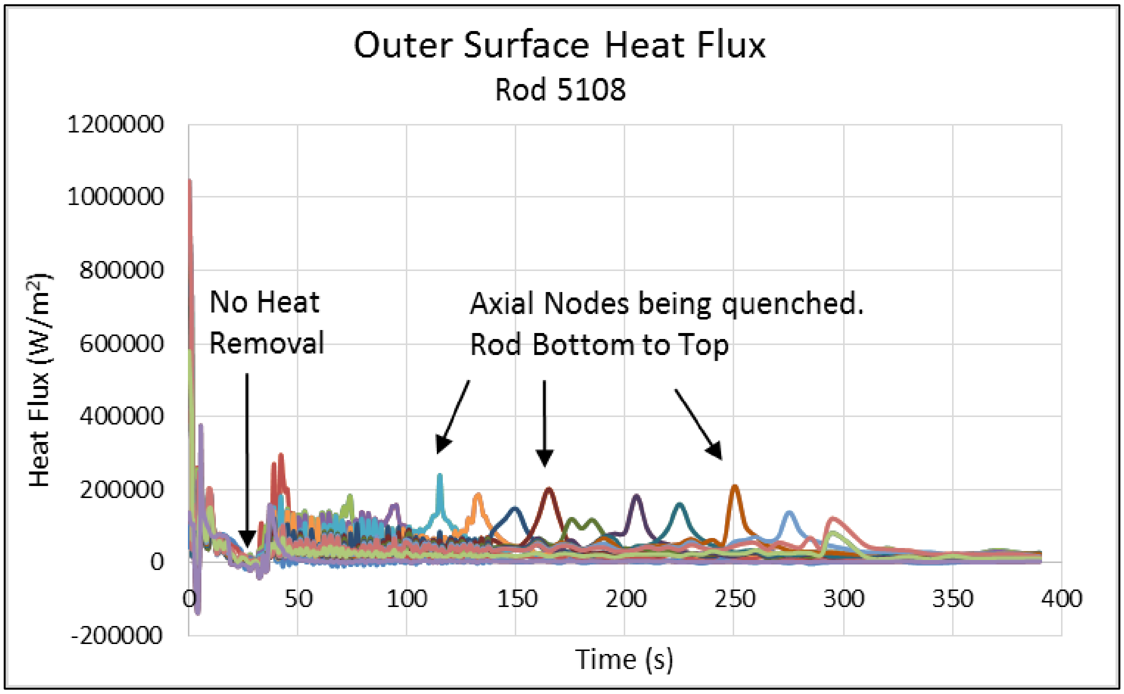

Figure 5.8: Outer surface heat flux for hottest rod in W4LP LBLOCA at EOC

At this point in the transient, the stored energy from operation is not a driving force in further heating of the cladding, as the cladding temperature has exceeded the minimal fuel temperature that was reached at ~16s. If no decay power and cladding oxidation existed, then the cladding could only heat up to a temperature at which the energy is balanced between the fuel and cladding. However, the fuel temperatures continue to increase from a peak centerline temperature low of 1039K at 16s up to a maximum of 1169K at 44ss, further heating the cladding. The fuel centerline and cladding surface temperatures are shown in Figure 5.9. Each line in the cladding graph that has a sharp vertical drop to 390K is showing an axial node that is quenched (from bottom to top), with the bottom node quenched at ~40s and the top node being quenched at ~300s.

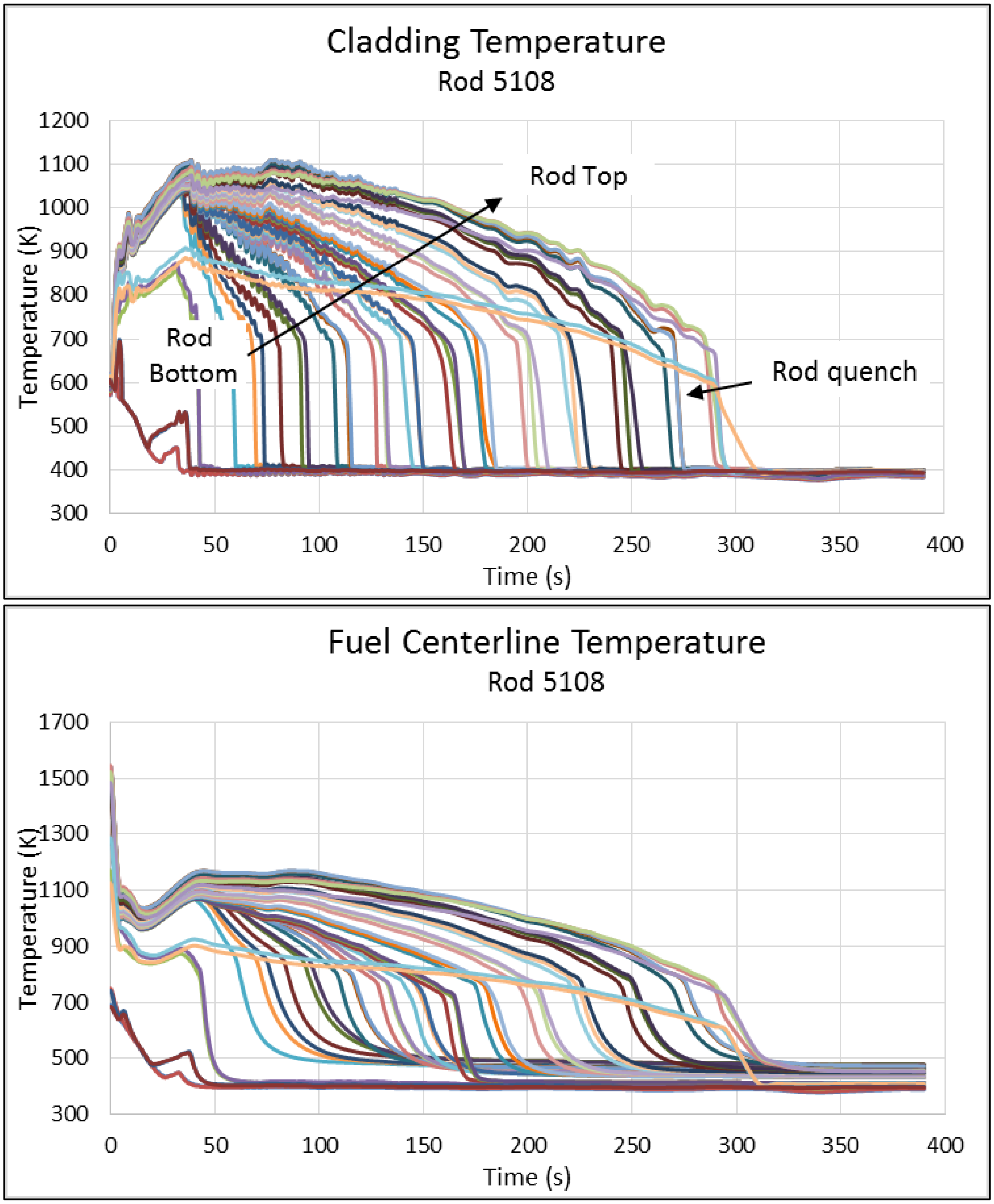

Figure 5.9 Cladding outer surface temperature for hottest rod in W4LP LBLOCA at EOC

After discussions with Stephen Bajorek, the Senior Technical Advisor for T/H in the NRC's Office of Nuclear Regulatory Research, it was decided to not allow fuel rod failure during the TRACE analysis. If TRACE predicts failure before FRAPTRAN, then the fuel would be cooled more rapidly and earlier, potentially leading to under-predictions of fuel rod failure. Additionally, plastic deformation of the cladding before rupture will lead to an increased surface area for heat removal, and if this is predicted earlier in TRACE (which has been shown) then the FRAPTRAN results will be affected. The fuel failure and dispersal analysis will be calculated using the FRAPTRAN analysis with the coolant conditions predicted by TRACE.

### 5.1.4 Fuel Dispersal Analysis

With the cladding temperatures in each case reaching over 1000K, the FRAPTRAN analysis was performed due to the expectation of fuel rod failure under these conditions. With the scope of the analysis focused on realistic conditions, the nominal ECCS plant response (2 trains of ECCS available) conditions were analyzed at BOC, MOC and EOC. The variations in fuel rod conditions, due to both the steady-state analysis and the transient response, are expected to have an impact on the quantity of fuel dispersed. The first requirement for FFRD is that the cladding must have failed. The number of rods failed at each cycle time is shown in Table 5.3. The number of rods failed was calculated using the NRC's FRAPTRAN-1.5 for all three cycle times and at EOC using the modification to fix cladding displacement in restart file (FRAPTRAN-1.5-Mod1) and the modification to use permanent cladding strain in FRAPTRAN (FRAPTRAN-1.5-Mod2). The results calculated at EOC for the three code versions are as expected. Using a larger cladding strain in FRAPTRAN-1.5 reduces the void volume, thus increasing rod pressure and likelihood of rod failure. The results using Mod1 and Mod2 are very similar due to the permanent radial inward displacement of the cladding being synonymous to the cladding permanent strain values. Unless noted otherwise, the results discussed were calculated using the official version of FRAPTRAN-1.5.

Table 5.3: Number of failed rods in W4LP core under LBLOCA at BOC, MOC and EOC

| | W4LP 2 Trains of ECCS Rod Bursts | | | |
|---|---|---|---|---|
| | Cycle Time | BOC | MOC | EOC |
| FRAPTRAN-1.5 | # Rods Ruptured | 21252 | 21252 | 26928 |
| | % of Core | 41.70% | 41.70% | 52.85% |
| FRAPTRAN-1.5-Mod1 | # Rods Ruptured | - | - | 25740 |
| | % of Core | - | - | 50.52% |
| FRAPTRAN-1.5-Mod2 | # Rods Ruptured | - | - | 25476 |
| | % of Core | - | - | 50% |

The total number of failure rods being larger at EOC than at BOC is due to the increase in internal rod pressure. The differences in PCT are only ~15K lower at EOC than at BOC but the internal rod pressure is considerably higher, especially with high powered 2nd and 3rd cycle rods that have undergone a large amount of fission gas release after ~45 GWd/MTU. The fuel rod rupture map at the three cycle times is shown in Figure 5.10. The ruptures for the BOC and MOC analysis are confined to the inner vessel ring, whereas in the EOC analysis all of the rods in the inner ring and some rods in the outer ring also failed.

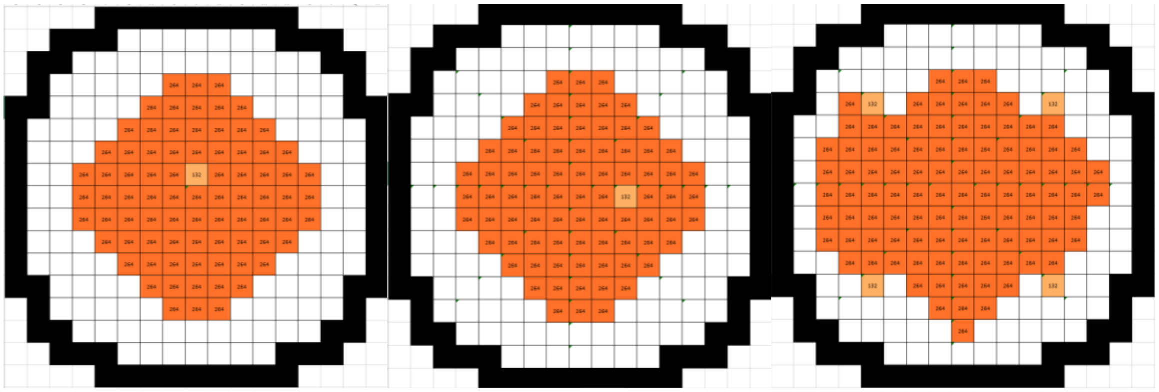
(a) (b) (c)

Figure 5.10: Core wide fuel rod rupture consensus at (a) BOC, (b) MOC and (c) EOC

Once the rod has been determined to have failed, the next criteria analyzed is the cladding strain at failure for both the failure node and the nodes above and below the failure location. The cladding permanent plastic hoop strain calculated by FRAPTRAN is extracted for every rod analyzed at every axial location.  The time at which the node fails and the strain at failure is also extracted and is shown in Figure 5.11.

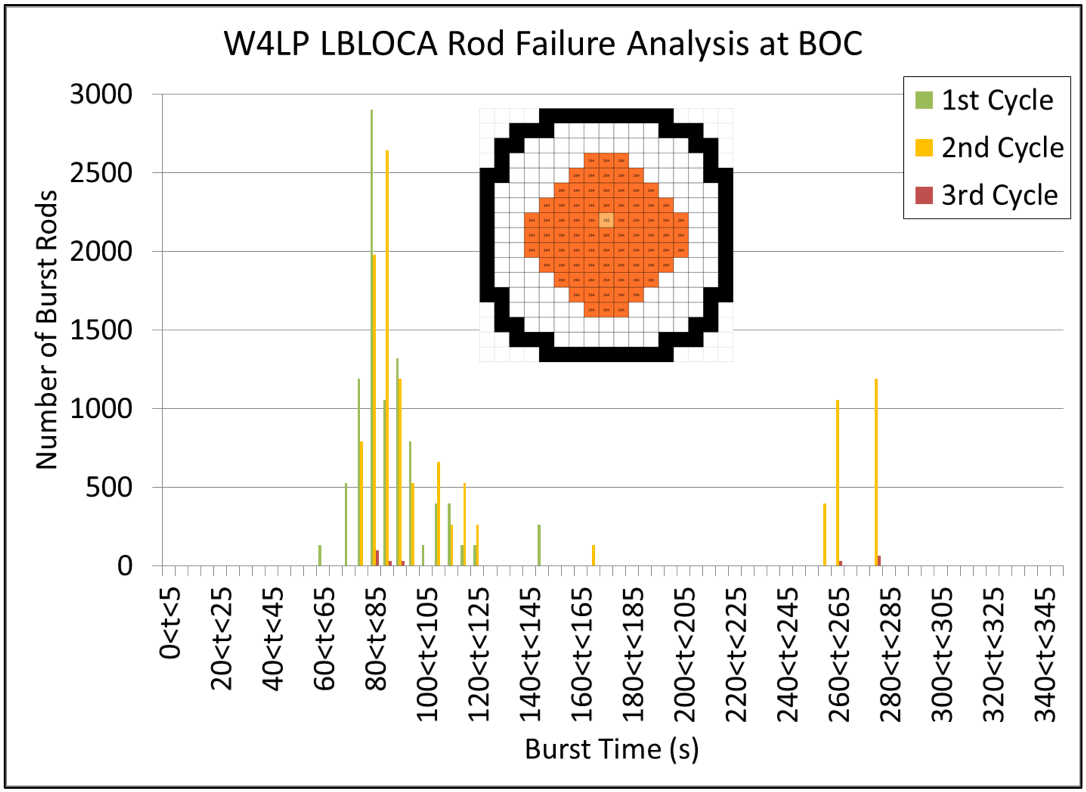

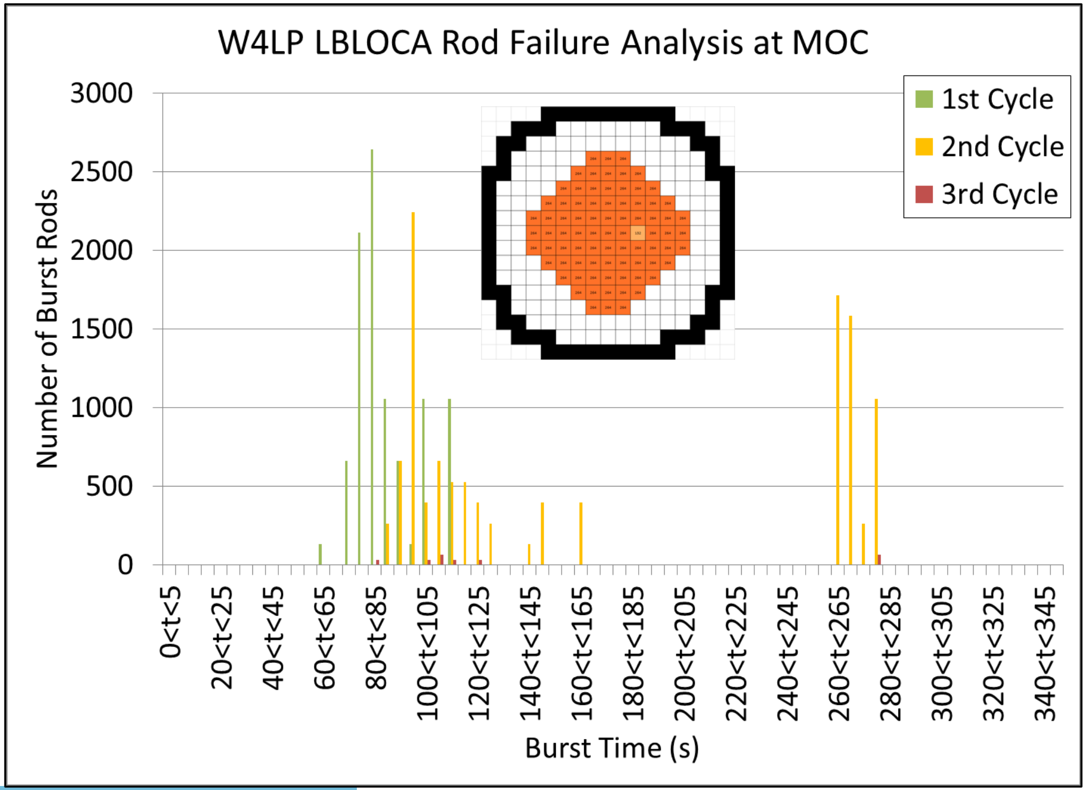

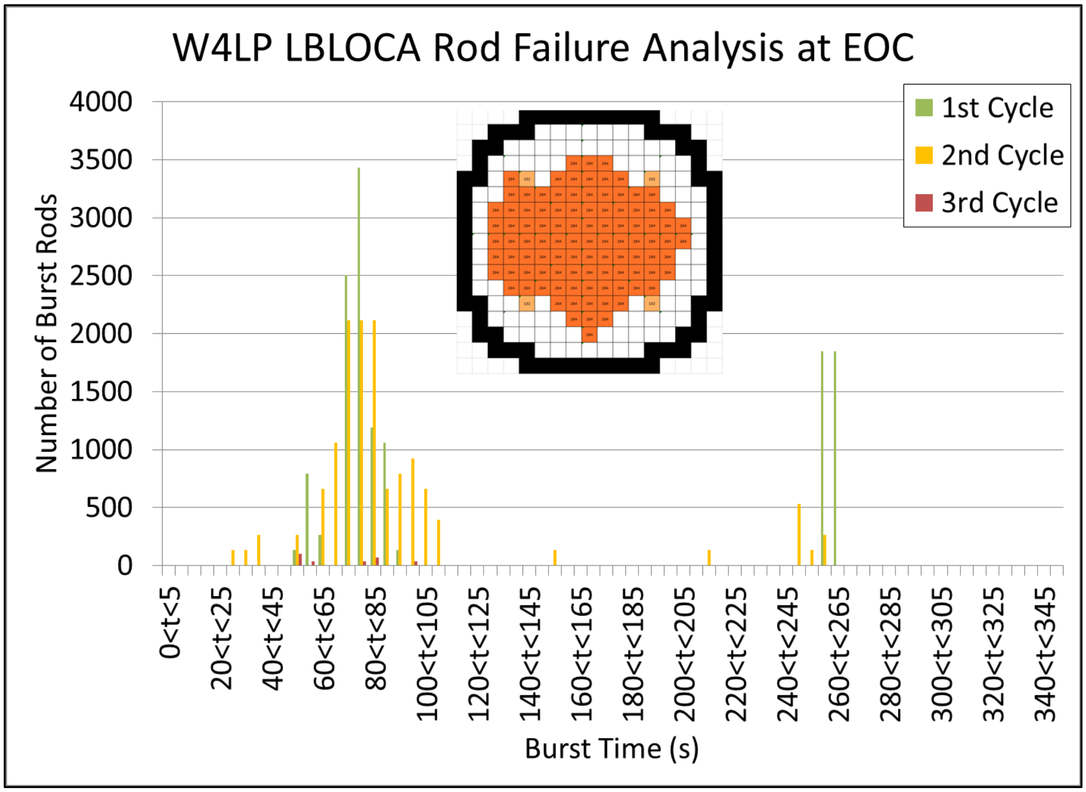

Figure 5.11: Fuel rod failure times for W4LP LBLOCA at BOC, MOC and EOC

There are two distinct regions of fuel rod failure times, the first being between 60 ~ 150 seconds and the second being 250 ~ 285 seconds. In the first region, the cladding temperatures remained near their peak temperature for an extended period of time. At BOC and MOC, the 1st cycle rods have the most stored energy and decay heat (due to the higher operating power) and all fail within this time, along with the majority of the 2nd cycle rods also failing during this time. At EOC, the rods typically rupture earlier than at BOC despite the lower cladding temperature. This is due to the increased internal rod pressure requiring a lower cladding temperature for failure. The average ballooning strain of the rods during the first region was typically ~38%, which indicates that rod-to-rod contact was predicted to occur. The second region of rod failure is during the quench, in which the average ballooning strain was in the 5-15% range. The cladding strain at failure is shown in Figure 5.12 for the EOC analysis.

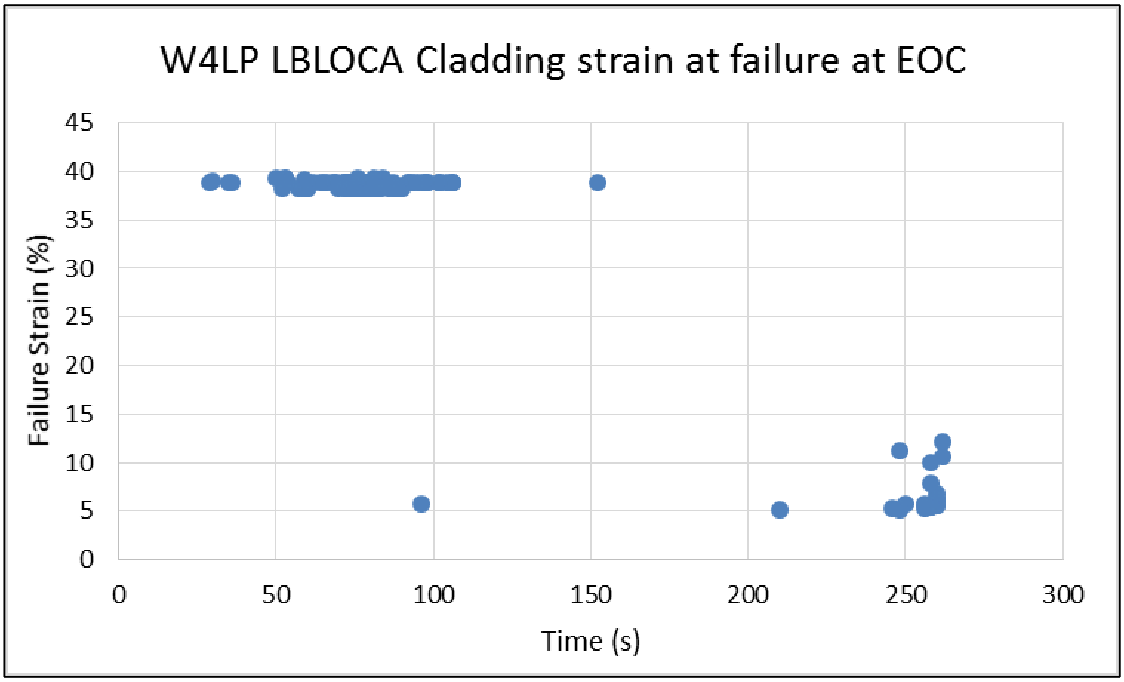

Figure 5.12: Cladding failure strain versus failure time for W4LP LBLOCA at EOC

The ballooning strain for each fuel type at each cycle time analyzed is shown in Figure 5.13. It is important to understand which rods are capable of achieving high cladding strains for determining the potential dispersal quantity. The fuel particle size is based on burnup, with higher burnup fuel having a smaller particle size distribution. It is therefore important to understand which rods (i.e. fresh fuel rods or rods in the core for long periods of time) are bursting and at what strains. The cladding strain determines whether or not the fuel is axially mobile, with higher cladding strains allowing for axial fuel mobility and the potential for dispersal. High burnup, high strain fuel rods will produce very different quantities of dispersed fuel compared to low strain, low burnup rods. This study takes this analysis one step further by analyzing within the cycle at different times in order to assess the fuel under various power and burnup conditions.

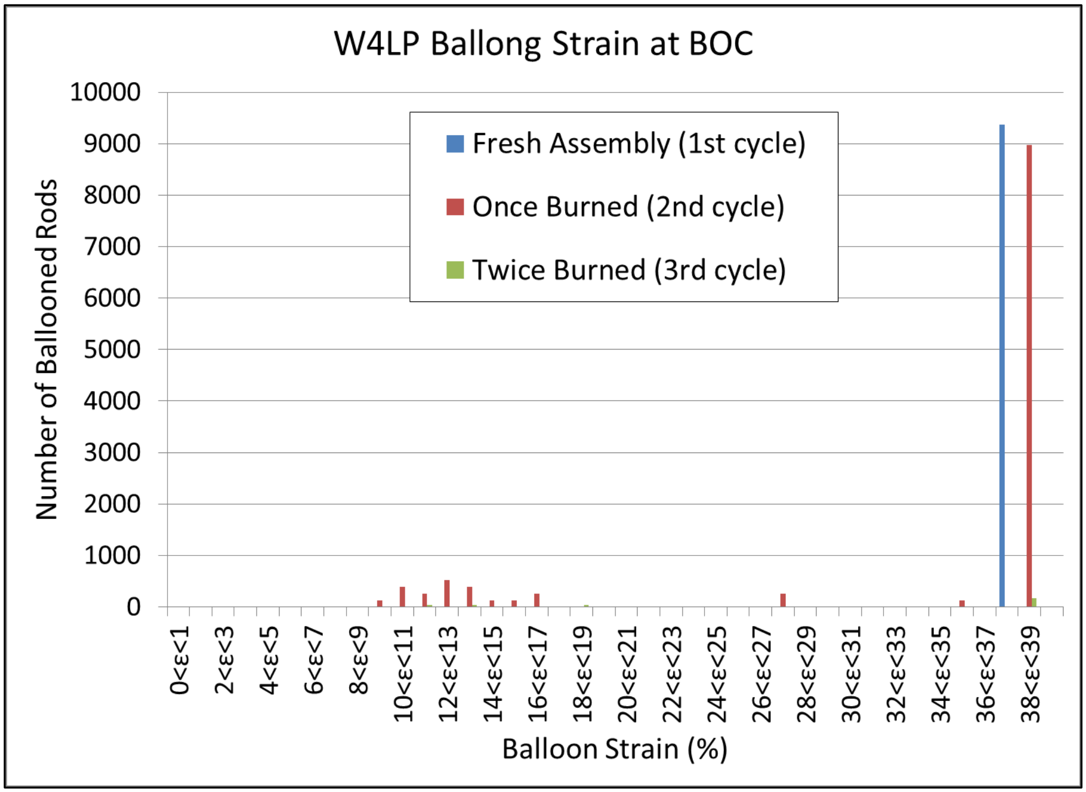
W4LP Ballong Strain at BOC

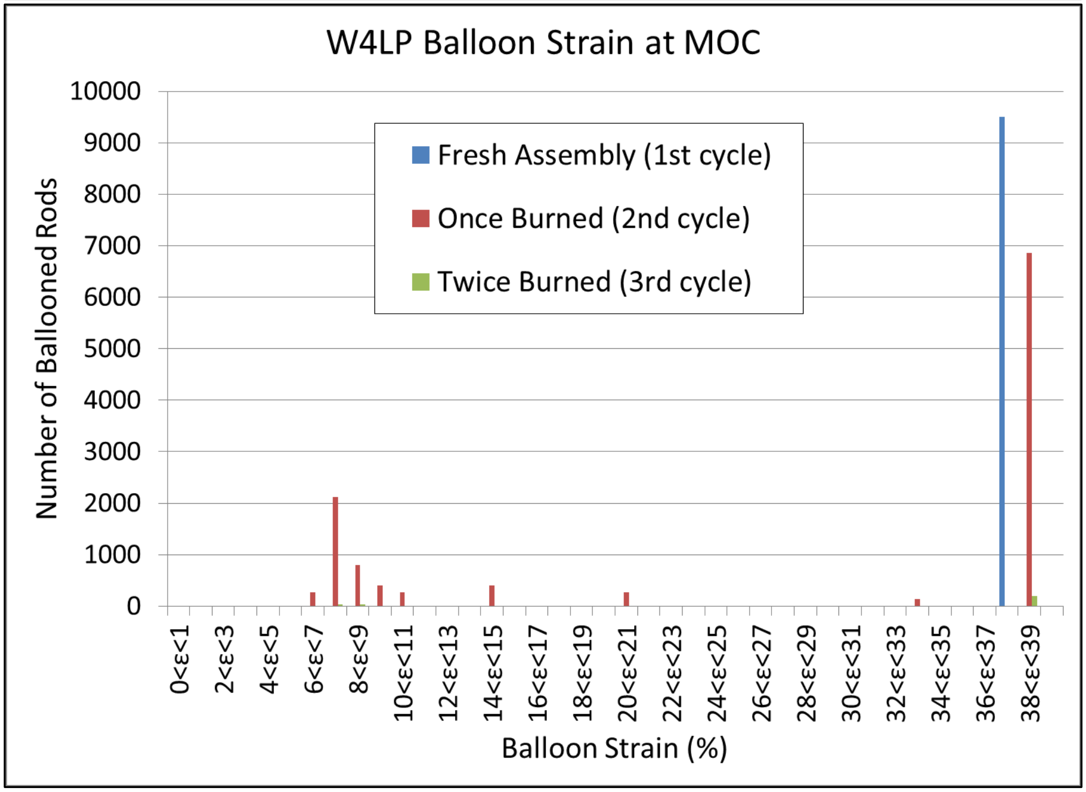
W4LP Balloon Strain at MOC

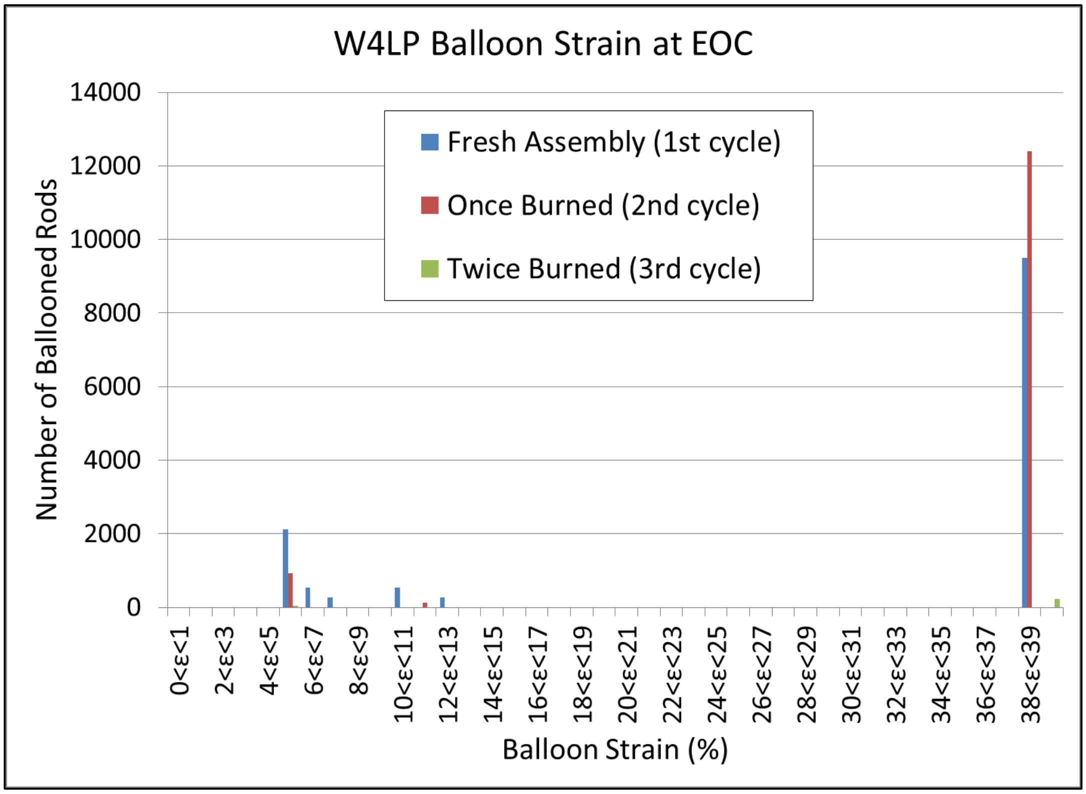

Figure 5.13: Cladding balloon strain inventory for W4LP LBLOCA at BOC, MOC and EOC

The remaining criteria for dispersal is the fuel fragmentation size able to leave the rupture opening. However, the size of the rupture cannot be calculated using FRAPTRAN; rather assumptions to the size are made based on experimental results, with an approximate size of 1mm. Therefore, all particles less than 1mm will be considered dispersible and assumed to escape the cladding during the cladding rupture. The assumption for required particle size is consequently linked with the burnup criteria, as this affects the particle size distribution and therefore the fraction of particles that meet the size requirement. It is important to understand that currently the data on the influence of particle size distribution as a function of burnup resulting from fuel rod ballooning and burst under LOCA conditions is limited. Therefore, several linear interpolations were performed between the two experimental results from NRC's Studsvik LOCA tests, shown in Figure 5.14.

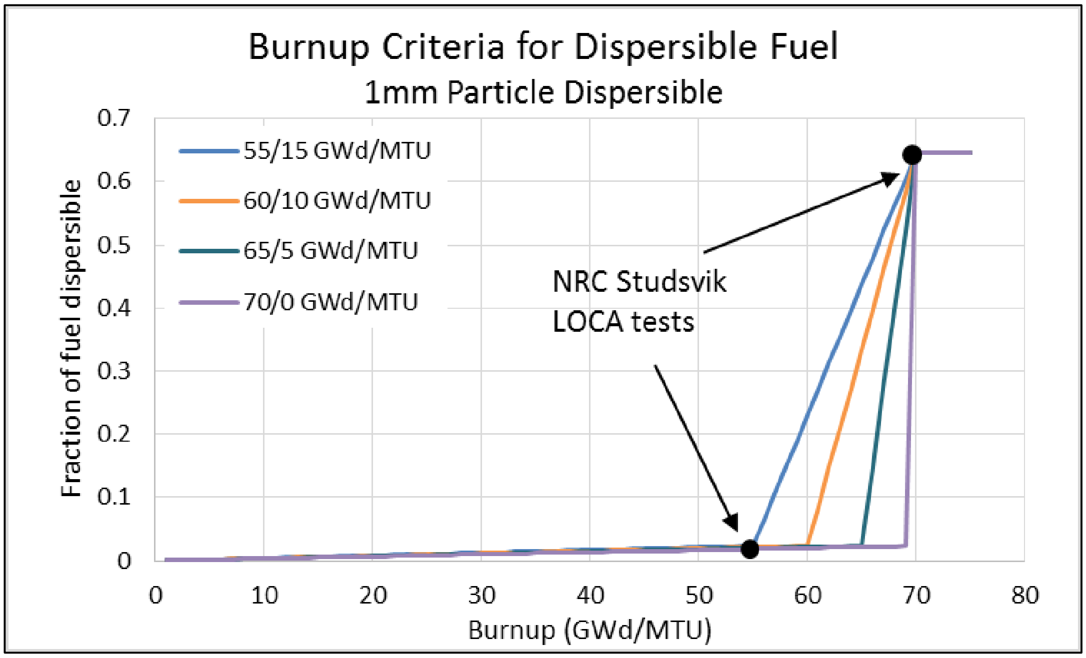

Figure 5.14: Fraction of fuel fragments less than 1mm using various interpolation methods

It was assumed that fresh fuel will have no particles <1mm. The first data point was taken at ~55GWd/MTU burnup and showed a fraction of fine particles (<1mm) of 2.3%. The second data point was taken at ~70 GWd/MTU and showed a fine particle fraction of 64.5%. A third data point can be added for Halden test IFA-64.5 at ~91.5 GWd/MTU burnup where almost 100% of the particles are fine. However, for the current analysis the nodal burnup values do not exceed 70 GWd/MTU. [Note: In September 2014, additional data was released (made non-proprietary) at WRFPM concerning the burnups for the particle size distribution. The nodal burnup values are higher than what was reported (i.e. 55 and 70 GWd/MTU), with the reported values being closer to rod average. However, the lower thresholds were already used in this work, thus providing a more conservative potential quantity of dispersed fuel.] The particle size distribution at 55 GWd/MTU is commonly referred to as a coarse particle size distribution due to the majority of particles being coarse, whereas the distribution at 70 GWd/MTU is considered a fine particle size distribution. The limited data makes it unclear as to where the transition between a coarse and fine particle size distribution begins, understanding only that it occurs between 55 and 70 GWd/MTU. A simplified linear interpolation was method was performed between the lower and upper bounds with variations between 55 and 70 GWd/MTU in determining where the transition starts. It was always assumed that it ended by 70GWd/MTU. Between fresh fuel and the start of the transition, linear interpolation was also performed to capture any fragmentation that might occur before the start of the transition. The more conservative approach is to assume that the transition starts at 55 GWd/MTU, as this captures more fine fuel fragments due to the burnup of the fuel being less than 70 GWd/MTU. The effect of dispersed fuel as a function of particle size burnup threshold is shown in Figure 5.15.

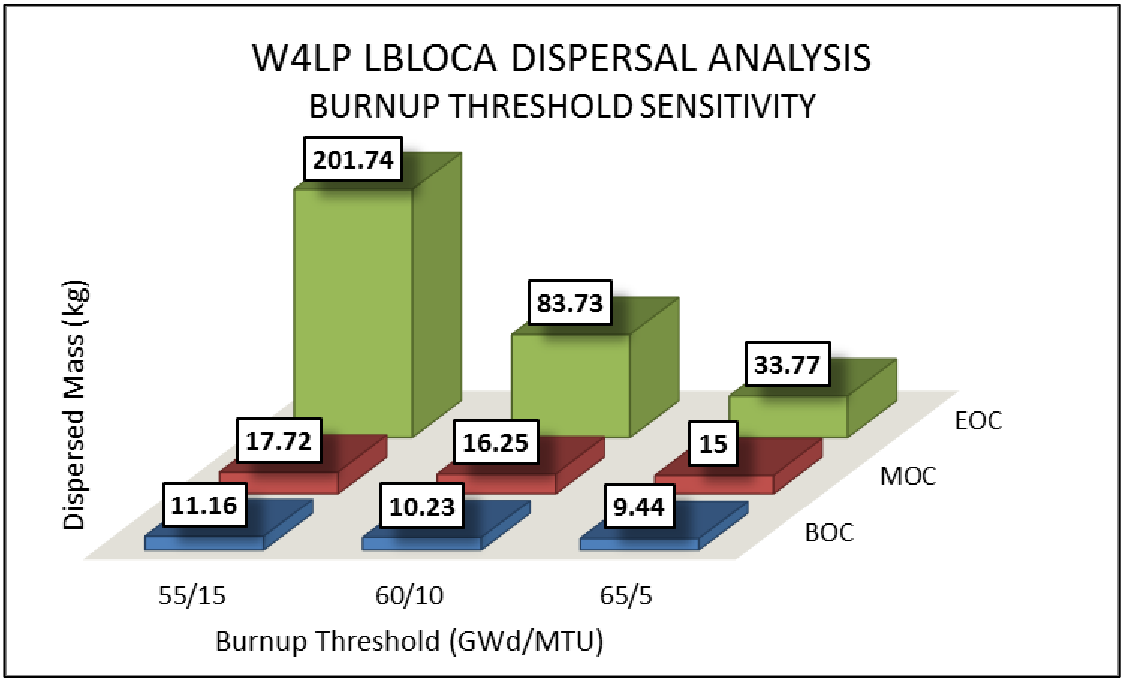

Figure 5.15: Fuel dispersal sensitivity to burnup threshold

Figure 5.15 illustrates the importance of performing these calculations at various cycle times. The impact of fuel burnup on the dispersal analysis can be seen in analyzing the EOC conditions compared to the BOC conditions, noting that the EOC analysis resulted in ~27% more failed rods than the BOC and MOC analysis. The BOC and MOC cases are relatively insensitive to the burnup threshold, due to the fact that the failed fuel has not achieved these burnups. The sensitivity lies in the fact that linear interpolation used between 0 GWd/MTU and the point at which coarse particle size distribution begins will result in an increased mass the lower the transition starts. It is clear that with the EOC analysis, the fuel burnup reaches the transition between fine and coarse particles at 55/15 GWd/MTU and 60/10 GWd/MTU burnup thresholds. The quantity of dispersed fuel with the high burnup threshold is 3.6x higher at EOC than BOC, whereas with the low threshold the quantity is 18.1x higher at EOC. The average transition value of 60/10 GWD/MTU, which resulted in a 1.6x quantity increase at MOC and an 8.2x increase at EOC, will be used in the remaining analysis.

The cladding strain showed to have a strong sensitivity to mass of fuel dispersed between the three cycles and within the cycles. The sensitivity to cladding strain decreased from BOC to EOC, due to a combination of rod power, stored energy and internal rod pressure. At BOC, decreasing the cladding strain from 7% to 3% resulted in 4.46x as much fuel dispersed, compared to 4.07 and 3.25 at MOC and EOC, respectively. Lowering the cladding strain threshold increases the number of axial nodes which contain fuel that is mobile and therefore considered dispersible. The analysis is shown in Figure 5.16.

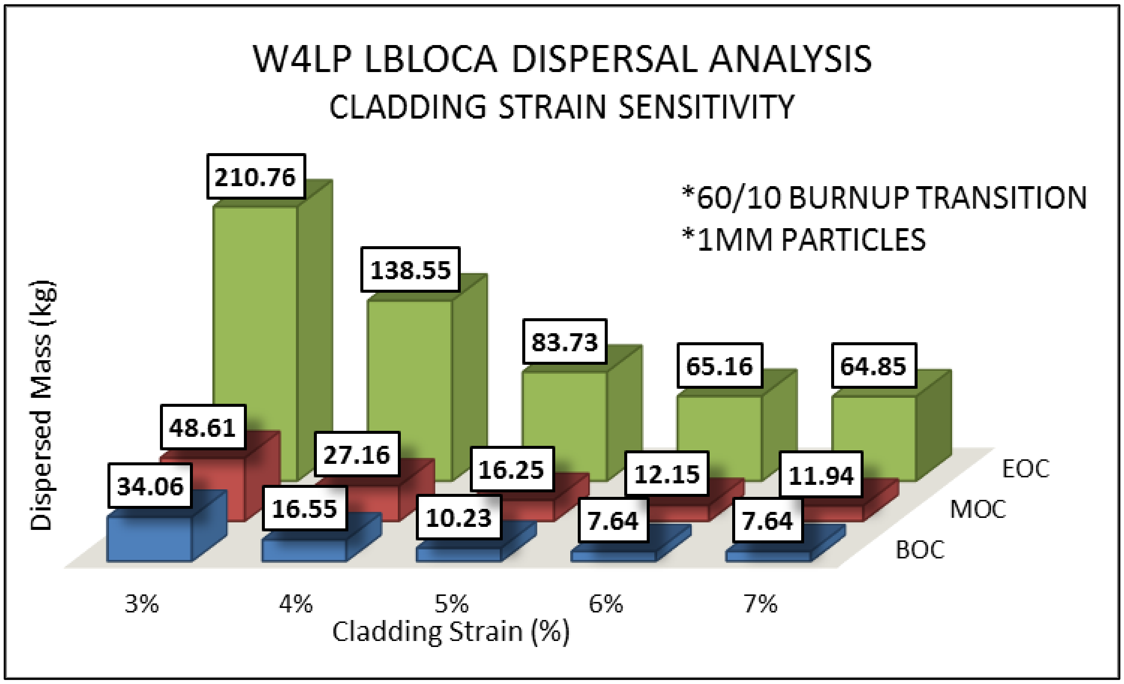

Figure 5.16: Fuel dispersal sensitivity to cladding strain assuming a 60/10 GWD/MTU particle size distribution and 1mm particles are dispersible

Further analysis into the cladding strain criteria shows a reversed trend from what is shown in Figure 5.15. If the assumption is made that all of the fuel in the mobile axial regions of the fuel rod is dispersible, then the conditions at BOC are the most limiting rather than EOC. Although the peak cladding temperatures are similar at BOC and EOC, the higher internal rod pressure at EOC causes the rods to fail faster. The quicker failure reduces the ability for the other nodes outside of the ballooning node to plastically deform before the instability strain is reached in the ballooning node. This is likely compounded by FRAPTRAN's limit to only one node being able to balloon and the plastic deformation stopping for all other nodes. A sensitivity to the node size and its effect on fuel dispersal due to FRAPTRAN's ballooning model is explored in section V.4.2. The potential dispersible fuel mass per failed rod is shown in Figure 5.17.

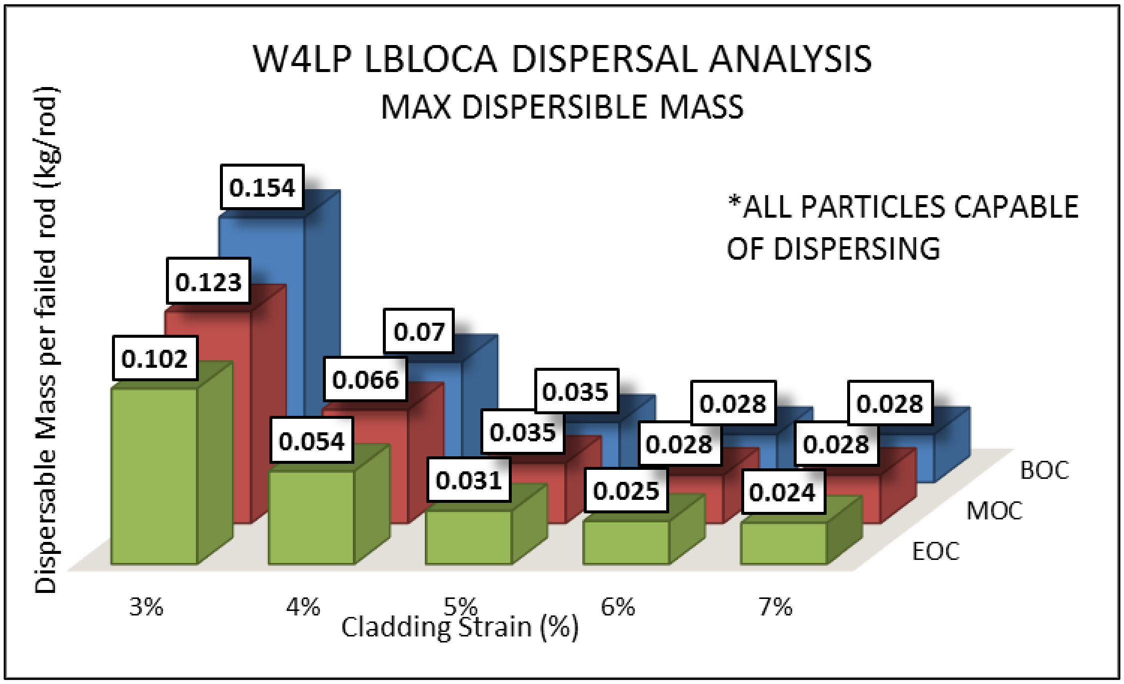

Figure 5.17: Amount of fuel available at nodes that meet cladding strain criteria for dispersal for W4LP LBLOCA

Based on experimental data described in Chapter 2, the possibility of all of the fuel being dispersed out of the cladding during a LOCA is unlikely. The current NRC regulations on cladding ductility under LOCA conditions (proposed 10 CFR 50.46c) are designed to prevent the cladding from becoming brittle. As shown in Figure 1.3.1 of the TMI-2 accident, the loss of cladding ductility resulted in a thermal shock during reflood that caused the cladding to shear, which would then allow coarse fuel fragments (>1mm) to be released from the fuel rod.

## 5.2 CE-PWR

### 5.2.1 Steady-State Analysis

The assembly-average radial peaking factors at BOC, MOC and EOC were available in the FSAR report, along with the previous location of the assemblies in the core. The power at the assembly's previous location(s) was used to re-create the power history for each assembly-average rod, assuming that the core had been at equilibrium over the past several cycles. However, this resulted in unrealistic power histories for ~2/3 of the 2nd and 3rd cycle rods (meaning the assembly-average burnup was well beyond the licensing limit). The power history for these rods was re-constructed using the same technique for the W4LP. The combinations of first, second and third cycle power histories were optimized to achieve an assembly-average burnup limited to ~62 GWd/MTU. Some of the rods resulted in a burnup of 63 GWd/MTU, which were considered to be acceptable as representative of lead-test assemblies (LTA). The power histories developed for this core design are shown in Figure 5.18.

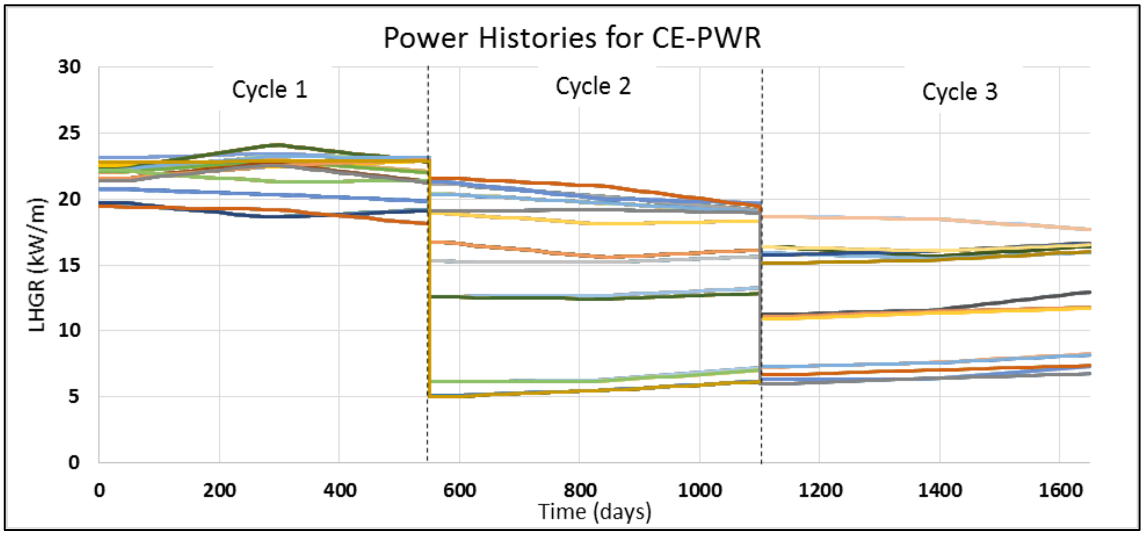

Figure 5.18: Power histories used in CE-PWR FRAPCON Analysis

The core power map at BOC, MOC and EOC is shown in Figure 5.19.

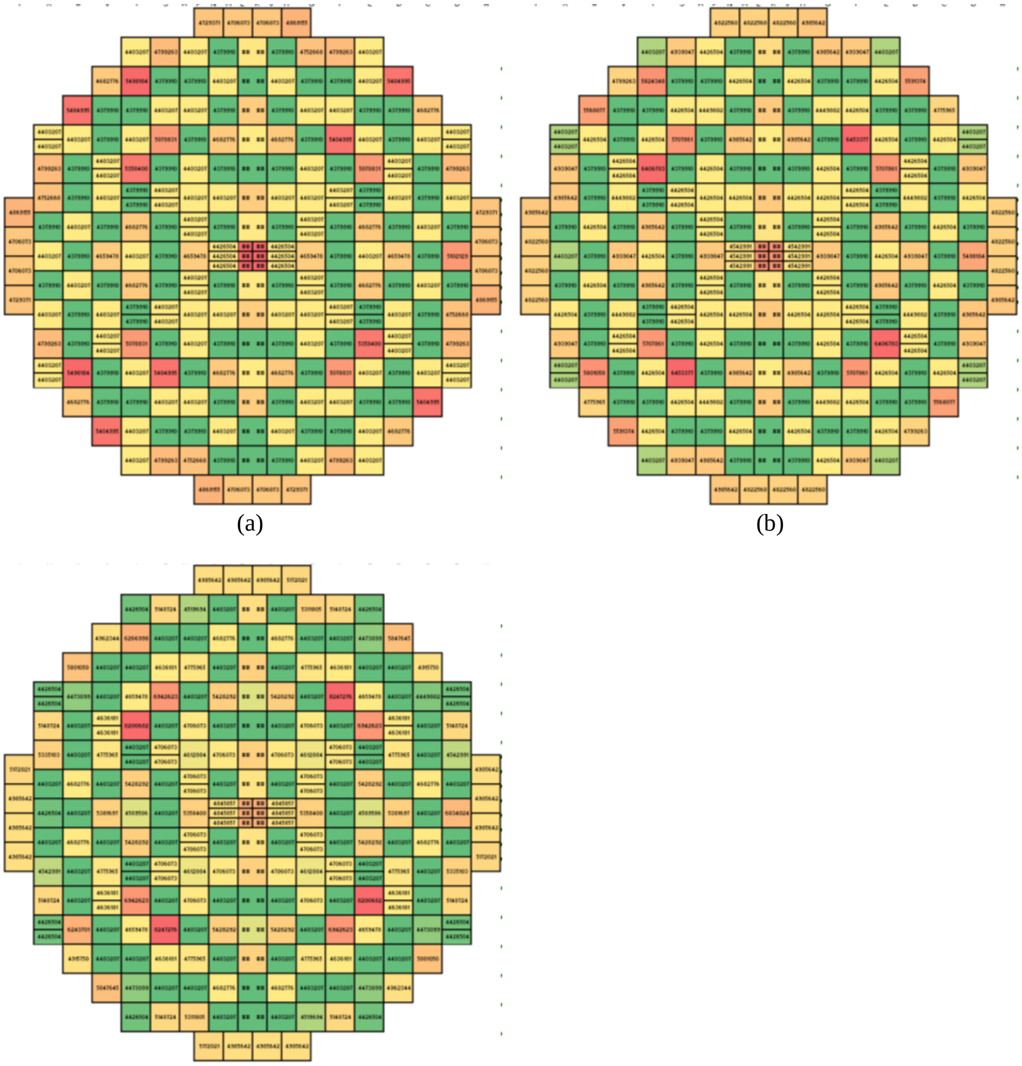

(a)

(b)

(c)

Figure 5.19: CE-PWR core power map at (a) BOC, (b) MOC and (c) EOC

The steady-state analysis revealed that the fuel rods were not at nearly as high of internal rod pressure compared to the W4LP plant at EOC, as shown in Table 5.4. This is attributable to the nearly 10% increase in as-fabricated void volume. The core average internal rod pressure was 9.0 MPa with the maximum assembly average rod pressure of 10.537 MPa. The average oxide layer thickness was 14.05µm, decreased ~6µm. The stored energy in each rod was also lower. However, due to the fact that the CE-PWR has more rods (51,212) than the W4LP (50,952) the decrease in total stored energy within the core is not reduced by the same amount.

Table 5.4: Core average rod parameters at EOC between W4LP and CE-PWR plants

| Plant | Core Average Parameters at EOC | | | |
|---|---|---|---|---|
| | Pressure (MPa) | Oxide Thickness (μm) | Stored Energy (kJ) | Total Stored Energy (GJ) |
| W4LP | 9.819 | 21.089 | 324.148 | 16.516 |
| CE-PWR | 8.997 | 14.055 | 310.060 | 15.879 |
| Difference | -8.37% | -33.36% | -4.35% | -3.86% |

Although the cladding used in both reactors is the same (ZIRLO$^{TM}$), there is a stark difference in oxide thickness between the plants. One major reason is the coolant temperatures at which the reactors operate. Both cores have a nearly identical temperature rise across the fuel of ~35 Kelvin. However, the coolant inlet temperature in the CE-PWR is ~9 Kelvin lower than in the W4LP, meaning the coolant temperature at the fuel rod plenum is also the same amount cooler. Despite similar surface heat fluxes across the cladding, the lower coolant temperatures significantly reduce the corrosion thickness. The W4LP operated at higher pressure to accommodate the hotter coolant temperature. The values obtained for the oxidation thickness calculations are in-line with the FRAPCON-3.5 assessment data. It is important to understand that the core-average values are the axial average thickness across all of the 1st, 2nd and 3rd cycle rods. For example, the highest powered 2nd cycle rod at EOC has a maximum thickness of 80μm but an average thickness of 40.3μm, whereas the lowest powered 1st cycle rod has a maximum oxide thickness of 14 μm and an average thickness of 7.98μm.

### 5.2.2 Transient Analysis

Both a LBLOCA and a SBLOCA were modeled in TRACE for the CE-PWR. The peak cladding temperatures for the LBLOCA at BOC, MOC and EOC were 975K, 970K and 951K, respectively. The PCT's are shown in Figure 5.20. During the blowdown phase of the transient (first ~50 seconds), the BOC had the highest initial temperature due to the higher power and stored energy of the fresh fuel. The PCT before the start of reflood (~105s) was significantly higher for the BOC rods than the MOC rods by ~50K, which were 59K hotter than the EOC rods.

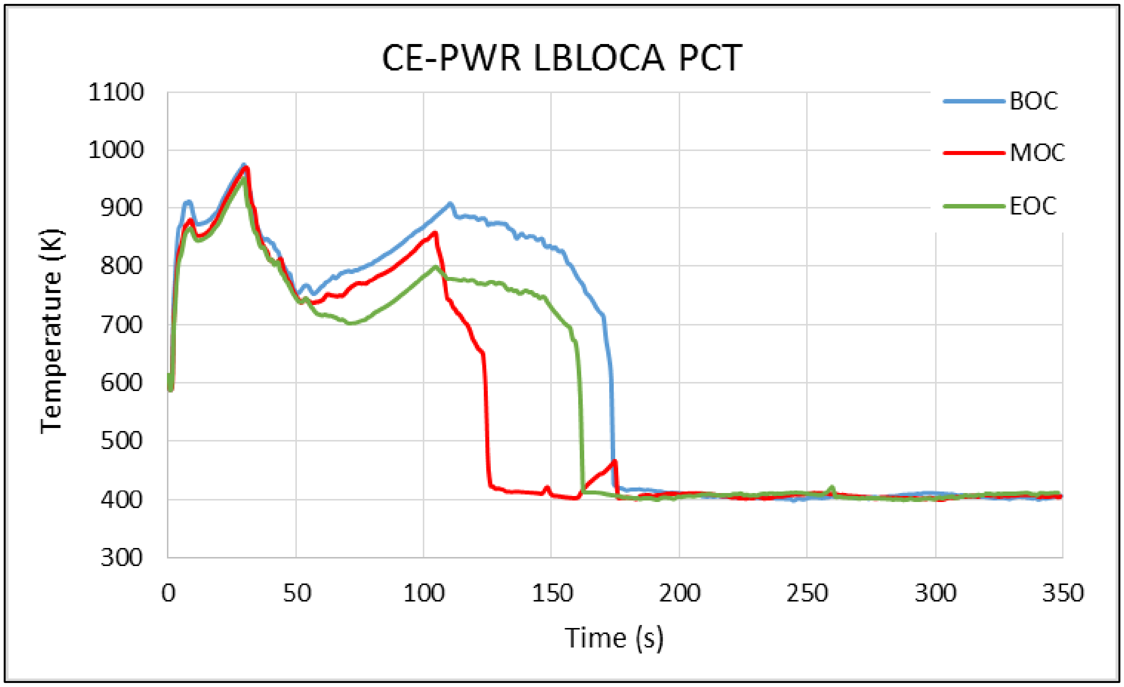

Figure 5.20: Peak cladding temperature for CE-PWR under LBLOCA accident conditions

The PCTs were over 100K lower than those obtained in the W4LP. The lower cladding temperatures, combined with the lower internal rod pressure, was expected to result in less (if any) fuel rod failures than the W4LP. However, dues to the fuel rod ballooning and failure model starting at temperatures as low as 940K, the FRAPTRAN analysis was still performed at BOC, MOC and EOC conditions. The FRAPTRAN analysis yielded no ballooning for any of the rods at any of the cycle times, and consequently no fuel rod failure. With no failed fuel rods, no possibility of fuel dispersal exists. With the predicted coolant and cladding temperatures, no transient oxidation occurred for any of the rods.

The peak cladding temperatures for the SBLOCA were significantly lower than the temperatures for the LBLOCA, shown in Figure 5.21. The PCT for BOC, MOC and EOC was 785K, 789K and 768K, respectively. The MOC had the highest PCT due to having the highest powered rods at MOC, subsequently also having the most decay power. Unlike the LBLOCA, the stored energy is not the driving force for PCT as the heat is removed from the fuel in the first 20-30 seconds.

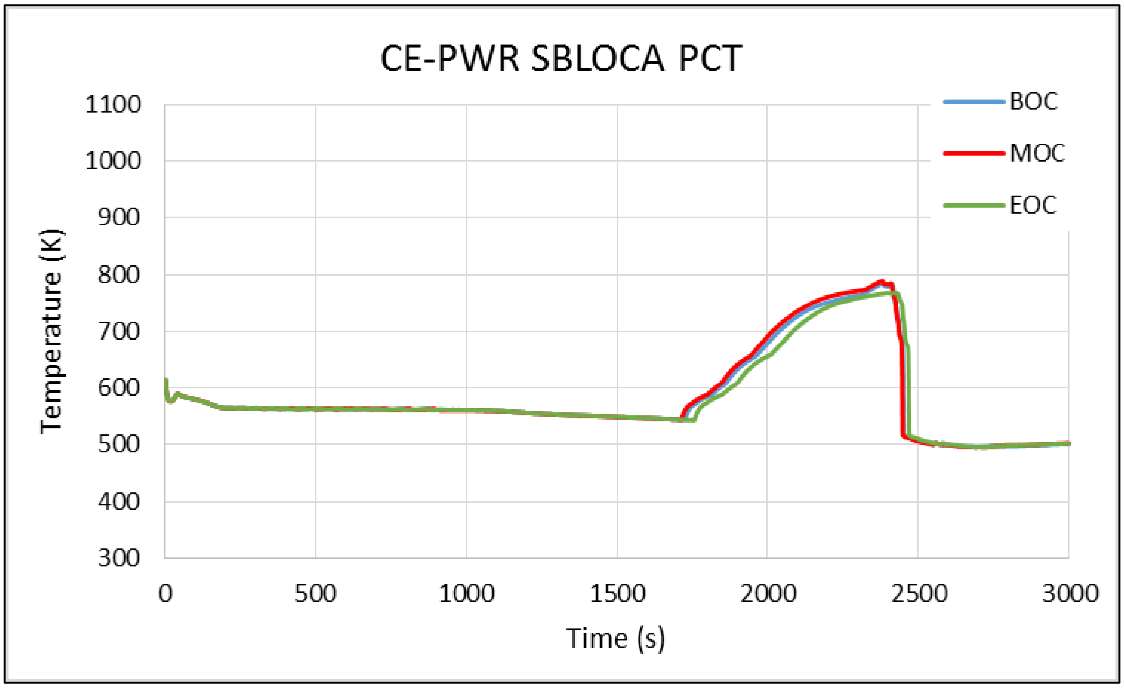

Figure 5.21: Peak cladding temperature for CE-PWR under SBLOCA accident conditions

There is a significant difference in the system response between the LBLOCA and the SBLOCA. The core rapidly depressurizes to ½ its original value in the less than 4.0 seconds and to 1/10 its original value by 17.5 seconds during the LBLOCA. During the SBLOCA, it takes ~160seconds to depressurize to ½ the original pressure and never gets below ~1.5 MPa. This is illustrated in Figure 5.22.

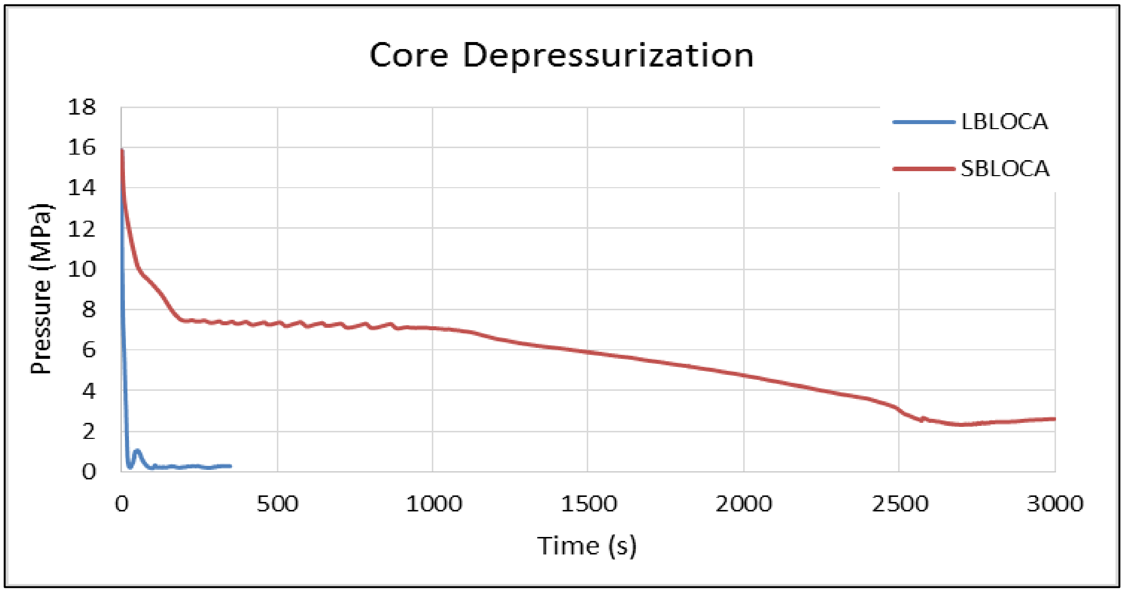

Figure 5.22: CE-PWR core depressurization for LBLOCA and SBLOCA

With the ability of the core to maintain some pressure and not rapidly lose all of the liquid water inventory, the cladding temperatures remain lower. The core liquid level drops below the fuel height after 45s. However, it does not drop down to uncover the significant powered sections until ~1700s. At this point, due to the decay heat and the rod not being able to transfer its energy to the liquid, leads to the takeoff in cladding temperatures. The core starts to refill by 2390s, thus the reason for the drop in cladding PCT by 2470s. The liquid and vapor mass flow rates leaving the core are shown in Figure 5.23.

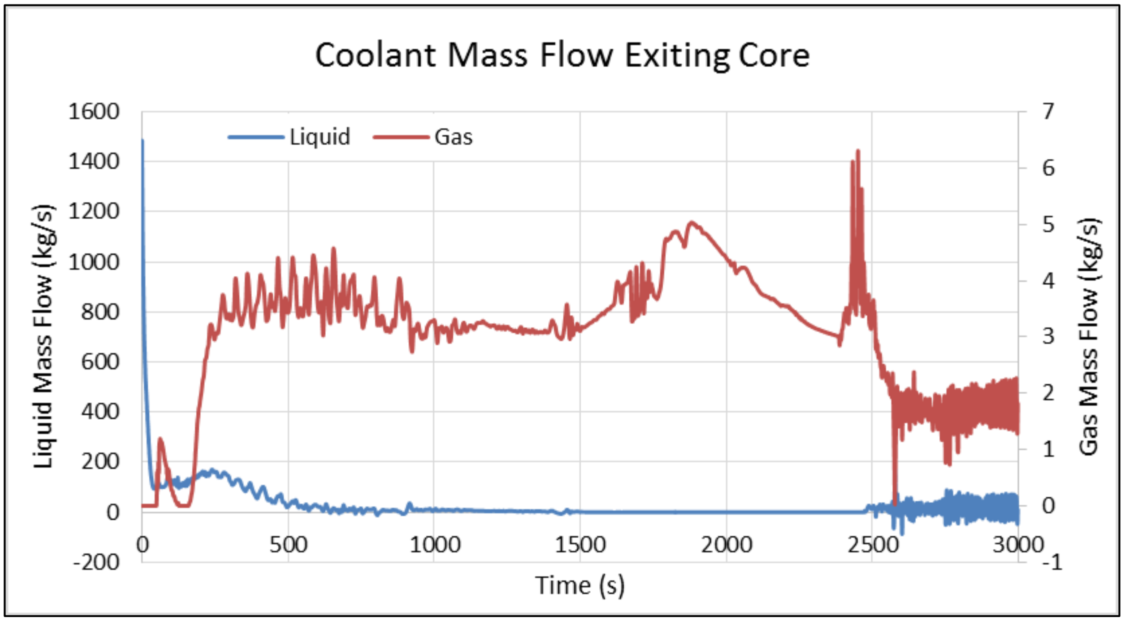

Figure 5.23: Core mass flow rates exiting core for CE-PWR SBLOCA

The lower cladding temperatures for the SBLOCA compared to the LBLOCA indicate that there is no possibility for fuel rod failure under these conditions. Again, no fuel rod failure results in no fuel dispersal. Under different conditions, i.e. reduced response of ECCS systems, fuel rod failure and dispersal might be predicted. However, under the nominal plant response and core design, no dispersal is expected to occur.

## 5.3 GE-BWR/4

### 5.3.1 Steady-State Analysis

The data available in the FSAR and core reload report for the GE-BWR/4 were the BOC and EOC assembly-average radial peaking factors and burnup values. The MOC peaking factor was calculated to match the known EOC burnup value through linear interpolation. The LHGR used in previous cycles for the 2nd and 3rd cycle assemblies was calculated by adjusting the current cycle core-average power for 1st and 2nd cycle rods to match the known BOC burnup value. For the 3rd cycle rods, the fraction of burnup that occurs over the 1st and 2nd cycle was varied to maximize the internal rod pressure, but due to the relatively low power and temperatures the rods operated at, this was shown to not have a major impact. Based on the FSAR report, the plant performed a 10% power coastdown before shutting down for refueling. The power histories used in this analysis are shown in Figure 5.24.

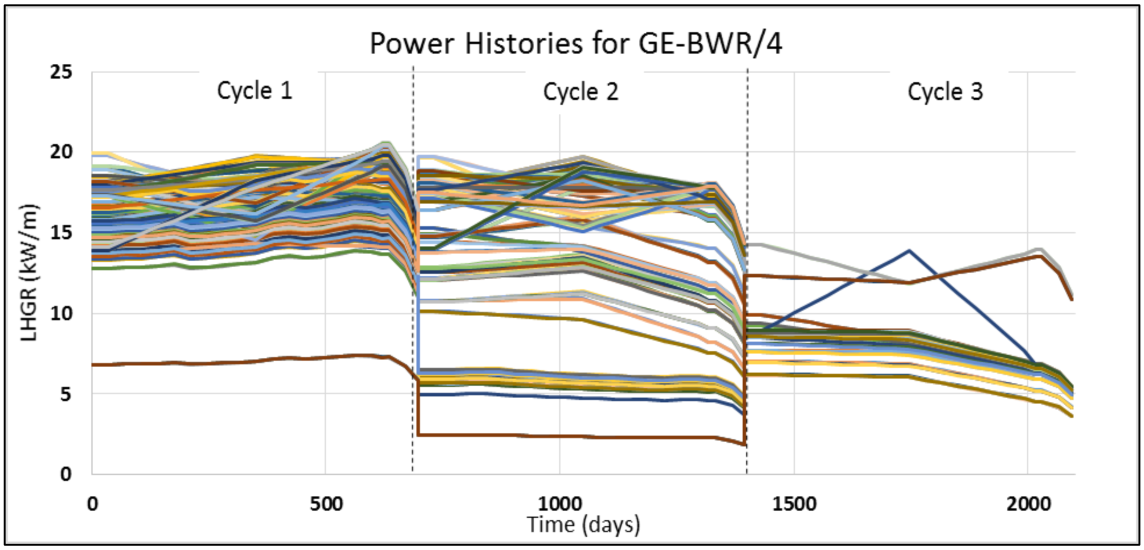

Figure 5.24: Power histories used in GE-BWR/4 FRAPCON Analysis

With the TRACE VESSEL component not being divided into azimuthal sectors, there was no division of the assemblies modeled across coolant zones. This resulted in a total of 764 FRAPCON runs, each with its own independent power history. Unlike the rods modeled in the PWR case, the known burnup values at EOC for each assembly kept the powers lower to match the operational burnup values rather than the licensing burnup limit. The relatively lower power in the BWR rods coupled with the low discharge burnup (compared to the W4LP rods) resulted in significantly less FGR for the high burnup rods due to the lower fuel temperatures. The as-fabricated internal rod pressure was also significantly lower (~0.65 MPa compared to ~2.4 MPa for both PWR cases), therefore resulting in lower EOC internal rod pressure. The core-average internal rod pressure at EOC was 2.32 MPa, with the highest rod reaching 3.20 MPa. For comparison, the W4LP

EOC core-average internal rod pressure was 9.82 MPa for the updated analysis. The lower internal rod pressure will produce lower tensile cladding hoop stress once the system begins to depressurize in the LOCA from ~7.03 MPa.

The average stored energy in the full length fuel rods is nearly identical to the average energy in the W4LP rods at EOC. The average stored energy for a rod in the BWR/4 is 375, 363 and 325 kJ at BOC, MOC and EOC, respectively, compared to 321, 308 and 324 kJ for the W4LP. The decrease with cycle time in the GE-BWR/4 is due to the reduction in the thermal resistance of the gas-gap. Although the rods operate at a lower power than in the W4LP, the fuel temperatures are similar due to the BWR fuel design where the pellet has a larger diameter and thicker cladding, increasing the thermal resistance of both materials. . It is important to also note that the mass of fuel in the GE-BWR/4 rods is nearly 31% higher than the W4LP rods (2.44 and 2.33 kg/rod for the GE and AREVA fuel designs, respectively, compared to 1.82 kg/rod for the Westinghouse 17x17 design).

Cladding corrosion by EOC resulted in an average cladding oxide thickness of 13.9µm, equivalent to an ECR of 2.29%. The maximum and minimum rod average ECR in the core was 3.23% and 1.31% for 3rd and 1st cycle rods, respectively.

### 5.3.2 Transient Analysis

The GE-BWR4 was analyzed with both a SBLOCA and a LBLOCA. As shown in Figure 5. 25, the peak cladding temperatures were 743K at BOC and MOC, while reaching 777K at EOC.

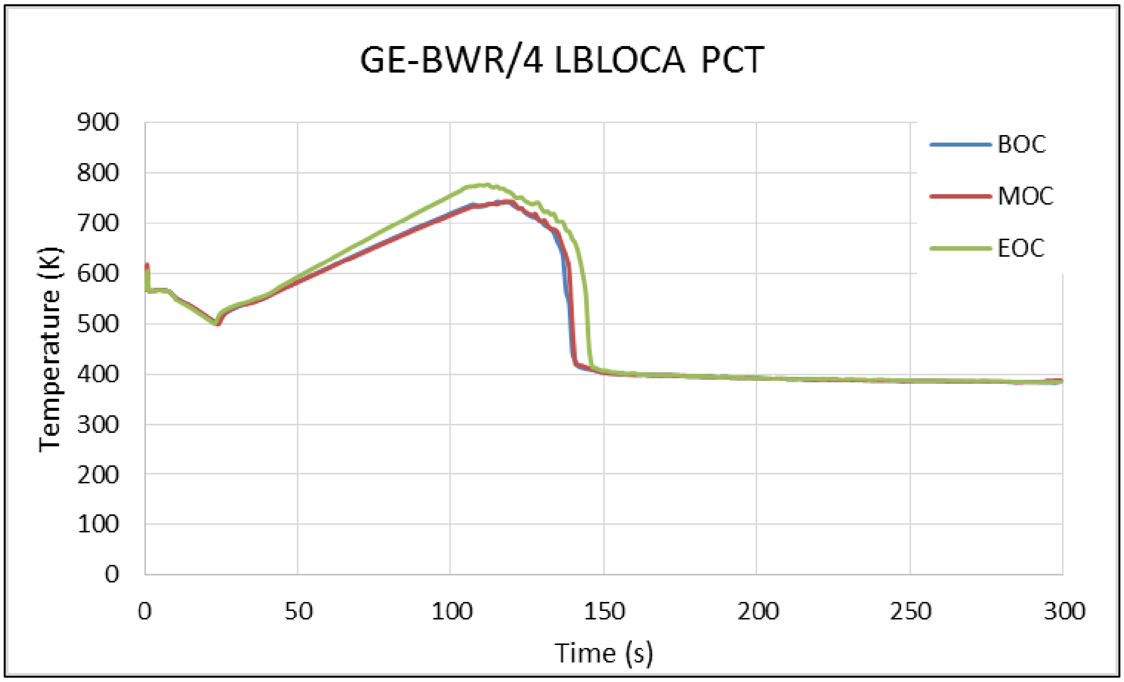

Figure 5.25: GE-BWR/4 LBLOCA peak cladding temperatures at BOC, MOC and EOC

The peak cladding temperatures reached during the GE-BWR/4 LBLOCA are lower than those reached in the W4LP and CE-PWR. During the blowdown phase, the vessel does not immediately depressurize and lose the liquid inventory in the core. Unlike in the PWR LBLOCA, a rapid increase in cladding temperature does not occur due to the heat removal being sufficient to remove the stored energy from the fuel (this will be further shown in the SBLOCA analysis). The core begins to depressurize after ~10s, causing the liquid to flash to steam and reducing the ability to remove heat from the fuel rod. The heat up is less rapid than in the PWR LBLOCA cases due to decay heat alone causing the rise in temperature. Once the core reflood starts at ~105s, the liquid level increases and is able to remove the heat from the fuel rods. The liquid level rises above the fuel by ~140s for the BOC and MOC cases and ~5s later for the EOC case, due to the hotter fuel temperatures.

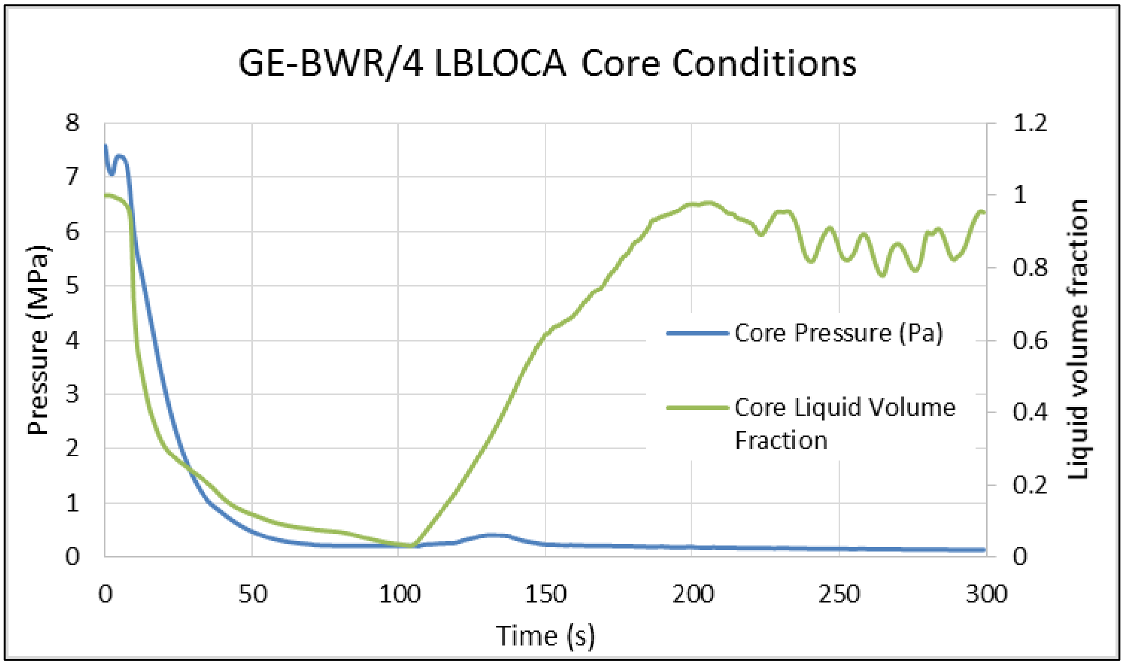

Figure 5.26: GE-BWR/4 LBLOCA core coolant conditions at EOC

For the GE-BWR/4 LBLOCA, the decay heat was the driver for determining which rods would result in the highest cladding temperatures. As seen in Figure 5.24, the power that many of the rods are at before the LBLOCA (the time immediately before the coastdown) is the highest of any time during the cycle, meaning the most decay heat would be coming from those rods at that time. The internal rod pressures are also significantly lower, on the order of 2-3x lower than similarly powered rods in the PWRs. Due to no fuel rod failures calculated in the FRAPTRAN analysis for the CE-PWR, it can be concluded that no fuel rod failures will exist for this analysis.

The SBLOCA resulted in higher PCT's than the LBLOCA, albeit at much later times. The PCT increased to 764K at BOC, 783K at MOC and 812K at EOC, as shown in Figure 5.27.

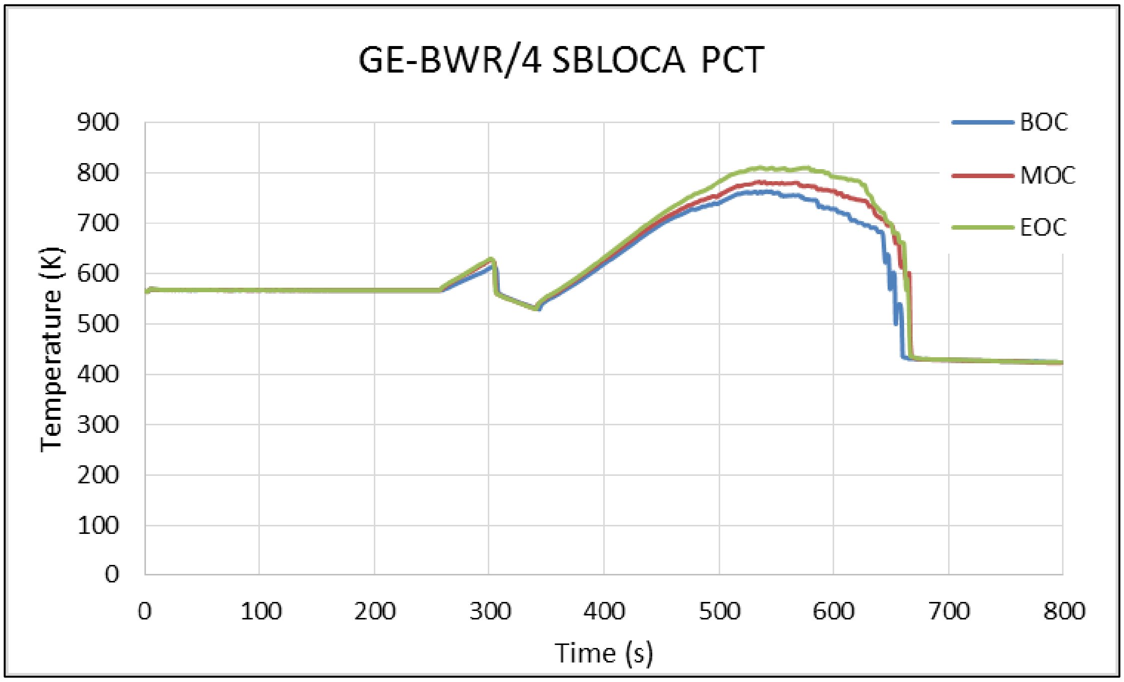

Figure 5.27: GE-BWR/4 SBLOCA peak cladding temperatures at BOC, MOC and EOC

As with the LBLOCA, the core is able to remain covered during the start of the transient, allowing the stored energy of the rods to be removed and the decay heat to be the driver for PCT. It is not until ~200 seconds when significant liquid volume begins to leave the core, and at ~300s the system depressurizes due to the actuation of the automatic depressurization system (ADS) valves. The core pressure and liquid volume fraction throughout the transient is shown in Figure 5.28.

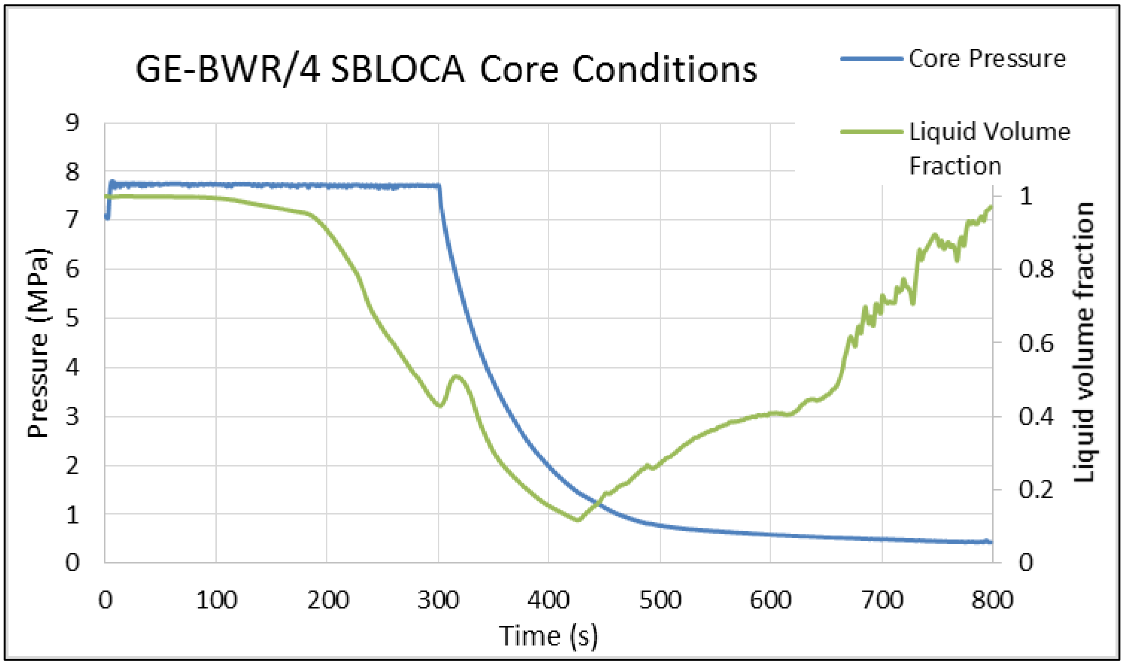

Figure 5.28: GE-BWR/4 SBLOCA core coolant conditions at EOC

Starting around 255s, Figure 5.27 shows that the cladding temperatures start to rise. This is due to the lack of any liquid coolant flow coming into the channels starting at ~230 seconds. At this point, the vapor fraction at the top of the rod approaches 1.0 and the heat flux is reduced by over 90%. From 230 to 300s, there is minimal heat removal capability and the water continues to boil to vapor, thus increasing the vapor fraction further down the rod (from top to bottom). Since the rod cannot easily transfer the energy created by decay heat to the vapor, the rod temperature increases. The vapor fraction and heat flux are shown in Figure 5.29 for various axial elevations.

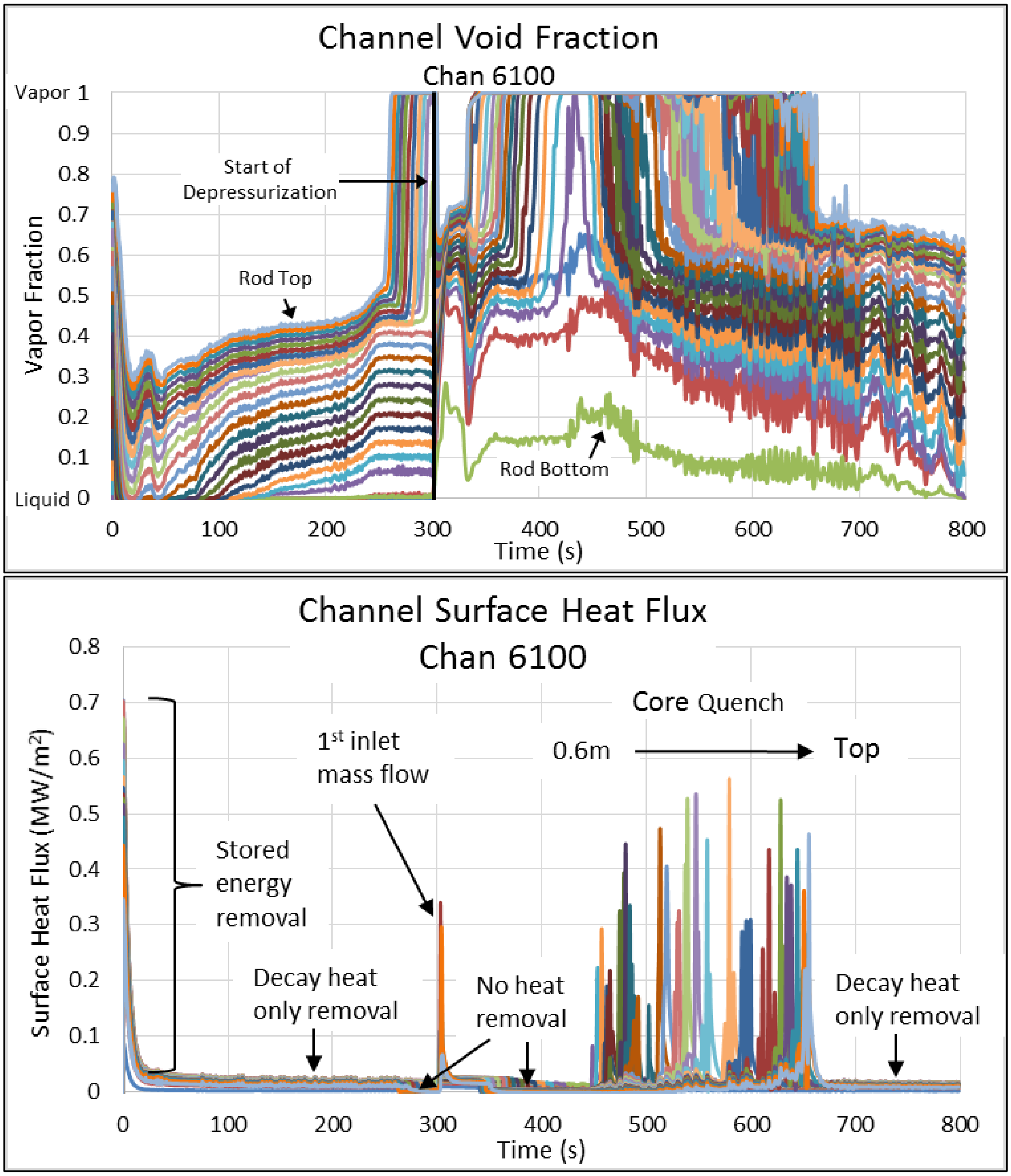

Figure 5.29: Coolant conditions and heat removal for hottest channel in SBLOCA

At 300s, a small amount of reflood is introduced into the core during the depressurization. The liquid is able to remove the stored energy from the rods and bring the temperature back down to coolant temperature. The temperature of the reflood liquid is lower than the liquid previously in the core, hence the reason the cladding temperature goes lower than where it had held steady for the first 250s. The liquid mass flow rate for the hottest channel is shown in Figure 5.30.

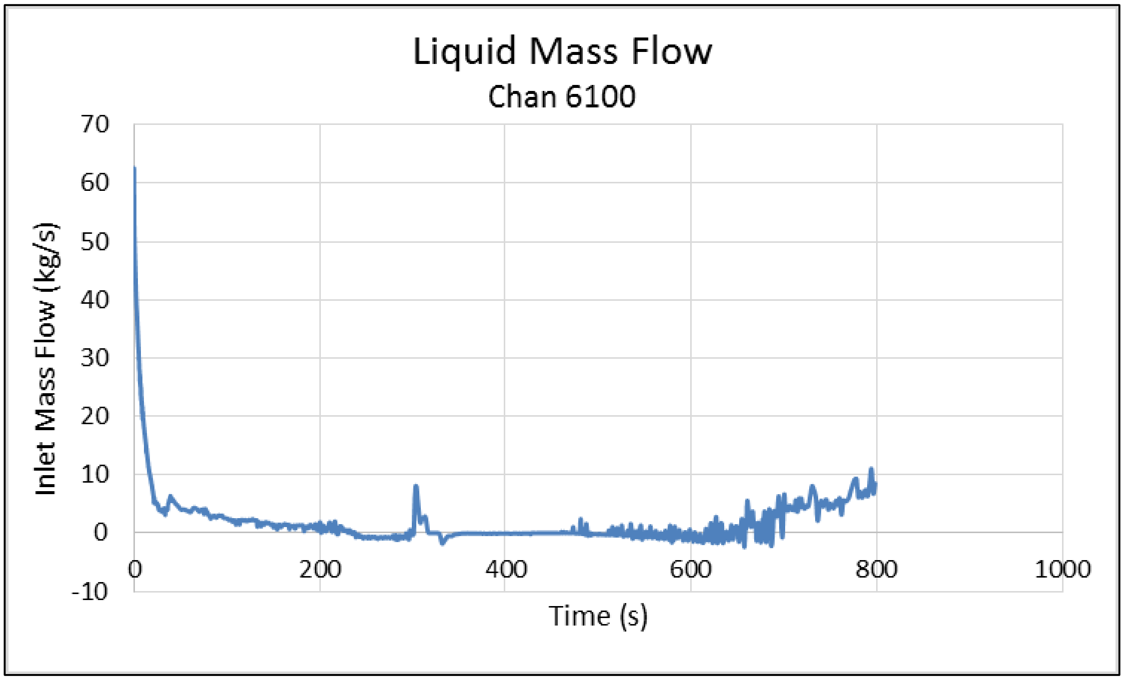

Figure 5.30: Liquid mass flow into hottest channel for SBLOCA

There is another loss of coolant flow ~15s later, allowing the fuel to again heat up. This time the loss of coolant flow into the channel is for much longer duration (~160s), allowing more of the fuel to be exposed to vapor. Due to the fuel getting hotter along the (nearly) entire axial length of the rod, it takes longer to completely re-quench the rod. As the fuel rod is quenched from the bottom to the top, there is a 210s delay from when the lowest node that was exposed to nearly all vapor (Node 4, elevation = 0.61m) until the top of the rod is cooled. The fuel centerline and cladding surface temperatures throughout the SBLOCA are shown in Figure 5.31.

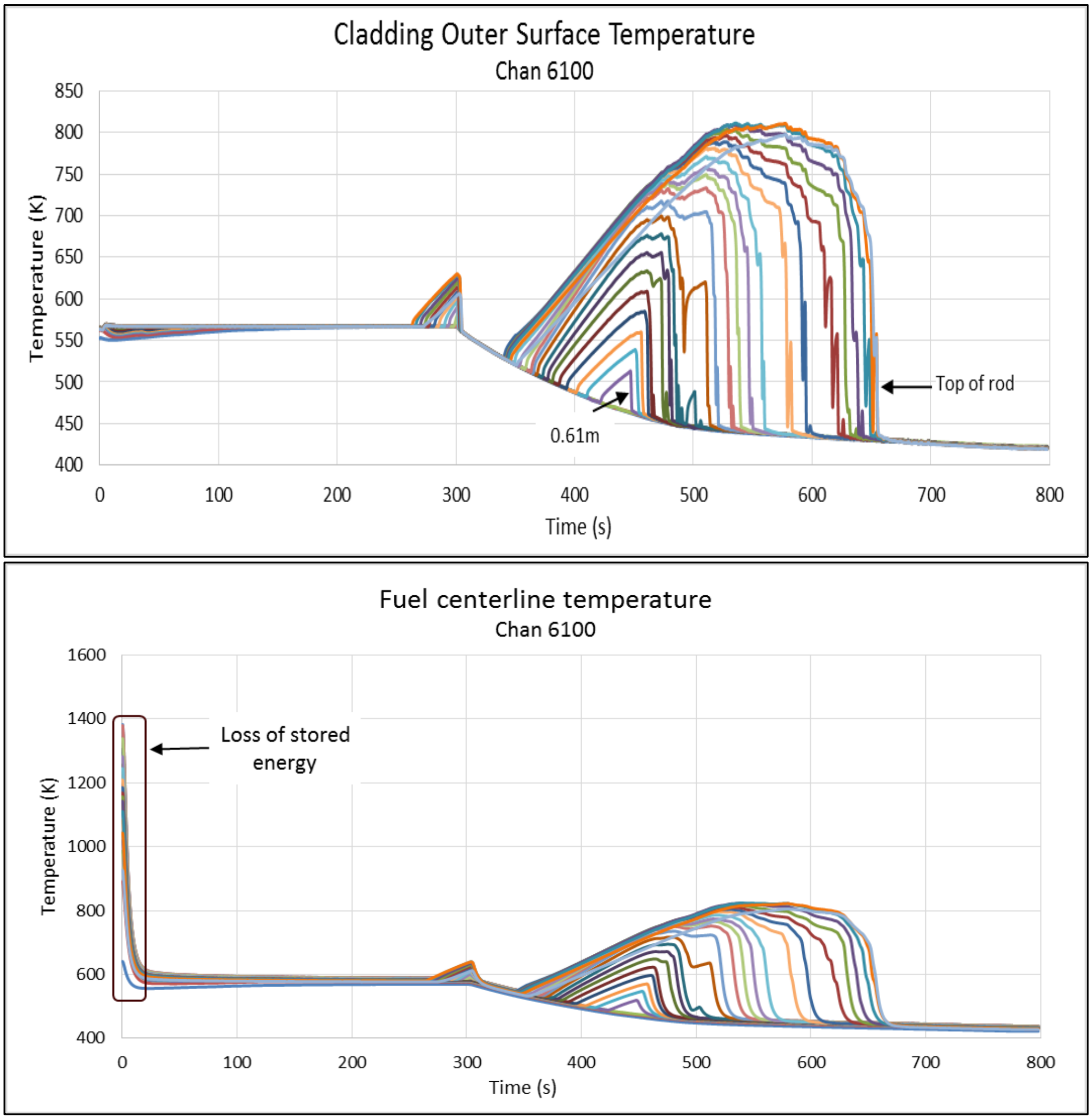

Figure 5.31: Cladding and fuel temperatures for hottest channel during SBLOCA

As stated earlier, the fuel stored energy from operation in both the LBLOCA and SBLOCA was not a major driving force for the cladding PCT. The reason for this is illustrated in Figure 5.31, showing that he time to significantly reduce fuel temperatures occurs over the first 10-20s. During operation, the maximum fuel centerline temperature for the hottest rod was calculated as 1383K. By 5s it was reduced to 916K, by 10s it was reduced to 700K and by 20s it was reduced to 615K. The largest thermal gradient from the fuel centerline to the cladding outer surface was seen during operation. By 20s, the largest temperature gradient was 20K whereas during operation it was 817K. Throughout the SBLOCA, the gradient remained nearly constant in the 15-25K range. The gradient was the lowest when the vapor fraction would approach 1.0. This was due to having essentially two insulating boundaries on the fuel rod, one at the fuel centerline and the other at the cladding outer surface. However, once the rod was quenched and the outer surface cooled, thermal gradients of up 225K existed due to the poor thermal conductivity of $UO_2$.

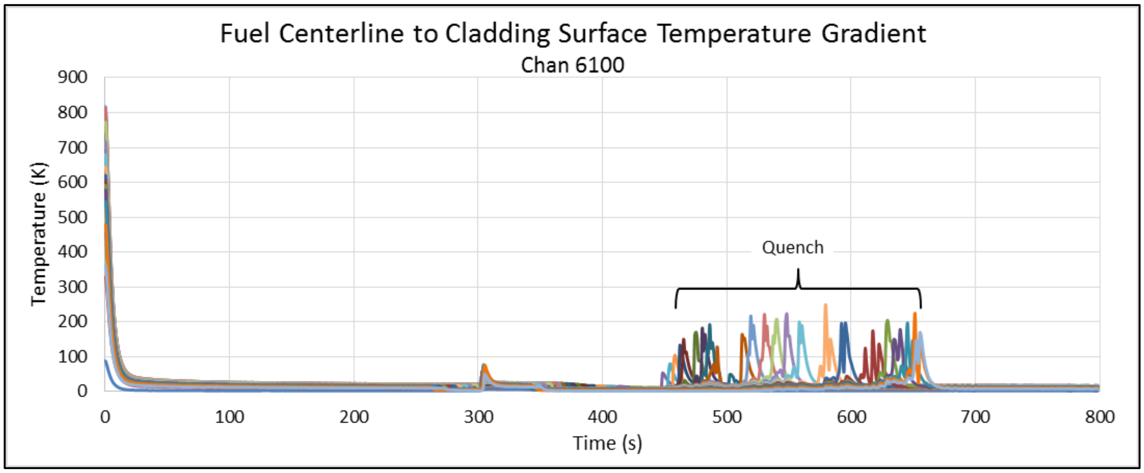

Figure 5.32: Fuel rod temperature gradient for hottest channel during SBLOCA

Despite the higher temperatures in the SBLOCA compared to the LBLOCA, the cladding temperatures for the SBLOCA are again too low to cause any fuel rod failure with the corresponding internal rod pressures. The temperatures were also too low to allow for any transient oxidation to occur. A FRAPTRAN analysis was performed for the SBLOCA but as expected resulted in no cladding plastic deformation or ballooning. No failed fuel rods results in no fuel dispersal for either transient analysis for the GE-BWR/4.

## 5.4 SENSITIVITY ANALYSIS

A sensitivity analysis was performed on the W4LP for both the steady-state and transient analysis on the modeling parameters used in the study and the assumptions used for the fuel dispersal analysis. The modeling parameters analyzed were the nodalization for the axial and radial thermal and mechanical analysis, the fission gas release model and the number of timesteps. The sensitivity to the dispersal analysis was a analyzed by adjusting the minimum cladding strain threshold, burnup relationship to fuel particle size and the maximum particle size allowed for dispersal outside of the cladding. The dispersal analysis is also sensitive to the modeling parameters based on FRAPTRAN's fuel rod failure models.

### 5.4.1 Steady-State Analysis

The FRAPCON analysis performed in the previous studies used the default values for fission gas release and axial/radial thermal-mechanical analysis. The timesteps were also kept within the recommended range (> 0.1 day and <= 50 days). With the modifications made to the code during this study, the ability to increase the nodalization allows for a sensitivity analysis beyond any previous capability with the code. The influence of pressure, fission gas release and cladding oxidation was compared to the reference case with the default nodalization scheme. The sensitivity to each parameter was analyzed individually, with the parameters shown in Table 5.5, resulting in a total of 4,712 cases analyzed (19 sensitivities x 248 cases). Due to the modifications to FRAPCON previously mentioned in which all of the arrays became dynamic, this is the first sensitivity study capable of performing this level of detail.

Table 5.5: Modeling parameters used in FRAPCON sensitivity study

| Sensitivity Case # | # axial nodes (na) | # radial nodes (nr) | Axial/Radial Combination (na x nr) | # fission gas release nodes (ngasr) | Timestep size (im) |
|---|---|---|---|---|---|
| 1 | 21 | 17 | 21 x 17 | 45 | 50 days |
| 2 | 42 | 17 | 42 x 17 | 45 | 50 days |
| 3 | 144 | 17 | 144 x 17 | 45 | 50 days |
| 4 | 389 | 17 | 389 x 17 | 45 | 50 days |
| 5 | 42 | 9 | 42 x 9 | 45 | 50 days |
| 6 | 42 | 17 | 42 x 17 | 45 | 50 days |
| 7 | 42 | 34 | 42 x 34 | 45 | 50 days |
| 8 | 42 | 100 | 42 x 100 | 45 | 50 days |
| 9 | 21 | 9 | 21 x 9 | 45 | 50 days |
| 10 | 42 | 17 | 42 x 17 | 45 | 50 days |
| 11 | 144 | 34 | 144 x 34 | 45 | 50 days |
| 12 | 389 | 100 | 389 x 100 | 45 | 50 days |
| 13 | 42 | 17 | 42 x 17 | 22 | 50 days |
| 14 | 42 | 17 | 42 x 17 | 45 | 50 days |
| 15 | 42 | 17 | 42 x 17 | 90 | 50 days |
| 16 | 42 | 17 | 42 x 17 | 45 | 0.5 day |
| 17 | 42 | 17 | 42 x 17 | 45 | 1 day |
| 18 | 42 | 17 | 42 x 17 | 45 | 5 days |
| 19 | 42 | 17 | 42 x 17 | 45 | 50 days |

The parameters analyzed during the sensitivity study were internal rod pressure, fission gas release and cladding oxidation, all three parameters of interest for LOCA analysis. The axial analysis showed a net decrease in core-average internal rod pressure when increasing the nodalization. The low power rods tended to show a slight increase in internal rod pressure while the high powered rods showed a slight decrease in internal rod pressure. The gram moles of gas produced stayed nearly identical for all cases. The average oxide layer thickness was decreased as the number of nodes increased. The reason for the change in oxide thickness is likely due to the linear interpolation used to determine the coolant temperatures from the conditions (and locations at which the conditions exist) provided from the TRACE analysis. The lower oxide thickness, if a result of slightly lower temperatures at some axial nodes, would contribute (along with the lower coolant conditions) to the decreased internal rod pressure by reducing the thermal resistance of the cladding. The core-average conditions are shown in Table 5.6.

Table 5.6: Influence of axial nodalization on core-average EOC parameters

| **Axial node variation (na)** | | | | |
|---|---|---|---|---|
| | **21** | **42** | **144** | **389** |
| **Internal rod pressure (MPa)** | 9.822 | 9.819 | 9.816 | 9.816 |
| **Gram moles of gas** | 0.01882 | 0.01883 | 0.01883 | 0.01883 |
| **Avg oxide layer thickness (μm)** | 21.01 | 21.089 | 21.084 | 21.083 |

The radial nodalization analysis showed an opposite trend with respect to the number of nodes and internal rod pressure compared to the axial nodalization. Increasing the number of radial nodes increased the internal rod pressure, with the core average pressure increasing by 0.81% from 9 nodes to 100 radial nodes. All of the rods saw an increase in internal rod pressure when increasing the number of radial nodes. The increase in internal rod pressure is likely due to the decrease in free volume that can be occupied by the gas and increase in gas temperature, the result of increased fuel thermal expansion. The increase in fuel thermal expansion with increasing radial nodalization is a result of higher nodal temperatures caused by the linear interpolation of the parabolic temperature profile in the fuel. As with Euler's method of integration, the more divisions made in a non-linear equation the more accurate the prediction is to the true solution. The total fuel surface displacement at EOC is ~2.4 μm greater with 100 radial nodes than 9 radial nodes, resulting in a higher fuel centerline temperature of 5.7K at the hottest point with a volume average temperature increase of ~3K. The oxide thickness was not changed between the cases analyzed, as expected, due to the surface heat flux and coolant conditions being identical between all three cases. The core-average results of the radial discretization are shown in Table 5.7.

Table 5.7: Influence of radial nodalization on core-average EOC parameters

| **Radial node variation (nr)** | | | | |
|---|---|---|---|---|
| | **9** | **17** | **34** | **100** |
| **Internal rod pressure (MPa)** | 9.786 | 9.819 | 9.86 | 9.867 |
| **Gram moles of gas** | 0.0188 | 0.01883 | 0.01883 | 0.01884 |
| **Avg oxide layer thickness (μm)** | 21.089 | 21.089 | 21.089 | 21.089 |

The combination of axial and radial nodalization variations resulted in the same trends as seen in each of the changes of the nodalization individually. As seen with the increase in axial nodalization, the axial oxide layer thickness increased from 21.01μm to 21.083 μm. The internal rod pressure increased with the same trend seen for the radial node variation shown in Table 5.7. The gram moles of gas remained nearly unchanged.

Increasing the number of nodes used in fission gas release modeling was shown to decrease the fission gas release from the fuel into the gas-gap. Consequently, the internal rod pressure also decreases with an increase in the number of fission gas release nodes. As with the radial nodalization, there was no change in cladding oxidation. The results are shown in Table 5.8.

Table 5.8: Influence of fission gas release nodalization on core-average EOC parameters

| **Fission gas release radial node variation (ngasr)** | | | |
|---|---|---|---|
| | **22** | **45** | **90** |
| **Internal rod pressure (MPa)** | 9.821 | 9.819 | 9.818 |
| **Gram moles of gas** | 0.018837 | 0.01882 | 0.01883 |
| **Avg oxide layer thickness (μm)** | 21.089 | 21.089 | 21.089 |

The largest difference in the sensitivity to the modeling parameters was shown when altering the timestep sizes. Two issues with the code were encountered, the first being related to fuel swelling and the second being related to fission gas release. Fuel swelling for $UO_2$ is a function of burnup only, starting after 6 GWd/MTU with a swelling rate of 0.062 volume percent per GWd/MTU, up to 80 GWd/MTU burnup. However, it was noticed that the fuel swelling was different for the cases analyzed - although the nodal burnup values were identical. The difference in fuel swelling resulted in a difference in fuel permanent outward strain, with the 1 day timestep having a smaller value than the 50 day timestep case. This difference in swelling altered both the internal rod pressure (by changing the void volume in the gap) and the cladding strain at EOL (by altering how much the cladding can creep in before hard contact). At BOL, it was also noticed that there were significant differences in fuel centerline temperatures due to the difference in gap conductance. With a nodal burnup of 3.4 GWd/MTU, the centerline temperature for the 1 day timestep case was 49 Kelvin lower than for the case using 50 day timesteps. The differences in fuel displacements calculated by the two analyses are shown in Figure 5.33.

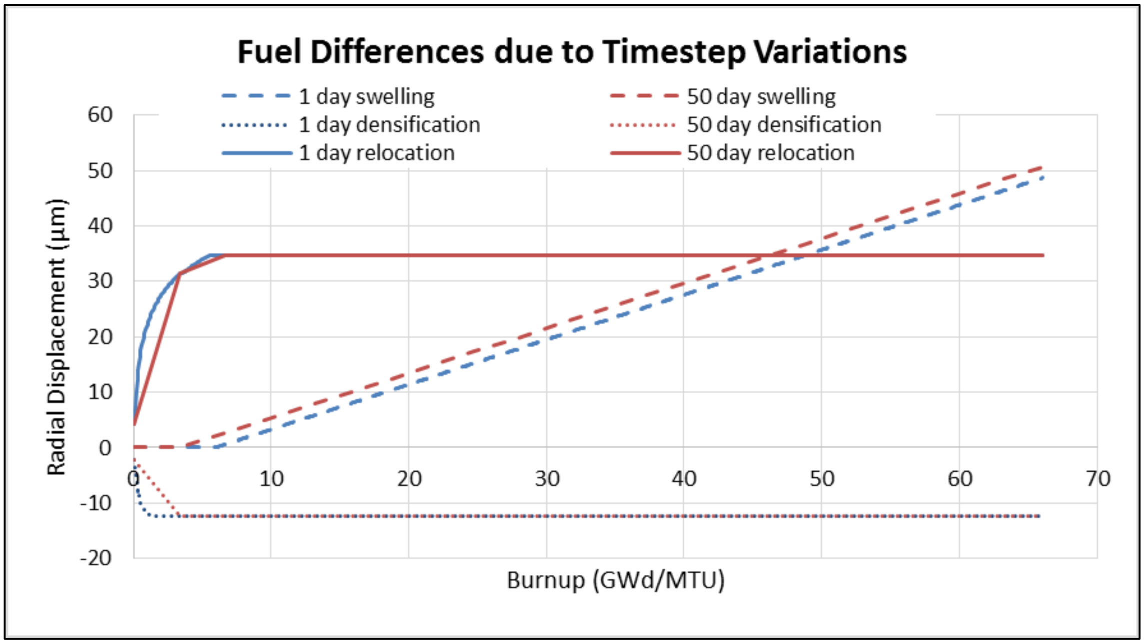

Figure 5.33: Differences in fuel swelling and relocation due to variations in calculation timesteps

The reason for the difference in fuel swelling lies in the way the code is written, which is reproduced in Figure 5.34. Once the burnup exceeds the starting threshold (6

GWd/MTU), the volumetric strain is assumed to have occurred over the entire burnup step. The 50 day timestep case reached the burnup threshold during the second step (at 100 days), meaning that the swelling was applied for the entire 50 day burnup increment. However, the 1 day timestep case reached the threshold at 90 days, meaning that swelling only occurred for 10 – 1 day increments (total of 10 days) rather than an entire 50 day burnup increment. This will need to be better assessed in future work to determine if the coding needs to be re-written to better understand at which point the threshold was reached rather than the assumption that it should be applied over the entire timestep.

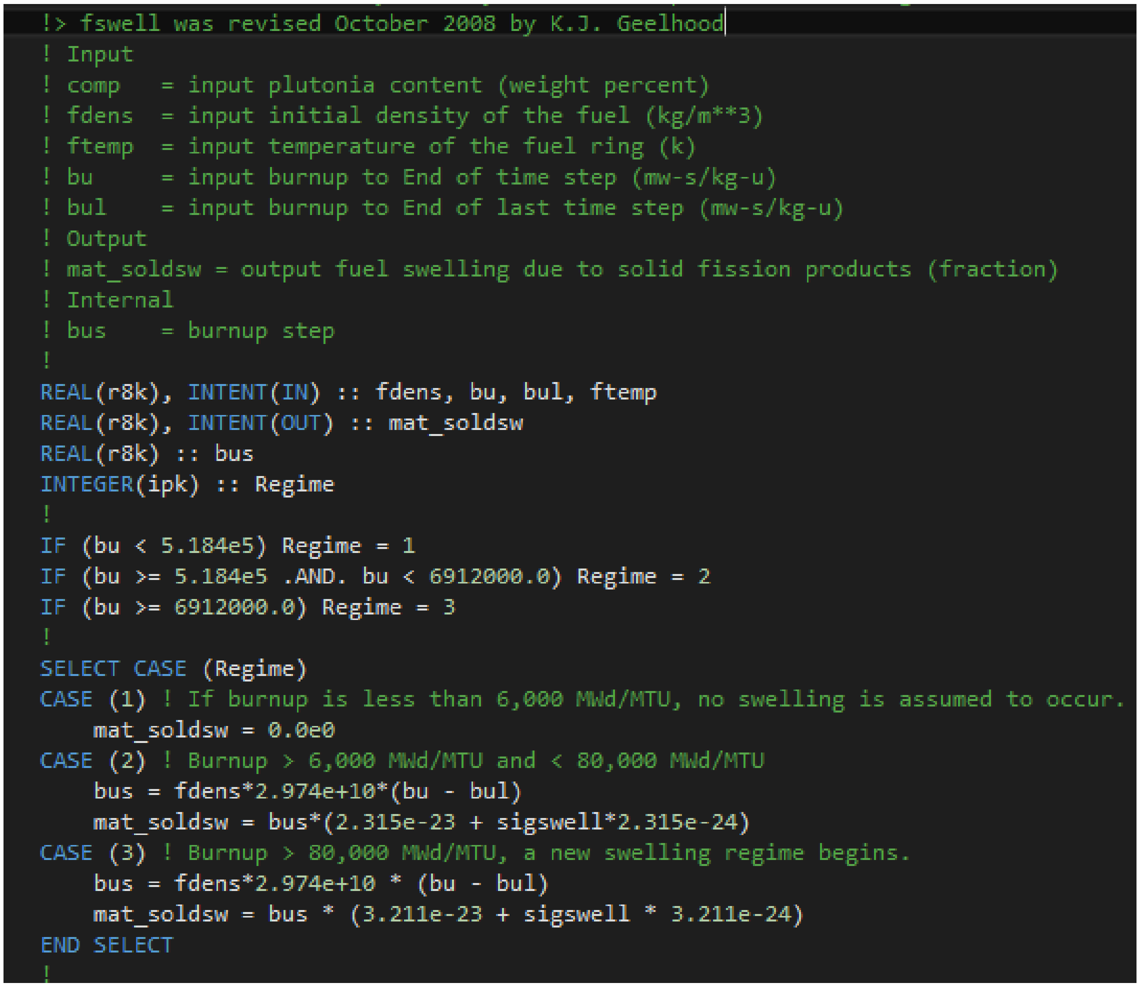

```
!> fswell was revised October 2008 by K.J. Geelhood
! Input
! comp   = input plutonia content (weight percent)
! fdens  = input initial density of the fuel (kg/m**3)
! ftemp  = input temperature of the fuel ring (k)
! bu     = input burnup to End of time step (mw-s/kg-u)
! bul    = input burnup to End of last time step (mw-s/kg-u)
! Output
! mat_soldsw = output fuel swelling due to solid fission products (fraction)
! Internal
! bus    = burnup step
!
REAL(r8k), INTENT(IN) :: fdens, bu, bul, ftemp
REAL(r8k), INTENT(OUT) :: mat_soldsw
REAL(r8k) :: bus
INTEGER(ipk) :: Regime
!
IF (bu < 5.184e5) Regime = 1
IF (bu >= 5.184e5 .AND. bu < 6912000.0) Regime = 2
IF (bu >= 6912000.0) Regime = 3
!
SELECT CASE (Regime)
CASE (1) ! If burnup is less than 6,000 MWd/MTU, no swelling is assumed to occur.
    mat_soldsw = 0.0e0
CASE (2) ! Burnup > 6,000 MWd/MTU and < 80,000 MWd/MTU
    bus = fdens*2.974e+10*(bu - bul)
    mat_soldsw = bus*(2.315e-23 + sigswell*2.315e-24)
CASE (3) ! Burnup > 80,000 MWd/MTU, a new swelling regime begins.
    bus = fdens*2.974e+10 * (bu - bul)
    mat_soldsw = bus * (3.211e-23 + sigswell * 3.211e-24)
END SELECT
!
```

Figure 5.34: FRAPCON code for $UO_2$ swelling

### 5.4.2 Transient Analysis Nodalization

The transient analysis was also analyzed using a variation in axial nodalization. There were several reasons for only the analyzing the sensitivity to the axial nodalization. The differences between the default radial nodalization and the increased nodalization values from the steady-state analysis showed that there were no significant differences in the parameters of interest. Second, the study would be beyond the current capabilities with the available tools/resources due to the increased demand for both computational time and data storage for FRAPTRAN compared to FRAPCON. Lastly, it is believed that the axial nodalization can have a major impact on the quantity of fuel dispersed due to FRAPTRAN's ballooning model. The FRAPTRAN ballooning model assumes that once an axial node reaches the instability strain and begins to balloon, all other axial nodes become fixed and additional permanent cladding deformation for those nodes is stopped. This will lead to differences due to the strain criteria currently employed for dispersal calculations. There are currently no guidelines provided in FRAPTRAN documentation for recommended node size to use for ballooning calculations. The LOCA assessment cases use a wide variation in node size ranging from ~6.0cm – 30.5cm, as shown in Table 5.9.[K.J. Geelhood, 2014]

Table 5.9: Axial nodalization used in LOCA assessment cases for FRAPTRAN-1.5

| Test | Rod Height (m) | Pellet Height (m) | # Axial Nodes | Node Height (m) | # Pellets / Node |
|---|---|---|---|---|---|
| IFA 650-5[1] | Proprietary | Proprietary | 9 | Proprietary | 1.468 |
| IFA 650-6/7[1] | Proprietary | Proprietary | 9 | Proprietary | 1.616 |
| MT-1,4,6A[2] | 3.658 | 9.531E-03 | 12 | 0.305 | 9.754 |
| PBF11C R1-R3[3] | 0.915 | 1.524E-02 | 9 | 0.102 | 2.040 |
| TREAT FRF-2[4] | 0.610 | 1.143E-02 | 10 | 0.061 | 1.627 |

[1] IFA-650 Series testing at Halden reactor
[2] Materials Test 1, 4 & 6 in National Research Universal reactor at Chalk River NL
[3] Power Burst Facility LOC-11C R1-R3
[4] Transient Reactor Test Facility FRF-2 test

Regardless whether the axial node size is 1cm or 100cm, that node is the only one allowed to deform further once ballooning starts. If the node ballooning is the only node that is over the strain limit, then the quantity of fuel contained within that node will be the only fuel allowed to disperse. This means that the quantity of dispersible fuel would be directly correlated to the nodalization used in the analysis, making it an extremely sensitive parameter. An illustration of this sensitivity is shown in Figure 5.35, with indications of the node size used in the assessment cases and the default node size recommended by FRAPTRAN for the full length PWR rods modeled in the W4LP study.

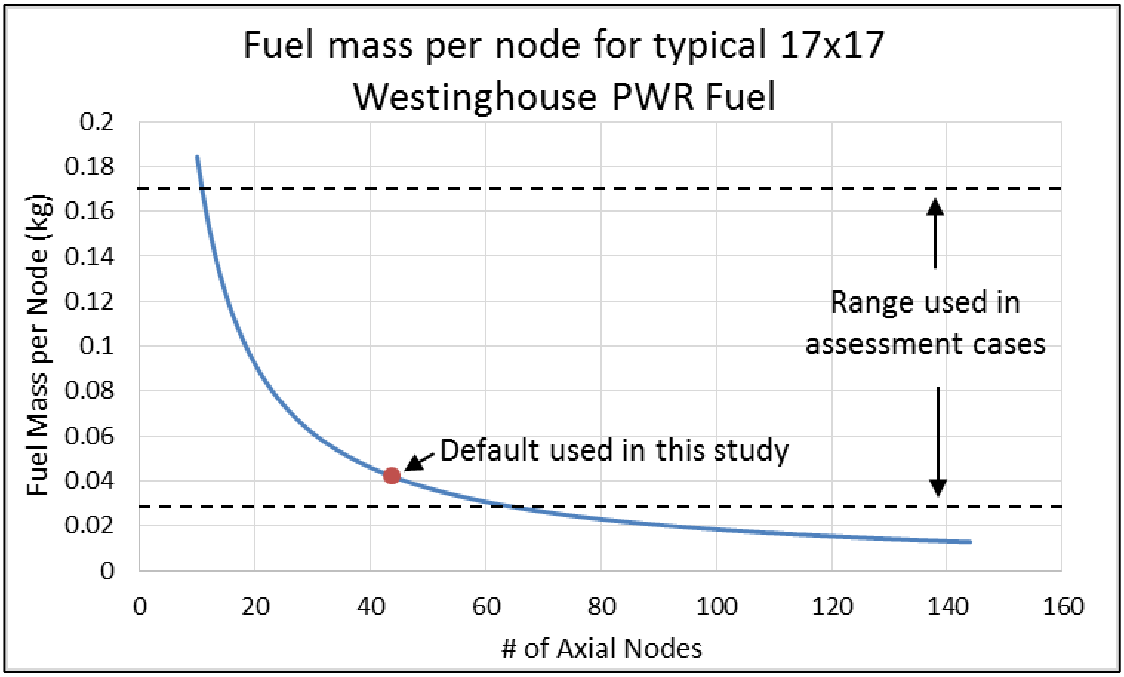

Figure 5.35: Fuel mass per node for typical 17x17 Westinghouse fuel

To assess the sensitivity to the quantity of dispersed fuel, three cases were analyzed with axial nodalization of 21, 42 and 144 nodes. It is important to note that each case required different FRAPCON runs due to the restart file requiring the same number of axial nodes as the FRAPTRAN case. However, as discussed earlier, the sensitivity to the axial nodalization was found to be relatively insignificant, although decreasing the nodalization showed to slightly decrease the internal rod pressure. The total number of fuel rods that failed was noticed to slightly decrease as the number of nodes increased between each analysis, as seen in Table 5.10.

Table 5.10: Sensitivity of core wide fuel rod failure to axial nodalization

| # Axial Nodes | # Rods Failed | Fraction of Core (%) |
|---|---|---|
| 21 | 29964 | 58.81% |
| 42 | 26928 | 52.85% |
| 144 | 26268 | 51.55% |

Each case was then analyzed using a 3%, 5% and 7% cladding strain requirement for dispersible fuel above and below the rupture location. At low cladding strains (3%), no significant differences were noticed between the different axial nodalization. This is due to the fact that cladding strains of 3% were reached before any node reached the instability strain and began the ballooning calculation. Between all three cases, a 3% cladding strain was calculated to occur over a similar axial rod length of approximately 0.25 meters. Therefore, the quantities of dispersed fuel are not sensitive to the node size in this region given that the length of the node was less than the 3% deformation region. This is illustrated in Figure 5.36 for a 1st cycle rod that reaches the maximum allowable ballooning strain due to rod-to-rod contact.

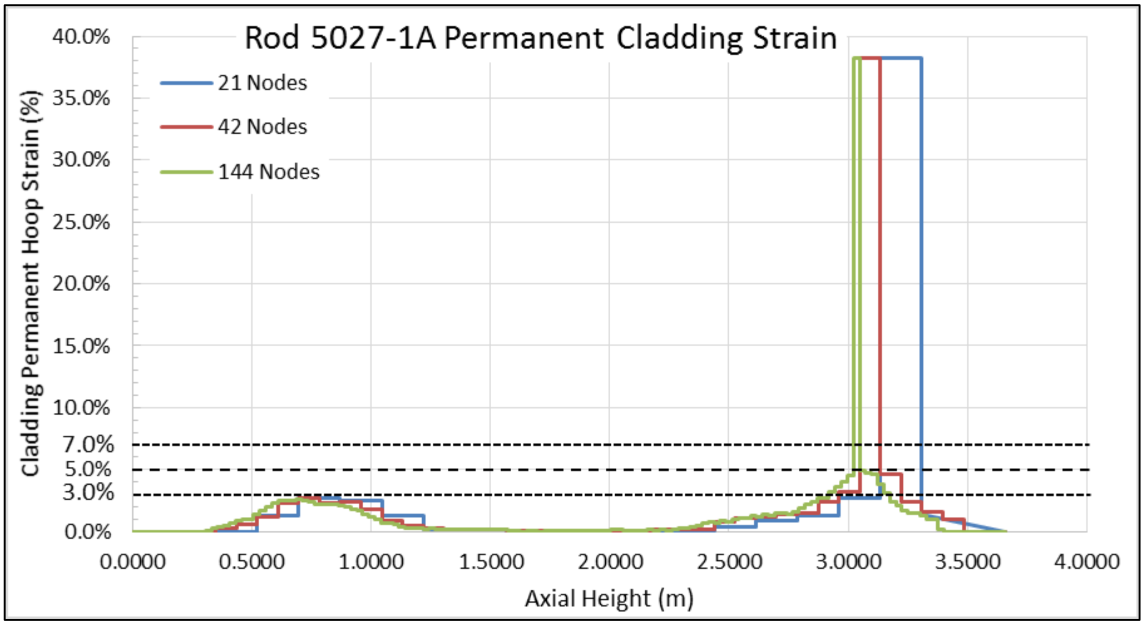

Figure 5.36: Cladding permanent strain calculated by FRAPTRAN for a 1st Cycle Rod at EOC

However, the cladding instability strain was typically reached before a 5% cladding permanent strain was achieved for any node, leading to large differences in the total amount of dispersed fuel with a required cladding strain of at least 5%. At this strain requirement, the quantity of dispersed fuel became largely dependent on the size of the node as a consequence of the only node reaching this point being the ballooning node. The sensitivity of the quantity of dispersed fuel to node size is shown in Figure 5.37, assuming a 1mm particle is able to escape the opening and the burnup transition from coarse to fine particles occurs linearly between 60 and 70 GWd/MTU.

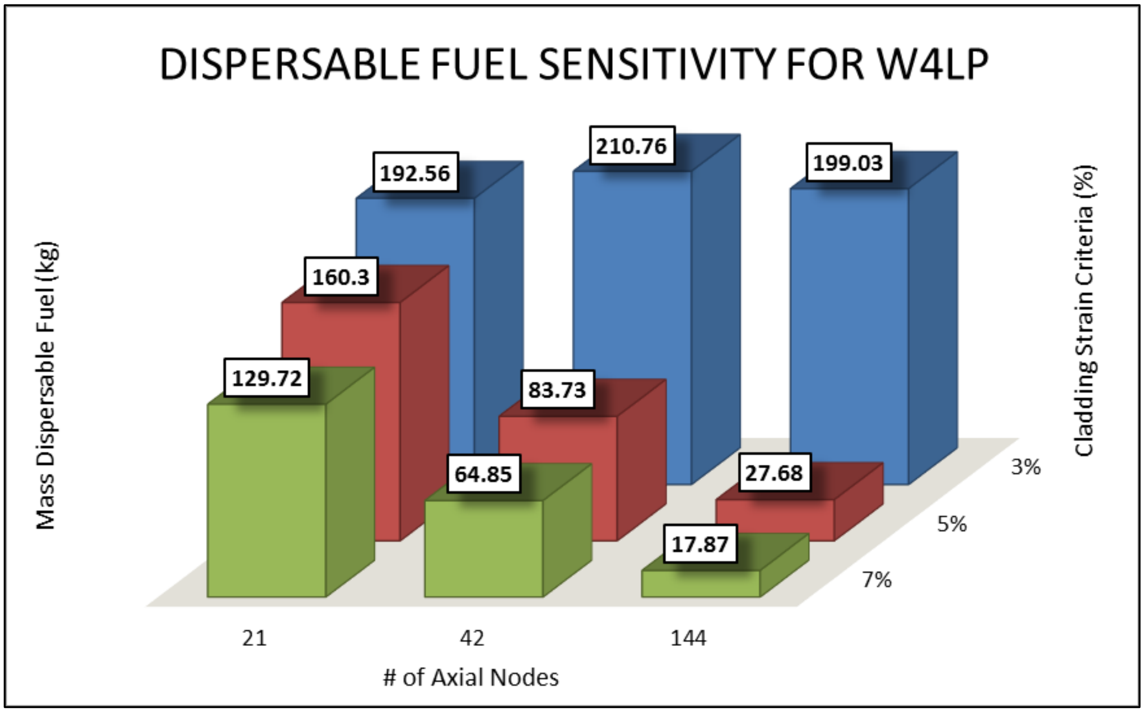

Figure 5.37: Sensitivity of Dispersible Fuel to Axial Nodalization Assuming 1mm Particles are Dispersible with a Particle Size Transition Between 60-70 GWd/MTU

As illustrated in Figure 5.35, both the 21 and 42 axial node cases fall within the range used to analyze rods in the FRAPTRAN LOCA assessment cases. It is clear that the default values for nodalization used in this study do not provide the most conservative estimates of fuel dispersal with cladding strains beyond 3%. Future work should be performed with the FRAPTRAN code to further vet the credibility of only allowing 1 node to balloon over a wide range of node sizes.

### 5.4.3 Individual Rod Analysis

One major goal of this research was to reduce the coarse fuel rod nodalization used in typical LOCA analysis. The study thus far was performed by modeling each assembly individually using an average assembly rod rather than using the typical mass binning of multiple assemblies. Understanding the differences in rod power distribution and the use of IFBA rods within an assembly, it was decided to perform the analysis to the highest level of detail available by modeling each fuel rod individually. All 50,952 rods of the W4LP plant were analyzed through the burnup analysis using FRAPCON and the transient analysis using FRAPTRAN. For the FRAPCON analysis, it was determined which rods were modeled as IFBA rods based on their location within the assembly and the assembly IFBA loading pattern, reproduced in Figure 5.38. Due to the lack of more detailed as-fabricated conditions for the IFBA rods, the internal fill rod pressure was kept the same as the non-IFBA rods.

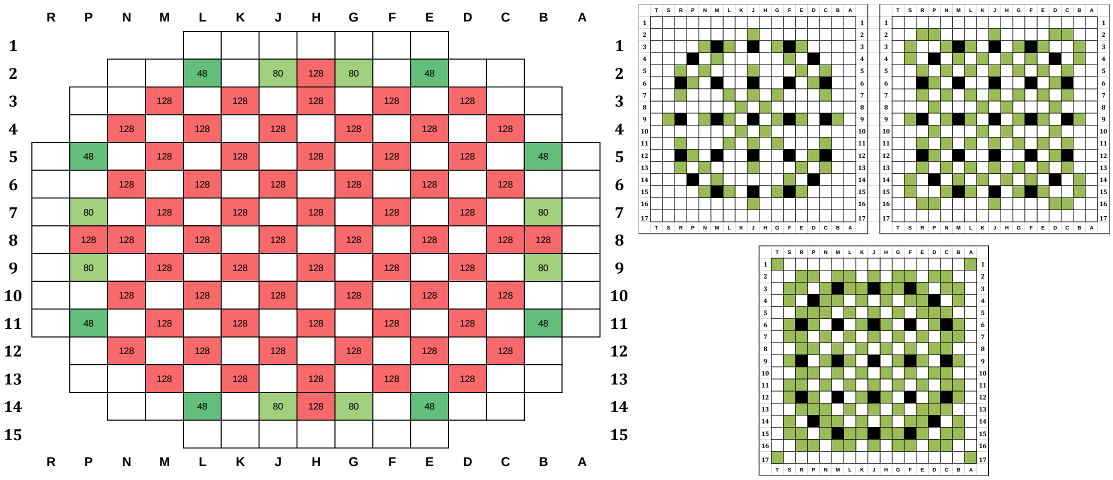

|  | R | P | N | M | L | K | J | H | G | F | E | D | C | B | A |  |
|---|---|---|---|---|---|---|---|---|---|---|---|---|---|---|---|---|
| 1 |  |  |  |  |  |  |  |  |  |  |  |  |  |  |  | 1 |
| 2 |  |  |  |  | 48 |  | 80 | 128 | 80 |  | 48 |  |  |  |  | 2 |
| 3 |  |  |  | 128 |  | 128 |  | 128 |  | 128 |  | 128 |  |  |  | 3 |
| 4 |  |  | 128 |  | 128 |  | 128 |  | 128 |  | 128 |  | 128 |  |  | 4 |
| 5 |  | 48 |  | 128 |  | 128 |  | 128 |  | 128 |  | 128 |  | 48 |  | 5 |
| 6 |  |  | 128 |  | 128 |  | 128 |  | 128 |  | 128 |  | 128 |  |  | 6 |
| 7 |  | 80 |  | 128 |  | 128 |  | 128 |  | 128 |  | 128 |  | 80 |  | 7 |
| 8 |  | 128 | 128 |  | 128 |  | 128 |  | 128 |  | 128 |  | 128 | 128 |  | 8 |
| 9 |  | 80 |  | 128 |  | 128 |  | 128 |  | 128 |  | 128 |  | 80 |  | 9 |
| 10 |  |  | 128 |  | 128 |  | 128 |  | 128 |  | 128 |  | 128 |  |  | 10 |
| 11 |  | 48 |  | 128 |  | 128 |  | 128 |  | 128 |  | 128 |  | 48 |  | 11 |
| 12 |  |  | 128 |  | 128 |  | 128 |  | 128 |  | 128 |  | 128 |  |  | 12 |
| 13 |  |  |  | 128 |  | 128 |  | 128 |  | 128 |  | 128 |  |  |  | 13 |
| 14 |  |  |  |  | 48 |  | 80 | 128 | 80 |  | 48 |  |  |  |  | 14 |
| 15 |  |  |  |  |  |  |  |  |  |  |  |  |  |  |  | 15 |
|  | R | P | N | M | L | K | J | H | G | F | E | D | C | B | A |  |

Figure 5.38: W4LP IFBA Loading Pattern (left), Assembly IFBA loading pattern for 48 rods (top left), 80 rods (top right) and 128 rods (bottom).

The rod power distribution within the assembly was also taken from the W4LP FSAR, which provided an assembly average power distribution at BOL and EOL. Understanding that the assembly average distribution is not truly representative of all assemblies (and due to non-symmetry, will change which rods see certain coolant conditions based on the orientation of the assembly as it is placed in the core), due to lack of additional data this was the most realistic conditions obtainable for this type of analysis. Linear interpolation was used to develop the power histories at time steps between the BOL and EOL states of the rod. The burnup for the highest and lowest rods in the assembly fell within +/- 5% of the assembly average rod. The assembly power distribution at BOL and EOL are reproduced in Figure 5.39.

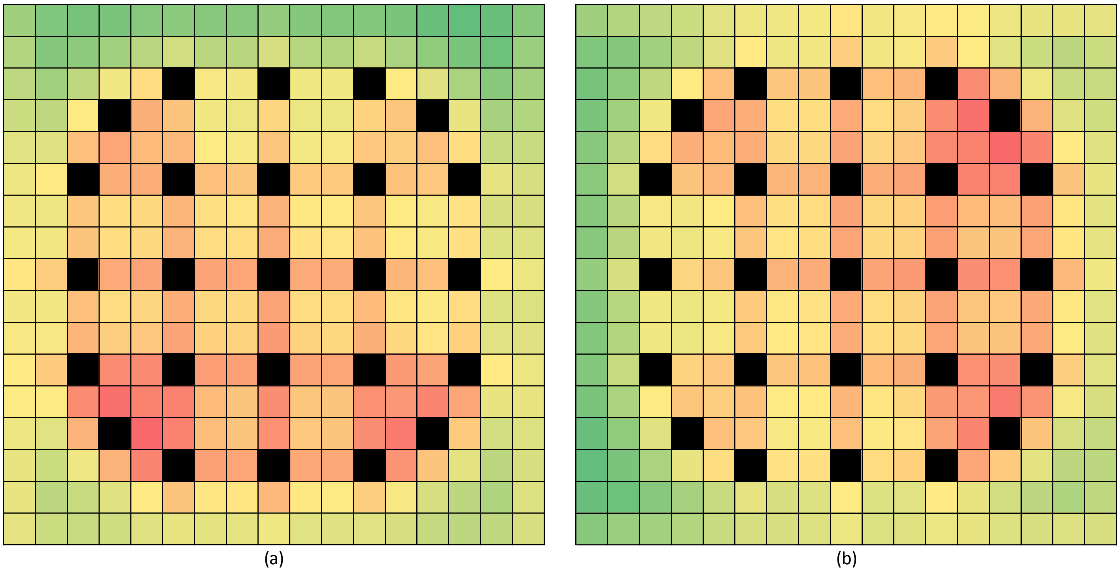

Figure 5.39: Assembly Power Distribution at (a) BOL and (b) EOL

The steady-state analysis yielded similar results between modeling all rods and modeling assembly-average rods. Several important parameters analyzed between both cases are shown in Table 5.11.

Table 5.11: Core average and maximum rod conditions at EOC

| | Core Average Parameters at EOC | | |
|---|---|---|---|
| Modeling Type | Pressure (MPa) | Oxide Thickness (µm) | Stored Energy (kJ) / Total core Stored Energy (GJ) |
| Assembly Average | 9.819 | 21.089 | 324.148 / 16.516 |
| Individual Rods | 9.900 | 21.090 | 324.246 / 16.521 |
| | Core Maximum Parameters at EOC | | |
| | Pressure (MPa) | Oxide Thickness (µm) | Stored Energy (kJ) |
| Assembly Average | 15.352 | 40.322 | 403.200 |
| Individual Rods | 19.681 | 42.690 | 429.050 |

The average internal rod pressure increased from 9.819 to 9.9 MPa, a change of less than 1%. The differences are due to (1) the addition of modeling the IFBA rods and the increased Helium production associated with the B-10 depletion, and (2) capturing the hottest rods whose increased FGR due to the high temperatures was missed by modeling the average rod. The other core average parameters remained relatively unchanged, with the change in average oxide thickness nearly zero and the stored energy increasing by ~0.3%. However, as expected, the maximum rod values were higher for the individual rod analysis. The highest internal rod pressure increased by ~28%, resulting in an internal rod pressure much higher than the system pressure. It should be noted that this was an IFBA rod, and if the fill pressure were lower than the non-IFBA rods, the resulting final pressure would be lower. The assembly with the highest internal rod pressure is shown in Figure 5.40.

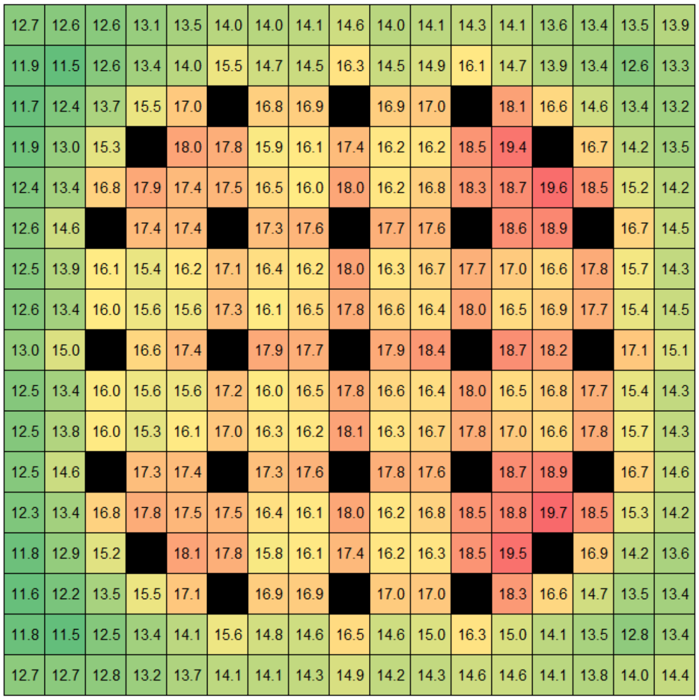

| | | | | | | | | | | | | | | | | |
|---|---|---|---|---|---|---|---|---|---|---|---|---|---|---|---|---|
| 12.7 | 12.6 | 12.6 | 13.1 | 13.5 | 14.0 | 14.0 | 14.1 | 14.6 | 14.0 | 14.1 | 14.3 | 14.1 | 13.6 | 13.4 | 13.5 | 13.9 |
| 11.9 | 11.5 | 12.6 | 13.4 | 14.0 | 15.5 | 14.7 | 14.5 | 16.3 | 14.5 | 14.9 | 16.1 | 14.7 | 13.9 | 13.4 | 12.6 | 13.3 |
| 11.7 | 12.4 | 13.7 | 15.5 | 17.0 | ■ | 16.8 | 16.9 | ■ | 16.9 | 17.0 | ■ | 18.1 | 16.6 | 14.6 | 13.4 | 13.2 |
| 11.9 | 13.0 | 15.3 | ■ | 18.0 | 17.8 | 15.9 | 16.1 | 17.4 | 16.2 | 16.2 | 18.5 | 19.4 | ■ | 16.7 | 14.2 | 13.5 |
| 12.4 | 13.4 | 16.8 | 17.9 | 17.4 | 17.5 | 16.5 | 16.0 | 18.0 | 16.2 | 16.8 | 18.3 | 18.7 | 19.6 | 18.5 | 15.2 | 14.2 |
| 12.6 | 14.6 | ■ | 17.4 | 17.4 | ■ | 17.3 | 17.6 | ■ | 17.7 | 17.6 | ■ | 18.6 | 18.9 | ■ | 16.7 | 14.5 |
| 12.5 | 13.9 | 16.1 | 15.4 | 16.2 | 17.1 | 16.4 | 16.2 | 18.0 | 16.3 | 16.7 | 17.7 | 17.0 | 16.6 | 17.8 | 15.7 | 14.3 |
| 12.6 | 13.4 | 16.0 | 15.6 | 15.6 | 17.3 | 16.1 | 16.5 | 17.8 | 16.6 | 16.4 | 18.0 | 16.5 | 16.9 | 17.7 | 15.4 | 14.5 |
| 13.0 | 15.0 | ■ | 16.6 | 17.4 | ■ | 17.9 | 17.7 | ■ | 17.9 | 18.4 | ■ | 18.7 | 18.2 | ■ | 17.1 | 15.1 |
| 12.5 | 13.4 | 16.0 | 15.6 | 15.6 | 17.2 | 16.0 | 16.5 | 17.8 | 16.6 | 16.4 | 18.0 | 16.5 | 16.8 | 17.7 | 15.4 | 14.3 |
| 12.5 | 13.8 | 16.0 | 15.3 | 16.1 | 17.0 | 16.3 | 16.2 | 18.1 | 16.3 | 16.7 | 17.8 | 17.0 | 16.6 | 17.8 | 15.7 | 14.3 |
| 12.5 | 14.6 | ■ | 17.3 | 17.4 | ■ | 17.3 | 17.6 | ■ | 17.8 | 17.6 | ■ | 18.7 | 18.9 | ■ | 16.7 | 14.6 |
| 12.3 | 13.4 | 16.8 | 17.8 | 17.5 | 17.5 | 16.4 | 16.1 | 18.0 | 16.2 | 16.8 | 18.5 | 18.8 | 19.7 | 18.5 | 15.3 | 14.2 |
| 11.8 | 12.9 | 15.2 | ■ | 18.1 | 17.8 | 15.8 | 16.1 | 17.4 | 16.2 | 16.3 | 18.5 | 19.5 | ■ | 16.9 | 14.2 | 13.6 |
| 11.6 | 12.2 | 13.5 | 15.5 | 17.1 | ■ | 16.9 | 16.9 | ■ | 17.0 | 17.0 | ■ | 18.3 | 16.6 | 14.7 | 13.5 | 13.4 |
| 11.8 | 11.5 | 12.5 | 13.4 | 14.1 | 15.6 | 14.8 | 14.6 | 16.5 | 14.6 | 15.0 | 16.3 | 15.0 | 14.1 | 13.5 | 12.8 | 13.4 |
| 12.7 | 12.7 | 12.8 | 13.2 | 13.7 | 14.1 | 14.1 | 14.3 | 14.9 | 14.2 | 14.3 | 14.6 | 14.6 | 14.1 | 13.8 | 14.0 | 14.4 |

Figure 5.40: Internal rod pressure analysis for highest powered 128 IFBA rod assembly (MPa)

The maximum average oxide thickness increased by ~5.9%, resulting in an increased average ECR to ~7.5% (from ~7%). The highest stored energy increased by

~6.4%. The FRAPCON individual rod analysis for the entire core shows that an assembly-average analysis is a very good representation of the average fuel rod conditions existing in the core. Although the peaking rods are missed, their conditions are well balanced by the lower powered rods.

For the coolant conditions using TRACE, it was quickly determined that the capabilities of the code will not allow for modeling in this fine of detail. The current analysis required the use of a specially developed executable to handle the memory requirements, so simplifications were made to determine the boundary conditions for the individual rods. The assembly average heat structure was again modeled in TRACE, using peaking rods to model the highest and lowest power in the assembly at EOC. The conditions imposed on FRAPTRAN were taken in the same manner as before, however this time using a linear interpolation function to predict the conditions for the individual rods. If the rod power was below the assembly average power, the linear interpolation was performed off of the lowest power rod and the assembly average rod by using the power of the rod being analyzed. The same process was repeated for higher powered rods, using the linear interpolation from the assembly average rod and the highest power rod.

As would be expected, the high powered peaking rods had higher PCT than the assembly average rods while the low powered peaking rods had lower PCT. The overall maximum temperatures were 1102.7, 1128.5 and 1144.0K for the low, average and high powered rods respectively. The PCT for each rod type is shown in Figure 5. 41. The figure also shows that there are slight differences in the times at which the cladding is cooled back down to the coolant temperature, with the later times corresponding to the higher power rods.

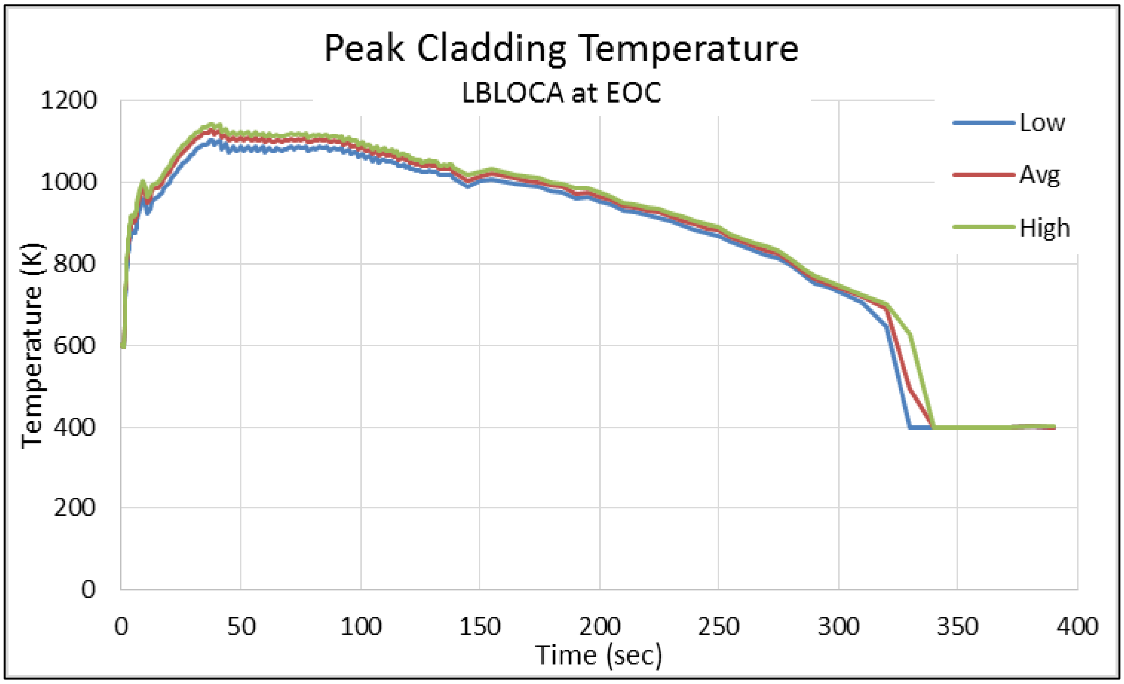

Figure 5.41: Overall peak cladding temperature (PCT) for low-powered rod, average rod and high-powered rod modeled within each assembly of the core.

The FRAPTRAN analysis was conducted using the average rod, low-powered rod and high-powered rod for each assembly. In order to assess if the assembly-average rod analysis produced a good representation of the number of failed rods in the core, the rods in the assembly were subdivided into three groups with 11% represented by the low-powered rod, 72.3% by the assembly average rod and the remaining 16.7% by the high-powered rod. The fraction represented by each rod type was based on the relative number of rods within the assembly that fell in the power ranges analyzed. As expected, there were several assemblies that had a peaking rod fail but the assembly average rod did not fail, while similarly there were assemblies where the average rod failed but the lowest powered rod did not. Out of the 248 heat structures modeled in TRACE (representing 193 assemblies), 149 peak rods failed, 140 assembly average rods failed and 125 low powered rods failed (indicating the entire assembly would have failed). The total number of failed rods was decreased by 0.7% compared to using the assembly-average rod analysis. It is important to understand that by going into this level of detail, the computational time for the TRACE run was increased ~400% (to 11.3 days) and the FRAPTRAN analysis time was increased by 3x while only providing a minimal amount of additional clarity in the overall results.

### 5.5 ADVANCED MATERIALS

The advanced fuel and cladding materials were analyzed under both steady-state and transient conditions for the W4LP. It was assumed that all of the fuel in the core was homogeneous and kept as consistent as reasonably possible to the typical 17x17 Westinghouse fuel assembly design. The fuel designs for each combination were optimized to negate the possibility of PCMI before the onset of the LOCA. The stored energy in the core, the cladding PCT and the # of failed rods were analyzed for comparison to the typical $UO_2$/Zirc core. The fuel combinations analyzed are shown in Table 5.12.

Table 5.12: Fuel designs analyzed for typical W4LP steady-state and transient analysis

| **Design** | **Fuel** | **Cladding** |
|---|---|---|
| 1 | $UO_2$ | ZIRLO$^{TM}$ |
| 2 | $UO_2$ | SiC |
| 3 | UC | SiC |
| 4 | UN | SiC |
| 5 | $U_3Si_2$ | SiC |

### 5.5.1 Fuel Design

Due to the brittle nature of SiC coupled with its high elastic modulus, the ideal design with SiC would assume that no PCMI occurs. With FRAPCON's rigid pellet model, any expansion of the fuel onto the cladding results in the same strain applied to both materials. Therefore, in the absence of creep with a high elastic modulus, a small strain can result in cladding failure. Due to the W4LP being limited by its thermal rating, the

LHGR of the fuel rods is kept identical. The fuel assembly outer dimensions are also kept identical as to allow for direct replacement of the current fuel. The rod-to-rod pitch and cladding outer diameter were kept constant. However, the cladding thickness was increased for SiC based on the available dimensions provided for Westinghouse Duplex SiC cladding tube design. This design consists of a monolithic dense SiC inner layer (12-20 mils) and a SiC/SiC composite layer (12-15 mils).[Lars Hallstadius, 2012] Due to the range of cladding thicknesses, the average value for each layer was used in the analysis. The SiC cladding resulted in a thickness of 29.5 mils (0.7493 mm), which is ~1.3 times thicker than typical Zirconium based PWR claddings. This increase in cladding thickness, with the same cladding outer diameter (OD) dimensions, will result in a smaller fuel radius than with $UO_2$. However, the higher uranium density will allow the advanced fuels to achieve similar burnup values, understanding that the advanced fuels were designed to reach burnup beyond that of $UO_2$. The uranium density of each fuel design is shown in Table 5.13.

Table 5.13: Uranium density for current and advanced fuels

|  | $UO_2$ | UC | UN | $U_3Si_2$ |
|---|---|---|---|---|
| Theoretical density (g/cm$^3$) | 10.96 | 13.63 | 14.32 | 12.2 |
| Uranium fraction | 0.881 | 0.952 | 0.944 | 0.927 |
| Uranium density (g/cm$^3$) | 9.661 | 12.974 | 13.524 | 11.313 |
| Relative uranium mass | 1 | 1.343 | 1.4 | 1.171 |

With a fixed cladding OD, and a cladding thickness of 0.7493mm, the fuel diameter is estimated based on variations in gap thickness that result in no PCMI. Variations in fuel dimensions from the original design will play a role in reaching equivalent burnup values between fuel types, as depicted in Figure 5.42. Decreasing the fuel radius decreases the mass of uranium, therefore shorting the time at power required to achieve the same burnup value. By decreasing the fuel radius, the void volume increases thus allowing for more space to be occupied by the gases (thus in theory a lower rod pressure – however, increased temperatures due to larger thermal resistance may negate this advantage).

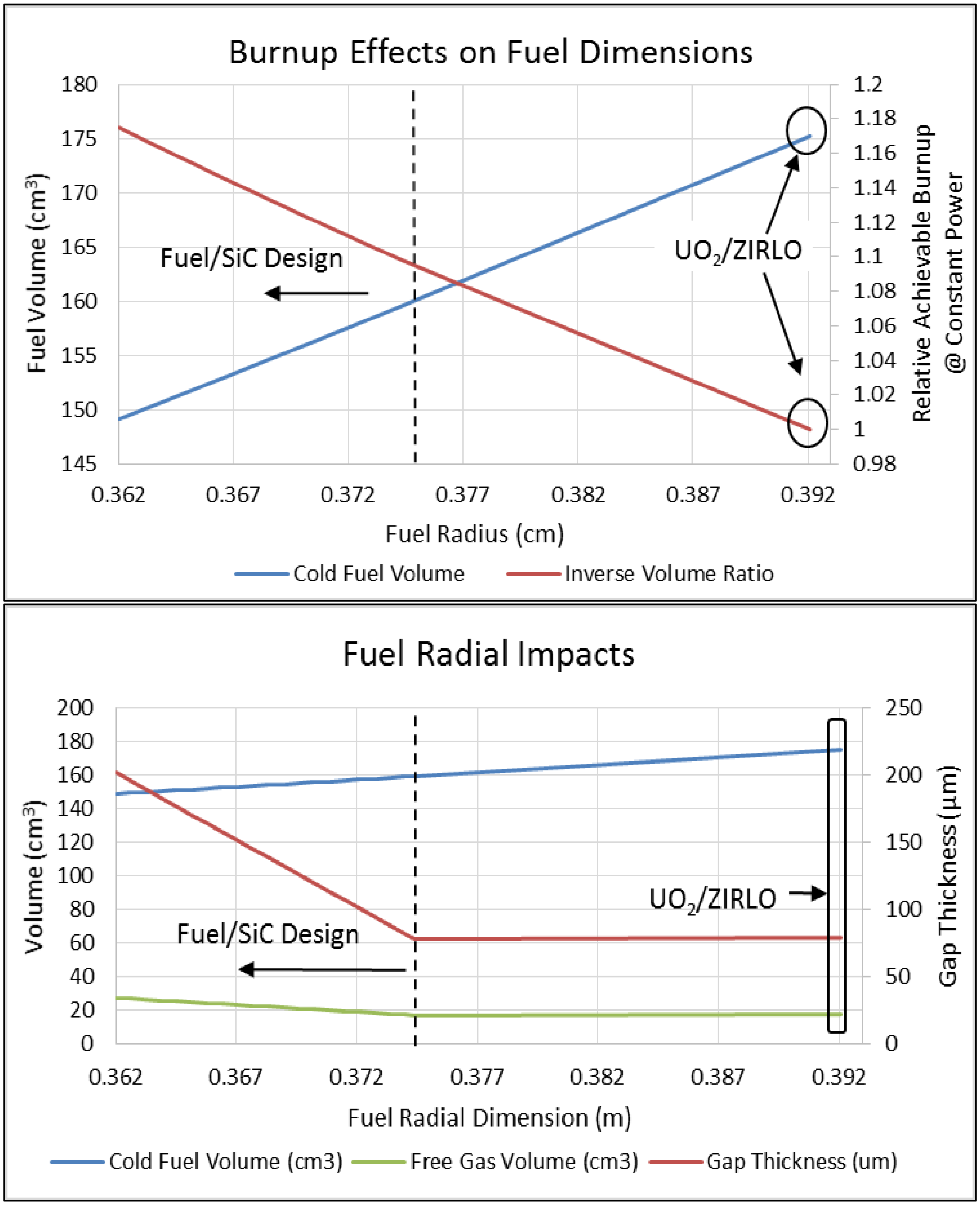

Figure 5.42: Effects of changing fuel dimensions on relative burnup

Understanding uncertainties in measured data for fuel swelling on the limited available data, a 5% uncertainty will be assumed in the swelling values to require that the fuel stop short of reaching the cladding under realistic operation. The distance the fuel must stop short of the cladding is illustrated in Figure 5.43 based on the EOC burnup. However, for the core analysis the 5% increase in swelling will not be assumed.

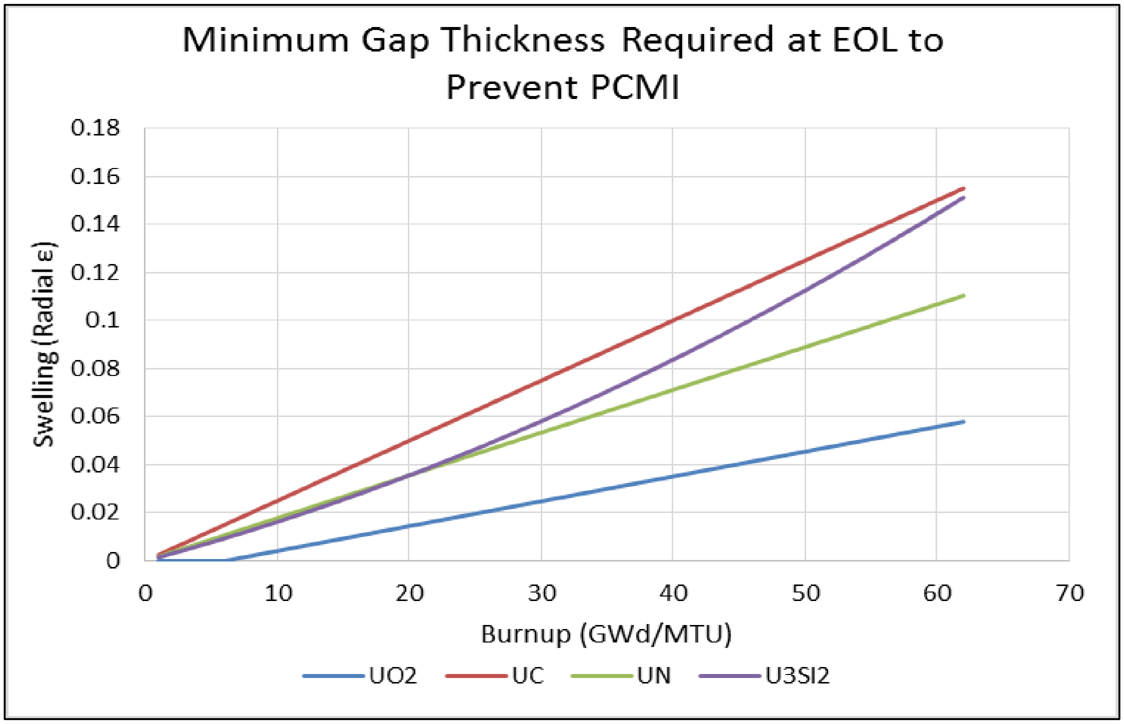

Figure 5.43: Minimum fuel strain that must be left before reaching the cladding in order be acceptable for use in W4LP design, assuming a 5% uncertainty in fuel swelling

The highest powered 2nd and 3rd cycle rods will be analyzed by using known assembly peaking factors and intra-assembly rod peaking factors throughout the cycle for a typical W4LP. For the intra-assembly analysis, the rod with the highest peaking factor at BOL, the highest peaking factor at EOL and the overall highest average peaking factor will be analyzed (illustrated previously by the assembly power distribution in Figure 5.39). The highest power rods are the most limiting rods when the only deformation mechanisms are fuel swelling and thermal expansion, dependent on burnup and fuel temperatures, respectively. The worst-case assembly in the core was determined by analyzing the maximum interfacial pressure between the fuel and cladding at all axial locations, based on the aforementioned goal of having no interfacial pressure. The fuel radius was continually decreased until no hard contact was made for all of the cases modeled. The power history and burnups of the most limiting rods analyzed are shown in Figure 5.44 and Table 5.14, respectively.

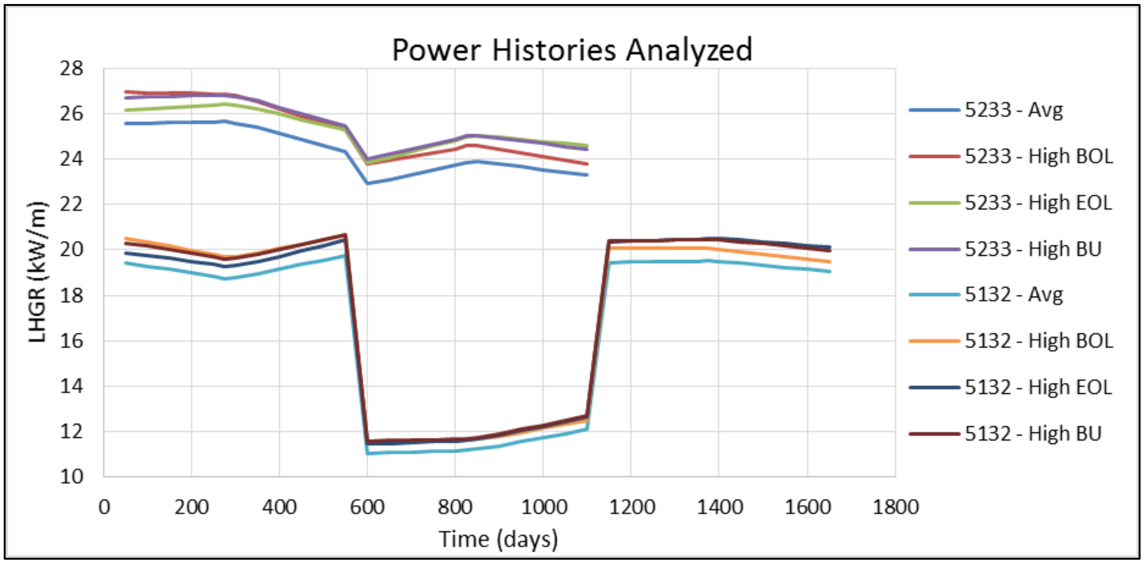

Figure 5.44: Power histories analyzed for each fuel design to determine most limiting fuel rod

Table 5.14: Burnups for most limiting rods

| | Rod Burnup (MWd/MTU) | |
|---|---|---|
| Power History | 5233 (1A2A) | 5132 (1T2V3A) |
| Average | 60941 | 62519 |
| Highest BOL Power | 63293 | 64923 |
| Highest EOL Power | 63341 | 64992 |
| Highest Burnup | 63810 | 65464 |

Due to the poor thermal conductivity of the $UO_2$ fuel combined with the relatively low fuel swelling rate, the most limiting fuel rod was the highest burnup 2nd cycle rod (denoted 5233 – High BU in Figure 5.44). This was the hottest rod with only slightly less burnup than the rods in the other assembly, indicating that the thermal expansion was a major contributor to PCMI. This is further illustrated by the fact that the fuel radius of the most limiting rod in assembly 5132 needed to be reduced by 1.44%, whereas the most limiting rod in assembly 5233 needed to be reduced by 2.14%, indicating a decreased fuel radius by a factor of ~1.5. Although the decreasing fuel radius increases the void volume, the increased thermal resistance caused an increase in temperatures that correspondingly increased both fission gas release and internal rod pressure. The pressure values are significantly higher (>2-3x) than those obtained for $UO_2$/Zirc, attributable to both increased thermal resistance of the gap and of the cladding. The results of interfacial pressure and corresponding internal rod pressure are shown in Table 5.15.

Table 5.15: Interfacial pressure and internal rod pressure for $UO_2$/SiC fuel design for most limiting rods in W4LP

| Fuel Radius (cm) | $UO_2$ Interfacial Pressure (MPa) | | | | | | | |
|---|---|---|---|---|---|---|---|---|
| | 5233 - Avg | 5233 - High BOL | 5233 - High EOL | 5233 - High BU | 5132 - Avg | 5132 - High BOL | 5132 - High EOL | 5132 - High BU |
| 0.3744 | 996.78 | 1064.96 | 1083.72 | 1086.61 | 519.88 | 625.6 | 715.88 | 707.82 |
| 0.374 | 938.03 | 1006.01 | 1024.42 | 1027.66 | 464.22 | 569.62 | 658.37 | 650.78 |
| 0.3734 | 852.74 | 920.66 | 938.58 | 941.89 | 380.47 | 485.72 | 573.86 | 566.57 |
| 0.3728 | 766.28 | 833.85 | 851.5 | 855.23 | 297.61 | 402.07 | 489.59 | 482.64 |
| 0.3721 | 665.9 | 733.6 | 750.7 | 754.84 | 201.55 | 305.35 | 392.35 | 385.4 |
| 0.3715 | 581.54 | 649.21 | 665.74 | 670.33 | 119.49 | 222.94 | 308.84 | 302.4 |
| 0.3709 | 496.55 | 564 | 580.35 | 585.19 | 37.98 | 141.44 | 226.46 | 220.03 |
| 0.3702 | 398.92 | 466.4 | 481.97 | 487.47 | 0 | 47.06 | 130.65 | 124.55 |
| 0.3696 | 315.13 | 382.29 | 397.37 | 403.16 | 0 | 0 | 48.83 | 42.78 |
| 0.369 | 231.62 | 298.53 | 313.26 | 319.34 | 0 | 0 | 0 | 0 |
| 0.3683 | 135.86 | 202.29 | 216.12 | 222.54 | 0 | 0 | 0 | 0 |
| 0.3677 | 53.73 | 120.14 | 133.01 | 140.17 | 0 | 0 | 0 | 0 |
| 0.3671 | 0 | 0 | 50.33 | 58.22 | 0 | 0 | 0 | 0 |
| 0.3664 | 0 | 0 | 0 | 0 | 0 | 0 | 0 | 0 |
| 0.3658 | 0 | 0 | 0 | 0 | 0 | 0 | 0 | 0 |

| Fuel Radius (cm) | $UO_2$ Internal Rod Pressure (MPa) | | | | | | | |
|---|---|---|---|---|---|---|---|---|
| | 5233 - Avg | 5233 - High BOL | 5233 - High EOL | 5233 - High BU | 5132 - Avg | 5132 - High BOL | 5132 - High EOL | 5132 - High BU |
| 0.3744 | 26.929 | 31.14 | 33.341 | 33.537 | 15.967 | 18.795 | 20.498 | 20.464 |
| 0.374 | 27.279 | 31.473 | 33.7 | 33.936 | 16.309 | 19.106 | 20.753 | 20.802 |
| 0.3734 | 27.867 | 32.22 | 34.427 | 34.571 | 16.654 | 19.486 | 21.135 | 21.185 |
| 0.3728 | 28.389 | 32.772 | 35.039 | 35.26 | 17.026 | 19.875 | 21.561 | 21.653 |
| 0.3721 | 29.069 | 33.481 | 35.862 | 36.046 | 17.319 | 20.211 | 22.187 | 22.123 |
| 0.3715 | 29.583 | 34.269 | 36.527 | 36.761 | 17.381 | 20.467 | 22.344 | 22.516 |
| 0.3709 | 30.114 | 34.924 | 37.443 | 37.555 | 17.398 | 20.586 | 22.576 | 22.609 |
| 0.3702 | 30.888 | 35.948 | 38.489 | 38.64 | 17.226 | 20.44 | 22.577 | 22.596 |
| 0.3696 | 31.522 | 36.659 | 39.309 | 39.446 | 17.07 | 20.404 | 22.464 | 22.428 |
| 0.369 | 31.759 | 37.281 | 40.042 | 40.294 | 17.006 | 20.244 | 22.131 | 22.085 |
| 0.3683 | 32.306 | 37.952 | 40.97 | 41.138 | 17.324 | 20.111 | 21.879 | 22.04 |
| 0.3677 | 32.502 | 38.445 | 41.472 | 41.716 | 17.745 | 20.421 | 21.997 | 22.215 |
| 0.3671 | 32.578 | 38.343 | 41.898 | 42.069 | 18.15 | 21.007 | 22.38 | 22.508 |
| 0.3664 | 32.506 | 38.579 | 41.737 | 41.957 | 18.99 | 21.848 | 23.117 | 23.256 |
| 0.3658 | 33.139 | 38.66 | 41.653 | 41.843 | 20.018 | 22.87 | 24.075 | 24.206 |
| 0.3652 | 33.623 | 39.152 | 41.814 | 42.187 | 21.244 | 23.996 | 25.254 | 25.359 |
| 0.3645 | 34.911 | 40.051 | 42.387 | 42.661 | 22.71 | 25.56 | 26.736 | 26.835 |

The worst rod in the core for the $U_3Si_2$/SiC fuel design was the overall highest burnup rod in the core (a 3rd cycle fuel rod with an average peaking factor within the assembly of 1.047, denoted 5132 – High BU in Figure 5.44). Unlike the UO2/SiC case, the increased thermal conductivity offset the thermal expansion so that the fuel swelling was the main driving force for contact. To reach a state of no PCMI, the fuel radius was decreased by 1.44%. The internal rod pressure also increased with increasing gap thickness due to increased fuel (and consequently, gas) temperatures, but not to the same extreme as seen with UO2. A slight drop in rod pressure was noticed for most cases once the gas-gap reached a sufficiently high value due to the combined effects of increased void volume and good fuel thermal conductivity. The results of the analysis are shown in Table 5.16.

Table 5.16: Interfacial pressure and internal rod pressure for $U_3Si_2$/SiC fuel design for most limiting rods in W4LP

| Fuel Radius (cm) | $U_3Si_2$ Interfacial Pressure (MPa) | | | | | | | |
|---|---|---|---|---|---|---|---|---|
| | 5233 - Avg | 5233 - High BOL | 5233 - High EOL | 5233 - High BU | 5132 - Avg | 5132 - High BOL | 5132 - High EOL | 5132 - High BU |
| 0.3744 | 770.21 | 869.5 | 854.19 | 861.43 | 798.48 | 890.6 | 882.8 | 911.35 |
| 0.374 | 682.23 | 797.31 | 772.97 | 812.69 | 731.33 | 817.51 | 797.72 | 847.57 |
| 0.3734 | 585.25 | 688.97 | 695.13 | 702.92 | 623.79 | 709.47 | 722.36 | 736.64 |
| 0.3728 | 462.13 | 580.53 | 592.36 | 585.08 | 506.09 | 592.52 | 608.19 | 620.54 |
| 0.3721 | 345.32 | 453.9 | 443.75 | 458.36 | 375.07 | 471.31 | 484.98 | 502.95 |
| 0.3715 | 218.78 | 344.2 | 333.69 | 374.05 | 268.77 | 367.49 | 377.23 | 392.12 |
| 0.3709 | 139.78 | 243.11 | 251.71 | 230.28 | 163.82 | 265.81 | 272.92 | 283.31 |
| 0.3702 | 0 | 89.71 | 120.4 | 104.06 | 36.93 | 132.45 | 127.23 | 150.78 |
| 0.3696 | 0 | 0 | 0 | 0 | 0 | 31.35 | 35.06 | 41.22 |
| 0.369 | 0 | 0 | 0 | 0 | 0 | 0 | 0 | 0 |
| 0.3683 | 0 | 0 | 0 | 0 | 0 | 0 | 0 | 0 |

| Fuel Radius (cm) | $U_3Si_2$ Internal Rod Pressure (MPa) | | | | | | | |
|---|---|---|---|---|---|---|---|---|
| | 5233 - Avg | 5233 - High BOL | 5233 - High EOL | 5233 - High BU | 5132 - Avg | 5132 - High BOL | 5132 - High EOL | 5132 - High BU |
| 0.3744 | 15.398 | 16.066 | 16.036 | 16.242 | 15.19 | 15.669 | 15.731 | 15.796 |
| 0.374 | 15.948 | 16.618 | 16.594 | 16.757 | 15.718 | 16.239 | 16.288 | 16.374 |
| 0.3734 | 16.779 | 17.517 | 17.536 | 17.636 | 16.555 | 17.125 | 17.181 | 17.264 |
| 0.3728 | 17.632 | 18.407 | 18.489 | 18.573 | 17.409 | 17.981 | 18.077 | 18.192 |
| 0.3721 | 18.669 | 19.49 | 19.585 | 19.724 | 18.445 | 19.034 | 19.147 | 19.235 |
| 0.3715 | 19.651 | 20.561 | 20.636 | 20.776 | 19.395 | 20.021 | 20.155 | 20.245 |
| 0.3709 | 20.624 | 21.543 | 21.717 | 21.787 | 20.325 | 21.076 | 21.228 | 21.243 |
| 0.3702 | 20.947 | 22.604 | 22.879 | 22.989 | 20.935 | 22.237 | 22.391 | 22.478 |
| 0.3696 | 20.37 | 22.59 | 22.829 | 23.302 | 20.338 | 22.525 | 22.699 | 23.113 |
| 0.369 | 19.849 | 22.502 | 22.799 | 23.219 | 19.71 | 21.743 | 22.012 | 22.521 |
| 0.3683 | 19.904 | 22.514 | 23.389 | 23.784 | 19.047 | 20.972 | 21.17 | 21.612 |

As with $U_3Si_2$, the most limiting rod for the UC/SiC fuel design was the highest overall burnup rod due to the improved thermal conductivity and increased swelling. The swelling rate implemented for UC resulted in the highest fuel swelling, requiring a larger gap to eliminate PCMI. The gap thickness was increased by ~20% compared to $U_3Si_2$ and by ~100% compared to the 17x17 Westinghouse $UO_2$/Zirc design. The required fuel dimension is the same size as the UO2/SiC design. The analysis for UC/SiC is shown in Table 5.17.

Table 5.17: Interfacial pressure and internal rod pressure for UC/SiC fuel design for most limiting rods in W4LP

| Fuel Radius (cm) | UC Interfacial Pressure (MPa) | | | | | | | |
|---|---|---|---|---|---|---|---|---|
| | 5233 - Avg | 5233 - High BOL | 5233 - High EOL | 5233 - High BU | 5132 - Avg | 5132 - High BOL | 5132 - High EOL | 5132 - High BU |
| 0.3744 | 1320.76 | 1403.91 | 1411.36 | 1425.91 | 1343.86 | 1427.9 | 1434.94 | 1449.83 |
| 0.374 | 1248.23 | 1331.79 | 1339.24 | 1353.92 | 1271.6 | 1355.99 | 1363.09 | 1377.99 |
| 0.3734 | 1139.29 | 1223.54 | 1230.99 | 1245.75 | 1163.08 | 1248.09 | 1255.19 | 1270.22 |
| 0.3728 | 1030.35 | 1115.16 | 1122.67 | 1137.57 | 1054.48 | 1140.12 | 1147.22 | 1162.39 |
| 0.3721 | 903.14 | 988.71 | 996.22 | 1011.19 | 927.69 | 1014.01 | 1021.18 | 1036.42 |
| 0.3715 | 794 | 880.18 | 887.7 | 902.8 | 818.96 | 905.83 | 913 | 928.38 |
| 0.3709 | 684.79 | 771.59 | 779.11 | 794.35 | 710.09 | 797.59 | 804.83 | 820.27 |
| 0.3702 | 557.25 | 644.75 | 652.31 | 667.69 | 583.01 | 671.2 | 678.44 | 694.03 |
| 0.3696 | 447.84 | 535.96 | 543.55 | 559.04 | 473.99 | 562.78 | 570.04 | 585.76 |
| 0.369 | 338.35 | 427.09 | 434.69 | 450.3 | 364.88 | 454.27 | 461.54 | 477.37 |
| 0.3683 | 210.48 | 299.93 | 307.55 | 323.3 | 237.45 | 327.54 | 334.84 | 350.79 |
| 0.3677 | 100.79 | 190.85 | 198.49 | 214.34 | 128.15 | 218.82 | 226.14 | 242.21 |
| 0.3671 | 0 | 81.7 | 89.35 | 105.31 | 0 | 110.03 | 117.37 | 133.54 |
| 0.3664 | 0 | 0 | 0 | 0 | 0 | 0 | 0 | 0 |
| 0.3658 | 0 | 0 | 0 | 0 | 0 | 0 | 0 | 0 |

| Fuel Radius (cm) | UC Internal Rod Pressure (MPa) | | | | | | | |
|---|---|---|---|---|---|---|---|---|
| | 5233 - Avg | 5233 - High BOL | 5233 - High EOL | 5233 - High BU | 5132 - Avg | 5132 - High BOL | 5132 - High EOL | 5132 - High BU |
| 0.3744 | 12.462 | 12.489 | 12.526 | 12.519 | 12.368 | 12.391 | 12.423 | 12.417 |
| 0.374 | 13.013 | 13.044 | 13.084 | 13.076 | 12.908 | 12.934 | 12.968 | 12.962 |
| 0.3734 | 13.886 | 13.933 | 13.979 | 13.973 | 13.766 | 13.808 | 13.848 | 13.843 |
| 0.3728 | 14.783 | 14.853 | 14.905 | 14.9 | 14.645 | 14.708 | 14.753 | 14.749 |
| 0.3721 | 15.9 | 15.979 | 16.039 | 16.035 | 15.731 | 15.805 | 15.858 | 15.855 |
| 0.3715 | 16.958 | 17.045 | 17.113 | 17.109 | 16.759 | 16.841 | 16.899 | 16.896 |
| 0.3709 | 18.063 | 18.178 | 18.254 | 18.249 | 17.836 | 17.935 | 18.001 | 17.998 |
| 0.3702 | 19.447 | 19.605 | 19.697 | 19.696 | 19.178 | 19.322 | 19.401 | 19.402 |
| 0.3696 | 20.662 | 20.86 | 20.967 | 20.973 | 20.344 | 20.535 | 20.628 | 20.637 |
| 0.369 | 21.977 | 22.196 | 22.318 | 22.323 | 21.598 | 21.809 | 21.914 | 21.922 |
| 0.3683 | 23.641 | 23.943 | 24.087 | 24.096 | 23.2 | 23.48 | 23.603 | 23.614 |
| 0.3677 | 25.026 | 25.464 | 25.632 | 25.652 | 24.541 | 24.934 | 25.079 | 25.098 |
| 0.3671 | 25.383 | 26.918 | 27.141 | 27.207 | 25.278 | 26.376 | 26.548 | 26.596 |
| 0.3664 | 24.126 | 26.621 | 27.032 | 27.479 | 24.018 | 26.636 | 27.015 | 27.417 |
| 0.3658 | 23.164 | 25.4 | 25.792 | 26.18 | 22.926 | 25.243 | 25.607 | 26.025 |

The UN fuel design resulted in the largest pellet, attributable to both the highest thermal conductivity in the temperature range of interest (800-1100K) and its low swelling rate compared to the other two advanced fuels. The total volumetric swelling at 62 GWd/MTU for UN was ~1.5 vol% larger than the net swelling for $UO_2$(~3.5 vol%), while for UN and $U_3Si_2$ the net swelling was ~4.5 vol% larger. The internal rod pressure of the acceptable fuel design for UN/SiC was the lowest of all fuel designs. The reduced swelling allows for a small gap size, reducing the thermal resistance of the gap, as well as decreasing the reduction in plenum void volume as a result of fuel axial expansion caused by swelling and thermal expansion. The results of the UN/SiC analysis are shown in Table 5.18.

Table 5.18: Interfacial pressure and internal rod pressure for UN/SiC fuel design for most limiting rods in W4LP

| Fuel Radius (cm) | UN Interfacial Pressure (MPa) | | | | | | | |
|---|---|---|---|---|---|---|---|---|
| | 5233 - Avg | 5233 - High BOL | 5233 - High EOL | 5233 - High BU | 5132 - Avg | 5132 - High BOL | 5132 - High EOL | 5132 - High BU |
| 0.3744 | 568.93 | 631.04 | 636.99 | 647.71 | 584.1 | 646.69 | 652.31 | 663.23 |
| 0.374 | 496.91 | 559.45 | 565.42 | 576.22 | 512.34 | 575.35 | 580.98 | 591.98 |
| 0.3734 | 388.81 | 451.99 | 457.98 | 468.91 | 404.63 | 468.25 | 473.9 | 485.02 |
| 0.3728 | 280.64 | 344.46 | 350.47 | 361.52 | 296.84 | 361.09 | 366.77 | 377.99 |
| 0.3721 | 154.34 | 218.91 | 224.94 | 236.12 | 170.99 | 235.95 | 241.66 | 253.02 |
| 0.3715 | 45.99 | 111.2 | 117.25 | 128.55 | 63.02 | 128.61 | 134.34 | 145.82 |
| 0.3709 | 0 | 22.68 | 0 | 29.34 | 0 | 0 | 26.97 | 38.55 |
| 0.3702 | 0 | 0 | 0 | 0 | 0 | 0 | 0 | 0 |
| 0.3696 | 0 | 0 | 0 | 0 | 0 | 0 | 0 | 0 |

| Fuel Radius (cm) | UN Internal Rod Pressure (MPa) | | | | | | | |
|---|---|---|---|---|---|---|---|---|
| | 5233 - Avg | 5233 - High BOL | 5233 - High EOL | 5233 - High BU | 5132 - Avg | 5132 - High BOL | 5132 - High EOL | 5132 - High BU |
| 0.3744 | 15.614 | 16.118 | 16.177 | 16.265 | 15.797 | 16.321 | 16.379 | 16.471 |
| 0.374 | 16.167 | 16.69 | 16.753 | 16.842 | 16.344 | 16.884 | 16.945 | 17.039 |
| 0.3734 | 17.03 | 17.592 | 17.663 | 17.758 | 17.198 | 17.778 | 17.847 | 17.946 |
| 0.3728 | 17.899 | 18.49 | 18.569 | 18.668 | 18.048 | 18.66 | 18.736 | 18.841 |
| 0.3721 | 18.961 | 19.599 | 19.689 | 19.793 | 19.09 | 19.744 | 19.83 | 19.939 |
| 0.3715 | 19.819 | 20.582 | 20.685 | 20.799 | 19.962 | 20.713 | 20.81 | 20.928 |
| 0.3709 | 19.582 | 21.154 | 21.319 | 21.541 | 19.849 | 21.4 | 21.561 | 21.753 |
| 0.3702 | 18.926 | 20.601 | 20.711 | 21.054 | 19.072 | 20.661 | 20.862 | 21.149 |
| 0.3696 | 18.469 | 20.168 | 20.188 | 20.561 | 18.472 | 19.942 | 20.139 | 20.401 |

Due to differences in fuel swelling and thermal expansion (all advanced fuels have no relocation), each fuel type was determined to have it its own optimal fuel fabrication parameters to prevent the possibility of PCMI. These parameters are shown in Table 5.19.

Table 5.19: Fuel design parameters

| Dimension (m) | Fuel Design | | | | |
|---|---|---|---|---|---|
| | $UO_2$/ZIRLO$^{TM}$ | $UO_2$/SiC | $U_3Si_2$/SiC | UC/SiC | UN/SiC |
| Fuel OD | Proprietary | 7.328E-03 | 7.380E-03 | 7.328E-03 | 7.404E-03 |
| Gap Thickness | Proprietary | 1.587E-04 | 1.327E-04 | 1.587E-04 | 1.207E-04 |
| Clad ID | Proprietary | 7.645E-03 | 7.645E-03 | 7.645E-03 | 7.645E-03 |
| Clad OD | Proprietary | 9.144E-03 | 9.144E-03 | 9.144E-03 | 9.144E-03 |
| Plenum Length | Proprietary | 0.209906 | 0.209906 | 0.209906 | 0.209906 |
| Plenum Volume minus spring ($m^3$) | Proprietary | 8.509E-06 | 8.509E-06 | 8.509E-06 | 8.509E-06 |

The differences in fuel dimensions result in changes of U-235 content available for fission. Assuming an enrichment of 4.5% for the typical 17x17 Westinghouse fuel design, the mass content of U-235 ($m_{U235}$) in each rod was calculated using Equation 5.1, using the density of uranium in the fuel matrix ($\rho$), the cold volume of fuel ($V$) and the U-235 enrichment ($\varepsilon$).

$$m_{U235} = \rho * V * \frac{235*\varepsilon}{(235*\varepsilon+238*(1-\varepsilon))} \qquad 5.1$$

Although the fuel dimensions are smaller for the advanced fuel designs, the uranium density is higher which can offset the fuel volume loss. The U-235 content available in each rod with the same 4.5% enrichment is shown in Table 5.20. The increase in uranium density is greater than the fuel volume loss, resulting in the advanced fuel designs having an increase in U-235 content per rod. Neutronics permitting (noting that SiC has a lower thermal cross section than Zr), the advanced fuel designs would be able to attain the same U-235 content by reducing the enrichment. By keeping the enrichment the same, the advanced fuels would be able to achieve higher burnup than with $UO_2$. However, the $UO_2$/SiC design is incapable of reaching the same U-235 content without exceeding the enrichment limit of 5%. Therefore, a direct replacement of the 17x17 current design with the constrained imposed in this study could prove problematic in trying to achieve the same burnup.

Table 5.20: U-235 content for advanced fuel designs assuming typical 17x17 design with enrichment of 4.5% U-235

| Parameter | Fuel Design | | | | |
|---|---|---|---|---|---|
| | $UO_2$/ZIRLO$^{TM}$ | $UO_2$/SiC | $U_3Si_2$/SiC | UC/SiC | UN/SiC |
| Fuel OD (cm) | Proprietary | 7.328E-01 | 7.380E-01 | 7.328E-01 | 7.404E-01 |
| Fuel volume ($cm^3$) | 1.752E+02 | 1.528E+02 | 1.550E+02 | 1.528E+02 | 1.560E+02 |
| Uranium density ($g/cm^3$) | 9.661 | 9.661 | 12.974 | 13.524 | 11.313 |
| U-235 content (g) | 75.263 | 65.641 | 89.411 | 91.890 | 78.482 |
| Required enrichment to reach same mass of U-235 (%) | - | 5.16%* | 3.79% | 3.69% | 4.32% |

* Above current enrichment limit of 5% U-235

### 5.5.2 Steady-State Analysis

The W4LP plant was analyzed to reach the same EOC conditions for each new fuel design by achieving the same assembly-average discharge burnup as the original W4LP plant design with typical 17x17 Westinghouse ($UO_2$/ZIRLO$^{TM}$) fuel. Due to the increased uranium content in the advanced fuel designs, the plant operated with a cycle length > 18 months (550 days), which is typical of the current design. The $U_3Si_2$, UN and UC fuel designs operated with cycle lengths of 569.73, 685.65 and 644.16 days, respectively, which the $UO_2$/SiC design reached the same burnup at 481.5 days.

Due to the poor thermal conductivity of the SiC cladding after 1 dpa, combined with its increased thickness, the gas temperatures are consistently higher than with current $UO_2$/Zirc designs. The higher temperatures offset any gains in free volume due to the design criteria that would help balance the rod pressure. The internal rod pressures, shown in Table 5.21, are higher for any advanced fuel design with SiC cladding compared to current design. It is important to note that the average designed cladding thickness values were used in this analysis, meaning the high range of cladding thickness values would yield much more detrimental results. The internal rod pressure for average rod in the high powered assemblies yields internal pressures much greater than that of the coolant. For zirconium-based claddings, this is problematic due to cladding creep out. The continued rise in internal rod pressure due to increased temperatures and fission gas release will cause a thermal feedback that can lead to cladding lift-off. To avoid this condition, the cladding creep out rate is limited to be less than or equal to the fuel swelling rate. [GE14 design report – Non Proprietary] However, the SiC cladding has been modeled not to creep, thus avoiding this phenomena. The high cladding tensile stress caused by the high internal gas pressure may lead to failure, especially under LOCA conditions where the gas pressure remains high due to the temperatures but the secondary (coolant) pressure declines rapidly.

Table 5.21: Internal rod pressure analysis

| Core Average @ EOC | | |
|---|---|---|
| Fuel Design | Core Average Rod Pressure (Mpa) | Max Assembly Average Rod Pressure (Mpa) |
| $UO_2$ - Zirc | 9.822 | 15.180 |
| $UO_2$ - SiC | 14.198 | 32.616 |
| UC - SiC | 13.804 | 21.836 |
| UN - SiC | 11.783 | 17.979 |
| $U_3Si_2$ - SiC | 11.912 | 18.998 |

The stored energy in the fuel, which has been touted as one of the major benefits of the advanced fuel designs under accident scenarios, is shown in Table 5.22 for the entire core. Again, the increased thermal resistance of the SiC results in higher fuel temperatures, thus increasing the stored energy. As expected, a drastic increase in stored energy (~23%) was noticed between $UO_2$/ZIRLO$^{TM}$ and $UO_2$/SiC due to the increased thermal resistance of the cladding. A decrease in stored energy was calculated for the UC, UN and $U_3Si_2$ fuel designs compared to the current design due to the lower operating temperatures and specific heat.

Table 5.22: Core-wide fuel stored energy

| Core Average @ EOC | | |
|---|---|---|
| Fuel Design | Stored Energy in fuel (J) | Net change (%) |
| $UO_2$ - Zirc | 1.652E+10 | - |
| $UO_2$ - SiC | 2.039E+10 | 23.43% |
| UC - SiC | 1.483E+10 | -10.22% |
| UN - SiC | 1.365E+10 | -17.34% |
| $U_3Si_2$ - SiC | 1.411E+10 | -14.57% |

A difference in which rods contained the most stored energy was noticed between the fuel designs. For the $UO_2$/ZIRLO$^{TM}$ design, the high powered 2nd cycle rods contained the most stored energy due to the degradation of thermal conductivity with burnup. However, the high powered 1st cycle rods were more dominant for the $UO_2$/SiC design due to the increase in gap conductance caused by the fuel design criteria of preventing PCMI. As a whole, no rods in the $UO_2$/ZIRLO$^{TM}$ design contained less stored energy than their corresponding rod in the $UO_2$/SiC design. A schematic of stored energy is shown in Figure 5.45.

(a) (b)

Figure 5.45: Fuel stored energy in each assembly for a (a) $UO_2$/ZIRLO$^{TM}$ fueled core, (b) $UO_2$/SiC fueled core

Comparing the $UO_2$/ZIRLO$^{TM}$ design to the UN/SiC design again shows vast differences in the fuel stored energy. The high thermal conductivity of the UN (as well as UC and $U_3Si_2$) fuel at all temperatures and burnups resulted in the largest driver for stored energy being based on the gap conductance. Higher burnup fuel decreased the gap size, thus reducing the thermal resistance and allowing the fuel to operate at cooler temperatures. For UN/SiC, the fuel with the highest stored energy at EOC was the lower burnup, 1st cycle fuel rods. The stored energy comparison is shown in Figure 5.46.

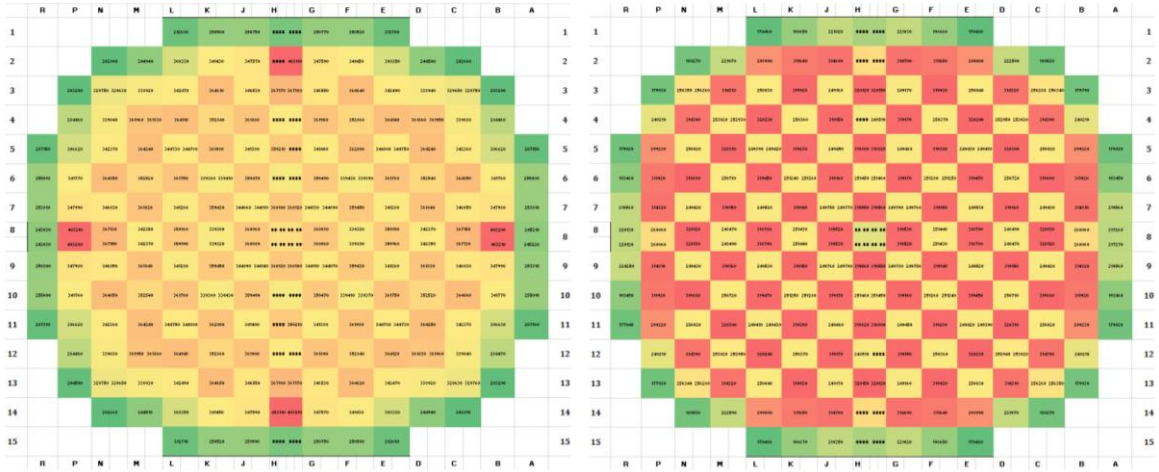

(a) (b)

Figure 5.46: Fuel stored energy in each assembly for a (a) $UO_2$/ZIRLO$^{TM}$ fueled core, (b) UN/SiC fueled core

The decrease in thermal conductivity of the SiC makes the $UO_2$/SiC design very unattractive. The high thermal conductivity of the advanced fuels is able to overcome the cladding thermal resistance and result in overall less stored energy, making them more feasible candidates. The $U_3Si_2$/SiC design has a decrease in stored energy in all of the rods of 15.7% - 42.1%, and a resulting net decrease of ~30% in total fuel stored energy. The comparison of these two fuel types is shown in Figure 5.47.

(a) (b)

Figure 5.47: Fuel stored energy in each assembly for a (a) $U_3Si_2$/SiC fueled core, (b) $UO_2$/SiC fueled core

Despite the increased thermal conductivity and lower fuel centerline temperature, the fraction of melting temperature operated by the fuel is significantly higher for the $U_3Si_2$/SiC fuel design due to its lower melting point compared to $UO_2$/Zirc. The thermal conductivity degradation of SiC drives the fuel centerline temperatures up for the UN, UC and $U_3Si_2$ fuel designs during the first few GWd/MTU burnup. After that, fuel swelling decreases the gap size more rapidly than the thermal conductivity of SiC degrades, causing the thermal resistance of the gap to decrease more significantly than the thermal resistance of the cladding increases. However, that is not the case with $UO_2$ due to fuel relocation and the thermal conductivity degradation with burnup. In both of the$UO_2$ cases, the fuel temperature decreases with burnup over the first ~5 GWd/MTU due to fuel relocation decreasing the size of the fuel/cladding gap. The decrease is not as dramatic in the SiC clad case compared to the ZIRLO$^{TM}$ case due to the increased thermal resistance of the cladding from thermal conductivity degradation and the SiC cladding is not creeping inwards to reduce the gap size. After ~25 GWd/MTU, the fuel temperatures continue to increase despite the drop in row power due to the drop in thermal conductivity and the increased fuel size. The fuel types analyzed as a function of their melting temperature are shown in Figure 5.48.

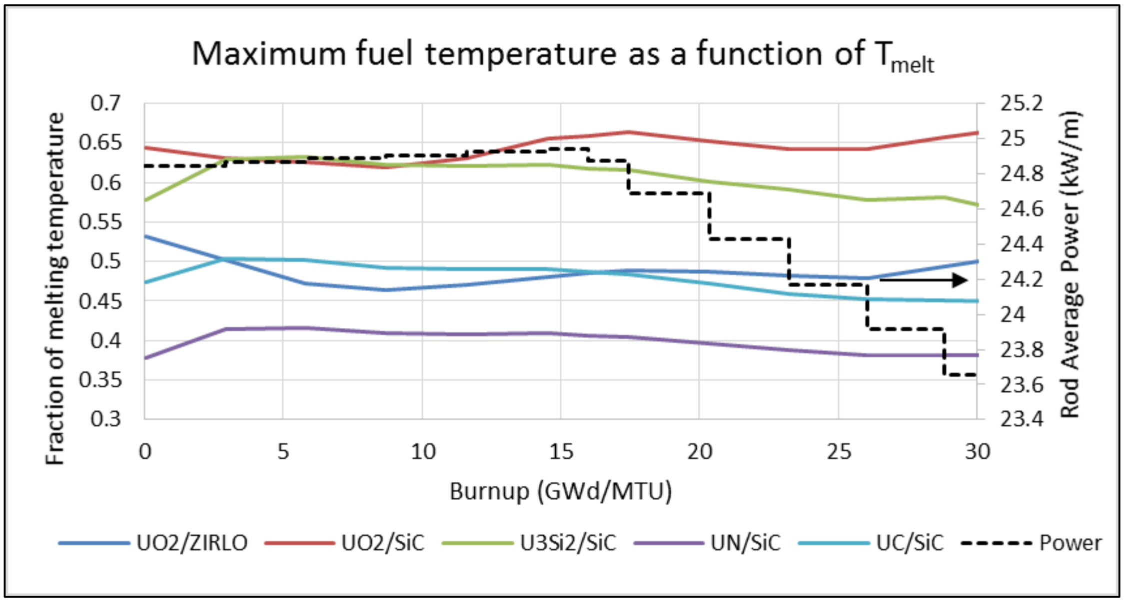

Figure 5.48: Fraction of melting temperature during normal operation for hottest fuel temperature rod (1st cycle rod)

The major concern during normal operation about the fraction to melt is what might occur to the fuel temperatures during a power spike. To assess the potential impact, FRAPCON was used to analyze the fuel temperature in a 50% power spike at the EOC condition for the rods analyzed in Figure 5.47. The results are shown in Table 5.23.

Table 5.23: Fuel impacts of a 50% power spike to 36.49 kW/m at EOC

| Fuel Impacts of 50% Power Spike | | | |
|---|---|---|---|
| | Time | $U_3Si_2$/SiC | $UO_2$/ZIRLO$^{TM}$ |
| Max Temp (K) | Before | 1086 | 1484 |
| | After | 1297 | 2047 |
| Fraction to Melt | Before | 0.56 | 0.509 |
| | After | 0.669 | 0.702 |
| Hoop Stress Increase (MPa) | | 8 | 220 |

The $U_3Si_2$/SiC design experienced a much less dramatic increase in fuel centerline temperature than $UO_2$/ZIRLO$^{TM}$ due to the improved thermal conductivity of the fuel. Despite the lower melting temperature, the fraction of centerline temperature to melting temperature of the $U_3Si_2$ remained lower than that of $UO_2$. With the $U_3Si_2$ fuel temperatures remaining lower, the thermal expansion was also lower, eliminating PCMI during the spike. Conversely, the $UO_2$ case resulted in an increase in cladding hoop stress of ~220MPa. To better understand the time sensitivity of the power spike on fuel temperatures and cladding stress, a FRAPTRAN analysis should be performed in future work.

### 5.5.3 Transient Analysis

All of the fuel designs were analyzed in TRACE under a LBLOCA scenario at EOC. For the SiC cladding cases, cladding rupture was turned off to allow for a sensitivity study to failure criteria. Due to the brittle failure mechanism of the cladding, not allowing it to rupture is not expected to have a significant impact on the results due to the lack of flow blockage that is typical with zirconium based claddings. Each fuel design analyzed has the same core power distribution and, consequently, decay heat. The only difference between designs will be the stored energy contained within the fuel at the onset of the transient.

At 12s into the transient, the PCT is ~53K lower for UN/SiC and ~40K lower for $U_3Si_2$/SiC and UC/SiC compared to $UO_2$/ZIRLO$^{TM}$. Alternatively, the $UO_2$/SiC PCT is 109K hotter. By 35s, the $UO_2$/SiC PCT is 116K hotter than $UO_2$/ZIRLO$^{TM}$ while the other advanced fuels are 30-50K lower. The $UO_2$/SiC case ran to 80.0s, but based on the analysis of the other fuels during the LBLOCA, the maximum PCT for the $UO_2$/SiC core is expected to be slightly above the maximum value at 35s of 1217.6K. The delay in the $UO_2$/SiC fuel design LBLOCA analysis running to completion is likely due to the large thermal gradients in the fuel due to the poor thermal conductivity of both the fuel and clad, as well as the large gap size to prevent PCMI. Due to the increase in thermal resistance to fuel heat removal of the rods (larger gap, thicker/less conductive clad) being consistent across all rods in the core, the PCT rod for the $UO_2$/SiC case is the same as in the $UO_2$/ZIRLO$^{TM}$ case. The PCT for each fuel design in the LBLOCA analysis is shown in Figure 5.49.

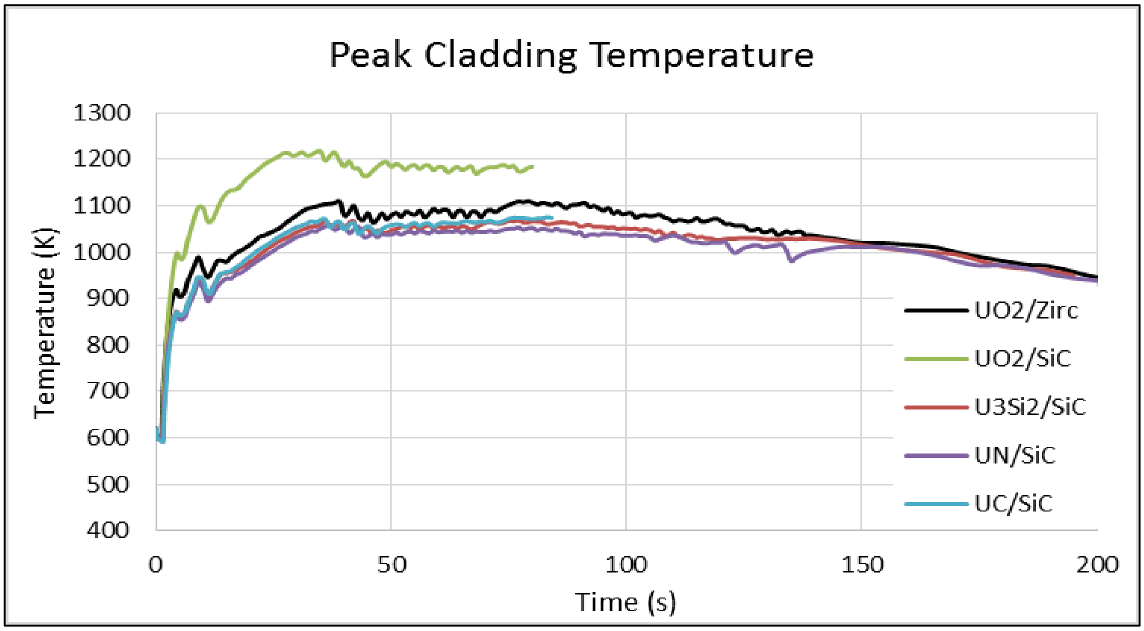

Figure 5.49: Peaking cladding temperature for various advanced fuel designs for a W4LP under LBLOCA conditions

With the design criteria to eliminate PCMI, the only driving force for cladding primary stress for any of the advanced fuel designs is the pressure differential on the cladding. The cladding stress was analyzed for the hottest rod in the $U_3Si_2$/SiC design. This rod contained the highest internal rod pressure, which would result in the highest cladding stress in the core. The internal rod pressure remains above 10 MPa through the first 200 seconds of the LBLOCA due to the high gas temperature. However, the coolant quickly depressurizes, decreasing the external pressure on the rod from 15.9 MPa to less than 1 MPa by 17 seconds. The cladding changes from compression to tension by 2.4 seconds and remains in tension for the remainder of the transient. The forces applied to the cladding are shown in Figure 5.50.

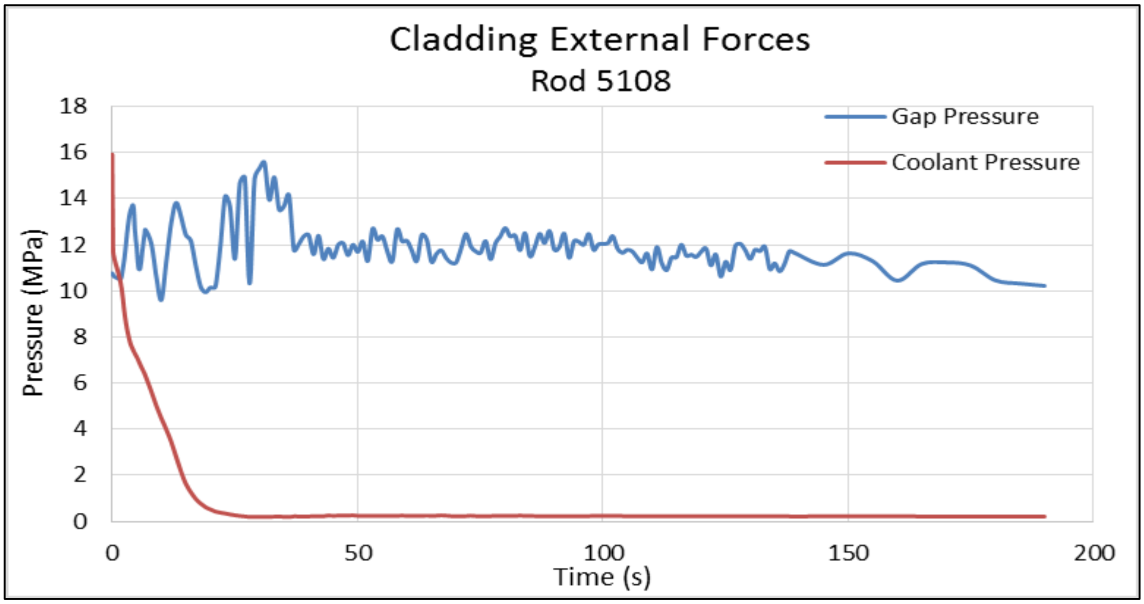

Figure 5.50 Internal rod pressure and external coolant pressure acting on highest powered $U_3Si_2$/SiC rod under LOCA conditions

The hoop, axial and Von Mises stresses for the cladding are calculated in Figure 5.51. The calculations are based on FRAPTRAN's stress analysis, where the radial stress is neglected and the hoop stress and axial stress are uniform across the cladding.[FRAPTRAN-1.5 Code Description] The cladding stresses remain well below the yield stress of SiC, which has been reported as low as 200 MPa for the fibers and 250-325 MPa for composities. It is important to note that the yield stress is strongly dependent on the fabrication, especially with respect to the composite density. However, the maximum stress in the cladding doesn't approach ½ of the lowest reported value of failure stress. The cladding stress distribution is likely the only place where the increased cladding thickness (~30% over typical Zircaloy designs) benefits the fuel performance.

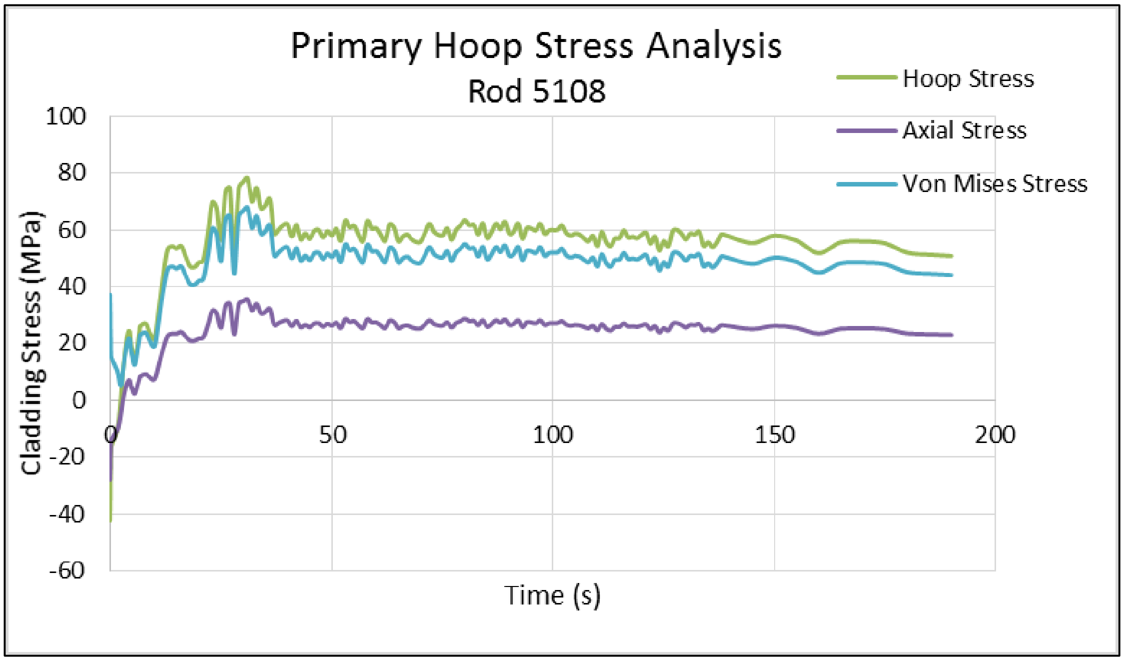

Figure 5.51: Primary hoop stress analysis for $U_3Si_2$/SiC fuel design in LBLOCA

As mentioned in Chapter 2, it has been shown that the temperature gradient associated with SiC can result in extreme thermal stresses in the material in an accident scenario.[Ahn, 2006] The TRESCA theory was used to analyze the cladding secondary thermal stresses throughout the transient. The thermal stresses in the cladding are at their highest value when the reactor is in operation but are reduced by an order of magnitude within 1.5 seconds after the reactor has been scrammed. Based on the secondary axial stress, the cladding would not meet the ASME stress criteria during normal operation (primary + secondary stress must be less than ultimate tensile stress and 2x yield stress).[Ahn, 2006]. The primary stress requirements (primary stress must be greater than 2/3 of yield stress and 1/3 of ultimate tensile stress) are the most limiting within 15 seconds into the transient. These stresses are shown in Figure 5.52. It can be concluded that the thermal stress in the cladding cannot be ignored and must be taken into consideration during the fuel design.

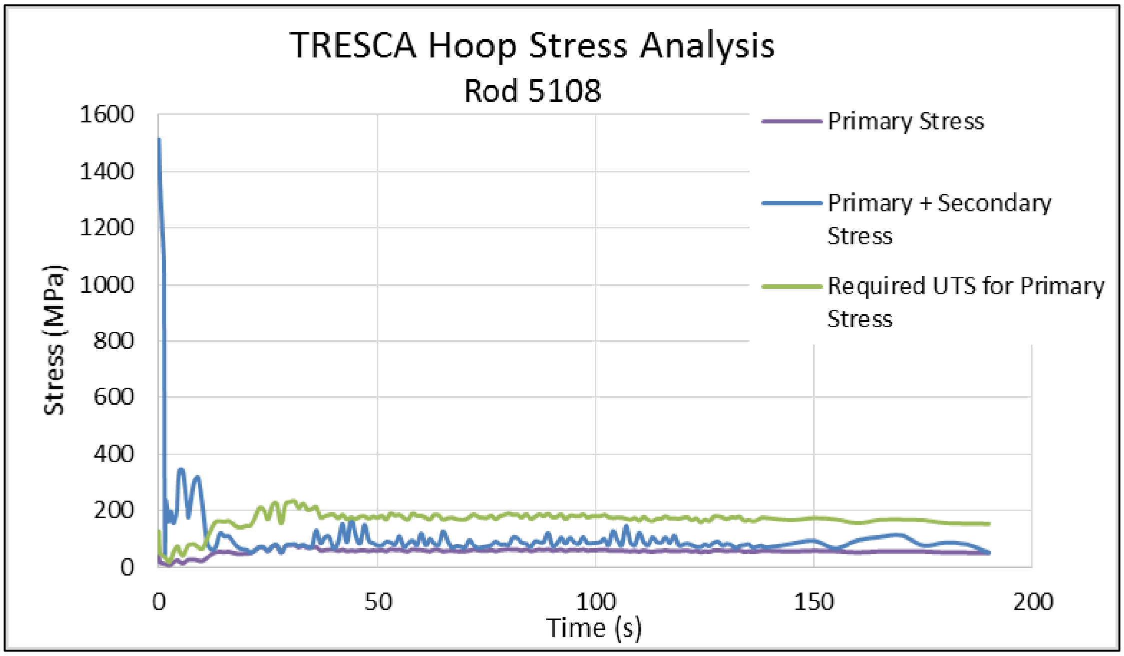

Figure 5.52: TRESCA hoop stress analysis for $U_3Si_2$/SiC fuel design under LBLOCA conditions

To assess the impact of the advanced fuels under an accident scenario where the decay heat rather than stored energy is the driving force for PCT, such as the GE-BWR/4 SBLOCA, a TRACE analysis was performed where the heat removal is lost and the rod power is based on the decay heat. The TRACE analysis consists of a single rod that is at the coolant temperatures in the GE-BWR/4 SBLOCA of 550K until the heat flux goes to 0.0 and the rod heats up from decay heat until it melts. The rod power is based on the decay heat starting at the time in which the cooling is lost due to depressurization in the GE-BWR/4 SBLOCA analysis at 300.0s. The results are shown in Figure 5.53.

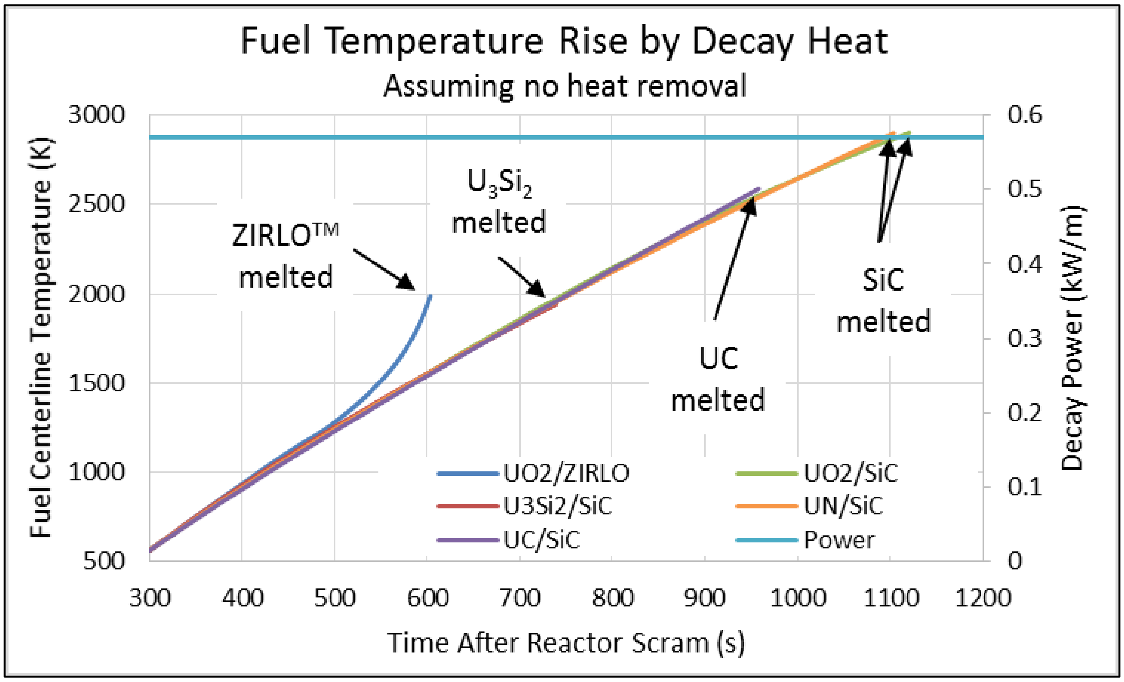

Figure 5.53: Fuel temperature rise due to decay heat representative of GE-BWR/4 SBLOCA coolant conditions

The first fuel design to melt is the UO2/ZIRLO™ 17x17 Westinghouse design. The fuel fails at 603s after losing cooling for 303s. The fuel fails due to the ZIRLO™ cladding melting temperature being exceeded. Unlike the SiC clad designs, the oxidation reaction occurs when the cladding exceeds 1073K, causing the total power generated to be higher than the other cases. This is shown in Figure 5.53 where the fuel temperature begins to follow an exponential curve. The next fuel design fails at 438.4s after losing cooling. The $U_3Si_2$/SiC design fails when the $U_3Si_2$ melts. The same failure occurs for the UC/SiC design, 658.4s after losing cooling. The UN/SiC and $UO_2$/SiC designs fail at 1104s and 1121s, respectively. Both designs fail when the SiC cladding temperature exceeds 2900.0K. The poor thermal conductivity of the $UO_2$ is rather beneficial in that it allows for an additional 17s before the cladding is melted due to the time required for the energy to reach the cladding. Understanding this is a simplistic approach, the results show that the SiC cladding can provide a significantly increased time before failure with the assumption that no cladding oxidation occurs. It also shows the importance of fuel melting temperature and, despite the poor performance of $UO_2$/SiC under normal conditions, it is capable of withstanding the longest time before failure in a complete loss of coolant accident scenario when the fuel stored energy has been removed.

# CHAPTER 6

## CONCLUSIONS AND FUTURE WORK

### 6.1 CONCLUSIONS

Full core fuel performance studies are complex, time and computationally intensive studies that must be carefully planned and analyzed from the start. The first task in performing these types of analyses is establishing a deep understanding of the codes being used. As this study has shown, even using codes developed for use by the same organization can have vastly different capabilities and limitations. Thermal hydraulics codes provide more realistic reactor coolant conditions than fuel performance codes, while fuel performance codes provide the detailed thermo-mechanical analysis for in-reactor fuel rod changes. By understanding the limitations of using FRAPCON for modeling the in-reactor conditions, the modifications made to the code provide an improved code-to-code consistency and a better representation of the conditions external to the rod. It has been shown that the modifications to use these conditions can have a significant (>10%) impact on determining the criteria relevant for licensing, such as cladding corrosion. To better assess how well these modifications improve or alter the corrosion calculations, a detailed analysis into the corrosion assessment data needs to be performed using the known reactor conditions. The current assessment shows that FRAPCON tends to both over predict and under predict oxide thicknesses at certain axial elevations by as much as 40% or more.

[K.J. Geelhood, 2014] This study showed that the ability to both over predict and under predict oxide layer thickness can be attributed by the inability to properly match coolant temperatures to in-reactor conditions using FRAPCON's default coolant model.

Although FRAPCON is designed to create a restart file for FRAPTRAN, it was determined that the conditions were not identical between the codes. The differences resulted in changes in important failure and dispersal criteria, such as internal rod pressure and cladding deformation. The improvements made to the restart file provided more resembling conditions of FRAPCON in FRAPTRAN, although it was noticed that additional modifications still need to be made. It was shown that despite the improvements, the overall difference in the analysis of an entire core in a LBLOCA was nearly identical with respect to number of rods failed. The improved model for gamma-ray heating in FRAPTRAN was shown to not have as significant of an impact as the model in FRAPCON, although it provides a more realistic calculation of how the energy deposition changes with coolant density (whereas previously it was independent of coolant conditions).

The updates to TRACE to use axially-dependent parameters to better match FRAPCON showed improvement in fuel temperature analysis compared to FRAPCON. However, it was determined that the impact of burnup degradation of $UO_2$'s thermal conductivity was much more significant for matching fuel temperatures than properly accounting for changes in gap thickness. This study has proved that TRACE's models produce conservative results (higher temperature, more stored energy) compared to FRAPCON's best-estimate fuel rod models.

The full core LOCA analyses showed significantly different results between plant and fuel rod designs. The W4LP plant had an overall PCT of 1110K, resulting in cladding oxidation and a significant amount of fuel failure. The W4LP had 41.7% of the fuel in the core fail at BOC and MOC with 52.8% failing at EOC. Alternatively, the CE-PWR plant response during the LBLOCA resulted in cladding temperatures ~100K lower than in the W4LP. The CE-PWR 16x16 fuel rod design had ~10% more void volume than the W4LP 17x17 fuel design, resulting in ~1MPa lower core-average internal rod pressure despite similar operating powers. The combination of reduced pressure and lower temperature eliminated any fuel rod failure in the CE-PWR, compared to over ½ of the W4LP core failing.

The GE-BWR/4 had a significantly different plant response than the PWRs. Unlike in the PWRs, the GE-BWR/4 had a significantly increased time during depressurization until the liquid flashed to steam. This resulted in the ability to remove the stored energy from the fuel, resulting in the decay heat alone being the driver for PCT. The lower external coolant pressure allows for a lower internal fill gas pressure, with the EOL rod pressures being 3-5x smaller than that for the W4LP. The significantly lower rod pressure and PCT resulted in no fuel failure during the SBLOCA or LBLOCA. In order to have fuel rod failure, the time the rod is without any cooling would need to be significantly increased compared to the PWR LOCA cases. Even if failure were to occur, the assembly average burnup for the GE-BWR/4 was significantly lower than the PWR cases and would therefore have a smaller fraction of dispersible fuel.

The FRAPTRAN analysis on the W4LP showed that the possibility of fuel rod failure and dispersal exists even under realistic conditions. Although the conditions analyzed for the CE-PWR and GE-BWR/4 did not predict fuel rod failure, the likelihood of fuel rod failure and dispersal still exists in these plant designs under “non-ideal” LOCA plant responses. The nominal failure criteria resulted in ~0.23% of the fuel in the reactor being dispersed in the W4LP LBLOCA at EOC. It has been shown that there is significant sensitivity to both the assumptions made for fuel particle size distribution with respect to burnup and the cladding strain required for fuel to be axially mobile. When more experimental data becomes available, the nominal conditions and variability shall be better understood for predicting the conditions that will result in FFRD. Due to the state of the current FRAPTRAN code and input generators, it is not feasible to perform a full analysis on each rod in the reactor core in a reasonable amount of time (magnitude of several months).

The sensitivity analysis on nodalization and rod detail used in this study showed that the values chosen were very reasonable. The steady-state full core analysis showed negligible differences with regard to nodalization. The individual rod analysis also showed small (<1-2%) deviations in core average rod conditions. The FRAPTRAN transient analysis showed minimal differences in fuel rod failure with respect to nodalization. The dispersal calculations also produced similar results with variations in nodalization using the nominal dispersal criteria, but can vary significantly when the dispersal criteria is changed from nominal values. The rod detail used in FRAPTRAN, combined with the thermal hydraulic rod analysis from TRACE, was proven to be sufficient to calculate the number of failed rods in the core when using an assembly-average rod. The TRACE executable was specifically developed for this analysis, and was pushed to the limit when analyzing only an assembly-average, high-powered and low-powered rod within each assembly. The time required to go into the greater level of detail in modeling each rod individually proved to not provide any significant differences in results.

The advanced fuel design analysis shows that improvements can be made in some areas in using SiC as a cladding while significant issues arise in others. The key area of improvement with using the SiC cladding is the elimination of the exothermic oxidation reaction under LOCA conditions. For the LBLOCA analyzed, the maximum temperature of the SiC cladding was ~945°C, which is lower than the conditions tested which showed oxidation of the SiC cladding as reported in Chapter 2. However, the thermal stresses in the SiC cladding during operation showed that significant concerns arise due to the thermal gradient across the clad. Designing a fuel to retrofit a 17x17 assembly with the poor thermal conductivity of SiC combined with the brittle nature of the cladding has proven problematic. The $UO_2$/SiC design resulted worse operating conditions than $UO_2$/ZIRLO$^{TM}$ in terms of fuel temperatures and internal rod pressure. Whereas the most limiting assembly for $UO_2$/ZIRLO$^{TM}$ had a rod average internal rod pressure of 15.18 MPa, the same rod in the $UO_2$/SiC design had a rod pressure of 32.6 MPa. Despite the lower fuel temperatures of the advanced fuels of UN, UC and $U_3Si_2$, the core-average rod pressure was increased in all three designs. The lower temperatures did however lower the stored energy in the fuel rods, resulting in a decrease in PCT during the LBLOCA transient by 35-50°C. With the lower melting temperature of $U_3Si_2$ compared to $UO_2$, the fraction of melting temperature reached during the transient (56% vs 40% of $T_{melt}$) was significantly higher. This could be of major concern if the cooling is not restored as quickly and the decay heat continues to drive up temperatures.

Implementing the advanced fuel designs in the GE-BWR/4 are not expected to significantly improve the LBLOCA or SBLOCA analysis due to the driving force for PCT in those studies being based on decay heat rather than stored energy. It was shown that when following the same sequence of events as the SBLOCA, all of the SiC fuel designs would provide an increased time until fuel rod failure. The $U_3Si_2$ fuel proved to fail first, as expected, due to the lowest melting temperature, followed by UC. The $UO_2$ and UN fuel designs with SiC cladding failed by the melting of the cladding rather than the melting of the fuel, under the assumption of no heat removal. The improved thermal conductivity benefit of the UC, UN and $U_3Si_2$ fuels was shown to actually cause the fuel to fail first under the transient conditions due to the improved ability to transfer the energy generated by decay heat to the cladding.

## 6.2 FUTURE WORK

Future work with FRAPCON and FRAPTRAN should look at ensuring temperatures, rod pressure and cladding deformation are identical between codes when using the restart file. Some parameters found to need further attention include the inability to model gas in fuel cracks and the FRAPTRAN radial dimensions used for the fuel calculations not matching the dimensions at each axial node in FRAPCON. Future work with the new model implemented into FRAPTRAN for gamma-ray heating should include performing the same study for additional fuel designs (i.e. 16x16 PWR, 10x10 and 11x11 BWR fuel) or coupling the code with a neutronics code such as PARCS to allow for increased flexibility in dimensions and materials.

To further reduce conservatisms in the LOCA analysis, TRACE should be modified to allow for a 2-D burnup profile of the fuel. It is also recommended that future work be performed to allow TRACE to use FRAPCON files (i.e. a restart file) to import the rod conditions rather than require a complex data storage system as was used in this analysis. If not performed with TRACE, it is envisioned that the NRC's SNAP user-interface be modified to allow for this external coupling/data transfer between codes. Ideally, this interface will also be able to support the FRAPTRAN analysis by (1) linking the FRAPCON restart files to the FRAPTRAN analysis and (2) exporting the TRACE coolant conditions to FRAPTRAN.

Although it was started in this work, the full coupling of TRACE and FRAPTRAN would be the ideal next step in full core fuel rod modeling and failure analysis. FRAPTRAN was modified to be able to store the data required to model multiple rods, yet due to the time constraints of this project this was not fully tested. It is envisioned that once coupled, the PARCS neutronics that is currently coupled into TRACE shall be linked with FRAPTRAN to provide a more detailed map of where energy is deposited during the transient. However, the memory and computational time requirements must also be considered and the TRACE code improved upon (i.e. made to run parallel) to make this a feasible analysis.

With the current scope of the fuel dispersal analysis being to quantify the amount of fuel dispersed under realistic operating conditions, the next step in the overall analysis is to analyze where the particles will travel to and what the consequences are. Near-term further work in the dispersal quantification analysis should be made on the experimental side rather than the modeling side. Due to the high costs associated with LOCA testing, there is limited data currently available for FFRD under LOCA conditions. Additional testing could allow for a better understanding of the particle size distribution with burnup and whether there are additional phenomena that play into particle size beyond burnup. Additional work in the FRAPTRAN modeling should include modeling axial fuel relocation during ballooning and the associated increased source term and net thermal conductivity degradation of the fuel. The ballooning model should also be further assessed to determine guidelines designed to capture the size of the balloon region.

Recommended future work for the advanced fuel study would be a re-assessment of the models used in the analysis and the fuel design criteria. The fuel swelling models used for UN, UC and $U_3Si_2$ were the most limiting in the design criteria of eliminating PCMI. Several mechanisms were based on $UO_2$ models, such as densification and fission gas release, which need to be explored further due to differences in melting temperatures (especially with $U_3Si_2$). If the elimination of PCMI is to remain the design criteria, then exploration into thinner claddings should be made to see how the reduced thermal resistance will help internal rod pressure at EOL and the ability to remain below the cladding stress limits. Lower gas-gap temperatures will lower fuel temperatures as well as reduce internal rod pressure, both of which will be beneficial in the LOCA analysis by reducing stored energy and cladding stress, respectively.

# REFERENCES

Ahn, K. (2006). *Comparison of Silicon Carbide and Zircaloy4 Cladding during LBLOCA.* Massachusetts Institute of Technology.

Brad J. Merrill, S. M.-S. (2013). SIC MODIFICATIONS TO MELCOR FOR SEVERE ACCIDENT ANALYSIS APPLICATIONS. *TopFuel 2013*, (pp. 59-64). Charlotte, NC.

C. Sauder, A. M. (2013). Assessment of SiC/SiC Cladding for LWRs. *TopFuel 2013*, (pp. 951-956). Charlotte, NC.

C.P. Deck, H. K. (2012). Fabrication of SiC-SiC composites for fuel cladding in advanced reactor designs. *Progress in Nuclear Energy*, 38-45.

C.W. Lee, F. P. (1982). Thermal properties of neutron-irradiated SiC; effects of boron doping. *Journal of Nuclear Materials*, 678-684.

Carpenter, D. (2006). *Assessment of Innovative Fuel Designs for High Performance Light Water Reactors.* Massachusetts Institute of Technology.

Carroll, S. (2014). *Implementation and Evaluation of Fuel Creep Using Advanced Light-Water Reactor Materials in FRAPCON-3.5 (Master's thesis).* Columbia: University of South Carolina.

David Carpenter, G. K. (2007). Modeling of Silicon Carbide Duplex Cladding Designs for High Burnup Light Water Reactor Fuel. *ICAAP 2007*, (pp. 1465-1473). Nice, France.

Dawu Xiao, Y. L. (2010). High Strain Rate Deformation Behavior of Zirconium at Elevated Temperatures. *Journal of Material Science and Technology*, 878-882.

Desktop Aeronautics, Inc. (2007, January). *Applied Aerodynamics: A Digital Textbook.* Stanford. Retrieved from Applied Aerodynamics: A Digital Textbook.

DiCarlo, J. A. (2004). *High-Performance SiC/SiC Ceramic Composite Systems Developed for 1315C (2400F) Engine Components.* NASA/TM-2004-212729.

Division of Safety Analysis. (2012). *TRACE V5.0 THEORY MANUAL.* Rockville: U.S. NRC.

E. Kolstad, W. W. (2011). High burn-up fuel behavior under LOCA conditions as observed in Halden experiments. *IAEA Technical Meeting on Fuel Behavior and Modelling Under Severe Transient and LOCA Conditions.* Mito, Japan.

George Newsome, L. L. (2007). Evaluation of neutron irradiated silicon carbide and silicon carbide composites. *Journal of Nuclear Materials*, 76-89.

GPU Nuclear Corp, NEI. (2001, March). *Three Mile Island Accident.* Retrieved from World Nuclear Association: http://www.world-nuclear.org/info/Safety-and-Security/Safety-of-Plants/Three-Mile-Island-accident/#.UnOeUJ3D-Uk

Griffith, A. (2013). *Accident Tolerant Fuels.* U.S. Department of Energy.

H.E. Khalifa, C. D. (2012). SILICON CARBIDE COMPOSITE FABRICATION AND MECHANICAL AND THERMAL PERFORMANCE FOR NUCLEAR REACTOR APPLICATIONS. *Fusion Science and Technology*, 375-380.

Hallman, L. H. (2013). *Advanced Fuels Modeling: Evaluating the Steady-State Performance of Carbide Fuel in Helium-Cooled Reactors Using FRAPCON 3.4 (Master's thesis).* Columbia: University of South Carolina.

Harvey, J. (1963). *Pressure Vessel Design: Nuclear and Chemical Applications.* Princeton, NJ: D. Van Nostrand Company Inc.

Henri Bailly, D. M. (1999). *The Nuclear Fuel of Pressurized Water Reactors and Fast Neutron Reactors.* Lavoisier Publishing, Inc.

Herbert Feinroth, G. M. (2013). Silicon Carbide Triplex Cladding: Recent Advances in Manufacturing and Testing. *TopFuel 2013*, (pp. 928-935). Charlotte, NC.

Ian E. Porter, T. W. (2014). Fuel performance assessment when modeling gamma heating during steady-state and transient scenarios. *Proceedings of ICAPP 2014*, (p. Paper 14344). Charlotte.

Ian E. Porter, T. W. (2014). Potential Impacts of Modeling Full Reactor Cores Using Combined Fuel Performance and Thermal Hydraulics Codes. *Nuclear Technology*.

Joaquin Ramirez-Rico, J. M.-F. (2012). Effect of oxidation on the compressive strength of sintered SiC-fiber bonded ceramics. *Materials Science and Engineering*, 394-399.

John R. Lamarsh, A. J. (2001). *Introduction to Nuclear Engineering* (3rd ed.). Upper Saddle River: Prentice Hall.

Ju Ang Jung, S. H. (2013). Feasibility study of fuel cladding performance for application in ultra-long cycle fast reactor. *Journal of Nuclear Materials*, 596-605.

K. Matsunaga, T. I. (1999). Mechanical properties of Si-Ti-C-O fibre-bonded ceramic using satin weave. *Journal of Materials Science*, 1505-1511.

K.E. Metzger, T. K. (2014). Model of U3Si2 Fuel System Using BISON Fuel Code. *Proceedings of ICAPP 2014*, (p. Paper 14343). Charlotte.

K.J. Geelhood, W. L. (2011). *FRAPCON-3.4: A Computer Code for the Calculation of Steady-State Thermal-Mechanical Behavior of Oxide Fuel Rods for High Burnup.* Washington: Office of Nuclear Regulatory Research.

K.J. Geelhood, W. L. (2011). *FRAPTRAN 1.4: A Computer Code for the Transient Analysis of Oxide Fuel Rods.* Washington: Office of Nuclear Regulatory Research.

K.J. Geelhood, W. L. (2014). *FRAPCON-3.5: A Computer Code for the Calculation of Steady-State, Thermal-Mechanical Behavior of Oxide Fuel Rods for High Burnup.* Washington: Office of Nuclear Regulatory Research.

K.J. Geelhood, W. L. (2014). *FRAPCON-3.5: Integral Assessment.* Washington: Office of Nuclear Regulatory Research.

K.J. Geelhood, W. L. (2014). *FRAPTRAN-1.5: Integral Assessment.* Washington: Office of Nuclear Regulatory Research.

Ken Yueh, D. C. (2010, March 08). Clad in Clay. *Nuclear Engineering International*.

Laboratory, O. R. (June, 2011). *Scale: A Comprehensive Modeling and Simulation Suite for Nuclear Safety Analysis and Design.* UT-Battelle.

Lahoda, E. (2010). *Looking Beyond Standard LWR Fuel.* Westinghouse Electric.

Lars Hallstadius, S. J. (2012). Cladding for high performance fuel. *Progress in Nuclear Energy*, 71-76.

Li, B.-S. (2013). *Pellet Cladding Mechanical Interactions of Ceramic Claddings Fuels Under Light Water Reactor Conditions (Master's thesis).* Columbia: University of South Carolina.

M. Flanagan, P. A. (2012). *Observations of Fuel Fragmentation, Mobility and Release in Integral, High-Burnup, Fueled LOCA Tests.* Draft NUREG.

N. Cocera, N. R. (2011). Oxidation resistance of highly porous CVD-SiC coated Tyranno fiber composites. *Journal of the European Ceramic Society*, 1155-1164.

Naslain, R. (1997). Chemical reactivity in the processing and the interactions with the envornment of ceramic matrix composites. *Solid State Ionics*, 959-973.

Neil Todreas, M. K. (1990). *Nuclear Systems 1 - Thermal Hydraulics Fundamentals.* New York: Taylor & Francis.

Neil Todreas, M. K. (2010). *Nuclear Systems* (2nd ed., Vol. 1). Boca Raton: Taylor & Francis.

O.N. Pierron, D. K. (2003). Tensile specimen geometry and the constitutive behavior of Zircaloy-4. *Journal of Nuclear Materials*, 257-261.

Opila, E. J. (2003). Oxidation and Volatilization of Silica Formers in Water Vapor. *Journal of American Ceramic Society*, 1238-1248.

Parlindungan Yonathan, J.-H. L.-H.-J.-Y. (2009). Improvement of SiCf/SiC density by slurry infiltration and tape stacking. *Materials Research Bulletin*, 2116-2122.

Patrick A.C. Raynaud, I. E. (March 13-14, 2014). Methodology for Core-Wide Estimates of Fuel Dispersal During a LOCA. *Public meeting of Fuel Fragmentation, Relocation and Dispersal.* Washington, DC: U.S. NRC. Retrieved from http://pbadupws.nrc.gov/docs/ML1406/ML14066A485.pdf

Patrick Raynaud, I. P. (2014). Predictions of Fuel Dispersal During a LOCA. *Proceedings of WRFPM 2014,* (p. Paper 100026). Sendai.

Peter Askeljung, M. B. (2011). Results of Integral, High-Burnup, Fueled LOCA Tests and Companion Testing with AS-Fabricated and Pre-hydrided Cladding. *IAEA Technical Meeting on Fuel Behavior and Modeling Under Severe Transient and LOCA Conditions.* Mito-City, Japan.

Peterson, C. (1989, March 28). *Continuing Cleanup: $1 Bil. and Counting.* Retrieved from The Washington Post: http://www.washingtonpost.com/wp-srv/national/longterm/tmi/stories/cleanup032889.htm

Pink Tentacle. (2011, April 01). *High-Resolution Photos of Fukushima Daiichi*. Retrieved from Pink Tentacle: http://pinktentacle.com/tag/fukushima/

Price, R. (1977). Properties of silicon carbide for nuclear fue particle coatings. *Nuclear Technology*, 320.

Raynaud, P. (2011). *Fuel Dispersal During a LOCA: Generic Issue Proposal.* NRC.

Raynaud, P. (2012). *Fuel Fragmentation, Relocation, and Dispersal During the Loss-of-Coolant Accident.* Office of Nuclear Regulatory Research. U.S.NRC.

Raynaud, P. (2013). Core-wide Estimtes of Fuel Dispersal During a LOCA. *TopFuel 2013,* (pp. 636-643). Charlotte, North Carolina.

Rohm and Haas Co. (n.d.). Retrieved from http://www.cvdmaterials.com/sicprop2.htm

S. Ray, S. J. (2013). Preliminary Assessment of the Performance of SiC Based Accident Tolerant Fuel in Commercial LWR Systems. *TopFuel 2013*, (pp. 943-950). Charlotte, NC.

Samuel Glasstone, A. S. (1981). *Nuclear Reactor Engineering* (3rd ed.). New York: Van Nostrand Reinhold.

Serope Kalpakjian, S. R. (2010). *Manufacturing Engineering & Technology* (6th ed.). NJ: Prentice Hall.

Steven C. Johnson, R. E. (2012). Severe Accident Modeling of a PWR Core with Different Cladding Materials. *ICAPP '12*, (p. 12175). Chicago.

Tadashi Maruyama, M. H. (2004). Relationship between dimensional changes and the thermal conductivity of neutron-irradiated SiC. *Journal of Nuclear Materials*, 1022-1028.

Takaaki Koyanagi, S. K. (2013). Effect of differential swelling between fiber and matrix on the strength of irradiated SiC/SiC composites. *Journal of Nuclear Materials*, S380-S383.

Team, X.-5. M. (2008). *MNCP - A General Monte Carlo N-Particle Transport Code, Version 5*. Los Alamos: Los Alamos National Security.

The Washington Post. (1999). *Three Mile Island: 20 Years Later*. Retrieved from The Washington Post: http://www.washingtonpost.com/wp-srv/national/longterm/tmi/gallery/photo10.htm

U.S. NRC. (n.d.). *10 CFR 50.46 Acceptance criteria for emergy core cooling systems for light-water nuclear power plants.*

Youho Lee, C. Y. (2012). Oxidation of SiC Cladding Under Loss of Coolant Accident (LOCA) Conditions in LWRs. *ICAPP '12*, (p. 12265). Chicago.

Yutai Katoh, H. K. (2002). Low Temperature Swelling in Beta-SiC Associated with Point Defect Accumulation. *Materials Transactions*, 612-616.

Yutai Katoh, L. S. (2012). Radiation effects in SiC for nuclear structural applications. *Current Opinion in Solid State and Materials Science*, 143-152.

Z. Li, R. B. (1986). Thermal expansion of the hexagonal (4H) polytype of SiC. *Journal of Applied Physics*, 612-614.

Z. Li, R. C. (1986). Thermal expansion of the cubic (3C) polytype of SiC. *Journal of Materials Science*, 4366-4368.